



Universidade do Minho
Escola de Ciências

Ana Célia Araújo Vila Verde

Modelling of dental laser ablation

Tese de Doutoramento
Ciências

Trabalho efectuado sob a orientação da
Professora Marta Maria Duarte Ramos

September 2005

Anexo 3

DECLARAÇÃO

Nome: Ana Célia Araújo Vila Verde

Endereço electrónico: avilaverde@fisica.uminho.pt

Telefone: 253 604320_5323 Braga

Número do Bilhete de Identidade: 10829917

Título tese: Modelling of dental laser ablation

Orientador(es): Prof. Marta Maria Duarte Ramos

Ano de conclusão: 2005

Designação do Ramo de Conhecimento do Doutoramento: Ciências

É AUTORIZADA A REPRODUÇÃO INTEGRAL DESTA TESE APENAS PARA EFEITOS DE INVESTIGAÇÃO, MEDIANTE DECLARAÇÃO ESCRITA DO INTERESSADO, QUE A TAL SE COMPROMETE.

Universidade do Minho, 16 / 09 / 2005

Assinatura: _____

Aos meus pais, por tudo.

Acknowledgements

The work described in this Thesis was done in collaboration with Prof. Marshall Stoneham (Department of Physics and Astronomy, University College London) and Prof. Gavin Pearson (Institute of Dentistry, Queen Mary University of London).

The project associated with the research developed in this Thesis was funded by Fundação para a Ciência e a Tecnologia (FCT) under project no. POCTI/ESP/37944/2001 (supported by the European Community Fund FEDER) and by PhD. fellowship number SFRH/BD/4725/2001.

Gostaria de agradecer à Prof. Marta Ramos por ser, numa palavra, uma grande orientadora deste trabalho de doutoramento: porque esteve sempre disponível para discutir dúvidas, resultados e conclusões, por orientar o seguimento do trabalho, por encorajar a iniciativa e o pensamento independente, pelas palavras de encorajamento, que nunca faltaram. Um grande abraço, mas esse, pela amizade.

Obrigado, Nocas, porque seria uma pessoa pior se não te tivesse conhecido. Este trabalho não teria sido possível sem a tua amizade e ajuda, sem o teu trabalho e dedicação ao grupo. Além de tudo isto, trabalhar sem ti teria sido muito menos divertido...

To Prof. Marshall Stoneham I would like to express my gratitude for the scientific guidance provided throughout these four years of work, for always asking (lots of) questions that made me think and for the words of praise, that helped build my self-confidence. Thank you also for taking the time to talk to me when I was in doubt as to what future career options to make.

I would like to thank Prof. Gavin Pearson for providing the initial motivation for this work and for the scientific meetings that helped me understand the issues related to dental laser ablation and minimally invasive dentistry which were most pressing to understand and solve.

Ao Dr. Gustavo Dias, Prof. Ricardo Ribeiro e Prof. Joaquim Carneiro gostaria de agradecer a disponibilidade demonstrada para responder às minhas questões, especialmente na parte inicial do meu programa doutoral, quando a minha inexperiência nestas coisas computacionais vinha ao de cima todos os dias...

A todos os meus professores, por terem incentivado o meu gosto pelo conheci-

mento e por terem acreditado em mim, o meu obrigado.

A todas as pessoas que trabalham no departamento de Física da Universidade do Minho, pela simpatia e boa vontade demonstrada de todas as vezes que precisei de ajuda, o meu obrigado.

Gostaria de agradecer também ao Sr. Armando Mendes, pelos cuidados demonstrados a resolver problemas do disco no meu computador, que evitaram que todos os meus dados desaparecessem no final do meu quarto ano de trabalho...

Aos amigos de sempre (correndo o risco de fazer plágio, O Pessoal!), o meu obrigado pela alegria que me deram ao longo destes anos e por não levarem a mal todas as festas em que saí mais cedo porque o dia seguinte era sempre dia de trabalho...

Um abraço forte, forte às amigas mais especiais do mundo (Raquel, Rita e Sandrine), porque crescer com vocês, em todos os aspectos da vida, foi e continua a ser maravilhoso. Também sem vocês eu seria uma pessoa pior.

Aos meus pais e irmãos, pelo apoio dado ao longo de todos estes anos, pela paciência nos momentos em que estive ruim de aturar, pelos momentos em que não estive presente, não tenho palavras para expressar o que sinto.

Finally, to my husband, Kramer, for bringing out the best in me, for believing in me, for allowing me to be more than I could ever be by myself.

Braga, Portugal
Setembro de 2005

Ana Vila Verde

Resumo

Modelização do processo de evaporação por laser dos dentes

O objectivo final do trabalho descrito nesta tese consiste na determinação dos melhores parâmetros de funcionamento de lasers de modo a ser possível escavar túneis compridos e estreitos através do esmalte e da dentina, um dos procedimentos necessários para se proceder a um tratamento minimamente invasivo da cárie dentária. Primeiramente é apresentada uma revisão da literatura onde são identificadas as gamas de valores dos parâmetros de funcionamento do laser para as quais são esperados os melhores resultados, e são identificados os problemas que necessitam de ser resolvidos. Os lasers que deverão produzir os melhores resultados com o mais baixo custo financeiro são os de CO_2 e os de Er:YAG, com pulsos de duração na ordem dos microsegundos e com arrefecimento por água. Os problemas a resolver incluem os danos mecânicos infligidos ao material e a possibilidade da água de arrefecimento absorver grande parte da radiação incidente e deste modo impedir que sejam produzidos túneis compridos. Após uma breve introdução ao Método dos Elementos Finitos (a ferramenta de modelização utilizada neste trabalho), são apresentados os modelos produzidos para o estudo da interacção entre os lasers de CO_2 e Er:YAG e o esmalte dentário e os resultados obtidos com esses modelos, para o regime sub-ablativo. Finalmente, são apresentadas as conclusões principais obtidas com este trabalho, sendo dada particular ênfase às linhas de acção práticas que estas sugerem para se obterem melhores resultados experimentais, e são delineados trabalhos futuros que interessa desenvolver nesta área.

Abstract

Modelling of dental laser ablation

The ultimate aim of the work described in this Thesis is to determine the optimal laser operating parameters to drill long, narrow tunnels through enamel and dentine, necessary to treat dental caries in a way that minimizes the amount of material removed from the tooth. In order to do this, a review of the literature is first presented in which the ranges of laser parameter values for which the best results exist are narrowed down and the issues to be solved are identified. It is expected that CO₂ and Er:YAG lasers with microsecond pulse duration and water cooling will produce the best results at a minimum financial cost. Issues to be addressed include the extent of mechanical damage caused by the lasers and whether the cooling water will absorb a large fraction of the incident radiation and thus prevent the material from being ablated. After a brief introduction to the Finite Element Method (the modelling tool used throughout this work), the models designed to investigate ablation of dental enamel by the CO₂ and Er:YAG lasers are described and the results obtained for a sub-ablative regime are presented. Finally, the main conclusions obtained by this work are given and the practical guidelines to obtain better results when ablating dental enamel are presented. A brief indication of the work to be done in the future concludes this Thesis.

Contents

Acknowledgements	v
Resumo	vii
Abstract	ix
Contents	x
List of Figures	xiii
List of Tables	xvii
List of Abbreviations	xxi
1 Teeth, caries and dental care	1
1.1 The structure of teeth	1
1.2 Caries	6
1.3 Brief description of conventional caries treatment	8
1.4 Minimally invasive caries treatment	10
1.4.1 Current state-of-the-art in minimally caries treatment	10
1.4.2 A new minimally invasive surgical treatment for dental caries	14
2 Generic considerations on laser irradiation of tissues	19
2.1 Introduction	19
2.2 Very long laser exposures: photochemical interactions	20
2.3 Ultrashort short laser exposures: plasma induced ablation	21
2.4 Picosecond, nanosecond and microsecond laser pulses	24
2.4.1 Picosecond and nanosecond pulses: photodisruption	24
2.4.2 Picosecond laser pulses: plasma-induced ablation	25
2.4.3 Nanosecond pulses: photoablation	26
2.4.4 Microsecond pulses: thermal interaction	29
2.5 Conclusion	33
3 Experimental evidence on picosecond, nanosecond and microsecond pulses in dentistry	35
3.1 The optical properties of enamel and dentine	36
3.2 The temporal profile of laser pulses	42
3.3 Lasers primarily absorbed by water and organic material	44
3.3.1 The Er:YAG lasers	44

3.3.2	The ultraviolet lasers	52
3.4	Lasers primarily absorbed by the mineral	59
3.4.1	The YSGG lasers	60
3.4.2	The CO ₂ lasers	65
3.5	Summary and conclusion	71
4	Further considerations on ablation of enamel by mid-IR lasers	75
4.1	The mechanisms of ablation of enamel by mid-IR lasers	75
4.2	The role of water	77
4.3	Influence of the laser spatial intensity profile	84
4.4	Absorption and scattering by the ablation plume	86
4.5	Conclusion	90
5	The modelling tools to use: the finite element method	91
5.1	General description of the FE method	91
5.2	Obtaining the temperature and stress maps	94
5.2.1	The equations to solve	94
5.2.2	The algorithms to use	96
5.3	Obtaining the natural frequencies of a structure: the natural frequency extraction algorithm	101
5.4	The mesh	102
6	Description of models, results and discussion	107
6.1	Boundary conditions	107
6.1.1	Model description	108
6.1.1.1	Boundary conditions for stress analyzes	110
6.1.1.2	Boundary conditions for thermal analyzes	114
6.1.2	Results and discussion	115
6.2	Influence of the enamel structure on its response to laser irradiation: the water layer models	125
6.2.1	Model description	125
6.2.2	Results and discussion	132
6.2.2.1	The influence of the microstructure and the laser wavelength	132
6.2.2.2	The influence of the mesh and material parameters	137
6.3	Influence of water pores on the response of enamel: the macropores model	140
6.3.1	Model description	141
6.3.2	Results and discussion	143
6.4	Influence of pore size on the temperature and stress distribution: the nanoscale pore models	148
6.4.1	Description of the finite element model	149
6.4.1.1	Results and discussion	154
6.4.2	Description of the analytical stress model	161
6.4.2.1	Results and discussion	163

6.5	Investigating the influence of the pulse duration on the stress levels: the pulse duration models	165
6.5.1	Model description	166
6.5.2	Results and discussion	167
7	Conclusions and future work	171
Annex 1:	names of input files for the simulations reported	191
Annex 2:	example of a UMAT subroutine used to model the EOS of water	193
Annex 3:	summary table for Chapter 3	199

List of Figures

1.1	Cross-sectional image of a tooth.	2
1.2	Enamel crystallites.	3
1.3	The hydroxyapatite crystallite orientation in the rods.	3
1.4	Electron micrograph of a cross-section through enamel rods.	4
1.5	Enamel hardness and Young's modulus for the mesial half of a maxillary tooth.	5
1.6	The dentinal tubules.	6
1.7	Enamel caries seen by polarized light.	7
1.8	Minimally invasive occlusal cavity prepared by air abrasion.	12
1.9	Examples of the extent of material removal done by currently available MI surgical procedures to treat caries.	13
3.1	Infrared transmission spectrum of dental enamel between 2.5 μm and 12 μm	36
3.2	Fourier transform infrared spectra of human dental enamel and dentine between 2.5 and 20 μm	37
3.3	Reflectance spectra of dentine between 6 and 14 μm	38
3.4	Absorbance spectra of dentine between 200 and 2500 nm.	39
3.5	Absorbance spectra of HA between 200 and 780 nm.	40
3.6	Temporal pulse shape for a free-running laser.	43
3.7	Temporal pulse shapes for various laser systems.	43
3.8	Polarized light image of 100 μm thick cross sections of enamel ablated by an Er:YAG laser.	51
3.9	Examples of mechanical damage in dentine caused by a KrF laser at $\lambda = 248$ nm.	55
3.10	Mechanical damage when ablating dentine with a 355 nm Nd:YAG laser.	57
3.11	Thermal damage when ablating dentine with Er:YSGG lasers.	64
3.12	Ablation depth in bovine enamel for the free-running and Q-switched Er:YSGG laser with and without water.	64
4.1	Fourier image of Er:YAG laser-induced acoustic signal on enamel.	78
4.2	Simplified HA phase diagrams in the presence and absence of water vapor.	80
4.3	Absorption coefficient of water at 2.94 μm as a function of the energy density.	82
4.4	Change in the effective absorption coefficient of water at 9.6 and 10.6 μm as a function of deposited energy per unit volume.	83

5.1	Control volume for one-dimensional heat conduction.	95
5.2	Initial configuration of a rod with a concentrated load, P, at the free end.	97
5.3	Configuration of a rod with a concentrated load, P, at the free end, at the beginning of the second increment	98
5.4	Free-body diagram of a rod with a concentrated load, P, at the free end.	99
5.5	Mass-spring system.	101
5.6	Example of linear and quadratic elements.	103
5.7	Example of full and reduced integration elements.	104
6.1	Geometry of models <i>Large</i> and <i>TestBC1</i>	112
6.2	Temperature distribution for model <i>Large</i> , at the end of the laser pulse. .	117
6.3	Comparing the temperature maps obtained for models <i>Large</i> and <i>TestBC2</i> .	118
6.4	Von Mises stress for model <i>Large</i> and model <i>TestBC1</i>	119
6.5	Comparing the nodal displacement and Von Mises stress values for mod- els <i>Large</i> , <i>TestBC1</i> using appropriate BC's and <i>TestBC1 not</i> using the appropriate BC's.	120
6.6	Comparing the nodal displacements as a function of time for models <i>Large</i> and <i>TestBC2</i>	122
6.7	Comparing the Von Mises Stress values at the center of the irradiated face for models <i>Large</i> , <i>TestBC2</i> using appropriate BC's and <i>TestBC2</i> <i>not</i> using the appropriate BC's.	124
6.8	Cross-sectional view of enamel rod model.	126
6.9	The structure of model <i>RodsWL</i>	126
6.10	Temperature maps at the end of the laser pulse for models <i>RodsWL</i> and <i>RodsHom</i>	132
6.11	Nodal displacement at the end of the 0.35 μ s laser pulse for model <i>RodsWL</i> .	133
6.12	Minimum and maximum principal quasi-static stress at the end of 0.35 μ s for models <i>RodsWL</i>	134
6.13	Minimum and maximum principal quasi-static stress at the end of 0.35 μ s for model <i>RodsHom</i>	135
6.14	Temperature (in kelvin) at the end of the 0.35 μ s CO ₂ laser pulse for models <i>RodsHom</i> and <i>CubesHom</i>	138
6.15	Quasi-static stress maps at the end of the 0.35 μ s laser pulse for models <i>RodsHom</i> and <i>CubesHom</i>	139
6.16	The overall geometry of model <i>RodsPores</i>	141
6.17	Temperature at the end of a single 0.35 μ s laser pulse for model <i>RodsPores</i> .	143
6.18	Minimum and maximum principal quasi-static stress at the end of 0.35 μ s for models <i>RodsHom</i> , <i>RodsWL</i> and <i>RodsPores</i>	146
6.19	Minimum and maximum principal quasi-static stress at the end of 0.35 μ s for elements composing the rod sheath in models <i>Rod-</i> <i>sHom</i> , <i>RodsWL</i> and <i>RodsPores</i>	147
6.20	Geometry of model <i>SmallPore70</i>	149
6.21	Von Mises stress as a function of time for models <i>SmallPore70</i> and <i>Cubes</i> .	155
6.22	Temperature distribution at the end of the laser pulse for simulation SmallPore70Er_water_2e10	158

6.23	Von Mises stress at $t = 0.44 \mu s$ for the 70 m pore model with Er:YAG laser.	159
6.24	Von Mises stress as a function of time for the central top element for two different pulse durations: 0.1 and 10 μs	169

List of Tables

2.1	Dissociation energies of selected chemical bonds.	27
2.2	Thermal and acoustical relaxation time for various optical absorption coefficients.	30
3.1	Optical properties of human dental enamel obtained experimentally. . .	38
3.2	Optical properties of human dentine obtained experimentally.	40
6.1	Laser and simulation parameters used in models <i>Large</i> , <i>TestBC1</i> and <i>TestBC2</i>	109
6.2	Mechanical properties of enamel and Restrain-layer used in models <i>Large</i> and <i>TestBC1</i>	110
6.3	Geometrical parameters for models <i>Large</i> , <i>TestBC1</i> and <i>TestBC2</i>	115
6.4	Distinguishing simulation parameters to assess the effect of using appropriate boundary conditions on the temperature and stress generated in a material.	116
6.5	Maximum and average Von Mises stress at the end of 250 μ s for several elements in models <i>Large</i> and <i>TestBC1</i>	121
6.6	Laser parameters for simulations <i>RodsHom</i> , <i>RodWL</i> and <i>CubesHom</i>	127
6.7	Material properties used in models <i>RodsHom</i> , <i>CubesHom</i> and <i>RodsWL</i>	128
6.8	Geometric parameters for models <i>Rods</i> and <i>Cubes</i>	130
6.9	Relevant parameters for simulations <i>CubesHom</i> , <i>RodsHom</i> and <i>RodsWL</i>	131
6.10	Minimum and maximum principal quasi-static stress at the end of the 0.35 μ s laser pulse for model <i>RodsWL</i>	136
6.11	Ultimate tensile and compressive strength for enamel and hydroxyapatite. . . .	136
6.12	Minimum and maximum quasi-static principal stress values for model <i>RodsHom</i> and model <i>Cubes</i>	138
6.13	Laser parameters used in model <i>RodsPores</i>	142
6.14	Distinguishing simulation parameters used for models <i>RodsHom</i> , <i>RodsWL</i> and <i>RodsPores</i>	142
6.15	Parameters used for the Equation of State for water.	151
6.16	Properties of enamel used in models <i>SmallPore</i>	152
6.17	Geometrical parameters for the three models <i>SmallPore</i>	153
6.18	Laser parameters used in models <i>SmallPore</i>	153
6.19	Distinguishing simulation parameters for models <i>SmallPore</i>	154
6.20	Time-averaged Von Mises Stress values for simulations <i>Cubes_CO2.1.2e10</i> and <i>SmallPore70CO2_hom.1.2e10</i>	156

6.21	Maximum temperature and pressure reached at the end of the laser pulse for the various pore-sizes in models <i>SmallPore</i>	158
6.22	Parameters used in the stress-strain relationship for a spherical pore surrounded by an infinite medium.	162
6.23	Maximum pressure reached at the pores as a function of temperature, obtained using the analytical pore-model.	164
6.24	Von Mises stress as a function of pulse duration for model <i>Cubes</i>	168
6.25	Von Mises stress as a function of pulse duration for model <i>Cubes</i> (using the same temperature distribution for all the simulations).	169

List of Abbreviations

A - Area.

ADJ - Amelodentinal junction; the interface between enamel and dentine.

ArF - Argon fluoride. This laser emits at 193 nm.

BC - Boundary condition.

BRL - Bottom Restrain-layer.

CO₂ - Carbon dioxide. The CO₂ lasers emit between 9.3 and 10.6 μm .

CW - Continuous wave.

d - Global nodal displacement matrix.

DOF - Degrees of freedom.

E - Young's modulus.

EDTA - Ethilenediamine tetra-acetic acid; used to remove smear layer after drilling root canal.

E_{en} - Young's modulus of enamel.

E_{en+den} - Young's modulus of a layer composed of enamel and dentine.

en - Enamel.

EOS - Equation of state.

Er,Cr:YSGG - Erbium, chromium: yttrium, scandium, gallium, garnet. This laser emits at 2.78 μm .

Er:YAG - Erbium: yttrium, aluminum, garnet. This laser emits at 2.94 μm .

Er:YSGG - Erbium: yttrium, scandium, gallium, garnet. This laser emits at 2.79 μm .

E/V - Energy per unit volume.

F - Global force matrix.

FDA - Food and drug administration.

FE - Finite element.

FEL - Free electron laser.

FEM - Finite Element Method.

FTIR - Fourier Transform Infrared Spectroscopy.

FWHM - Full width at half maximum.

H - Hardness of a material (measures the material's resistance to deformation).

HA - Hydroxyapatite.

I - Intensity of the laser (energy per unit area and per unit time).

I_0 - Intensity of the laser at the center of the laser spot.

IR - Infrared.

K - Stiffness matrix.

K_{Ic} - Toughness of a material (measures the material's resistance to fracture in the presence of cracks).

KrF - Krypton fluoride. This laser emits at 248 nm.

ℓ - Length.

ℓ_{en} - Thickness of enamel measured in the XY plane.

$\ell_{en,expanding}$ - Thickness of enamel surrounding the model, measured in the XY plane, which is considered to suffer thermal expansion under the influence of the laser.

L_{LRL} - Thickness of the lateral Restrain-layer.

LRL - Lateral Restrain-layer.

MI - Minimally invasive.

Nd:YAG - Neodymium: yttrium, aluminum, garnet. This laser emits at 1.06 μm .

P - Pressure.

Q - Heat.

r - Radial distance from the center of the laser beam.

RL - Restrain-layer.

S. D. - Standard deviation.

SEM - Scanning electron microscope.

SRIFTS - Specular reflectance infra-red fourier transform spectroscopy.

T - Temperature.

t - Time.

TCP - Tricalcium phosphate.

TEM₀₀ - Transverse electromagnetic mode.

TPI - Terahertz pulse imaging.

UTS - Ultimate tensile strength.

UV - Ultraviolet.

UVA - Ultraviolet radiation in the 315 - 400 nm range.

UVB - Ultraviolet radiation in the 280 - 315 nm range.

UVC - Ultraviolet radiation in the 100 - 280 nm range.

V - Volume.

V_m - Volume per unit mass.

v/v - By volume.

VMS - Von Mises stress.

w - Radius of the laser beam at $1/e^2$ of the incident intensity, I_0 .

WL - Water layer.

w/w - By weight.

XeCl - Xenon chloride. This laser emits at at 308 nm.

XeF - Xenon fluoride. This laser emits at 351 nm.

z - Depth inside a material.

α - Thermal expansion coefficient.

ΔT - Change in temperature.

Δz_{BRL} - Thickness of the bottom Restrain-layer

Δz_{en} - Thickness of enamel measured along OZ.

Δz_{en+den} - Thickness of a layer of enamel and dentine measured along OZ.

$\Delta z_{en+den,expanding}$ - Thickness of a layer of enamel and dentine beneath the model, measured along OZ, which is considered to suffer thermal expansion under the influence of the laser.

ϵ - Strain.

κ - Thermal conductivity.

λ - Wavelength.

μ - Optical absorption coefficient.

$1/\mu$ - Optical absorption depth; the depth at which the intensity of radiation becomes $1/e$ of the incident intensity.

ν - Poisson's ratio.

ρ - Mass density.

σ - Stress.

τ_{ac} - Acoustic relaxation time.

τ_{ther} - Thermal relaxation time.

ϕ - Variance.

Chapter 1

Teeth, caries and dental care

In this chapter the generic structure of teeth will be described, together with the morphology and composition of the two tissues that are most commonly ablated during dental laser treatment: enamel and dentine. The description of enamel will be more complete than that of dentine, given that in this Thesis only the subject of enamel laser ablation is addressed. Subsequently the theme of dental caries will be introduced and the state-of-the-art in caries treatment will be described, highlighting the aspects that need to be improved. To conclude, the case for the need of minimally invasive caries treatment will be presented and the requirements of the laser technique being developed by Pearson and co-workers at Queen Mary Westfield College in London, United Kingdom, which provided the motivation for this work, will be emphasized.

1.1 The structure of teeth

Teeth, either deciduous or permanent, have the basic structure which can be seen in Fig. 1.1: the outer layer is the enamel, beneath it one finds dentine and at the center is the pulp of the tooth. The junction between enamel and dentine is called the amelodentinal junction (ADJ). Enamel and dentine are highly mineralized tissues displaying a complex mesostructure which still today fascinates researchers because of its beauty, functionality and complexity. Enamel is the hardest substance in the human body; in fact, its hardness is comparable to that of mild steel. It is mainly composed by hydroxyapatite (HA) mineral ($\approx 95\%$ by weight, or w/w), and it also contains small amounts of water ($\approx 4\%$ w/w) and organic material ($\approx 1\%$ w/w), which make up for the remaining material [2]. The actual percentages vary according to the source of the information because of the variability associated

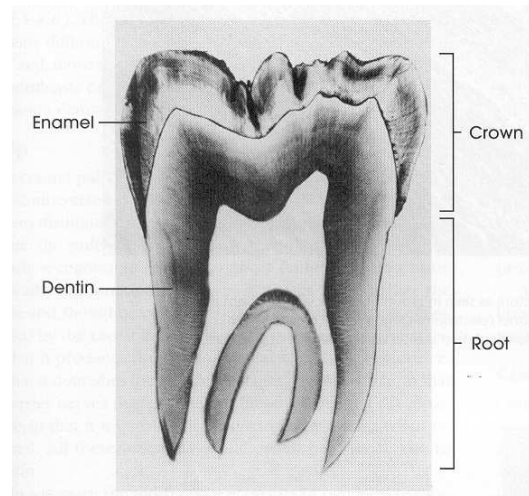
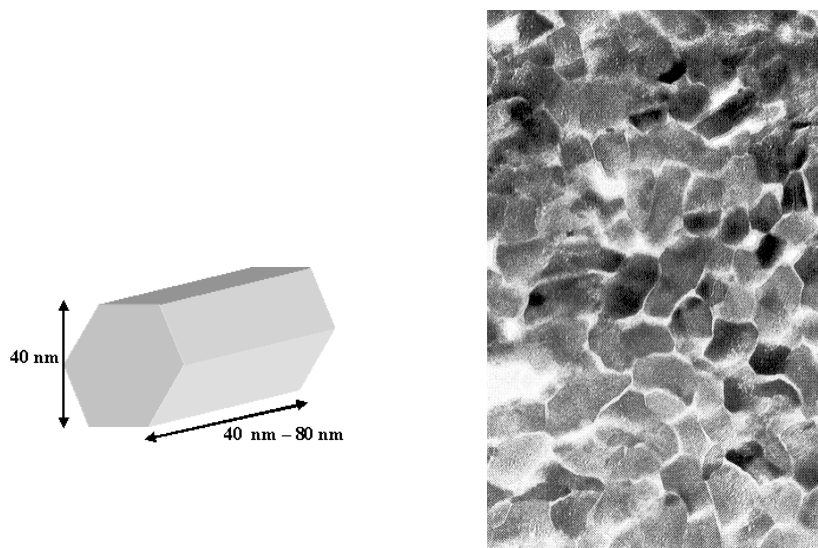


Figure 1.1: Cross-sectional image of a tooth; only hard tissue is shown. Source: ref. [1], pp. 3.

to the different samples used by each author and also the type of measurement technique used. For example, work by Dibdin [3] suggests that the total water in enamel may amount only to $2.0 \pm 0.4\%$ w/w, or $6.0 \pm 1.2\%$ by volume (v/v). Also, it is known that the degree of mineralization increases from the ADJ to the surface of the tooth, and that deciduous teeth have a lower mineral concentration and higher porosity than permanent teeth [4, 5].

HA has the chemical formula $\text{Ca}_{10}(\text{PO}_4)_6(\text{HO})_2$, but substituents such as Cl^- , F^- , Na^+ , K^+ , Mg^{2+} and CO_3^{2-} exist in the crystal lattice. The last substituent, carbonate, is the most important of all, representing 3% to 5% w/w. This mineral is organized in hexagonal crystallites that have an average diameter of 40 nm and length of 40 nm to 1 μm (see Fig. 1.2), which in turn organize into larger structures, called the enamel rods or prisms. The orientation of the crystallites in the rods obeys an intricate pattern which can be seen in Figs. 1.3 and 1.4. The enamel rods have an average diameter of approximately 5 μm , and extend from the enamel-dentine junction to the free surface of the tooth, being approximately perpendicular to that surface.

Water and organic material are mainly located in micropores at the interface between crystallites; the region of highest porosity is the boundary between enamel rods, the rod sheath. The pore surface-area and volume distributions in enamel are not known accurately, because of the difficulty in determining these quantities; however, work by Dibdin et al. [3] suggests that enamel has a minority of larger pores, holding approximately 0.3% v/v water and located mainly in rod boundaries, and a majority of smaller pores, holding approximately 6% v/v of water.



(a) A schematic representation of a single crystallite. (b) Electron micrograph of enamel crystallites. Organic material and water exist in the spaces between the crystallites. Source: ref. [1], pp. 218.

Figure 1.2: Enamel crystallites.

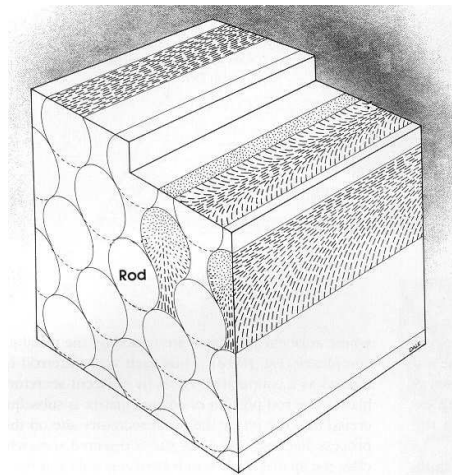


Figure 1.3: Fine structure of enamel, highlighting the orientation of the crystallites as a function of their position in the rod. Source: ref. [1], pp. 222.

The characteristic diameter of the smaller pores is thought to range from 2 nm to 20 nm [7], but the uncertainty associated with these values is high (could be as high as $\approx 50\%$). The diameter of the larger pores was not established in the literature. The water in enamel pores seems to behave like liquid bulk water as far as diffusion is concerned, even for pores as small as a few nanometers [8]; this

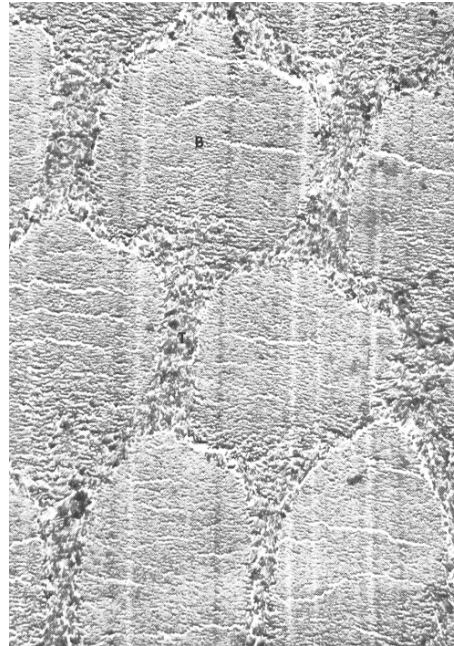


Figure 1.4: Electron micrograph of a cross-section through enamel rods. The orientation of the crystallites is different at the "bodies" B and at the "tails" T. (approximately $5000\times$.) Source: ref. [6], pp. 52.

observation is supported by theoretical and computational work done by Liu et al. [9] and Giaya et al. [10], indicating that water in pores made of an hydrophillic substance such as HA should behave like liquid bulk water.

The mechanical properties of enamel have been investigated extensively for over 30 years, but studies attempting to measure mechanical properties at a micrometer scale were possible only in the past 10 years. Cuy et al. [11] used nanoindentation to determine the hardness (H) and Young's modulus (E) of dental enamel for the mesial half of a maxillary M² tooth ¹, and have found that they vary significantly (over 50%) even within the same tooth, increasing between the ADJ and the free enamel surface as can be seen in Fig. 1.5. They related the observed variations mainly to changes in mineral content, and found them to be less dependent on the microstructure or rod alignment. However, other authors have found some evidence that the orientation of the rods and the location of the indentations (at the body of the rod or at the tail) have a significant influence on the values of E and H . For example, Habelizt et al. [12] have found that E and H can be higher by $\approx 20\%$ when measured in directions parallel to the enamel rods than in directions perpendicular to the rods. They also found that E and H are lower at the tails of the enamel rods and in the inter-rod enamel than at the bodies

¹The front half of the second upper molar.

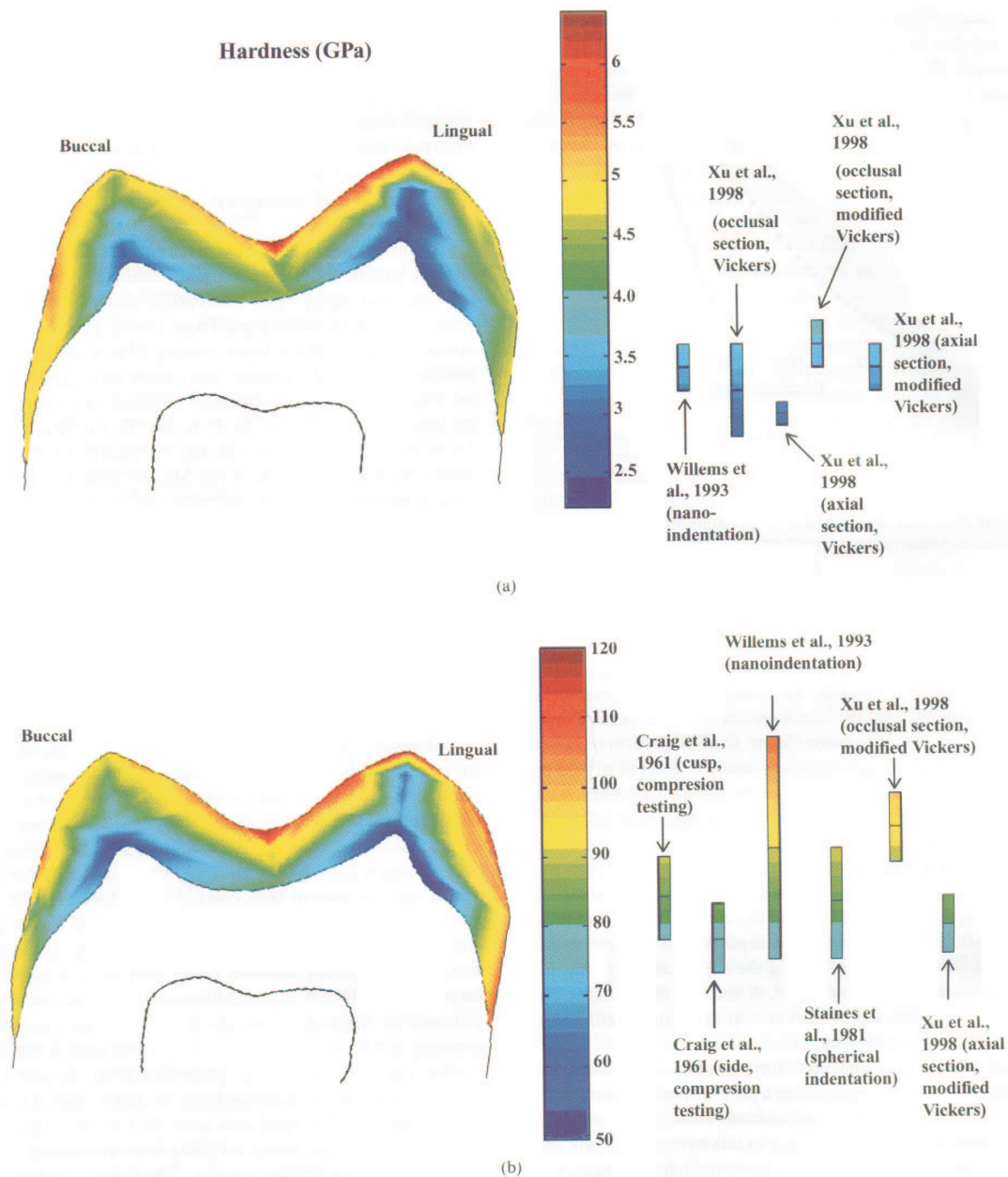


Figure 1.5: (a) Enamel hardness, H , and (b) Young's modulus, E , for the mesial half of a maxillary M^2 tooth determined by Cuy et al. by nanoindentation. The standard deviations for these averages range from 0.2 to 0.3 GPa for H and from 2 to 5 GPa for E . Average values of H and E that were reported by several other authors were included by Cuy et al. in the image. Source: ref. [11].

of the rods. They attributed these variations to the changes in the alignment of the apatite crystals which can be seen in the scheme in Fig. 1.3. This suggestion is supported by the results obtained by Spears [13] using Finite Element models in which the orientation of the crystallites and of the rod was explicitly accounted for.

Dentine is a much less mineralized tissue than enamel: it is composed of only $\approx 70\%$ w/w HA, $\approx 20\%$ w/w organic material and $\approx 10\%$ w/w water adsorbed on the surface of the mineral or in micropores between the crystallites. The organic material in dentine is mainly collagen (unlike enamel, which has no collagen), as well as some proteins. The structure of dentine is characterized by the presence of a large density of dentinal tubules (as many as 60 000 to 70 000 per square millimeter), which extend from the pulp of the tooth to the ADJ (see Fig. 1.6). Extending from the dentinal tubules at approximately 90° are the microtubules. The tubules are wider close to the enamel, where their characteristic diameter is 3 to 4 μm , than close to the pulp, where it is only $\approx 1 \mu\text{m}$. Although there is not yet a full consensus as to the content of the dentinal tubules, they are thought to hold tissue fluid and an odontoblast process², and to be lined by a thin layer of organic material. The dentine that forms the wall of the dentinal tubule is called the peritubular or intratubular dentine and has a much higher degree of mineralization ($\approx 40\%$) than the intertubular dentine [1].

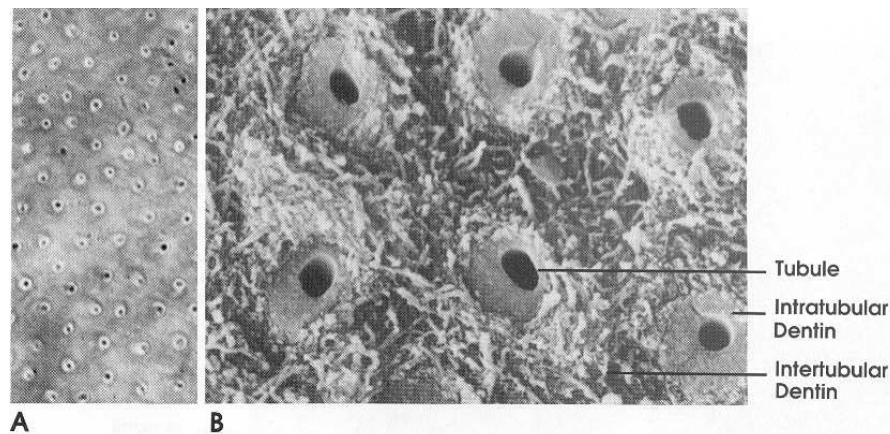


Figure 1.6: The structure of dentine, seen by light microscopy, A, and scanning electron microscopy (SEM), B. The dark central spots are empty dentinal tubules surrounded by intratubular dentine. Source: [1], pp. 158.

1.2 Caries

Dental caries is a disease caused by bacteria where these organisms demineralise the inorganic component of the tooth and disintegrate its organic component. A young carious lesion, one that affects only enamel, comprises several different

²Citoplasmatic extensions of the cells that form dentine, the odontoblasts.

areas when seen under the light microscope as in Fig. 1.7. The free surface of enamel is normally still mineralized, because although bacteria are demineralizing it, minerals present in the saliva can precipitate at the surface and thus counteract the effect of the bacteria. Below the surface, at the body of the carious site, is where most of the demineralization takes place. However, just below the body of the lesion one can find an area which was at some point demineralized by the bacteria but which was remineralized subsequently, and that has a dark appearance when seen under polarized light. Finally, below this dark area is a translucent zone, which is in fact the inner advancing front of the carious lesion. Caries is thus the result of a competition between the acid attacks by the bacteria

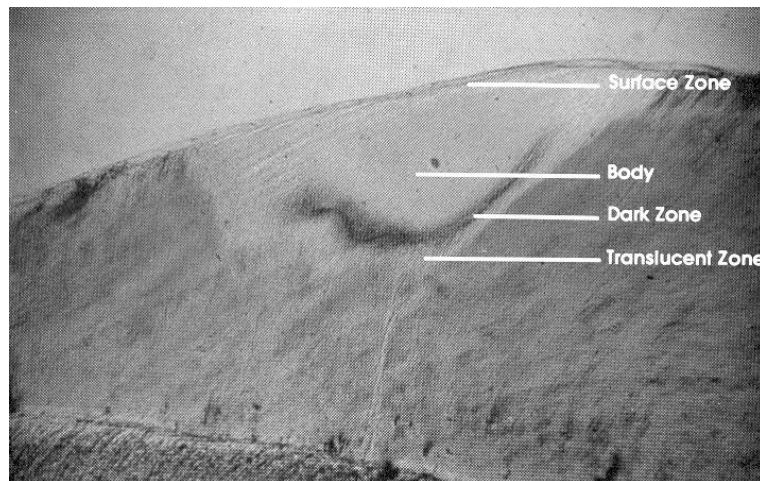


Figure 1.7: Enamel caries seen by polarized light. The translucent zone, dark zone, body of the lesion and surface zone are all visible. Source: [1], pp. 416.

and the physicochemical processes occurring naturally at the tooth that tend to deposit minerals back in enamel. This means that enamel can repair itself if the demineralization/remineralization equation is shifted to our favor, by reducing the concentration of bacteria, and that early carious lesions can be treated without any sort of invasive treatments, by simply maintaining adequate eating and oral hygiene habits. However, most people find it hard to do this consistently, which justifies the need for the work presented in this Thesis...

A mature carious lesion, which has reached dentine, is composed of two areas – the *infected layer* and the *affected layer* – frequently hidden from the eye by a thin enamel layer still intact. The infected layer contains large amounts of bacteria and has a soft consistency, because it is composed of "denatured and unstructured enamel and dentine debris" [14, 15]. The affected layer lies underneath the infected layer and is composed of demineralised dentine that still presents clearly defined

dentinal tubules supported by the collagen matrix. Like for enamel, the progression of the infection in dentine is a dynamic competition between the bacteria that demineralize dentine and the tooth's defense mechanisms, which consist in laying out a layer of highly mineralized tissue with low tubule density, called reparative or sclerotic dentine, attempting to stop the caries progression. However, without outside intervention the reparative processes are not enough to stop the spread of the caries, and bacteria eventually win the race thus causing pain and inflammation of the tooth. The various existing medical procedures to stop the progression of caries will thus be the subject of the next section of this Thesis.

1.3 Brief description of conventional caries treatment

The principles of the only type of caries treatment available until the 1990's were established at the end of the 19th century by G. V. Black. They were based on the principle of "extension for prevention" which meant that when treating a tooth for caries, the dentist should remove also the healthy tissue that was in regions with a high probability of developing *future* caries. Also, not only the infected dentine but all the affected dentine should be removed. The guidelines for cavity classification and preparation were tailored to the needs of the only cheap and available filling material – amalgam. An amalgam restoration needs to be extensive so that the strength of the material is increased, it needs 90° cavosurface margins³ for resistance to marginal fracture, straight internal walls and defined line angles, and a macroretentive design by convergence of walls or proximal grooves [14, 15]. These requirements in terms of cavity preparation mean that, after the removal of the infected and affected dentine, more healthy tissue has to be removed in making the cavity appropriately shaped. Once a tooth has been treated for caries, it will probably require more treatments in the future because of re-infection: for example, it is known that over 60% of all restorative dentistry in the United Kingdom is concerned with the replacement of restorations [16]. This leads to more loss of healthy tissue and a more complex restoration, which is more costly and has a higher probability of failing again. Eventually, the root of the tooth may need to be filled, or the tooth may need to be extracted and

³The top edges of the cavity.

replaced by dentures, bridges or implants [16, 17]. This cycle, termed "tooth death spiral" by some authors [18], is further enhanced by the fact that the dental bur causes notches in teeth adjacent to the tooth being treated in 75% [14, 15] to 95% [18] of all cases. These notches weaken enamel, increasing the probability of developing caries. On top of the discomfort, pain and loss of time caused to patients undergoing treatment of carious teeth, this treatment has significant financial impact both for the individual and for National Health Systems. Treating tooth decay costs the National Health Service of England and Wales ⁴ £173 million per year in simple, direct restorations (fillings) and £156 million per year in dental crowns [16]. Improving treatment of caries by making treated teeth less susceptible to failure can thus significantly improve the health of individuals and minimize the large financial cost of caries.

The search for an improved dental treatment led several teams to look for filling materials other than amalgam, for which the cavity design was less stringent and, therefore, that could provide a less invasive, more aesthetically acceptable treatment. During the 1990's, several new filling materials became available [18]: composite resins, glass ionomer cements, resin-modified glass ionomer cement and compomers, cast gold (this one was available before the 1990's) and other alloys. These are currently widely used, despite the fact that for some of them there is "limited evidence on their long-term clinical performance" [16]. Overall, and despite the grim picture painted above regarding amalgam fillings, this is still the material of choice to restore teeth when its dark color does not cause aesthetical problems: amalgam fillings are the most durable and cheapest. When aesthetics are an issue, composite restorations with dentine bonding, in particular those that use an acid primer, are normally used [16]. Composite materials do present an advantage against amalgam: they do not require the large cavity design described above because they have better adhesive properties [17]. This means that they can potentially be used in procedures in which the shape of the cavity after removing infected dentine does not allow for amalgam filling without further removal of healthy tissue, which would be of advantage despite the fact that they are slightly less durable than amalgam. However, a large fraction of dentists still provides caries treatment without maximizing the conservation of healthy dental tissue [14, 15].

The problems with current dental caries treatment are thus well identified: not enough emphasis is placed on prevention of caries; the amount of healthy tissue

⁴No information was available for Portugal.

removed during invasive treatment of caries is large, thus making the tooth structurally weaker; re-infection of treated sites occurs frequently, and each subsequent treatment makes the tooth weaker. Clearly, the way to improve this is to minimize intervention by emphasizing prevention and to maximize the preservation of healthy tissue when an invasive procedure is indispensable [14, 15]. Caries treatment research has been moving towards this goal for a few years now, under the general denomination of minimally invasive (MI) treatment of caries. A description of existing and future MI treatments for caries is the subject of the next Section.

1.4 Minimally invasive caries treatment

1.4.1 Current state-of-the-art in minimally caries treatment

Minimally invasive caries treatment is much more than a particular type of treatment for caries; it is an entirely different philosophy to the management and treatment of dental lesions, which aims at maximizing the preservation of healthy tissue and, consequently, at maintaining the integrity and functionality of the tooth. It is based on a holistic view of the patient with the aim of making the best treatment choices for each individual patient, rather than providing standardized treatments for typified lesions.

Providing minimally invasive dental care starts long before dental restorations have to be made and, ideally, would never allow lesions to progress that far. It begins with **proper diagnosis** of lesions, so that early lesions in enamel can be detected and treated using **remineralization techniques** [19] that stop the progression of caries and repair enamel. If the caries has already reached dentine, the MI approach would not recommend the placement of a restoration unless enamel cavitation had occurred or if patient discomfort, unacceptable form, function or poor aesthetics make it the best option [19]. Instead, the dentist attempts to **control the infection** by adequate hygiene of the mouth and to **monitor** the temporal evolution of the caries over extended periods of time. Finally, when an invasive intervention is deemed necessary, it is done **removing as little tissue as possible**. This procedure thus has the potential to maximize the useful life of the tooth and to avoid expensive (and painful!) implants, dentures and bridges, thus

contributing to the patient's well being in a way that is impossible with currently available dental treatments.

While the above described course of action seems simple to implement, there are difficulties associated with each of the steps described above due to the state of the current technology and to the reluctance in practitioners and patients to change procedures and daily habits. Early caries diagnosis is harder to do than it sounds, since young caries is not easily identified radiographically and may exist in areas not visible to the eye. Also, even when the lesion is visible, it is sometimes hard to distinguish between surface lesions that can be remineralized or slightly deeper lesions which may require a different treatment. To address this issue, several systems are being investigated that may help in the diagnosis; an example is the spectroscopic analysis of dental fluorescence [20], which can distinguish between dull, shiny and brown lesions in enamel and evaluate lesions with different degrees of activity. However, with the currently available diagnosis tools, today's dentist often has no choice but to remove some enamel and then visually inspect the site, in order to assess the extension of the lesion and thus determine the appropriate course of action [17]. Remineralization techniques consist on decreasing the cariogenic bacteria concentration at the site through adequate hygiene of the mouth [21], increasing the fluoride concentration in the mouth through adequate supplements [19] and, very recently, using synthetic enamel to reconstruct the carious site [22]. However, they require that the patients change their oral hygiene and eating habits, which they may not do to the extent necessary. Monitoring the evolution of enamel caries involves having dental checks with intervals between two and five years, since caries normally evolves very slowly⁵ and (again) depends on the existence of adequate diagnosis tools. A possible technique to be used in monitoring enamel thickness is terahertz pulse imaging (TPI), which can detect changes in the order of 10 μm in enamel thickness [23, 24]. Finally, the currently existing minimally invasive cavity preparation techniques, while representing a major improvement relative to the conventional ones, still remove large amounts of dental material as can be seen in Figs. 1.8 and 1.9.

Clearly, while preventive and reparative measures are the first choice to manage caries, it is unlikely that the need for invasive treatments will disappear. Consequently, it is necessary to create invasive techniques that remove less material than the currently available ones. Prof. Gavin Pearson⁶ and co-workers at Queen Mary

⁵Although the six-month interval has been recommended for over one hundred and forty years, there is no evidence to support the need of such frequent visits to the dentist [18].

⁶Formerly at the Eastman Dental Institute, London, UK.

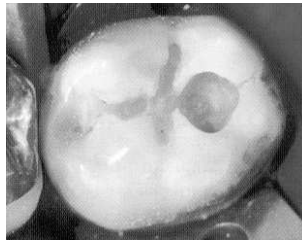
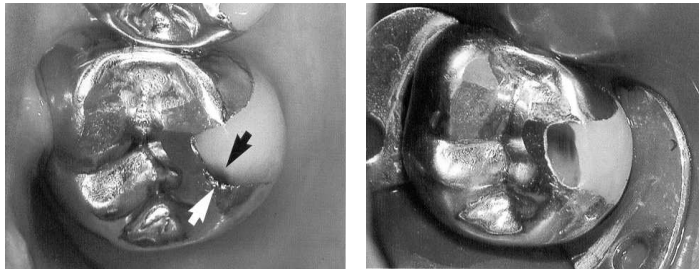
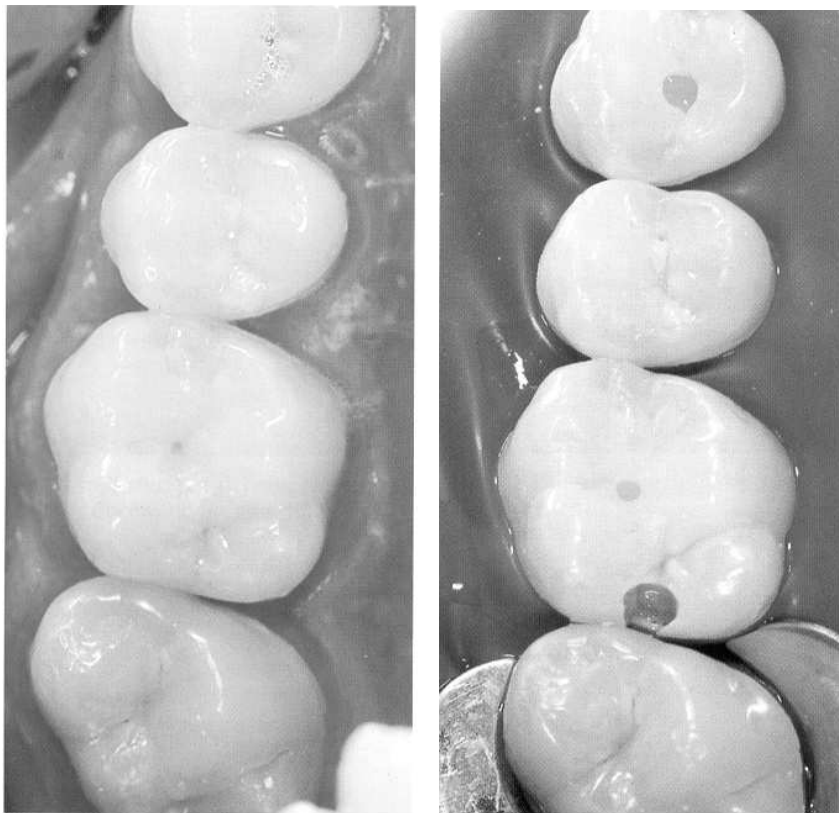


Figure 1.8: Example of the type of cavity prepared using currently available MI surgical procedures (in this case, air abrasion was used to prepare the cavities). Source: ref. [15].

Westfield College, in London, are addressing precisely this aspect of the minimally invasive caries treatment approach: the development of a better surgical treatment of caries. They propose a radically different technique, described in detail in the next Section, which relies on using very narrow tunnels to access the carious site.



(a) Example of a secondary caries developing at the margin of the metal restoration on tooth 27. Source: ref. [25].
 (b) Example of the minimally invasive correction of a restoration of tooth 27. Source: ref. [25].



(c) Clinically, the caries on teeth 26 (distal), 26 (occlusal) and 24 (occlusal) is hardly visible at first. Mirror view. Source: ref. [25].
 (d) Delicate rotating instruments were used to access all the carious lesions. The occlusal extent of caries on tooth 26 turned out to be very slight, but on tooth 24 very great. Note the danger of iatrogenic damage to the adjacent tooth when preparing the distal cavity on tooth 26. Source: ref. [25].

Figure 1.9: Examples of the extent of material removal done by currently available MI surgical procedures to treat caries.

1.4.2 A new minimally invasive surgical treatment for dental caries

The technique proposed by Pearson and co-workers consists on accessing carious sites by means of a tunnel not more than 0.5 mm in diameter, introducing a bactericidal substance to kill the bacteria instead of trying to remove the diseased tissue and, finally, sealing the tunnel. The differences between this new tunnelling technique and the currently available procedures, MI or otherwise, are significant, and the potential advantages are many: because the tunnel used to access the carious site should be very narrow and no attempt is made to further remove diseased material, the structural integrity of the tooth is maximized thus making it less likely to fail; also, because the contact area between the filling material and the tooth is reduced, it is less likely that the cavity seal will fail and thus that bacteria re-enter the site. This technique can thus greatly reduce the probability of a tooth becoming reinfected and, consequently, avoid the need to repair or replace the initial restoration.

However promising this technique is, there are technological problems that need to be solved before it can be used in practice. The first issue to be addressed is the diagnosis of caries: it is vital for this kind of treatment to be able to detect caries accurately with respect to location and extension, so that an appropriate tunnel can be drilled to access the carious site in the most favorable manner. This is easier to do if the caries is visible to the eye, but very often this is not the case. While a radiograph can be very helpful to diagnose caries, it sometimes happens that caries is undetected in radiographs. Also, radiographs only provide a two-dimensional image of the tooth, so it may not be possible to pin-point the 3-dimensional location and extension of caries simply by looking at a radiograph. New methods to diagnose caries are now emerging, such as laser-induced autofluorescence spectroscopy using a 337 nm nitrogen laser developed by Borizova et al. [26] or using a 655 nm diode laser like in DIAGNOdent⁷, or TPI [23, 24]. However, at the moment TPI has only been proved to detect lesions in enamel [24], and there is evidence to suggest that DIAGNOdent may not be as accurate in detecting dentinal caries as radiographic (digital or conventional) methods or even visual or tactile inspection [27]. While the fluorescence method described by Borisova et al. [26] seems promising to identify the depth of

⁷A commercial version of the method that uses a diode laser fluorescence device emitting at 655 nm.

dentinal carious lesions, the efficiency and effectiveness of the method were not directly compared with traditional means of identifying caries. Another method currently being developed is laser-induced frequency domain (i. e., modulating the frequencies of the laser) infrared photothermal radiometric and luminescence signals. The conjugation of photothermal radiometric and luminescence signals allows the method to be very reliable in detecting both deep and surface caries [28]. However, at the moment the experimental setup is still bulky and cannot be used by dentists in their practices. It may be possible that a conjugation of various methods, new and old, may soon provide enough 3-dimensional information about the location and extension of the caries to allow the practitioner to determine if drilling is necessary and to choose the appropriate site to drill a tunnel. However, at the moment these methods do not exist and, consequently, this aspect of the new minimally invasive surgical treatment of caries proposed here remains one of the most critical.

The second requirement of this technique is a tool capable of drilling narrow (diameter < 0.5 mm), high aspect-ratio tunnels through healthy enamel and dentine, as well as through carious tissue. The currently available dental burs are not a good option if the tunnels are to be this narrow, since they all tend to remove much more material than desired. Air abrasion systems, which consist on using a high velocity stream of aluminum oxide particles of 27 or 50 μm in diameter to ablate hard tissue, are also not able to produce the narrow tunnels necessary for this approach [17]. The only tool which can potentially be used to drill tunnels with the desired characteristics is the laser. Several types of lasers are already being used in practice to ablate dental hard tissue, but in the context of conventional cavity preparation, acting merely as replacements of the dental bur. Nevertheless, there are a number of wavelengths that have already been tested for ablation of dental hard tissue and there is a wealth of data available. A revision of the literature (see Chapters 2 and 3) indicates that Er:YAG ⁸and CO₂ ⁹ lasers, among others, may be very good wavelengths for the job, but that it is still necessary to optimize the laser operating parameters (pulse repetition rate, pulse duration, temporal and spatial profile) in order to obtain the best results. In order for lasers to be used in practice, they should drill the appropriate tunnel through dental hard tissues in an amount of time compatible with the duration of a normal visit to the dentist. At the same time, the laser must not cause unwanted side effects, such as cracking

⁸Erbium: yttrium,aluminum,garnet. This laser emits at 2.94 μm .

⁹Carbon dioxide. The CO₂ laser family emits between 9.3 and 10.6 μm .

or overheating of the pulp of the tooth. Although the dental bur is known to cause cracks in enamel to a depth of $\simeq 30 \mu\text{m}$ without the subsequent occurrence of bacterial reinfection, cracks deeper than that should be avoided. Regarding heating of the tooth pulp, the accepted rule-of-thumb is that the temperature at the pulp should not increase more than 5°C [29]. Despite the array of conditions that must be met by the laser, research into this aspect of MI surgical caries treatment is at an advanced stage, and one can expect appropriate laser systems to become available in the next few years.

Once ablation starts, it will be necessary to identify the type of material being ablated, so that one can ensure that the tunnel is not drilled beyond the carious site. One way of doing this could be through acoustic analysis, since experimentalists agree that the sound emitted during ablation varies strongly with the type of material being ablated. A simple microphone and sound analysis software, perhaps calibrated to account for the age of the patient or the type of tooth being treated, could help the practitioner identify with accuracy the material being ablated, without the need for bulky or expensive equipment. Saaf et al. [30] have done preliminary work showing that the intensity of the sound emitted during ablation varies markedly with the type of tissue being ablated (dental hard tissue, nasal bone and otic capsule¹⁰), but they have not specifically addressed the application referred here. Altshuler et al. [31] have demonstrated that the acoustic signal emitted by enamel can be easily distinguished from the signal emitted during ablation by dentine by using a microphone and Fourier transform analysis. However, further research should be conducted before one can have full confidence that this method has the necessary precision and accuracy for this application. Another alternative would be using real-time mass spectrometry. This technique will certainly identify the material being ablated. The main difficulty with implementing it in dental practice is the added cost it will represent. Still, if this proves to be the most reliable option available these disadvantages can be minimized by optimizing a mass spectrometry system to the particular analyzes it will have to make in the context of dental laser ablation.

As ablation proceeds it is also necessary to have a system that will evacuate the ablated material, since the degree to which the practitioner, equipment and personnel in the office become contaminated with bacteria and the bacteria are inhaled by the patient should be minimized [32].

Another requirement of this technique is a device to hold the laser tip and

¹⁰A highly calcified tissue found in the ear.

detection equipment in place during treatment. Since the aim is to have a tunnel not more than 0.5 mm in diameter, clearly the laser must not be handheld by the practitioner. This device must be small and safe to sit inside the patient's mouth, easy to install, remove and sterilize. It must allow access of the laser tip to all the free surfaces of the tooth and the correct positioning of this tip with a precision of 0.5 mm. Finally, once this device is clamped to the tooth being treated, one must be able to correct the position of the laser tip using external commands inserted in a computer, since correcting it by hand would limit the accuracy with which this can be done. In order to reduce the number of cables coming out the patient's mouth, communication between the device and the computer could be done by infrared (IR) radiation. It is the author's opinion that both the development of the device and of the positioning software that must go with it should not pose significant challenges to today's miniaturization technology, and thus should not prevent the commercial implementation of the approach being described here.

Once the tunnel has reached the carious site it is necessary to eliminate the cariogenic bacteria inside. While lasers like Nd:YAG¹¹ or Er:YAG have proved to decrease the number of bacteria in dental tissues [33, 34, 35], the procedure only works in the areas where the laser can focus directly. In the minimally invasive operative procedure being proposed here, where the diseased tissue is not ablated, the lasers will most likely not be able to decrease the concentration of bacteria to acceptable levels, since the radiation will not reach the entire extension of the diseased tissue. Instead, one can use photodynamic therapy or a bactericide substance to kill the bacteria. Prof. Pearson's group has been doing research in this topic and they now have verified that photo-activated toluidine blue O is effective at killing bacteria [36]. Once inserted through a narrow tunnel, toluidine blue O diffuses through dentine rapidly, killing bacteria not only at the surface but also through out all the thickness of the diseased dentine.

Finally, the tunnel must be sealed, so that bacterial reinfection can be avoided. The sealant must possess particular characteristics: it must have low viscosity, so it can flow through a narrow tunnel and, once in place, it should solidify into an material with mechanical properties that allow the tooth to be mechanically stable; it should adhere properly to the walls of the tunnel in order to minimize the risk of reinfection; it should enhance the tooth remineralization process by slowly releasing minerals and, finally, it should integrate with the esthetics of the tooth. Since the 1990's, a number of dental filling materials (composites and glass

¹¹Neodymium: yttrium, aluminum, garnet. This laser emits at 1.06 μm .

ionomers) that fulfil most of these requirements have entered the market; they are widely used today, in particular for restorations where esthetics are important. Despite extensive research until now, restorations made with these materials are still less durable than those made with amalgam. However, given that the tunnel restoration being described here is much smaller than anything done presently in practice, it is likely that existing composites or glass ionomers will perform adequately. The only aspect of these materials that may possibly need to be improved is the viscosity, since the existing materials were not designed to be used in very narrow cavities. Researchers at Queen Mary Westfield College, London, are addressing this issue, and a material with the appropriate physical and chemical characteristics is now available, according to Prof. Pearson.

The work described in this Thesis is concerned with the second requirement of the new technique being proposed here: the search for the optimal laser operating parameters to ablate enamel, dentine, cementum and carious tissue. Finding the best laser operating parameters is not an easy task, because ablation is a highly non-linear process and dental hard tissues have complex nano and microscale structures as well as inhomogeneous chemical compositions. Consequently, it is not easy or it is even impossible to extrapolate from existing results how different (untested) pulse durations, pulse repetition rates or temporal and spatial laser profiles will perform. To simply test all possible laser parameter combinations is also not viable, not only because of the sheer amount of work that this task would represent but also because lasers have limited tunability and some parameter combinations would be inaccessible. Thus there is a need for analytical and computational models that give insight into the relevant mechanisms leading to ablation and that possess sufficient predictive capability to be used in searching for optimal laser operating parameters. The following two Chapters represent the first step towards building those models: a revision of the existing literature regarding dental hard tissue ablation.

Chapter 2

Generic considerations on laser irradiation of tissues

Identifying the values for the various laser parameters that yield the best ablation results, starting from purely theoretical considerations or by simply analyzing the literature that describes experimental results, is an impossible task. Generic theoretical considerations are unable to account for the details of the material being ablated, for example, and the experimentally tested range of values of the various laser operating parameters is not large, because of limitations in the tunability of the equipment. However, both these procedures can and should be used to narrow down as much as possible the ranges of values for the laser operating parameters that are most likely to produce the best results. These ranges of values will then serve as starting points for the work which is the subject of this Thesis.

In this Chapter the influence of the various laser operating parameters on the outcome of laser irradiation will be evaluated generically, with support from particular examples, and the most adequate operating ranges for those parameters will be selected. In Chapter 3 the experimental results available on dental hard tissue ablation corresponding to the selected operating ranges will be evaluated, thus allowing to identify the laser wavelength/operating parameters combinations that will be used as starting points for the models described in this Thesis.

2.1 Introduction

The response of materials to laser irradiation depends on a variety of parameters, some related to the material itself or to the environment surrounding it, and some related to the laser. Material properties include the optical properties such as

absorption, scattering and reflection coefficients and the mechanical and thermal properties such as density, modulus of elasticity, thermal expansion coefficient, specific heat and thermal conductivity. Laser operating parameters include the wavelength, pulse duration, radiation intensity, pulse repetition rate (for pulsed lasers), spot size and spatial and temporal intensity profiles. Despite the number of parameters that have an influence in the outcome of irradiation of a material, mainly five different types of interactions have been identified: **photochemical interactions**, **thermal interactions**, **photoablation**, **plasma-induced ablation** and **photo-disruption** [2]. The main parameter that governs the type of interaction of lasers with materials is not so much the total amount of energy deposited in the material per unit area (the fluence) as the rate at which this energy is deposited: this means that, for a given laser fluence, the pulse duration is the principal factor determining the outcome of radiation. For this reason, the various Sections and Subsections in this Chapter are each concerned with describing the effects of laser pulses as a function of their pulse duration.

2.2 Very long laser exposures: photochemical interactions

In general, it is agreed that pulse durations on the order of seconds or higher induce mainly photochemical changes in materials, particularly at low fluences (provided they are reasonably well absorbed by tissue). These photochemical changes are certainly not desirable when the purpose of irradiation is the ablation of materials with minimal modification, and thus this combination of laser parameters seems far from optimal [2]. At very high fluences, irradiation may in fact lead to dental hard tissue ablation, as was observed by Murgo, Palamara, Ferreira et al.. Murgo et al. [37] used a 10.6 μm CO₂ laser with a 10 s pulse and very high fluence (650 J/cm²) to ablate enamel, and found that a single pulse can drill a crater 0.5 mm deep, without evidence of melting, charring or carbonization. Palamara, Ferreira et al. [38, 39] also used a continuous wave (CW) 10.6 μm laser without water cooling to ablate enamel (duration of exposure = 6 – 350 μs or 0.1 s, energy density = 5.3 – 200 J/cm²). Unlike Murgo et al., they found that the treated enamel surface presented evidence of melting and recrystallization, and also of cracking and cratering; similar results were obtained by Pogrel

et al. [40]. While results may differ to some extent when other wavelengths are used or when dentine is ablated instead of enamel, they strongly suggest that the CW or long-pulse lasers are not appropriate to drill tunnels through enamel or dentine in a clinically safe manner and with the necessary precision. Therefore, lasers operating in this manner were not further investigated in the work that led to this Thesis.

2.3 Ultrashort short laser exposures: plasma induced ablation

At the other end of the currently available pulse duration spectrum, one finds the femtosecond (10^{-15} s) lasers which, because of the extremely short pulse duration, interact with materials in a unique way. Femtosecond laser pulses have extremely high intensity even when the fluence per pulse is on the order of $0.1 - 10$ J/cm², which enables multiphoton absorption effects to take a prominent role in ablation. Consequently, the linear absorption coefficient of the irradiated material is less relevant in this case than for longer pulse durations. In fact, femtosecond laser ablation can occur even at wavelengths very poorly absorbed by the material [41, 42]. Femtosecond lasers will thus be discussed separately from longer pulsed lasers, for which the linear absorption coefficient of the material plays an important role.

As the femtosecond laser pulse hits the target, quasi free electrons are produced as a result of multiphoton coherent absorption of radiation. The free electrons can subsequently absorb radiation through inverse *bremstrahlung* absorption and transfer energy to electrons in the bound state, thus creating more quasi free electrons through impact ionization. This process is called "avalanche ionization" or "cascade ionization" [43] and creates a plasma in the material (which reaches a state called optical breakdown). Ablation occurs when a sufficiently dense plasma (10^{21} electrons cm⁻³) is created [42], thus the ablation mechanism in question here is **plasma-induced ablation**. One should note that the depth of the layer in which most of the energy is deposited is approximately $1 \mu\text{m}$. This, together with the fact that the energy is deposited into electrons much more rapidly (in the fs time scale) than it can be transferred to the bulk material (in a time scale of tens of picoseconds) [42], implies that the depth of the ablation crater can be controlled very precisely. Once the plasma is created (i. e. , above the optical breakdown

threshold), laser radiation can no longer propagate further down into the tissue, because it is absorbed by the quasi free electrons and also reflected by them. Only after the end of the laser pulse does ablation take place. Because of the slow rate of energy transfer from the electrons into the bulk, most energy leaves the material with the ejected material and, consequently, very little collateral damage is expected at the irradiated sites [44]. Also, the short and high intensity laser pulses generate very high pressures in the μm -thick irradiated layer, which then propagate as a very high frequency shockwave (frequency on the order of GHz). Such high frequency shockwaves dissipate into the material within $\simeq 1 \mu\text{m}$, and therefore mechanical damage is reduced, unlike what happens for picosecond long laser pulses [42, 44, 45], for which plasma-induced ablation also occurs. Work by Perez et al. [46] supports this conclusion since it suggests that the tensile component of the stress wave (the component most likely to induce mechanical damage, since brittle materials are typically stronger in compression than in tension) may only play a role at fluences close to the ablation threshold, and should disappear as the fluence becomes higher because of thermal softening of the material.

The above reasoning only holds for moderate fluences, however. If the fluence per pulse becomes very high, the dominant mechanism responsible for ablation will no longer be the formation of plasma, but the shock wave generated, and is called **photodisruption** [2]. At these higher fluences, the shock wave may have significant intensity (mechanical effects scale linearly with absorbed energy [2]) and may lead to serious damage to the material. This must be avoided in order to prevent the formation of cracks that may serve as reentry points for cariogenic bacteria.

These generic considerations suggest that femtosecond laser pulses at moderate fluences may be very good candidates for the job of drilling long tunnels through enamel and dentine. However, it is necessary to evaluate whether they in fact perform as desired on the materials in question here. In general, authors agree that femtosecond laser pulses can ablate solid materials, in particular *brittle* materials, in a very precise manner and with more reduced thermal and mechanical damage than what would be possible to obtain with any other longer pulse lasers [47, 48]. Femtosecond lasers at various wavelengths have been tested for ablation of carious and healthy enamel and dentine, and also pure HA, with very successful outcomes. Kruger et al. [49] investigated the outcome of a $\lambda = 615 \text{ nm}$ femtosecond laser (pulse duration = 300 fs, repetition rate = 3 Hz, fluence per pulse = 0.5 – 3 J/cm², 100 pulses per spot) on enamel and dentine, without wa-

ter cooling, and found that both materials could be ablated very precisely, with little or no evidence of melting, charring or cracking, and using much lower fluences (1 J/cm^2) than those necessary with longer laser pulses. Similar results were obtained by Rode et al. [50], who used comparable laser parameters but much higher repetition rates to ablate enamel using lasers with $\lambda = 780 \text{ nm}$ (pulse duration = 150 fs , repetition rate = 1 kHz , fluence per pulse = $2 - 21 \text{ J/cm}^2$, number of pulses per spot > 1000) and $\lambda = 400 \text{ nm}$ (pulse duration = 95 fs , repetition rate = 1 kHz , fluence per pulse = $2 - 36.5 \text{ J/cm}^2$, number of pulses per spot > 1000). They found that both pulse durations and wavelengths produced cavities with smooth surfaces and without any sort of thermal damage. Rode et al. also measured the intrapulpal temperature rise and found that, provided that air cooling was used, the intrapulpal temperature could be kept within clinically acceptable limits. Finally, they found that the ablation rates for enamel, while on the order of $1 - 2 \mu\text{m}$ per pulse and therefore low for removing large amounts of material, are certainly adequate to drill narrow long tunnels at these high repetition rates. These conclusions are also valid for dentine, as confirmed by work done by Serafetinides et al. [51], Armstrong et al. [52] (for ossicular bone), and Neev et al. [41], who all used comparable laser parameters (lower fluences and repetition rates but longer pulses in the femtosecond range).

These results strongly indicate that femtosecond lasers are thus potentially capable of drilling long tunnels through enamel and dentine, thus making them very good candidates for this job. However, the performance of a laser must be weighed against its size, ease of operation and cost. Femtosecond systems tend to be expensive and bulky; furthermore, an adequate delivery system such as an optical fiber is not yet available [53]. If a laser is to be used in a cost effective manner in a clinical setting, it must be used frequently; ideally, it should also be used in ablation and cutting of *soft* tissue, since these procedures make up a large fraction of the total work performed in dentistry. However, the lack of thermal damage inflicted to tissue suggests that it is unlikely that this laser will have a strong hemostatic effect. This feature makes it less appropriate for soft tissue procedures.

While it is natural that these drawbacks will be reduced or even eliminated as the research into femtosecond laser technology proceeds, the femtosecond lasers remain a poor choice for dental laser treatment in a clinical setting until this happens, and other possibilities should be explored.

2.4 Picosecond, nanosecond and microsecond laser pulses

In between the two extreme cases already discussed, one finds laser pulses with duration on the order of picosecond, nanosecond and microsecond, which will be discussed separately in this Section. For each and all of these pulse durations, the linear absorption coefficient of the material at a particular wavelength determines to a great extent the outcome of irradiation. Depending on the particular combination of material and laser operating parameters, irradiation may or may not result in ablation. If it results in ablation, the mechanisms by which material is ablated may vary substantially.

2.4.1 Picosecond and nanosecond pulses: photodisruption

For pulse durations between 10 ps and 100 ns and high radiation intensity ($10^{11} - 10^{16}$ W/cm²), optical breakdown of the material initiates because of thermionic emission (in which the electrons are released because of thermal ionization). However, the main effect governing ablation of the material is the very high intensity shock waves that are generated. Thus, the tissue is teared by mechanical forces, and the dominant ablation mechanism is called **photodisruption**. Unlike in the plasma-induced ablation regime, where damage is somewhat restricted to the optical breakdown area, the shock waves in photodisruption are able to travel outside the optical breakdown area, thus causing damage outside it also. This damage is, non-intuitively, more intense with longer (nanosecond) pulses, where it can affect areas on the order of millimeters, than with shorter pulses (see ref. [2], pp. 124).

The mechanism in question at these pulse durations and irradiation intensities strongly suggests that these will be less than adequate to ablate brittle materials such as dental hard tissues, because of the risk of developing deep cracks. In fact, this is what has been verified experimentally. Swift et al. [54] investigated the effect of various wavelengths on dental enamel using a FEL (free-electron laser) which emits 3.5 μ s macropulses, each comprising 10 000 ps pulses separated by 350 ps intervals. For all the wavelengths they tested (3.0 and 6.1 μ m – absorbed by water, 6.45 μ m – absorbed by the organic material, 8.2 and 9.2 μ m – absorbed by the mineral) and for the laser parameters used (repetition rate = 10 or 30 Hz,

fluence per macropulse¹ = 190 – 350 J/cm², 100 pulses per spot), they found that cracking occurred. This happened in all the samples, regardless of whether they displayed evidence of melting and resolidification (like the 9.2 μm wavelength) or not (all the others), which suggests that unwanted cracking is less a consequence of the temperatures reached at these high fluences than of the very small duration of the micropulses. Niemz [53] used a Nd:YLF² laser (pulse duration = 30 ps, repetition rate = 1 kHz, fluence per pulse³ = 140 J/cm², number of pulses per spot = 10) and again found evidence of cracks under SEM examination, which he attributed to the same cause [2]. Niemz used a very small laser spot (30 μm), much smaller than the one used by Lizarelli et al. (0.075 mm²), and drilled very precise craters of 1 m² area, which indeed suggests that mechanical damage may be reduced because of the small spot size and small energy per pulse. Still, in order to fully understand whether cracking is or is not caused by picosecond laser pulses, it would be good to use a more trustworthy methodology to detect cracks, such as dyeing the tooth prior to desiccation and examination by an optical microscope. Cracks can subsequently serve as entry points to bacteria and therefore cause reinfection to occur, and must be avoided for that reason. Given the little experimental information available and the fact that the existing information points to the existence of mechanical damage in enamel caused by the short pulse durations, the range of values for pulse duration and intensity of radiation discussed in this subsection are considered inadequate to obtain the best results in ablation of dental hard tissue, and will not be further considered in this Thesis.

2.4.2 Picosecond laser pulses: plasma-induced ablation

At lower energy densities than those necessary to ablate material by photodisruption using laser pulses with duration between 1 and 500 ps, **plasma-induced ablation** occurs. As was discussed previously (in subsection 2.3), plasma-induced ablation may also occur when femtosecond lasers are used. However, in the case of picosecond lasers, thermionic emission of electrons is more important than multiphoton coherent absorption in generating quasi-free electrons seeds, and the linear absorption coefficient of the material plays an important role in determining the outcome of irradiation. Hence, it was deemed appropriate to discuss plasma-

¹Not given by the authors; calculated based on reported values of energy per pulse and spot diameter, and assuming that fluence=energy/area.

²This laser emits at 1053 nm.

³Not given by author; calculated based on the laser spot diameter and energy per pulse.

induced ablation for picosecond lasers separately from femtosecond lasers.

Once a few quasi-free electrons are generated by thermionic emission, these will absorb incoming radiation by inverse Bremsstrahlung and will subsequently generate a cascade of electrons, according to what was already described in 2.3. While thermal damage is expected to be reduced when using picosecond laser pulses (the pulse duration is significantly shorter than the time that heat takes to diffuse out of the irradiated site), the occurrence of mechanical damage is likely since picosecond-long laser pulses are well below the acoustic relaxation time⁴ for wavelengths in which the absorption coefficient is between 100 and 1000 cm⁻¹, which should generate very high intensity acoustic waves [55]. The actual magnitude of these stress waves may vary extensively according to the other laser parameters used. In general, the extent of mechanical damage for shorter laser pulses is likely to be smaller than for somewhat longer pulse lasers (provided ablation is still occurring under stress confinement), since shorter pulses may have higher radiation intensity but will also have lower total energy, and therefore less energy is available to cause fracture [56]. However, it is not possible to conclude, based on simply generic considerations, whether they will perform adequately or not when used to ablate dental hard tissue; experimental information is necessary. Lizarelli et al. [57] have found that the Nd:YAG laser (pulse duration = 100 ps, repetition rate = 15 Hz, fluence per pulse not given, number of pulses = 450) can ablate enamel without causing melting, but some cracks are observed at the ablated site. Lizarelli et al. claims that the cracks are caused during the desiccation process that precedes SEM observation, but does not fully test this claim so the lack of mechanical damage cannot be confirmed. Since the author could not find more experimental information and there was indication that mechanical damage could be quite extensive in this regime, this pulse duration and intensity range was considered inadequate for the purpose in mind, and it will not be considered further.

2.4.3 Nanosecond pulses: photoablation

If pulse durations on the order of 10 to 100 ns and ultraviolet (UV) wavelengths (100 to 350 nm, or 12 to 3.5 eV) are used, the mechanism by which tissue is ablated is not thermal in nature but photochemical, and it is called **photoablation**. Lasers

⁴A more detailed explanation regarding the acoustical relaxation time will be given in Section 2.4.4

emitting in this region are ArF ⁵ at 193 nm (6.4 eV), KrF ⁶ at 248 nm (5.0 eV), XeCl ⁷ at 308 nm (4.0 eV) and XeF ⁸ at 351 nm (3.5 eV), among others. The absorbers in this region will most likely be the covalent bonds existing in the organic material making up enamel and dentine. Under these conditions the material decomposes because the energy of the photons is sufficient to break existing covalent bonds, as can be seen in Table 2.1. The excess energy not used in the dissociation

Type of bond	Dissociation energy (eV)
C=O	7.1
C=C	6.4
O—H	4.8
N—H	4.1
C—O	3.6
C—C	3.6
S—H	3.5
C—N	3.0
C—S	2.7

Table 2.1: Dissociation energies of selected chemical bonds. Source: ref. [2].

of the molecule remains in the molecular fragments as kinetic energy and these subsequently leave the material. Of course, the longer the wavelength the less likely it will be that the energy is used to break chemical bonds directly, and the more significant will become the unwanted thermal effects of ablation; in practice, only wavelengths inferior to 200 nm can be said to ablate material with a pure photoablation mechanism.

The fact that the main absorber of UV radiation should be the organic material existing in dental hard tissue, conjugated with its inhomogeneous distribution in enamel and dentine, suggests that the mesostructure of the material will play a role during ablation. It also indicates that the preferably ablated regions at the irradiated surfaces should be the dentinal tubule content, in dentine, and the rod boundaries in enamel. This may have an influence on the surface morphology of the irradiated site and, consequently, on the ability of the surface to bond to filling materials subsequently to ablation.

In general, ablation with UV wavelengths does not lead to significant melting or carbonization, thus making these lasers potentially good choices to drill long

⁵Argon fluoride.

⁶Krypton fluoride.

⁷Xenon chloride.

⁸Xenon fluoride.

tunnels through enamel and dentine. However, this pulse duration is rather close to the acoustic relaxation time of materials (at least for wavelengths at which the absorption coefficient is between 100 and 1000 cm^{-1}), as can be seen from Table 2.2, which means that it is possible that these lasers induce mechanical damage (cracks) in the material, because of the stress transients created. The likelihood of this happening cannot be ascertained purely based on generic considerations, though.

While this generic discussion indicates that UV lasers may also be good candidates for producing long tunnels through dental hard tissue, there are negative aspects to them, and these must be considered when evaluating their potential for the application in mind.

The main drawbacks of these UV/nanosecond lasers are their relatively large size and high cost, and the fact that they may cause cytotoxic effects in biological materials. While the first two issues may be solved with more investment and research, the third one will not. There is evidence that wavelengths as low as 193 nm [58] and as high as 355 nm may cause mutations in DNA, although these wavelengths present a much lower mutagenic risk than wavelengths in the UVB (280 – 315 nm) spectral range. Mutagenic risk is known to decrease strongly when moving from the UVC (100 – 280 nm) to the UVB and UVA (315 – 400 nm) spectral zones [59]. UV radiation between 240 and 260 nm [2] seems to be the most dangerous: it is strongly absorbed by DNA [59] and can generate free radicals in the tissue [60] thus having potential mutagenic effect. Within the UVC range, radiation around 200 nm seems to have lower mutagenic effect than radiation of higher wavelength, which is surprising. The reason for this is that proteins in the cell matrix seem to absorb strongly around 200 nm, thus protecting the cell nucleus from damage [2]. If this wavelength range is indeed to be used for dental laser ablation, a careful long-term evaluation of the mutagenic effects of these lasers on dental tissues must be done before they can be used in clinical practice.

Keeping these drawbacks in mind, it does seem that UV lasers with nanosecond laser pulses may be good candidates for the application in mind. Before making the final decision as to their potential, however, it is necessary to analyze the literature for experimental evidence supporting this. This analysis is rather lengthy and for that reason it is not presented here but in a separate Section (Section 3.3.2).

2.4.4 Microsecond pulses: thermal interaction

For pulse durations between 1 μs and 1 min, the response of the tissue to laser radiation is dominated by the temperature reached, and thus the **thermal interaction** regime dominates. In this regime, coagulation, vaporization (mostly of water, in biological tissues), carbonization or melting may occur, depending on the temperature reached. Of course, coagulation, carbonization and melting are undesirable effects if the goal is to ablate material. In order to minimize these effects, diffusion of heat from irradiated sites must be kept at a minimum. The timescale of heat diffusion from the irradiated sites may be estimated quite easily from Beer-Lambert's law and the heat diffusion equation applied to the case where the laser spot is large compared to the depth of penetration of radiation. Considering that Beer-Lambert's law holds reasonably well and neglecting the existence of scattering, the intensity of radiation inside the tissue, $I(z)$, obeys the relationship below:

$$I(z) = I_0 \exp(-\mu z) \quad (2.1)$$

where z is the depth inside the tissue, μ is the linear optical absorption coefficient and I_0 is the intensity of the incident radiation at the center of the laser spot. The optical absorption depth is defined as the depth at which the intensity of radiation becomes $1/e$ of the incident intensity, and is equal to $1/\mu$.

On the other hand, the thermal penetration depth, $z_{therm}(t)$, is estimated as

$$z_{therm}(t) = \sqrt{4\vartheta t} \quad (2.2)$$

from the solution to the one dimensional heat diffusion equation (see ref. [2] pp. 70 – 72), where ϑ is the thermal diffusivity. The thermal penetration depth is the distance at which the temperature has decreased to $1/e$ of its peak value at a particular instant in time.

Equating the optical absorption depth (or the beam spot diameter, if it happens to be smaller than the optical absorption depth), d , to the thermal penetration depth yields the typical timescale in which heat diffuses out of the irradiated volume of material defined by the optical penetration depth: the thermal relaxation time, τ_{ther} .

$$\tau_{ther} = \frac{d^2}{4\vartheta} \quad (2.3)$$

If thermal damage is to be minimized, then, the pulse duration must be made

shorter than τ_{ther} , which is normally referred to as operating under *thermal confinement conditions*. Therefore, the optimal pulse durations are ultimately a function of the optical properties of the material. For high absorption wavelengths, with absorption coefficients on the order of 100 to 10000 cm^{-1} , the thermal relaxation times are on the order of milliseconds to tenths of microseconds, as can be seen in Table 2.2. Therefore, pulse durations longer than the values references in Table 2.2

Absorption coefficient (cm^{-1})	Optical penetration depth (μm)	Thermal relax. time (s)	Acoustic relax. time (μs)
1	10000	50	1.5
10	1000	0.5	0.15
100	100	0.005	0.015
1000	10	5×10^{-5}	0.0015
10000	1	5×10^{-7}	0.00015

Table 2.2: Thermal and acoustical relaxation time for various optical absorption coefficients. Calculated using the material parameters for enamel: thermal diffusivity = 0.47 mm^2/s , density = 3100 kg/m^3 , specific heat = 880 $\text{J}/\text{kg}/^\circ\text{C}$, speed of sound = 6500 m/s [61]. The thermal relaxation times for dentine are similar. The acoustical relaxation times for dentine were not estimated.

will inevitably cause more extensive thermal damage and will thus be less preferable than shorter pulses, unless some sort of cooling mechanism such as water spraying is used. The effects of the cooling mechanism are difficult to predict so no attempt will be made at this point to draw conclusions on this issue based on solely on generic considerations; instead, the experimental evidence on the topic will be evaluated further on in this Thesis.

Another conclusion that can be drawn from Table 2.2 concerns the optimal absorption coefficient. A very high ($\gg 1000 \text{ cm}^{-1}$) absorption coefficient will imply that most of the energy will be absorbed in a layer of material less than 10 μm thick. Therefore, the depth of material ablated per pulse will be somewhat small, which indicates that ablation will proceed slowly unless high repetition rates are used. However, repetition rates may not be raised indefinitely, since at some point heat accumulation will occur from one pulse to the next and thermal damage will be more likely to occur. On the other hand, if the material has an absorption coefficient lower than 100 cm^{-1} , most of the radiation will be absorbed in a layer over 0.1 mm thick, which clearly does not enable us to obtain the necessary precision. This implies that the most adequate wavelengths will have an absorption coefficient in enamel and dentine between 100 and 1000 cm^{-1} , perhaps slightly

higher. This conclusion is valid for all pulse durations discussed in this Chapter (provided they are longer than femtoseconds, for which it has already been explained that the linear optical absorption coefficient plays a less prominent role).

The extent of mechanical damage induced in this pulse duration range is difficult to predict from generic considerations, because it depends extensively on the composition and structure of the irradiated materials. In particular in a material like human dental enamel – which contains water pores that absorb certain wavelengths very intensely – very high, localized, stress may be generated at the pores because of the expansion of liquid water and subsequent vaporization, which would otherwise not be generated in an homogeneous material. The pore stress is a function of the temperature at the pore and, consequently, may be thought of as *thermally induced stress*. Of course, the heated mineral also expands and thus experiences thermal induced quasi-static stress, made more intense under thermal confinement conditions since thermoelastic stress lasts for a time similar to τ_{ther} . This makes it likely that quasi-static thermoelastic stress plays a role during ablation even if it is less intense than the stress induced at the water pores, since damage to materials is a function not only of the stress intensity levels reached but also of the length of time they are active. However, for both these sources of mechanical damage it is not possible to infer, by simple generic considerations, the laser operating conditions that will minimize unwanted damage to the material while making ablation more efficient, in part because of the role played by the local material properties [56].

An irradiated material also experiences what is normally called *transient stress*, in which high amplitude acoustic waves propagate from the irradiated site to the rest of the tissue. These waves may have a significantly higher intensity than the quasi-static stress generated in the material, and therefore can play an active role during ablation; for the same reason, they may be responsible for extensive unwanted mechanical damage caused to the material.

The intensity of the pressure at the irradiated site (and, consequently, the intensity of the acoustic waves that propagate out of it) is maximized when heating takes place rapidly enough so that the heated volume does not have time to expand [56, 62], as can be seen from equation 2.4

$$\sigma_{ij} = \frac{3B}{1+\nu} [(1-2\nu)\epsilon_{ij}] - B\beta\Delta T\delta_{ij} \quad (2.4)$$

where σ_{ij} and ϵ_{ij} are the components of the stress and strain tensor, respectively,

B is the bulk modulus, β is the expansion coefficient, ν is the material's Poisson ratio, T is the temperature and δ is the Kronecker symbol. The first term of the expression describes the stress generated because of displacements in the material and the second term describes the stress generated when the material is heated at constant volume. As the material expands after being heated (that is, as the first term becomes larger than zero), it is obvious that the stress experienced by the material decreases (becomes less negative, i. e., less compressive). Therefore, the highest pressures will be reached when the laser pulse is shorter than the time it takes the heated volume to expand. The expansion time corresponds to the time an acoustic wave takes to travel the smallest distance, d , that characterizes the irradiated volume (either the laser spot diameter or the absorption depth), and is called the *characteristic time of acoustic relaxation*, τ_{ac} , which can be estimated by

$$\tau_{ac} = \frac{d}{c_s} \quad (2.5)$$

where c_s represents the speed of sound in the material. An estimate of the acoustic relaxation time for various absorption coefficients can be found in Table 2.2.

For wavelengths at which the absorption coefficient of enamel and dentine are in the optimal 100 to 1000 cm^{-1} range it is clear that the acoustic relaxation time in enamel is in the nanosecond scale, which is below the pulse duration range being discussed in this subsection. One can conclude that, using microsecond-long pulses, the thermal interactions dominate and the transient stresses induced in the material are likely not playing a determinant role in ablation. The transient stresses are only likely to be significant when the pulse duration is around or below the nanosecond range, something which was already discussed in the previous Subsections.

The above discussion on microsecond-long pulses indicates that, at first sight, there is nothing suggesting that lasers operating at these pulse durations will behave poorly, but nothing indicates clearly that they will behave better than other ranges of pulse durations either. It seems that the optimal results should be obtained when the optical absorption coefficient of the materials is on the order of 100 to 1000 cm^{-1} and when the pulse duration is made significantly shorter than the thermal relaxation time. It is possible that cooling of the irradiated sites may significantly reduce the thermal damage inflicted to the material and allow the use of higher pulse repetition rates, thus increasing the speed of ablation, but the optimal values for these parameters cannot be determined by generic

considerations only. The search for the optimal laser operating parameters for this pulse range will be further narrowed down in Chapter 3.

2.5 Conclusion

This generic discussion indicates that very long pulses (on the order of milliseconds or longer) are not adequate for the purpose being sought here. Various sub-millisecond pulse durations and fluence ranges may be adequate to ablate dental hard tissue.

Femtosecond laser pulses seem to be very good choices, since both unwanted thermal and mechanical side effects such as melting or cracking seem to be avoided due to the pulse characteristics. However, the size, complexity of operation and price associated with femtosecond lasers (they can cost as much as EUR 200 000), the lack of optical-fibre delivery systems and the fact that they will most likely not perform well in soft-tissue ablation makes them less than ideal to use in laser dentistry and drives the search for other laser systems. If other laser systems do not present these drawbacks and produce good results, the application of the minimally invasive procedure described in Chapter 1 in a clinical setting can be speeded up for several years, which is of significant interest.

For all other pulse durations (in which the linear absorption coefficient of the material plays an important role during ablation), the evidence presented in this Chapter indicates that good results may be obtained also, provided that the optimal laser operating parameters can be found. The generic discussion presented here has already considerably narrowed down the ranges of values of the laser operating parameters for which the optimal results are more likely to be obtained. The wavelengths that are most likely to yield the best results should have an absorption coefficient between 100 and 1000 cm^{-1} . UV laser pulses with nanosecond duration may perform adequately, although it is possible that they inflict mechanical damage to tissues. The same may be said of picosecond laser pulses, where even at lower fluences (where the photodisruption mechanisms does not dominate ablation), the intensity of stress transients may be high. Microsecond long laser pulses should perform better than nanosecond or picosecond pulses, provided that the pulse duration is made shorter than the thermal relaxation time of the material at that wavelength, so that thermal damage is kept to a minimum (however, it is necessary to evaluate whether, even under thermal confinement, the material

will need to be cooled by other methods); unwanted mechanical damage such as cracks is likely to be kept at a minimum when microsecond pulse durations are used, because stress transients are most likely small since the laser is operating outside stress confinement conditions.

Despite the considerable advance in identifying the best laser operating parameters that the discussion in this Chapter represents, the ranges of values for the laser operating parameters presented are still too broad. In order to further narrow them down, and thus make the final decision as to which non-femtosecond lasers are more likely to produce the best results, it is necessary to review the literature on experimental data available on ablation of dental hard tissues, something that will be done in Chapter 3.

Chapter 3

Experimental evidence on picosecond, nanosecond and microsecond pulses in dentistry

The aim of this Chapter is to critically evaluate the available experimental results on dental hard tissue laser ablation by picosecond, nanosecond and microsecond lasers only, which were selected in the previous Chapter as possible pulse durations to use for dental laser ablation. The wavelengths, pulse duration and intensities judged in Chapter 2 to be inappropriate to yield the best results will not be further discussed in the present Chapter. The aim of this review is to compare existing experimental results and select the most appropriate wavelengths and laser operating parameters to drill the high aspect-ratio tunnels necessary for the novel surgical caries treatment described in Chapter 1. This review is intended to be comprehensive, but not exhaustive, therefore not all representative available works will be mentioned. Before the actual review begins, however, a summary of the optical properties of enamel and dentine and a description of the typical temporal profile of various types of lasers will be presented. This information is necessary for the understanding of the review that follows. Subsequently, the effects of each combination of wavelength and laser operating parameters (the most relevant are pulse duration and fluence) in terms of thermal and mechanical damage caused to dental hard tissue will be described. Specifically, the occurrence of melting, resolidification, recrystallization, chemical modification, cracking or changes in the surface morphology will be discussed. The implications of these changes in the adhesion of filling materials to the surface and the surface resistance to acid dissolution and bacteria re-entering will be evaluated. Furthermore, the adequacy of the ablation rates for a clinical setting and the possibility of drilling long tunnels

will be assessed, and so will the likelihood of inflicting thermal damage to the pulp of the tooth. To conclude, a brief discussion summarizing the main findings, suggesting the laser operating parameters that are most likely to perform better in ablation of dental hard tissue and describing the issues that need to be addressed in order to use the existing lasers to drill high aspect-ratio tunnels through dental hard tissue will be presented.

3.1 The optical properties of enamel and dentine

If the objective is to ablate dental hard tissue in a precise way while minimizing thermal damage to the underlying tissues of the tooth (the pulp), the laser radiation must be highly absorbed by the tissues: the ideal optical absorption coefficient would be in the 100 to 1000 cm^{-1} range. Therefore, in order to identify which wavelengths should perform better, the optical properties of the tissues must be known or, if that is not possible, estimated based on the known properties of the components of the tissue.

The optical properties of dental hard tissues have been most intensively studied in the mid-IR, near IR and visible regions; the UV and far IR spectral regions have not been studied deeply, to the best of the author's knowledge. The absorption spectrum of human dental enamel between 2.5 μm and 12 μm is given in Fig. 3.1.

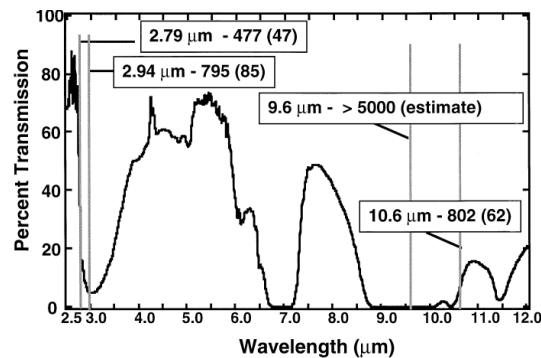


Figure 3.1: Infrared transmission spectrum through a 20 μm thick section of human dental enamel. The absorption coefficients were calculated from the mean of five samples of 50 μ thickness. The mean absorption coefficient \pm the standard deviation (S. D.) for each of the laser wavelengths of 2.94, 2.79, 9.6 and 10.6 μm is shown in the boxes. Source: ref. [63].

The principal absorbers in this region of the spectrum are the mineral OH^- at 2.79 μm , the free water at 2.9 μm (symmetric and asymmetric vibrations [2]), the CO_3^{2-} and amide [64] between 6 and 7 μm and the the symmetric and antisym-

metric PO stretching modes of PO_4^{3-} between 9 and 11 μm . There are a number of lasers that emit at these spectral regions, and that consequently are good candidates for ablation: the Er:YSGG and Er:YAG for the two wavelengths close to 3 μm , respectively, and the CO_2 laser, whose main wavelengths are 9.3, 9.6, 10.3 and 10.6 μm . Wavelengths around 7 μm most likely will be less appropriate, since the concentration of CO_3^{2-} decreases markedly when enamel is heated to temperatures up to $\simeq 400$ $^\circ\text{C}$ [65].

Comparing the absorption spectra of enamel and dentine between 2.5 and 20 μm (see Fig. 3.2), one finds that the absorption peak around 3 μm is higher in dentine, which is consistent with this material's higher water content (10% vs. 4% in enamel). The peaks between 6 and 7 μm are also higher in dentine, which was to be expected given this material's higher content in organic material. At the same time, while the mineral content of dentine is only 70% (lower than the 95% that make up enamel), one finds that dentine's mineral content is still high enough to ensure that the wavelengths between 9 and 11 μm continue to be highly absorbed by this material. Fig. 3.2 also tells us that the absorption of both materials between 12 and 20 μm is almost negligible.

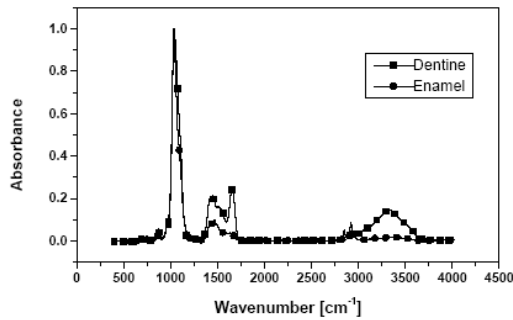


Figure 3.2: Fourier transform infrared (FTIR) spectra of human dental enamel and dentine between 2.5 and 20 μm . The samples were prepared by grinding enamel and dentine and pressing the powders into films of 0.5 mm thickness. Source: ref. [64].

While the above absorption spectra suggest a number of wavelengths that should be highly absorbed by the tissue, the reflectance and scattering of radiation must also be evaluated before selecting any particular wavelengths.

The reflectance of enamel varies widely in the mid-IR spectral region, between a minimum of 5% near 3 μm to a maximum of 50% at 9.6 μm , as can be seen in Table 3.1. Scattering is known to be very small at CO_2 wavelengths [66]. Other wavelengths in this region were not investigated, although in general it is expected to be small. The reflectance of dentine in this spectral region also varies strongly to a maximum of 85%, as can be seen in Fig. 3.3, which displays

Wavelength	Absorption coefficient (cm ⁻¹)	Scattering coefficient (cm ⁻¹)	Reflectance (%)
633 nm	66 [67]		
2.79 μm	477±47 [63]		5±2% [68]
2.94 μm	795±85 [63]		5±1% [68]
9.3 μm	5500 [69]	small [66]	37.5±0.5 [66]
9.6 μm	8000 [69]	small [66]	49.4±1 [66]
10.3 μm	1168±49 [69]	small [66]	15.8±0.1 [66]
	1125±75 [69]		
10.6 μm	819±62 [69]		13.2±0.2 [66]
	825±25 [69]	small [66]	
	802±62 [63]		

Table 3.1: Optical properties of human dental enamel obtained experimentally.

reflectance spectra obtained using specular reflectance infra-red fourier transform spectroscopy (SRIFTS) [70]. Finally, while measures of scattering in the mid-IR

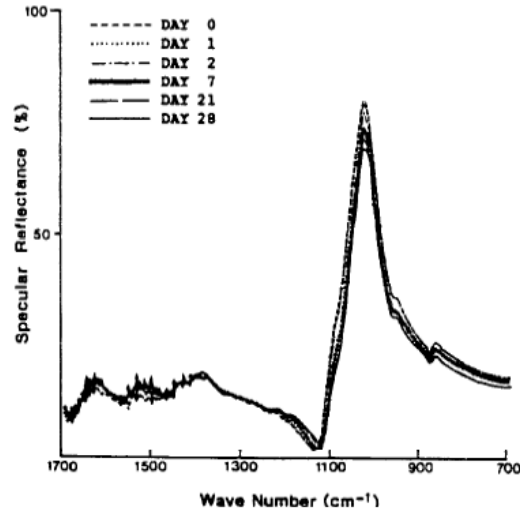


Figure 3.3: Specular reflectance infrared fourier transform spectroscopy (SRIFTS) spectra of dentine, stored in distilled water over 28 days, between 6 and 14 μm. The samples were prepared by cutting dentine into 0.75 mm disks. Note the maximum at approximately 10 μm. Source: ref. [70].

region are not available in the literature, it is likely that this parameter plays a less important role, at least for the most highly absorbed wavelengths. If the radiation is absorbed in a layer of a few 10's of micrometers, as is the case when the absorption coefficients are on the order of 800 cm⁻¹, even intense scattering should not significantly alter the shape of the volume penetrated by radiation. It thus

seem that the wavelengths around $10\ \mu\text{m}$ will be the ones in which the incident and absorbed radiation will differ more markedly, because of the high reflectance of the tissues in that spectral region. This difference should be accounted for when interpreting results, but should not be an obstacle to the performance at these wavelengths. The exception to this may be the $9.3 - 9.6\ \mu\text{m}$ spectral region, for which the possibility of injuring the patient should be investigated because as much as 50% of the incident radiation is reflected.

As one moves from the mid-IR to the near-IR (between $3\ \mu\text{m}$ and $750\ \text{nm}$), one finds that the absorption of dental hard tissues decreases markedly. However, absorption can still be quite significant in this region as can be seen in the absorption spectrum for dentine given in Fig. 3.4. The peaks at 1500 and $2000\ \text{nm}$ are particularly promising, and in fact correspond to lasers already tested for ablation of dental hard tissue: Nd:YAG at $1.570\ \mu\text{m}$, Tm:YAG at $2.006 - 2.025\ \mu\text{m}$ and Ho:YAG at $2.088-2.091$ and $2.127\ \mu\text{m}$. The peaks near $2\ \mu\text{m}$ correspond to an absorption peak of water [2]. The very small absorbance peak at $1000\ \text{nm}$ also matches the wavelength emitted by Nd:YAG lasers.

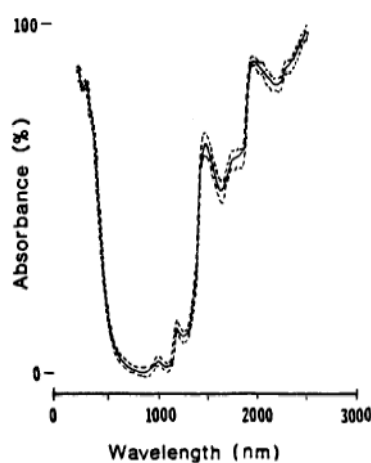


Figure 3.4: Absorbance spectra for dentine. The samples were prepared by cutting dentine into $0.75\ \text{mm}$ disks. The solid and broken lines correspond to freshly extracted teeth or teeth kept in storage, respectively. Source: ref. [70].

The absorption spectrum of enamel in the same spectral region could not be found in the literature. However, since the components of dentine and enamel are similar, and only their relative amounts vary, one can expect the absorption spectra of enamel to follow the trends visible in Fig. 3.4. No information could be found regarding the reflectivity or scattering of both enamel and dentine in the near-IR region.

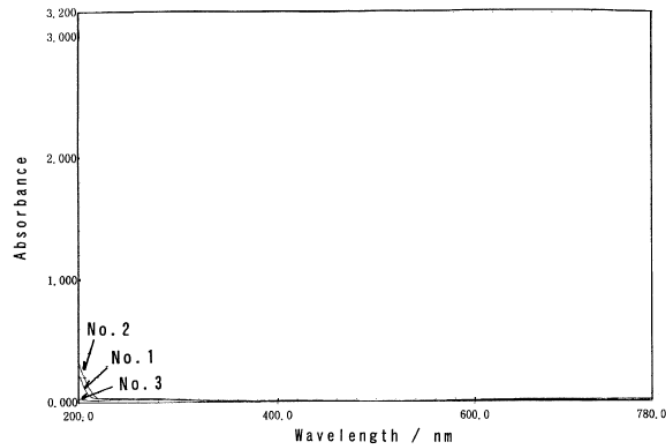


Figure 3.5: Absorbance spectra for artificial HA between 200 and 780 nm, for a sample heated at 100°C for 24 hours (curve number 1). The remaining curves correspond to HA heated at different temperatures and are not important for the work reported in this Thesis. Source: ref. [71].

Fig. 3.4, Tables 3.1 and 3.2, as well as the similarity in composition between enamel and dentine allow us to conclude that the visible part of the spectrum (400 to 750 nm) is not highly absorbed by neither of these materials. Therefore, lasers emitting in this spectral region are not good candidates for ablating hard tissue, and will not be discussed further.

Wavelength	Absorption coefficient (cm ⁻¹)	Scattering coefficient (cm ⁻¹)	Reflectance (%)
355 nm	2000-3000 [72]		
500 nm	6 [67]	1200 [67] 150 [67]	
633 nm	6 [67]	1200 [67]	
2.79 μm	988±111 [73]		
2.94 μm	2200 [73]		
9.3 μm	5000 [74]		8.6±1.7 [66] 40 [70]
9.6 μm	6500 [74]		16.7±0.5 [66] 85 [70]
10.3 μm	1198±104 [73]		10.3±0.6 [66] 40 [70]
10.6 μm	813±63 [73]		8.8±0.8 [66] 36 [70]

Table 3.2: Optical properties of human dentine obtained experimentally.

Fig. 3.4 indicates that UV (ultraviolet) radiation between 200 and 400 nm is

highly absorbed by dentine and, by analogy, it should be fairly absorbed by enamel. Pure HA does not seem to absorb strongly at this spectral region as can be seen in Fig. 3.5, although it is known that it absorbs sufficiently for ablation to occur [75, 76, 77, 78]. Unfortunately, it was not possible to find an absorption coefficient for neither enamel nor dentine in this spectral region, but Fig. 3.4 suggests that it is similar to the absorption coefficient of dentine at $2.94 \mu\text{m}$. Therefore, the absorption coefficient of dentine in the 200 to 400 nm range should be on the order of 100 to 1000 cm^{-1} . One can expect absorption to be higher in dentine than in enamel, given that dentine has a significantly higher content in organic material and water than enamel and, consequently, that dentine will be ablated more easily than enamel.

The optical properties given in the presented tables and figures were obtained using low fluence irradiation. It is unlikely that the values remain the same as the fluences increase because of the dependence of those properties with temperature, and even less so when chemical alterations like carbonization or charring take place. Fried et al. [66] evaluated the change in the optical properties of enamel and dentine at $\lambda = 9.6 \mu\text{m}$ (pulse duration = $100 \mu\text{s}$, repetition rate not given, fluence per pulse $< 2 \text{ J/cm}^2$) during irradiation, and found they did not change to any measurable extent. At higher fluences, they found that enamel displayed transient changes (i. e. , those that exist only for the duration of the laser pulse, consequence of the high temperatures felt at the irradiated site) but dentine showed both transient and permanent changes (changes that remain after the laser irradiation, because of the carbonization and vaporization of the organic component). Fried et al. found that at fluences higher than 5 J/cm^2 , the reflectivity of dentine increased by 30%, becoming closer to the value for enamel, which is consistent with preferential loss of organic material. Fried et al. also suggested that the reflectance of enamel at $\lambda = 9.3 \mu\text{m}$ and $\lambda = 9.6 \mu\text{m}$ seems to decrease with increasing temperature while the reflectance at $\lambda = 10.3 \mu\text{m}$ and $\lambda = 10.6 \mu\text{m}$ seems to behave oppositely. These results indicate that dynamic changes in the optical properties of dental hard tissues are non-intuitive and, ideally, should be accounted for when modelling the response of tissues to laser irradiation. However, the lack of experimental data for the wavelengths specifically addressed in the work described here have made it impossible to do so. Therefore, the author has consciously made the option of not to include the dynamic optical properties in the models. The influence of this approximation is instead discussed when analyzing results.

This revision of the literature regarding the optical properties of enamel and

dentine strongly suggests that the most appropriate lasers to ablate dental hard tissue should be the Er:YAG, CO₂ and UV ones, because the absorption coefficients at these wavelengths lie in the 100 – 1000 cm⁻¹ range. In fact, almost all the laser wavelengths mentioned above have been in fact tested for their potential to ablate dental hard tissue. In Sections 3.3 and 3.4 a comprehensive review of the literature concerning ablation of dental hard tissues will be presented. As it will become apparent, the characteristics of the ablated sites (smoothness, chemical changes, shape) and of ablation (ablation threshold, ablation rates) will not always be what one would expect based on the optical properties described in this Section. This is, most likely, partly a consequence of the fact that the optical properties of enamel and dentine are not locally constant: they change as a function of the local composition of these materials.

3.2 The temporal profile of laser pulses

Before proceeding, however, it is necessary to be familiar with the temporal profile of existing lasers, since this is one of the most important parameters governing the response of tissue to radiation. In general, few laser systems have a gaussian temporal profile like the one shown in Fig 3.7c. Free-running lasers, the most commonly used ones for dental laser ablation, currently have a pulse duration on the order of 100 – 300 μ s, but the temporal intensity profile is far from the ideal "top-hat" and Gaussian distributions. Free running laser (macro)pulses are typically composed of an array of micropulses with a duration on the order of microseconds; each micropulse is separated from the next by a few microseconds also; typical examples of the temporal profile of free-running lasers can be seen in Fig. 3.6 and in Figs. 3.7 b, d.

Free-electron lasers have a similar pulse structure to the free-running lasers, only the macropulses have a duration on the order of a few microseconds, and are composed of a train of micropulses each with a duration of 1 – 2 ps, separated from the next micropulse by hundreds of picoseconds.

Q-switched lasers, on the other hand, have a temporal profile which is much closer to Gaussian, but sometimes still present a higher spike at the beginning of the pulse (see Fig. 3.7 a, c) which has some consequences during ablation, as will be discussed below in this Chapter.

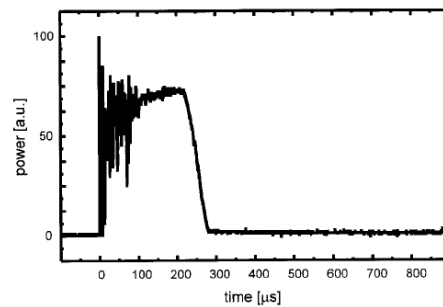


Figure 3.6: Temporal pulse shape for an Er:YAG flashlamp-pumped laser in free running mode. Each micropulse lasts approximately 0.5 to 5 μs and is separated from the next micropulse by 2 to 5 μs . Source: ref. [79].

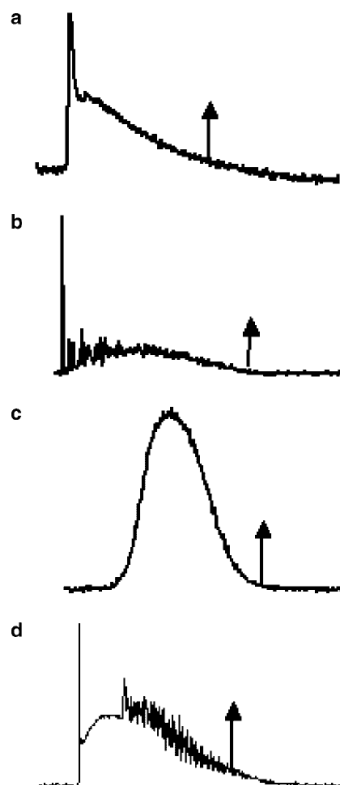


Figure 3.7: Temporal pulse shapes for various laser systems: (a) Argus Photonics 9.6 μm CO_2 laser (the arrow indicates 5 μs), (b) Pulse Systems LP-60 9.6 μm CO_2 laser (the arrow indicates 100 μs), (c) Schwartz 123 Q-switched Er:YSGG laser (the arrow indicates 0.5 μs), and (d) Schwartz 123 free-running Er:YSGG laser (the arrow indicates 200 μs). Source: ref. [80].

3.3 Lasers primarily absorbed by water and organic material

In this Section the experimental evidence on promising laser candidates which are preferentially absorbed by the water and organic material (the Er:YAG and the UV lasers) will be presented.

This overview of the literature will indicate that Er:YAG lasers seem good candidates to drill the narrow tunnels necessary for the tunnelling technique described in Section 1.4.2, but that the laser pulse parameters need to be tuned to minimize cracking while maintaining adequate ablation rates. For these reasons, the models developed further on in this Thesis will be concerned with Er:YAG lasers. Since ablation of enamel seems to pose more challenges than dentine, only enamel will be modelled. This review will provide indication as to the best operating parameters: the optimal pulse duration should be shorter than that normally used with free-running lasers because of the extent of thermal damage inflicted to tissue even in the presence of water cooling; however, it should not be less than one microsecond, since lasers as short as this have been proven to cause extensive mechanical damage.

With respect to the UV lasers, the review will indicate that the mechanical damage inflicted to dentine is too extensive to make these lasers the first choices for optimal minimally invasive procedures, so these lasers will not be investigated further.

3.3.1 The Er:YAG lasers

A great deal of authors have verified that Er:YAG lasers, emitting at $2.94 \mu\text{m}$, can indeed be used to ablate dental hard tissue to produce conventional cavities (in both size and shape), provided cooling is used. In fact, several lasers at this wavelength have been cleared by the USA Food and Drug Administration (FDA) and/or the European Union to do so. The commercial denominations of those lasers are DELightTM ¹ (ConBio), Fidelis Er, Fidelis Er II ² (Fotona), Fidelis Plus II ³ (Fotona; this laser combines the Er:YAG with the Nd:YAG lasers), KEY Laser

¹<http://www.conbio.com/dental/delight/default.asp>

²http://www.fotona.si/medical/fidelis_er.asp?flash=no

³http://www.fotona.si/medical/fidelis_plus.asp?flash=no

3⁴ (KaVo), OpusDuo E, OpusDuo EC⁵ (OpusDent; these systems combine the CO₂ and the Er:YAG lasers) and Smart 2940d⁶ (Deka). Despite the fact that this technology is already approved and considered safe, dental lasers are not generally well accepted by the majority of dentists, in the context of conventional cavity preparation. Part of the reason for this is cost (a laser system can cost more than ten times more than a drill system), but another reason is that there are still issues to solve to make the laser technology optimal. These issues include the chemical nature and morphology of the material at the surface of the crater, which influence the strength of the adhesion between the ablated surface and the filling material, and the extent of mechanical damage suffered by the tooth, which influences the tooth's mechanical stability, as will become apparent further on in this discussion.

It is generally agreed that Er:YAG lasers in free running mode should not be used to ablate either dentine or enamel without water cooling, because of the high risk of extensive thermal damage such as melting, resolidification and charring [81, 82, 83, 84]. Matson et al. used a free-running Er:YAG laser (pulse duration = 200 μ s, repetition rate = 2 Hz, fluence per pulse⁷ = 60 – 70 J/m², 240 pulses per spot) to ablate enamel, and found that using water cooling makes a significant difference on the outcome of ablation: the thermal damage is greatly minimized, with melting and recrystallization occurring only in small areas, and the enamel rod structure is exposed, thus increasing the surface capability for bonding. It should be noted, however, that Matson et al. make no specific mention of visible mechanical damage, so it is not possible to conclude from their study that Er:YAG enamel ablation using water cooling is assuredly free from that type of damage. The issue of the quality of the ablated site-surface in enamel was also investigated by Eguro et al. [85], using comparable pulse parameters to those used by Matson et al. (pulse duration = 250 – 500 μ s, repetition rate = 4 Hz, fluence per pulse⁸ = 52 J/cm², 250 pulses per spot). Eguro et al. found that, even when using water, ablated areas underwent compositional changes (α and β tricalcium phosphate, tetracalcium phosphate and other calcium phosphates were formed). The ablated sites had a scaly and uneven surface, showing micro-cracks and fused areas.

⁴http://www.kavo.com/En/produkte/therapie_instrumente/laser3/laser3.asp?navid=27&lan=En

⁵http://www.opusdent.com/site/product_applications/product.list.asp?fid=7&did=83

⁶http://www.dekalaser.com/prod_sch.php?type=ENG.40

⁷Not given by the authors; calculated based on the given values of pulse energy and spot size.

⁸Both the fluence and the number of pulses per spot were not given by the author, and were calculated based on the given values of energy per pulse, spot size and total energy deposited, according to fluence=energy/area and number of pulses=total energy/energy per pulse.

Ishizaka et al. [86] made a careful study of the quality of dentinal irradiated sites using a long-pulse Er:YAG laser with parameters comparable to those mentioned previously (pulse duration = 250 – 500 μs , repetition rate = 4 Hz, fluence per pulse⁹ = 21 – 36 J/cm², number of pulses per spot not given) and water cooling to sites treated using a dental bur, and found that irradiated sites showed alterations in color that do not appear on the sites treated with the dental bur. Although none of the sites displayed carbonization, cracking or changes in the crystallinity or level of mineralization, the irradiated site did show minor alterations in its chemical content. Furthermore, the dentinal tubules at the irradiated sites were empty, whereas they were filled with odontoblastic processes in the sites treated with the dental bur, which indicates that the organic material in the dentinal tubules is ablated preferentially. This observation is consistent with the high water content associated with the dentinal tubules. Eguro et al. [87] also investigated the ablated sites in dentine after having been irradiated with an Er:YAG free-running laser using water cooling (pulse duration = 250 – 500 μs , repetition rate = 4 Hz, fluence per pulse = 25 J/cm², 150 pulses per spot¹⁰) and found that the ablated dentinal surface had a scaly appearance, with open dentinal tubules and no evidence of melting, resolidification or cracking. It thus seem that dentine is less prone to suffer thermal or mechanical damage than enamel when Er:YAG lasers are used.

Now that the quality of the surface at the sites irradiated with free-running Er:YAG lasers was described, it is important to get an idea of the order of magnitude of the ablation rates for enamel and dentine that can be expected for this laser system when using comparable laser parameters to those mentioned previously in this Section. Majaron et al. [82] demonstrated that the Er:YAG laser in free-running mode (pulse duration = 230 – 300 μs FWHM¹¹, repetition rate = 5 Hz, fluence per pulse = 20 – 45 J/cm², 10 pulses per spot) and used in conjunction with water cooling can be used to speedily ablate both enamel and dentine, obtaining ablation rates in the order of tens of micrometers per pulse. Majaron et al. [82] studied the influence of water cooling on the Er:YAG ablation rates of enamel and dentine, using laser parameters similar to those used by Matson. Majaron and his team found that water spray reduces the ablation rates in dentine, but increases the ablation rates in enamel. The same observation using compara-

⁹Not given by the authors; calculated based on the given values of energy per pulse and spot size.

¹⁰Both the fluence and the number of pulses per spot were not given by the author, and were calculated based on the given values of energy per pulse, spot size and total energy deposited.

¹¹Full width at half maximum.

ble laser parameters was made by Stock et al. [88]. The decrease in the ablation efficiency of dentine can be explained if one assumes that, when water spray is used, a part of the radiation is not absorbed by dentine and is instead absorbed by water. In the case of enamel the same thing happens but, because the amount of water (the main absorber at this wavelength) in enamel is so small, the water spray prevents the enamel from dehydrating and thus increases the ablation rates. Majaron's work thus suggests that producing a long aspect-ratio tunnel may pose unexpected problems: it is reasonable to assume that, if the tunnel becomes partially filled with water, the ablation efficiency will decrease markedly. This supposition is supported by work done by Stock et al. [88] on enamel ablation using a KEY 2, KaVo GmbH laser (pulse duration = 400 μ s, repetition rate = 4 Hz, fluence per pulse¹² = 67 J/cm², 10 pulses per spot), which indicates that, if Er:YAG lasers are to be used to prepare large aspect-ratio tunnels, the laser operating parameters and the flux of water need to be optimized to yield the desired results. An alternative to using water is to use perfluorocarbon as a coolant. Perfluorocarbon is a non-toxic, non-reactive liquid which does not absorb at $\lambda = 2.94 \mu\text{m}$ [89] and that dissipates heat and acoustic stress effectively. It has been shown to perform very well for bone ablation at $\lambda = 2.94 \mu\text{m}$: Ivanov et al. [90] have demonstrated that a FEL laser (pulse duration = 4 μ s, repetition rate = 30 Hz, fluence per pulse = 30 – 50 J/cm², large number of pulses per spot) and a free-running laser (pulse duration = 250 μ s, repetition rate = 3 Hz, fluence per pulse = 20 – 70 J/cm², large number of pulses per spot) can ablate bone without any thermal or mechanical damage, and can produce very narrow grooves in this material. Their results can be extrapolated to dentine, because of the similar composition (60% HA, 27% collagen and 13% water for bone, versus 70% HA, 20% organic and 10% water for dentine). However, bone has a much higher water content than enamel, so it is possible that ablation of enamel at this wavelength without applying external water will become ineffective after a few laser pulses, because of tissue desiccation. Nevertheless, perfluorocarbon cooling remains a possibility to investigate if water cooling proves impossible to use when trying to drill long tunnels.

Eguro et al. [85] tested the adhesion strength of a composite to the surface of ablated sites on enamel and dentine. For enamel, using typical free-running laser parameters (pulse duration = 250 – 500 μ s, repetition rate = 4 Hz, fluence per pulse = 52 J/cm², 250 pulses per spot), his team found the adhesion strength of

¹²Not given by the authors; calculated based on given data.

the surface to be significantly lower than that produced by commercial bonding systems. However, they also pointed out that the strength of adhesion could be made much higher by treating the ablated surface with ultrasounds (using a commercially available device) prior to application of the resin filling material. They explained the increase in adhesion strength by the fact that the ultrasound treatment most likely removes the non-apatitic, poorly attached debris from the surface, thus increasing the adhesion strength. Similar results using identical laser parameters and water cooling were obtained by Otsuki et al. [91]. Otsuki et al. further confirmed that the flaky and glass-like portions of enamel existing at the ablation site need to be removed in order to increase adhesion strength to resins, and demonstrated that an adhesion strength high enough to ensure adequate sealing of cavities could be obtained when the irradiated sites were treated with air powder polisher *and* phosphoric acid prior to the placement of the resin. For dentine, using Er:YAG free-running laser (pulse duration = 250 – 500 μ s, repetition rate = 4 Hz, fluence per pulse = 25 J/cm², 150 pulses per spot) and water cooling, Eguro et al. [87] found that the adhesion strength of the irradiated surface to the composite resin was significantly lower than that obtained when a non-irradiated surface is treated with a phosphoric acid etch primer. Furthermore, when the irradiated surface is treated with the same acid etch primer before applying the composite resin, the adhesion strength is still slightly lower than for the non-irradiated, acid etched dentinal surface, but within clinically acceptable values. The same was observed by Ramos et al. [92] when using comparable, but not identical, laser parameters and various etching primers.

Apel et al. [93, 94] investigated the modification of the solubility of enamel previously irradiated using the Er:YAG laser and sub-ablative fluences without water cooling (pulse duration = 150 μ s, repetition rate = 5 Hz, fluence per pulse = 4, 6 and 8 J/cm², 125 pulses per spot) and found that irradiation did not create a more acid resistance surface. In fact, extensive and deep (over 100 μ m deep) cracking was observed in enamel, which provided points for easier acid attack. However, they also found that application of fluoride to the irradiated surfaces could make them more acid resistant than untreated surfaces. Information on the influence of Er:YAG irradiation in acid resistance of enamel when water is used could not be found, but it is likely that under these operating conditions the Er:YAG will not be able to cause the high temperature rises necessary to release carbonate from the enamel and thus increase this material's resistance to acid attack.

The water cooling plays a double role in Er:YAG ablation of dental hard tissue:

besides decreasing the extent of thermal damage, it prevents the pulp from overheating, as demonstrated by Cavalcanti et al. [95]. More specifically, Cavalcanti et al. [95] used an Er:YAG laser (pulse duration = 250 μ s, repetition rate = 10 Hz, energy per pulse¹³ = 350 mJ) and found that the temperature at the pulp, when water cooling is used, did not rise more than 5 °C, which is comparable to the temperature rise experienced at the pulp when a high-speed dental bur is used with water cooling (2 °C).

While the Er:YAG free-running lasers are the most commonly used, the unwanted side effects they cause have driven researchers to experiment shorter pulse durations (although still within the thermal interaction regime). Several authors have in fact made studies with the aim of directly comparing free-running (long-pulsed) and Q-switched (short pulsed) Er:YAG lasers on enamel and dentine. Ashouri et al. [84, 96] have found that the Q-switched laser (pulse duration = 0.15 μ s, repetition rate not given, fluence per pulse = 40 J/cm², 20 pulses per spot) produced uniform cuts through bovine enamel¹⁴ with minimal evidence of melting or cracking at much lower fluences than those necessary for the free-running laser (pulse duration = 200 μ s, repetition rate not given, fluence per pulse = 100 J/cm², 20 pulses per spot), when water was used for both lasers. When water was not used, Ashouri et al. found that both pulse durations caused extensive melting of the enamel.

Lee et al. [97] investigated the different effects caused by Q-switched and free-running Er:YAG lasers on dentine without the use of water cooling. They found that negligible charring was generated by the Q-switched laser, but a char layer was generated when using the long-pulse laser (fluence per pulse = 3 – 40 J/cm² for the Q-switched laser, and 12 – 300 J/cm² for the free-running laser; repetition rate and number of pulses per spot not given). These authors did not investigate the extent of cracking caused by the short pulse laser, but suggested that extensive damage might be present because of the short duration of the laser pulse. Interestingly, these authors also indicated that the noise produced during ablation with the Q-switched Er:YAG laser is loud enough to be irritating to the laser operator, which implies it is necessary to assess whether it could cause hearing problems to patients undergoing dental laser treatment. Fried et al. [98] also compared the effect of a Q-switched and a free-running Er:YAG laser on bone ablation without

¹³The author did not mention the fluence per pulse. Since he also did not mention the laser spot size, it is impossible to determine the fluence per pulse.

¹⁴Bovine enamel is similar in composition and structure to human enamel, so results can be extrapolated to human dental enamel.

water cooling. They found that while the ablation rates were significantly higher for the free-running laser, this laser also caused thermal damage like charring to occur, something that did not happen with the Q-switched laser (free running laser pulse duration = 300 μ s; Q-switched laser pulse duration = 0.5 μ s, repetition rate = 1 – 2 Hz, fluence per pulse = 1 – 100 J/cm², number of pulses per spot not given, but large). Papagiakoumou et al. [99] also investigated the differences between Q-switched and free-running Er:YAG lasers on dentine without water cooling, and found that the Q-switched laser (pulse duration = 190 ns FWHM, repetition rate = 1 – 4 Hz, fluence per pulse = 8 – 100 J/cm², 40 – 200 pulses per spot) produced well-shaped craters, with open dentinal tubules at the edge of the crater and neither carbonization nor melting. However, cracks were observed even for the lower fluences used. The free-running laser (pulse duration = 80 μ s FWHM, remaining parameters like for the Q-switched laser) had much higher ablation rates than the Q-switched laser, but generated charred dentine with small cracks when the highest fluences were used. For both lasers, the ablation rates saturated with fluences above 6 J/cm² (Q-switched) or 10 J/cm² (free-running) because of absorption of radiation by plasma in the ablation plume. It thus seem that the Q-switched laser, despite its much shorter pulse, must still be used with water cooling to prevent thermal damage, at least when ablating enamel, and that in any case tends to cause unwanted cracking in both enamel and dentine.

While the ablation rates for Q-switched lasers are lower than for the free-running, they are certainly still appropriate in the context of the minimally invasive dental treatment, provided that they do not decrease as the ablation crater becomes deeper. However, the effect of applied water on Q-switched Er:YAG laser ablation is likely to be similar to that observed for the free-running laser, that is, it is possible that drilling long aspect-ratio tunnels is made more difficult by accumulation of water in the ablation crater. On the other hand, Fried et al. [96] have demonstrated that they can drill high aspect-ratio grooves in enamel, as can be seen in Fig. 3.8, which seems to indicate that high aspect-ratio tunnels may be possible to produce with similar laser parameters.

It remains to be determined whether the adverse mechanical side effects caused to dentine by Q-switched lasers are minimized when water cooling is used, whether the irradiated surfaces experience marked changes in its chemical composition and on the adhesion strength between enamel or dentine and resin fillings, topics for which no information in the literature was found. Also, it is important to say that, while the thermal effect at the pulp of the tooth has not yet been assessed,

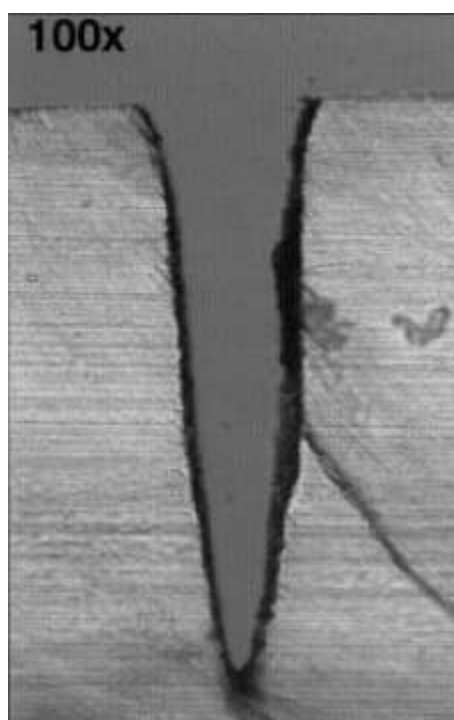


Figure 3.8: Polarized light image of 100 μm thick cross sections of enamel ablated by a Q-switched Er:YAG laser with water cooling (pulse duration = 150 ns, repetition rate = not given, fluence per pulse = 15 J/cm^2 , 20 pulses per spot). The crater is $125 \mu\text{m}$ wide and $490 \mu\text{m}$ deep. Source: ref. [96].

comparison with the free-running Er:YAG laser indicates that thermal damage to the pulp of the tooth is unlikely to occur if water cooling is used.

To end this Section on Er:YAG lasers, it is interesting to note that several authors have attempted to establish whether the Er:YAG laser could be used for other procedures of interest in dentistry: surface sterilization and decreasing dentinal hypersensitivity. This is of interest in clinical practice, since a piece of expensive equipment such as a laser is surely to become more attractive to dentists if it can be used for a variety of procedures. Moura et al. have shown that the Er:YAG laser (KaVo KEY laser 1242, KaVo Dental GmbH, pulse repetition rate = 10 Hz, energy per pulse¹⁵ = 52 or 110 mJ) does not seem to have sufficient antimicrobial activity to sterilize infected root canals [100]. However, other authors have reached an opposite conclusion using similar laser parameters: Hibst et al. [34], using a free-running Er:YAG laser (pulse duration $\simeq 250 \mu\text{s}$, repetition rate = 15 Hz, fluence per pulse = $1.70 - 0.85 \text{ J/cm}^2$, 10 to 40 pulses per spot) on carious enamel and dentine, found that bacteria could be eliminated even in strongly carious sites if a temperature of $100 \text{ }^\circ\text{C}$ could be reached at the sur-

¹⁵The authors did not disclose the pulse duration, the fluence and the number of pulses applied.

face after several laser pulses. Since the experimental procedure followed by these authors is robust (both teams irradiated diseased teeth and subsequently tested those teeth for evidence of bacterial activity) it seems likely that the Er:YAG laser does *reduce the bacterial count in dental lesions*, even though it may not eliminate bacteria entirely. Also, the Er:YAG laser, with similar operating parameters as used by Moura et al., seems not to perform as well as conventional smear layer removal solutions (like sodium hypochloride and EDTA¹⁶) to remove the smear layer (containing bacteria and organic and inorganic dental material) produced in root canals as a result using the dental bur during root canal treatment. Finally, there is evidence to suggest that a beneficial side effect of using this wavelength (energy per pulse = 5 - 10 mJ, repetition rate = 10 Hz) to ablate dental hard tissue is *decreased dentinal hypersensitivity* [101]. To conclude, it is important to note that using the Er:YAG laser to ablate dental hard tissue has the added advantage of being, in general, painless, even when done in cavities in the deep dentine, as demonstrated by Altshuler et al. in a study involving almost 400 treated sites *in vivo* [31]. This feature may be common to all laser wavelengths, since pain induced by the dental bur is thought to be related to the mechanical vibration induced by the bur.

This overview of the literature regarding Er:YAG lasers allows us to conclude that they seem promising candidates to drill the narrow tunnels necessary for the tunnelling technique described in Section 1.4.2, provided the laser pulse parameters can be tuned to minimize cracking while maintaining the ablation rates. This review indicates that the optimal pulse duration is most likely shorter than that normally used with free-running lasers because of the extent of thermal damage inflicted to tissue even in the presence of water cooling. At the same time, it should not be less than one microsecond, since laser pulses as short as this have been proven to cause extensive mechanical damage.

3.3.2 The ultraviolet lasers

In this subsection the effect of ultraviolet lasers at wavelengths 193, 248 and 355 nm on enamel and dentine will be discussed. While it is known through experimental evidence that the 193 and 248 nm wavelengths can ablate pure hydroxyapatite [75, 76, 77, 78], when ablating enamel and dentine at these wavelengths they display an etched-like surface which suggests that the organic component has a

¹⁶Ethilenediamine tetra-acetic acid.

higher absorption coefficient than the mineral. Therefore, these wavelengths were placed under the category of lasers preferably absorbed by the organic and water components of the tissues.

Wilder-Smith et al. [102] investigated the ablation rates and crater morphology of both enamel and dentine by the ArF laser ($\lambda = 193$ nm) without the use of water. For enamel (pulse duration = 15 ns, repetition rate = 10 Hz, fluence per pulse = 0.5 – 10 J/cm², 50 or 1800 pulses per spot) they found no evidence of carbonization. At the lower fluences, they found that the craters had smooth sides and walls, without evidence of cracking or melting. As the fluence and exposure times become higher, evidence of thermal and mechanical damage can be observed: melting, resolidification and cracking. For dentine (pulse duration = 15 ns, repetition rate = 10 Hz, fluence per pulse = 1 – 3 J/cm², 50 to 1800 pulses per spot), similar results were obtained: no areas of carbonization were found, but melting and resolidification were observed when the higher fluences and exposure times were used.

These authors did not evaluate the changes in surface chemical composition of enamel or dentine, although a comparison with other wavelengths and the fact that melting was observed and water was not used seem to suggest that the thermally affected layer may contain calcium phosphates other than HA.

Sealed dentinal tubules were clearly visible, particularly at higher fluences and exposure times. Similar results were obtained by Sánchez et al. [103], who used comparable, but not identical, ArF laser parameters on dentine (pulse duration = 23 ns, repetition rate = 5 Hz, fluence per pulse = 1 – 4 J/cm², 50 to 1000 pulses per spot): at lower fluences, Sánchez found a smooth dentinal floor with no evidence of sealed dentinal tubules or melting. As the fluence increases, the dentinal tubules become sealed as a consequence of dentine melting, and cracking of the crater floor occurs. Unfortunately, no information could be found in the literature on the irradiated surface adhesion strength to resin fillings, resistance to acids or pulpal heating.

The ablation rates for enamel determined by Wilder-Smith et al., although quite low (on the order of only less than a micron per pulse when lower fluences were used) are certainly high enough to drill a 2.5 mm tunnel in an acceptable time (less than 10 min). The ablation rates for dentine are of the same magnitude as for enamel. Although the ablation rates become higher as the fluence is increased, the rise is far from being directly proportional to the rise in fluence, so the best balance between higher ablation rates and minimization of thermal damage must

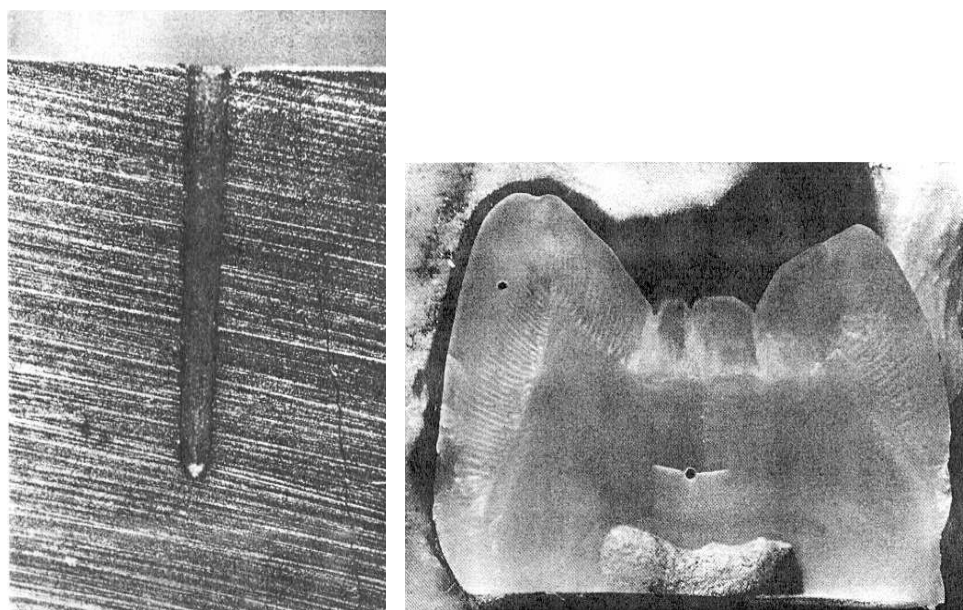
be found. While it was not yet demonstrated that this laser can indeed drill high aspect-ratio tunnels through dental hard tissue, an analogy with the KrF laser at $\lambda = 248$ nm (discussed next in this Section) which is absorbed by roughly the same substances, seems to indicate that this may be possible.

The experimental evidence in favor of selecting the ArF laser thus seem to be promising, but not abundant; however, this laser also presents significant disadvantages, such as its high price as compared to other laser systems (based on IR wavelengths), its large size and the fact that radiation at this wavelength may have cytotoxic effects [58]. Therefore, this laser is not the best candidate for the job.

Walter et al. [104] have investigated the effect of both the ArF and the KrF lasers on bone. Walter et al. did not disclose many of the laser parameters used (pulse duration not given, repetition rate not given, fluence per pulse = 0.25 J/cm^2 for the ArF, and 0.5 J/cm^2 for the KrF, number of pulses per spot not given), which makes it impossible to compare their work with the work of others. Nevertheless, their results hold by themselves and indicate that, for similar laser operating parameters, the extent of thermal damage caused by the KrF laser affects a layer twice as thick as that created by the ArF laser, which suggests that the $\lambda = 193$ nm laser may be a better choice in this aspect than the $\lambda = 248$ nm laser. As suggested in Section 3.1, Pearson et al. indicate that this laser seems to be principally absorbed by regions rich in organic material and, consequently, the ablated surfaces exposed the dentinal tubules and the enamel rods [105, 106].

Pearson et al. have demonstrated that the KrF laser at 248 nm (pulse duration = $15 - 20$ ns, repetition rate = 20 Hz, fluence per pulse = 15 J/cm^2 , $500 - 2500$ pulses per spot) without using water spray can ablate enamel and dentine. They found evidence of some thermal modification of the walls of the ablated site, in particular for enamel, and they propose that it can be minimized by making the pulse spatial intensity profile "top-hat" like. This would reduce the extension of tissue under radiation with intensity not high enough to produce ablation. However, the authors did not test this hypothesis. Pearson and co-workers make no mention of any mechanical damage to treated enamel, but long cracks in dentine are clearly visible in two of the figures shown in their papers (see Fig. 3.9). On the other hand, Fried et al. [107] using a laser emitting at 266 nm, a wavelength close enough to that emitted by the KrF laser so that results are comparable, found no evidence of chemical modification of the surface of the ablated site in bovine enamel when using lower fluences (pulse duration = 3 ns, repetition rate not given, fluence per pulse = $3 - 5 \text{ J/cm}^2$, 20 pulses per spot). This result suggests that by

carefully controlling the fluence used, unwanted thermal damage can be avoided.



(a) Micrograph showing the full length dentine tunnel preparation. Length of tunnel is 2.5 mm. Note the long crack parallel to the tunnel.

(b) Photomicrograph of a longitudinal section through the crown of the tooth showing irradiated sites in enamel and dentine. Note the crack radiating from the dentine lesion.

Figure 3.9: Examples of mechanical damage in dentine caused by a KrF laser at $\lambda = 248$ nm (pulse duration = 15-20 ns, repetition rate = 20 Hz, fluence per pulse = 15 J/cm^2 , 500-2500 pulses per spot). No water cooling was used. Source: ref. [108].

Pearson and co-workers have demonstrated that the KrF laser (pulse duration = 15 – 20 ns, repetition rate = 20 Hz, fluence per pulse = 15 J/cm^2 , 500 – 2500 pulses per spot) without using water spray can produce narrow (diameter inferior to 0.5 mm) and long (depth of 2.5 mm) tunnels through both enamel and dentine [108]. The ablation rates also proved to be sufficiently high to allow drilling a 3 mm long tunnel through enamel and dentine in under 4 minutes [105, 108]. While no specific measurements of the bond strength of resins to irradiated surfaces could be found in the literature, the smooth surfaces with exposed rod or tubule morphology seem to indicate that adhesion will be reasonable. In any case, work by authors using other wavelengths (like those found in refs. [85, 87]) indicates that it is possible to improve adhesion of irradiated sites by acid etching the surfaces after laser irradiation. The resistance to acid dissolution of the irradiated sites was also not assessed, but evidence obtained for other lasers indicates that it

can always be improved by application of topical fluoride [109].

Pearson et al. also did not measure the temperature changes experienced at the pulp of the tooth, so it cannot be affirmed at this time that the method is safe to use *in vivo*. Although it is possible that the temperature change at the pulp is within safe limits, further research exploring this issue needs to be conducted before ablation using these laser parameters can be considered safe for patients.

Despite the drawbacks enumerated above, the KrF laser may be used for the tunnelling technique described in Section 1.4.2, provided that the operating parameters can be optimized to ensure that thermal and mechanical damage are kept to a minimum. The major inconveniences of this laser are its large size (the apparatus used by Pearson and co-workers occupied an entire room), its high price compared to IR lasers and the very high cytotoxicity of this wavelength. Thus, this laser also does not seem to be the best candidate for the job.

The Nd:YAG laser operating at the third harmonic (355 nm) has also been tested for enamel laser ablation. Wheeler et al. [109] have proved that the 355 nm wavelength (pulse duration = 3 – 5 ns, repetition rate = 10 Hz, fluence per pulse = 1.3 – 8.3 J/cm², 10 pulses per spot) without using water cooling can ablate bovine enamel without evidence of fusion of the enamel prisms at the ablated site for all the fluences tested. The non-existence of enamel thermal damage at this wavelength was also verified by Fried et al. [107] using comparable laser parameters.

Wheeler et al. also demonstrated that the ablated sites exhibit the micrometer-scale morphology characteristic of enamel for all fluences tested (except for 1.3 J/cm², which is the threshold ablation fluence, where the surface modification is very small), and that the ablated site does not differ chemically from the untreated sites. They showed that the ablated surface adheres strongly to composite materials (although less strongly than a surface etched using an acid), and that the laser is thus an appropriate tool to modify the tissue surface to ensure adequate adherence of filling materials. Finally, Wheeler et al. showed that the enamel laser treated sites were less resistant to acid dissolution than untreated sites, something of significant importance because the laser treated sites would be more prone to develop caries. However, this tendency can be inverted if the topical fluoride is applied to the laser-treated sites; the acid dissolution rates of sites treated in this manner are actually 50% lower than for untreated enamel.

Different conclusions were reached by Sheth et al. [110] using the same wavelength and different, but comparable, laser parameters (pulse duration = 15 ns,

repetition rate = 30 Hz, fluence per pulse = 2 J/cm^2 , 30 pulses per spot) on dentine without water cooling: the ablated surface adhered *less* strongly to the filling material than an untreated surface. This author made a direct comparison of the results using the 355 nm wavelength on dentine with those obtained using an Er:YSGG and a CO_2 at $9.6\ \mu\text{m}$ (discussed in more detail in subsection 3.4), and found that the IR lasers are much better at preparing the dentinal surface for adhesion to composite materials than the KrF laser.

Dela Rosa et al. [80] also ablated dentine using a 355 nm laser (pulse duration = 5 ns, repetition rate not given, fluence per pulse = $2 - 50\ \text{J/cm}^2$, 10 pulses per spot) and similar parameters to those used by Sheth et al.. Therefore, results obtained by those two teams can be directly compared. Dela Rosa et al. observed minimal thermal damage in the ablated site, even when water was not used. On the other hand, extensive mechanical damage was observed, even when fluences as low as $5\ \text{J/cm}^2$ were used. The mechanical damage became more severe as the fluence increased and, surprisingly, was greater when water spray was used (see Fig. 3.10), something for which the authors provided no explanation.

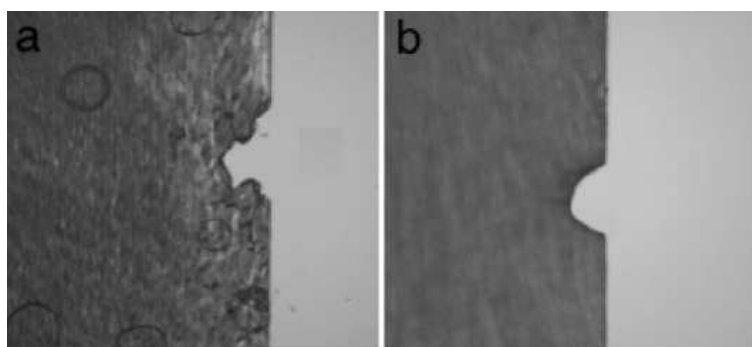


Figure 3.10: Polarized light images of the 355 nm Nd:YAG laser incisions with (a) and without (b) water (pulse duration = 5 ns, repetition rate not given, fluence per pulse = $10\ \text{J/cm}^2$, 10 pulses per spot). Field width is 1.8 mm. Source: ref. [80].

Sheth et al., on the other hand, found that the dentinal surface produced was highly uniform and showed no evidence of thermal damage, even without water.

Dela Rosa's results thus indicate that a 5 ns laser pulse at this wavelength will not produce appropriate results, despite having adequate ablation rates for dentine ($\simeq 5\ \mu\text{m}/\text{pulse}$ at a fluence of $20\ \text{J/cm}^2$). While one can suppose that a slightly longer laser pulse may decrease the extent of mechanical damage (as will be discussed further along in this Thesis, the duration of the laser pulse has a significant influence on the intensity of the stress transients generated in the material), this hypothesis has not been explored yet. One can conclude that

the 355 nm wavelength is a possible candidate for the tunnelling technique being proposed by Pearson et al. but, similarly to the 193 and 248 nm wavelengths lasers, its operating parameters must be optimized in order to decrease mechanical damage in the ablated sites before the laser can produce acceptable results. It should be noted that none of these authors attempted to produce long aspect-ratio cavities, something that Pearson et al. demonstrated that 248 nm radiation can do.

Neither Sheth et al. nor Wheeler et al. evaluated the pulp temperature during ablation but the lack of thermal damage suggests that the temperature rise at the pulp may be within acceptable levels; this conclusion would have to be tested experimentally, though.

Palamara et al. [39] investigated the effect on enamel of an excimer-dye laser emitting at 382.8 and 489.9 nm and with laser parameters (pulse duration = 10 ns, repetition rate = 30 – 50 Hz, fluence per pulse \simeq 30 J/cm², various number of pulses per spot) similar to those used by Dela Rosa et al.. The closeness of these wavelengths to the 355 nm wavelength and the fact their photon energy is inferior to the energy of most covalent bonds in organic molecules suggests that the mechanism of interaction with the tissue will be similar to that for the 355 nm laser; hence, the results obtained by Palamara et al. are discussed here in relationship with results obtained for the 355 nm laser. Palamara et al. found that the excimer-dye laser caused extensive melting, resolidification and recrystallization in enamel, which assumed a vitrified appearance, unlike what Sheth et al. found for the 355 nm laser and enamel. This is most likely a consequence of the much higher fluence per pulse used by Palamara. These authors did not mention the existence of cracks and pits in and around the crater sites, which is consistent with finds by Sheth et al. for enamel. While Palamara et al. did not investigate the temperature changes experienced at the pulp of the tooth during ablation, did not do experiments on dentine and did not assess the capability of these wavelengths to produce long tunnels through enamel and dentine, their results seem to indicate that these longer UV wavelengths are less appropriate to ablate enamel and dentine than the shorter UV wavelengths described previously.

In general, the results indicate that the extent of thermal damage inflicted to enamel and dentine is smaller for shorter wavelength UV lasers, which suggests that these shorter wavelengths will be more adequate for the task of drilling narrow tunnels through enamel and dentine. For each UV wavelength discussed in this subsection, the extent of thermal and mechanical damage seems to increase with

the number of pulses and increasing fluence. While the thermal damage may perhaps be minimized by using pulses with a "top-hat" spatial intensity profile, it is difficult to predict how the extensive mechanical damage caused by these lasers (in dentine, in particular) may be avoided since various factors (such as pulse duration and temperature rise) may lie in the cause of this type of damage. If the UV lasers are to be suitable lasers to drill narrow tunnels through enamel and dentine, then extensive work must be done to optimize their operating parameters before they are considered safe to use in a clinical setting. The mechanical damage inflicted to dentine is too extensive to make these lasers the first choices for optimal minimally invasive procedures, so these lasers will not be investigated further.

3.4 Lasers primarily absorbed by the mineral

In this Section, the experimental evidence on ablation of dental hard tissues by lasers which are primarily absorbed by the mineral (the YSGG and the CO₂ lasers) will be presented. This review will indicate that the potential of the CO₂ laser emitting at 10.6 μm has not been fully assessed yet, and that this laser may be a good candidate for the procedure in question here, despite the thermal damage that it may inflict under certain operating conditions. For these reasons, the effect of the 10.6 μm wavelength will be investigated in the remaining of this Thesis, together with the Er:YAG laser. Similarly to the Er:YAG laser, only the interaction with enamel will be studied, since the review will indicate that ablation of this material poses more challenges than dentine. The review will provide guidelines as to the best operating parameters to be used as a starting point for the models: the most appropriate pulse durations and repetition rates seem to lie in the range of 0.5 to 10 μs and 1 – 20 Hz, and water cooling seems to be determinant in minimizing thermal damage to dental hard tissue. This laser has the added advantage of being one of the least expensive equipments and being already extensively used in soft-tissue applications, which makes it a financially sound choice, something of importance in a procedure to be implemented commercially.

The evidence presented in this Section will indicate that the YSGG lasers are also good candidates for the minimally invasive procedure described in Chapter 1. Their cost is comparable to the cost of the Er:YAG lasers, and the issues to address before they can perform optimally are similar. However, given that these lasers interact with dental material in a similar manner to the CO₂ lasers, they will not be modelled specifically since results obtained for the CO₂ laser can be easily

extrapolated for these wavelengths.

3.4.1 The YSGG lasers

Evidence indicates that the Er:YSGG¹⁷ (2.79 μm) and Er,Cr:YSGG¹⁸ (2.78 μm) lasers ablate dental hard tissue with rather different results from the Er:YAG lasers. This happens because, even though the frequencies of the YSGG and YAG lasers are very close, the YSGG lasers are highly absorbed by the mineral in dental hard tissues, unlike the Er:YAG lasers.

At subablative fluences, the differences between the YAG and the YSGG lasers are less evident. Apel et al. [94] investigated the potential of both the Er:YAG (pulse duration = 150 μs at FWHM, repetition rate = 5 Hz, fluence per pulse = 6 J/cm², 125 pulses per spot) and the Er:YSGG (same parameters except fluence, which was 8 J/cm²) lasers, without water cooling, to increase the resistance of enamel to dissolution by acids. Decreasing the enamel acid dissolution rates may significantly delay or even prevent the onset of caries, and therefore has been the object of research lately. Apel et al. found that the laser parameters they used produced surfaces with a large density of cracks; note that there was no evidence of ablation, which was to be expected since the fluences used are below the ablation threshold for either laser. Apel et al. also found that the cracks propagated deeply into the tissue, as far down as 100 μm . While the treated sites presented lower acid dissolution rates than the untreated sites, the beneficial effect of the laser was proved to be highly reduced by the existence of the cracks: the crack edges showed signs of extensive demineralization. Apel et al. concluded that both the YAG and the YSGG lasers were unsuitable for laser treatment of enamel surfaces, unlike the CO₂ lasers, as will be discussed in more detail further along in this Chapter.

At very high fluences, however, the differences between the Er:YAG and the Er:YSGG¹⁹ laser ablation are not evident. Stock et al. [88] compared the quality of ablation of enamel and dentine by Er:YAG and Er:YSGG lasers in free-running mode (pulse duration = 400 μs , repetition rate = 4 Hz, fluence per pulse \simeq 65 J/cm² for both lasers, \simeq 10 pulses per spot), and found that it was similar: for both materials and both lasers (using water) they found no evidence of carbonization or fractures (although in his article it is not evident that

¹⁷erbium: yttrium, scandium, gallium, garnet

¹⁸erbium, chromium: yttrium, scandium, gallium, garnet.

¹⁹Erbium: yttrium, scandium, gallium, garnet. This laser emits at 2.79 μm .

they searched extensively for evidence of mechanical damage, since in some of the images of ablated sites they present there are visible cracks which they do not attempt to explain). However, even when using water spray Stock et al. found evidence of molten material at the bottom of the ablation craters in enamel. Interestingly, different conclusions were obtained by Freiberg et al., who compared the results obtained using the Er:YAG laser (pulse duration = 180 μ s, repetition rate = 20 Hz, fluence per pulse = 56 J/cm², number of pulses per spot not given) and the Er:YSGG laser (pulse duration = 50 μ s, repetition rate = 20 Hz, fluence per pulse = 31 J/cm², number of pulses per spot not given) on dental enamel when water cooling was used. For neither of these lasers did Freiberg et al. find evidence of melting and resolidification: the ablated surfaces displayed the rod morphology characteristic of enamel. These authors make no specific mention to mechanical damage induced on the ablated sites, though. The lack of thermal damage may be a consequence of the slightly lower fluence used by Freiberg et al., which suggests that even small variations in the laser operating parameters may translate into large differences in results.

At intermediate fluences, the differences between the Er:YAG and Er:YSGG become more evident: Fried et al. [68], on the other hand, using lower fluences and shorter macropulses (pulse duration = 150 μ s FWHM, repetition rate = 1 Hz, fluence per pulse = 27 J/cm² for Er:YSGG and fluence = 32 J/cm² for Er:YAG, 1 – 50 pulses per spot) and no water cooling only found evidence of melting and resolidification in enamel for the Er:YSGG laser, which is consistent with the higher absorption by the mineral at this wavelength. They also verified that the surface layer of the ablated sites in enamel and dentine could be easily removed with a brush, which strongly suggests that the laser parameters they used (and the fact that no water was applied) will not produce a surface which will adhere properly to any filling material, at least without further preparation. This suggestion is confirmed by work done by Sheth et al., described in more detail further down. No specific information was found on the extent of chemical modification suffered by enamel and dentine ablated with the YSGG lasers, although an analogy with results obtained for the Er:YAG and other lasers suggests that it will not be great when water cooling is used and may be extensive when external water is not applied.

For both YAG and YSGG lasers, Stock et al. [88] confirmed the results obtained by Majaron et al. [82], which indicate that ablation rates for enamel are lower than for dentine for both lasers. Ablation rates are high enough to ablate a long tun-

nel in a clinically acceptable time. These authors found that the Er:YSGG laser caused higher temperatures in the material, but, at the same time, was slightly less efficient at ablating dental hard tissue than the Er:YAG laser, which is rather unexpected since its lower absorption coefficient (400 instead of 800 cm^{-1}) and similar reflectance would suggest that it would behave oppositely. This conclusion is supported by Fried et al. [68] who used an Er:YAG laser with identical parameters to the Er:YSGG laser (pulse duration = 150 μs FWHM, pulse repetition rate = 1 Hz, fluence = 5 – 6 J/cm^2). Fried et al. proposed an explanation for the apparent contradiction between the higher temperature reached in enamel and simultaneous higher ablation threshold when ablated by Er:YSGG lasers, as compared to Er:YAG lasers: they proposed that the outer few micrometers of enamel are relatively water free, and consequently they do not absorb Er:YAG radiation effectively. On the other hand, they stated that Er:YSGG radiation will be effectively absorbed in that region (because it is absorbed by the mineral). Given that the reflectance of enamel at these wavelengths is the same (see Table 3.1), Fried et al. concluded that the higher temperatures reached by enamel under Er:YSGG radiation were a consequence of the fact that the radiometry system they used only detected thermal radiation emitted from the outer layers of the material. However, Fried et al. did not further test this conclusion by ablating enamel samples previously deployed from their outer enamel. The author of this Thesis proposes it is possible that the observed behavior is instead a consequence of the different absorption coefficients of water and mineral at those wavelengths and of the temperature reached in water pores at the end of the micropulses, and will explore this hypothesis in Chapter 6, in the context of CO_2 and Er:YAG lasers. The CO_2 laser should behave similarly to the Er:YSGG laser, since both are high absorbed by the mineral as well as the water.

Another YSGG laser system, emitting at a slightly different wavelength, has also been tested for dental applications. This laser (pulse duration = 140 – 200 μs , repetition rate = 20 Hz, beam spot area = 0.442 mm^2 , output power²⁰ = 3 – 6 W) has been tested *in vivo* to prepare large cavities for fillings by Matsumoto et al. [111], with high patient acceptance (mainly because of the very low pain experienced) and good clinical outcome at a 30-day evaluation. However, the

²⁰The author did not provide the fluence per pulse and did not specify if the output power was per pulse, or averaged over larger time-scales, which makes it impossible to calculate the fluence with certainty. Nevertheless, it is likely that the output power is averaged over time and, in this case, the fluence used by Matsumoto varied between 35 and 70 J/cm^2 , which is comparable to the settings used by other authors.

effects of mechanical damage will only be detected with a long-term evaluation, so Matsumoto's results must be interpreted with care before long term evaluations or histological data of teeth treated *in vitro* become available.

The free-running YSGG laser is thus capable of ablating material; the main issue surrounding the use of this laser is the thermal damage inflicted to enamel under certain operating conditions, even when water cooling is used. Similarly to what happened with the Er:YAG laser, this drove researchers to investigate how a shorter pulsed laser would perform in comparison with a free-running YSGG laser. Sheth et al. [110] have evaluated the quality of Er:YSGG ablation sites in dentine in terms of surface morphology and adhesion strength to composite materials, both using a free-running laser (pulse duration = 200 μs , repetition rate = 3 Hz, fluence per pulse = 20 J/cm², 3 pulses per spot) and a Q-switched laser (pulse duration = 0.5 μs , repetition rate = 3 Hz, fluence per pulse = 10 J/cm², 3 pulses per spot). They found that the free-running Er:YSGG laser caused thermal damage in dentine even when used with water, which is consistent with the results obtained by Stock et al. [88]. They found that a significantly more uniform surface with minimal or no thermal damage was obtained using the Q-switched Er:YSGG laser and a water spray. This conclusion was confirmed by Dela Rosa et al. [80], who used very similar laser parameters (pulse duration = 0.5 μs , repetition rate not given, fluence per pulse = 20 J/cm², 6 pulses per spot) and found that the thermal damage was restricted to a 3 – 5 μm layer if water spray was used (see Fig. 3.11). The same conclusion also supported by Fried et al. [96], who used similar, although not identical, laser parameters for a Q-switched Er:YSGG laser. Fried et al. also verified that the ablation efficiency for enamel is much higher when the Q-switched laser is used, comparing to the free-running laser, as is apparent from Fig. 3.12. The extent of mechanical damage caused by the Q-switched laser was not specifically investigated by these authors, but it is possible that it occurs.

This smoother dentinal surface obtained with a Q-switched Er:YSGG laser also presented higher values of adhesion strength to composite material, comparable – but still significantly inferior – to those obtained using an acid etch. Sheth et al. [110] reached similar conclusions comparing the adhesion strength of dentine treated with Q-switched and free-running CO₂ lasers, something which is discussed in more detail in the next subsection. If one remembers that a free-running laser pulse is in fact composed of a series of micropulses with a duration of $\simeq 1 \mu\text{s}$, which is comparable to the the duration of the Q-switched laser pulses, then the results by Sheth et al. and Dela Rosa et al. indicate that high intensity, microsecond long

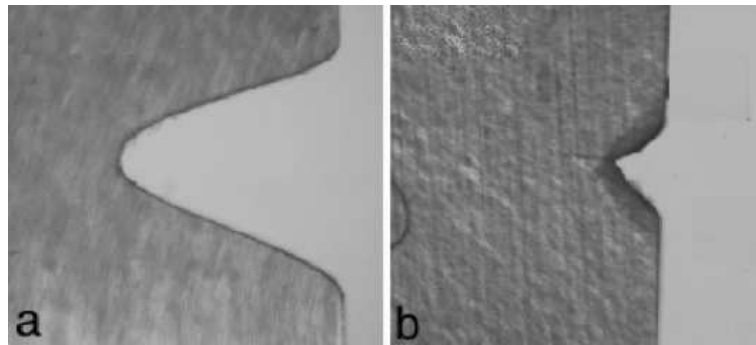


Figure 3.11: Polarized light images of the Q-switched, $2.79 \mu\text{m}$ Er:YSGG laser incisions with fluences of 18 and 20 J/cm^2 , respectively, with (a) and without (b) water (pulse duration = $0.5 \mu\text{s}$, repetition rate not given, fluence per pulse = 20 J/cm^2 , 6 pulses per spot). Field width is 1.8 mm . Source: ref. [80].

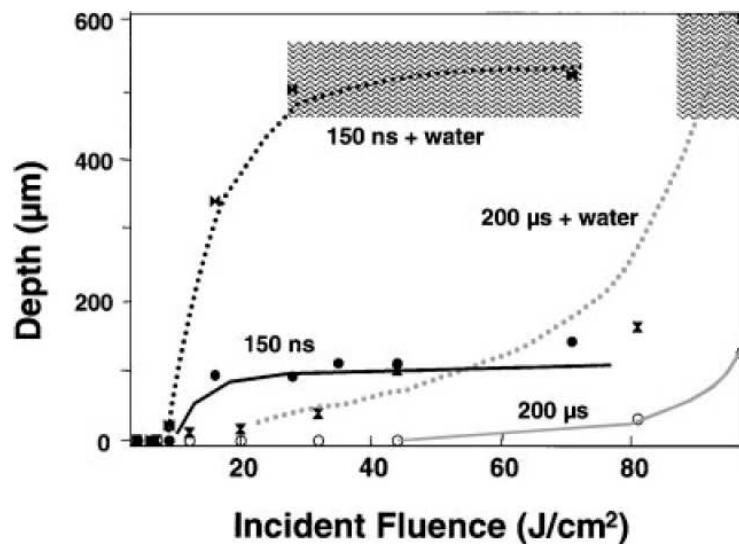


Figure 3.12: The ablation depth for bovine enamel at various irradiation intensities for the free-running ($200 \mu\text{s}$) and Q-switched (150 ns) Er:YSGG with (dotted line) and without (solid line) the addition of water. The shaded regions represent the fluence range in which smooth lateral cuts were achieved similar to those of Fig. 3.11 a. Five laser pulses per spot, $300 \mu\text{m}$ spot size. Source: ref. [96].

pulses at a low repetition rate seem to produce surfaces with less thermal damage and better adhesive properties than lower intensity, microsecond long pulses at higher repetition rates.

The pulpal temperature induced by the Er:YSGG lasers was not evaluated neither for the free-running nor for the Q-switched laser, but work by Cavalcanti et al. [95] using other lasers suggests it will be within acceptable levels, at least when water cooling is used.

The evidence presented in this Section indicates that, similarly to the Er:YAG

lasers, the YSGG lasers are also good candidates for the minimally invasive procedure described in Chapter 1. Their cost is comparable to the cost of the Er:YAG lasers, and the issues to address before they can perform optimally are similar. In fact, despite the existence of aspects that still need to be improved, the Er,Cr³⁺:YSGG lasers at 2.78 μm (free-running) are already being commercialized for conventional cavity preparation, under the denominations WaterlaseTM 21 (BIOLASE) and WaterlaseTM MD 22 (BIOLASE). Nevertheless, they were not further investigated in the work that led to this Thesis because the results that were obtained (using the Er:YAG and the CO₂ laser) can easily be extrapolated for this laser.

3.4.2 The CO₂ lasers

The CO₂ lasers emit at various wavelengths between 9.2 and 11.4 μm ; the strongest lines are those at 9.3, 9.6, 10.3 and 10.6 μm , and these are the most heavily investigated ones in the context of dental hard tissue laser ablation. While a large amount of information has been collected on ablation of dental hard tissues, these lasers are not currently being commercialized with this aim. Instead, the 10.6 μm wavelength is clinically used to cut and ablate soft tissue because of its good hemostatic properties, under the denominations NovapulseTM LX-20SP 23 (OpusDent), OpusDuoTM 24 (OpusDent) and Smart US20 25 (Deka Lasers).

Nelson et al. [112] assessed the response of human dental enamel to the four CO₂ wavelengths being evaluated in this subsection. Under similar laser operating parameters and nanosecond-long pulses (pulse duration = 100 – 200 ns, repetition rate = 0.67 Hz, fluence per pulse = 10 – 50 J/cm², 400 pulses per spot) and without using water cooling, they found that $\lambda = 9.3 \mu\text{m}$ produced the higher peak temperatures after the laser pulse ($1050 \pm 40 \text{ }^\circ\text{C}$) and that the peak temperature decreased as the wavelength increased (at $\lambda = 10.6 \mu\text{m}$ the peak temperature was $810 \pm 30 \text{ }^\circ\text{C}$ for the 50 J/cm² fluence). The temperature rise induced by the $\lambda = 10.3 \mu\text{m}$ is very similar to that induced by the $\lambda = 10.6 \mu\text{m}$ laser which, together with the very similar optical properties of enamel at these wavelength, suggests that the response of enamel to these two wavelengths will be almost

²¹<http://www.biolase.com/waterlase.html>

²²<http://www.biolase.com/waterlaseMD.html>

²³http://www.opusdent.com/site/product_applications/product.list.asp?fid=7&did=77

²⁴http://www.opusdent.com/site/product_applications/product.list.asp?fid=7&did=83

²⁵http://www.dekalaser.com/prod_sch.php?type=ENG_51

identical. The same can be said, although to a lesser extent, for the $\lambda = 9.3$ and $\lambda = 9.6 \mu\text{m}$ wavelengths. Nelson et al. found that all the wavelengths caused melting of the enamel surface, which was more extensive for the shortest wavelengths; the melted areas showed evidence of recrystallization (formation of larger HA crystals) and resolidification as amorphous material. At the higher fluences tested, the treated surfaces also presented cracks and fractures, sometimes hidden beneath the melted layer. They also evaluated the degree of chemical transformation in enamel induced by the the shortest wavelength at the highest fluence, and they found that it was significant: the IR spectra indicated that tetracalcium monoxide was formed and that the carbonate content of the treated sites was approximately one third of that in untreated enamel. These results indicate that, although all the CO_2 wavelengths can indeed ablate dental enamel, even pulses as short as 100 – 200 ns can cause prohibitive thermal and mechanical damage when ablating enamel. If these lasers are to be a possibility for the tunnelling technique, their operating parameters need to be optimized. In the remainder of this subsection I will discuss the results of using longer pulses for each of the four wavelengths in more detail.

Forrer et al. [113] compared effects of the four CO_2 wavelengths on bone, without water cooling, using various pulse durations. Forrer et al. found that, for a pulse duration of 0.9 μs (repetition rate = 0.5 Hz, 16 or 32 pulses per spot), the ablation thresholds increase with increasing wavelength, varying between $\simeq 1$ and 2.5 J/cm^2 . However, the heat of ablation²⁶ remains approximately the same. For these short laser pulses and $\lambda = 10.6 \mu\text{m}$, they found ablation to be more efficient at lower fluences than at higher fluences; the decrease in ablation efficiency at higher fluences was related to absorption by plasma observed to exist at the ablation site at these higher fluences. The surface of the ablated site when lower fluences were used presented no evidence of melting but, when the fluence used allowed the observation of plasma at the surface, melting occurs and a larger area of thermally altered material was detected. Different results were obtained by the same authors when using much longer laser pulses, at $\lambda = 10.6 \mu\text{m}$ (pulse duration = 250 μs): a melted surface was observed and an ablation site with a thicker thermally affected layer (50 – 70 μm thick) was formed. Extensive thermal damage and melting is observed both at low and at high fluences. Contrary to ablation by short pulses, the ablation by long pulses was more efficient when fluences above the plasma formation threshold were used. They concluded that

²⁶The heat of ablation is the energy per unit volume necessary to initiate ablation.

the shorter pulses they tested for $\lambda = 10.6 \mu\text{m}$ were preferable to the longer pulses because the extent of thermal damage caused to the tissue is much lower and the ablation efficiency is higher, allowing the use of high fluences still below the plasma formation threshold. This conclusion can be extrapolated to the other CO₂ wavelengths since the optical properties of HA and water, while varying for wavelengths 9.3 to 10.6 μm , are of the same order of magnitude. Forrer et al. verified that, although the ablation threshold for enamel at $\lambda = 10.6 \mu\text{m}$ is higher than at 9.3 μm for the short pulses they tested, at higher fluences (but still below the plasma formation threshold) the ablation depth per pulse is actually greater for $\lambda = 10.6 \mu\text{m}$, consequence of the greater penetration depth of the longer wavelength radiation. The authors concluded that a laser working at $\lambda = 10.6 \mu\text{m}$ and with a pulse duration on the order of a few microseconds would most likely yield the best results in ablating bone. As mentioned before, this conclusion should also apply to dentine, because of the similarities between the chemical composition of both materials.

Kimura et al. [114] investigated the effect of a pulsed $\lambda = 9.3 \mu\text{m}$ laser in dentine, without using water cooling, with the aim of increasing the resistance of dentine to acid attack. At the operating laser parameters they used (pulse duration = 300 μs , repetition rate not given, fluence per pulse = 53 or 61 J/cm², number of pulses per spot not given), they found that dentine was effectively ablated with some evidence of melted material but without cratering or cracking at the lased surface. However, they investigated the morphology below the surface of the treated area, and found that a large density of dentinal tubules was sealed there (unlike at the surface) and that some cracking below the surface had occurred. Fried et al. [74] also investigated the effect of long pulsed lasers at $\lambda = 9.3 \mu\text{m}$ (pulse duration = 100 μs , repetition rate = 1 Hz, 25 pulses per spot), and reached similar conclusions. They found that even fluences as low as 1 – 2 J/cm² caused large cracks and carbonization (note that the ablation threshold for dentine is 2 J/cm²). They also observed that the irradiated sites presented reduced content in carbonate and higher crystallinity when compared to non-irradiated sites. The same authors observed similar, but less marked, surface modification and thermal damage at the irradiated sites when using much shorter laser pulses and lower fluences (pulse duration = 6-8 μs , repetition rate = not given, fluence per pulse = 0.5 J/cm², number of pulses per spot not given).

Fried et al. [96, 84, 107] investigated the performance of a Q-switched CO₂ laser at 9.6 μm (pulse duration = 6 – 8 μs , repetition rate not given, fluence

per pulse = 70 J/cm², 20 pulses per spot) on bovine enamel. These authors found that, when water was not used, large regions in the ablation crater had a glazed appearance, indicative of thermal damage, and no signs of the desired apatitic phases. On the other hand, the same laser parameters used in conjunction with water yielded an enamel surface with a better surface morphology and with almost no chemical modification to the HA. Zuerlein et al. [115] also investigated this wavelength's capability for increasing enamel's resistance to acid attacks, and found that 20 pulses as short as 2 μ s and with a fluence as low as 2 J/cm² could achieve this to a high degree. However, even at these low fluences they found evidence of melting. Furthermore, Fried et al. [66] also suggest that the high specular reflectivity of enamel at 9.3 and 9.6 μ m (as high as 50 %) may be a safety issue in a procedure that is to be carried out inside the patient's mouth.

The CO₂ laser at 9.6 μ m has been shown by Dela Rosa et al. [80] to ablate dentine efficiently and with minimal thermal damage if used in Q-switched mode with water cooling (pulse duration = 5 μ s, repetition rate not given, fluence per pulse = 5 – 40 J/cm²). In fact, thermal damage was limited to a layer around 8 μ m thick when water was not used, and decreased to a 4 μ m thick layer when water was used; it should be noted that thermally induced chemical changes were not present in the thermally affected layer. However, when water was not used, char particles were present at the ablated site for all but the lowest fluences used. Dela Rosa et al. found no evidence of mechanical damage either with or without water. The same authors ablated dentine at this wavelength using similar repetition rates but much longer laser pulses from a free-running laser (pulse duration = 100 μ s, repetition rate not given, fluence per pulse = 5 - 40 J/cm²). At this longer laser pulse, they still could not observe any mechanical damage both with and without water, but they found that the thermally affected layer was thicker: \simeq 6 μ m when using water and \simeq 12 – 35 μ m without water. This time, thermally induced chemical changes were observed in the ablated site, both in the areas that had been lasered using a water spray as those that had not. Dela Rosa et al. also determined the ablation rates for dentine and found them to be on the order of tens to hundreds of micrometers per pulse, much higher than the ablation rates using excimer lasers.

Identical conclusions were reached by Sheth et al. [110], who used similar laser parameters to ablate dentine with and without water cooling (pulse duration = 6 μ s, repetition rate = 5 Hz, fluence per pulse = 15 J/cm², 10 pulses per spot for the Q-switched CO₂ laser, and pulse duration = 100 μ s, repetition

rate = 5 Hz, fluence per pulse = 20 J/cm², 10 pulses per spot for the free-running CO₂ laser). Sheth et al. went one step further and tested the ablated sites for the shear bond strength. They found that the dentinal surface ablated with the Q-switched CO₂ laser and water cooling presented the highest strength. Sheth et al. included in their work an evaluation of the shear bond strength of dentinal surfaces ablated by Er:YSGG (Q-switched and free-running) and Nd:YAG at 355 nm (already discussed in more detail earlier in this Section), and found that the highest bond strength of all was obtained using the Q-switched CO₂ laser with water cooling, and this was still inferior to that obtained using a standard acid etch on dentine. Neither of these authors measured the temperature change induced by the lasers on the pulp, but work by Cavalcanti et al. [95] indicates it is likely that the temperature rise at the pulp when using Q-switched lasers and water cooling will be acceptable, at least for the short pulses for which thermal damage at the ablated site was minimal.

Lee et al. [97] evaluated the influence of pulse duration in dentine ablation by a CO₂ laser at $\lambda = 9.6 \mu\text{m}$, and found that pulses of 10 μs cause no observable charring or melting in dentine when water was not used (repetition rate not given, fluence per pulse = 22 J/cm² for both lasers, varying number of pulses per spot), whereas pulses of 140 μs caused extensive charring. They subsequently evaluated the ablation rates at various fluences between 4.2 and 50 J/cm² and pulse durations between 0.8 and 10 μs , and found that much higher ablation rates (30 to 40 μm per pulse when fluence is 30 to 45 J/cm²) are obtained using 10 μs pulses than using 0.8 μs pulses, which make these slightly longer laser pulses better from a clinical point of view. They also found that ablation of dentine by the shorter pulsed CO₂ lasers generated high intensity noises, similarly to what happens when ablating the same material by Q-switched Er:YAG lasers, which seems to suggest that laser pulses with duration inferior to $\simeq 5 \mu\text{s}$ may be inadequate to provide dental treatment because of the possibility of causing damage to the patient's hearing. Work by Ertl et al. [116] seems to suggest that CO₂ laser pulses with duration lower than $\simeq 10 \mu\text{s}$ and high fluences²⁷ can produce sound pressure level in excess of 95 dB(A), at a distance of 25 cm from the ablation target, a sound level that is not allowed by workers protection law and may cause damage to hearing. Should lasers with these characteristics be considered to provide dental care, this possibility needs to be carefully evaluated to ensure patient's safety.

²⁷It is not possible to determine the fluences used in their study because of lack of data or incorrect data given in their paper.

Fried et al. [98] investigated the effect of pulse duration on ablation of bone by a $\lambda = 9.6 \mu\text{m}$ laser and no water cooling, and they found no evidence of thermal damage when the laser pulses were 5-8 μs long, for fluences between 1 and 30 J/cm^2 (repetition rate = 1 – 2 Hz, number of pulses per spot not given, but large), as compared to 10, 50 or 100 μs laser pulses. The ablation rates were higher for the 8 μs laser pulse than for the 5 μs laser pulse, mainly because the temporal profile of the 5 μs laser pulse has a very high intensity peak during the first 200 ns which causes plasma formation and, consequently, decreases the absorption of radiation by the tissue.

Zuerlein et al. [115] compared the efficiency of a CO_2 laser at $\lambda = 9.6$ and at $\lambda = 10.6 \mu\text{m}$ to increase enamel's resistance to acid attacks and they found that, even though the absorption coefficient of enamel at $\lambda = 9.6 \mu\text{m}$ is much higher than at $\lambda = 10.6 \mu\text{m}$, the $\lambda = 10.6 \mu\text{m}$ wavelength achieves the desired results with a lower number of pulses (pulse duration = 2 μs , repetition rate = 0.5 Hz, fluence per pulse = 2 J/cm^2 for $\lambda = 9.6 \mu\text{m}$ and 4 J/cm^2 for $\lambda = 10.6 \mu\text{m}$, 5 pulses per spot).

This review indicates that the CO_2 lasers tend to inflict serious thermal damage to dental hard tissue when water cooling is not used, in particular the 9.3 and 9.6 μm wavelengths that are most highly absorbed by the enamel. The results strongly suggest that the duration of the laser pulse, the pulse repetition rate and the use or not of water cooling strongly influence the outcome of ablation. The most appropriate pulse durations and repetition rates seem to lie in the range of 0.5 to 10 μs and 1 – 20 Hz, and water cooling seems to be determinant in minimizing thermal damage to dental hard tissue. The most appropriate wavelength to minimize thermal damage seems to be the 10.6 μm , which has a lower (although still acceptably high) absorption coefficient. The review indicates that the potential of this laser to ablate dental hard tissue has not been thoroughly assessed by the scientific community, and that it may perform well if the correct laser parameters are used. This potential, together with the fact that this is one of the least expensive equipments and that it is already extensively used in soft-tissue applications, makes it a good candidate for the procedure in question here, and thus this will be one of the wavelengths investigated in this Thesis.

3.5 Summary and conclusion

A table summarizing the review of the literature presented in this Chapter is given in Annex 3.

Examining this table one realizes that several points regarding the effect of particular combinations of wavelength and laser operating parameters have not been evaluated in this review, either because they are not available in the literature or because of limitations on the author of this Thesis. For some of these points, however, it is possible to extrapolate from information obtained from other wavelength and laser operating parameter combinations. Regarding the extent of pulpal heating, only evaluated for long-pulse Er:YAG lasers and considered to be within safe limits in this case, it is reasonable to assume that the pulp temperature will remain within acceptable limits for any of the wavelengths/parameters combinations evaluated, providing that water cooling is used. While it seems that some lasers generate enamel or dentinal surfaces with worse adherence properties than the same surface treated only with acid etch, it is also likely that this will not be an issue for any wavelength since it has been demonstrated that an irradiated surface can be treated by other methods (such as acid etching) that will increase its adherence to acceptable levels. The same can be said about the resistance of irradiated surfaces to acid dissolution: even in the cases where the acid dissolution is increased, subsequent treatment with fluoride can decrease it again to acceptable levels.

The only effects that should be considered in the choice of the most promising wavelength and laser operating parameters are thus the extent of thermal and mechanical damage inflicted on dental hard tissue ablation, the ablation rates, the possibility of drilling long tunnels and the cytotoxicity of the laser. This review of the literature indicates that short pulsed (up to 10 μ s) IR lasers are better candidates to produce long tunnels through dental hard tissue than UV lasers. UV lasers present several drawbacks that make them less good candidates for the job: the high extent of mechanical damage caused at the ablated sites, the possible mutagenic effects that some wavelengths may have, their low ablation rates, their high cost and relatively large size. While the free-running IR lasers ablate dental hard tissue efficiently, they seem to cause extensive thermal damage if water is not used during ablation. Because the use of water may be problematic when drilling long tunnels (water may accumulate at the tunnel and thus prevent ablation from taking place after some time), shorter pulsed IR lasers are a better choice. However, very short pulses (0.5 – 2 μ s) seem to cause more extensive mechanical damage

and are much less efficient at ablating material. The ideal IR pulse duration seems thus to lie in the 5-10 μs range, and evidence suggests that it may be possible to obtain very acceptable results, thus precluding the need to recur to femtosecond lasers.

IR lasers are preferable to UV and femtosecond lasers because they may also be used in other procedures, such as soft tissue surgery (the CO_2 laser at 10.6 μm in particular is very widely used for this) and even enamel whitening. The possibility of being used for more than one type of procedure makes them a more cost-effective choice from the clinician's point of view. For this reason, because the UV lasers did not present any marked advantages over the IR wavelengths and because much less experimental information is available for the UV than for the IR lasers, this Thesis is only concerned with investigating the effect of IR lasers in dental hard tissue. Only two IR lasers were chosen: the CO_2 laser at 10.6 μm , because it is potentially the most cost-effective equipment, both because it costs less and because it can be used for a variety of soft-tissue procedures, and the Er:YAG laser, because it is already widely used for hard tissue ablation and there is a wealth of experimental data available, necessary to develop, implement and validate our models. Furthermore, these lasers are representative of the two main categories in which IR lasers may be divided in the context of dental laser ablation: wavelengths mainly absorbed by the mineral and wavelengths mainly absorbed by the water. Thus, the models developed for these lasers can easily be modified to simulate the response of dental materials to any other mid-IR lasers such as the YSGG lasers (also good candidates) provided that the necessary optical properties of dental hard tissues are available at those wavelengths.

It is apparent from the discussion above that ablation of enamel poses more challenges than ablation of dentine: the ablation rates are lower, the extent of thermal and mechanical damage is normally much higher and, since it is in contact with the buccal environment, the resistance of the ablated site to acid dissolution is of extreme importance. For these reasons and because the duration of a PhD program is limited in time, the remaining of this thesis is concerned only with ablation of dental enamel by Er:YAG and CO_2 ($\lambda = 10.6 \mu\text{m}$) lasers.

In order to develop models that will contribute to optimize the ablation procedure in order to ensure that long tunnels can be produced, it is necessary first to understand which phenomena play the determining role in ablation and at which spatial scale they occur. Therefore, in the next Chapter the state-of-the-art in ablation mechanisms and models for the Er:YAG and CO_2 lasers and enamel will

be described, the influence of the various laser operating parameters (in particular those parameters not discussed already in Chapter 2) on the outcome of ablation will be discussed and the issues that are not yet sufficiently understood will be highlighted.

Chapter 4

Further considerations on ablation of enamel by mid-IR lasers

In this Chapter the state-of-the-art in the ablation mechanisms of enamel by Er:YAG ($\lambda = 2.94 \mu\text{m}$) and CO₂ ($\lambda = 10.6 \mu\text{m}$) lasers will be presented, and the influence of operating parameters such as water cooling, laser spatial intensity profile, absorption and scattering by the plume will be discussed in depth.

4.1 The mechanisms of ablation of enamel by mid-IR lasers

Despite the fact that the Er:YAG and the CO₂ lasers are absorbed equally well by enamel (absorption coefficient $\simeq 800 \text{ cm}^{-1}$ for both wavelengths) and have similarly low reflectance (5 – 10%) in enamel, they seem to cause very different thermal effects this material. Fried et al. [63] verified that, for similar laser operating parameters, the maximum temperature rise in enamel was only 150 °C for the Er:YAG lasers, and was close to 500 °C for the CO₂ laser (free-running pulse, fluence per pulse = 4 J/cm², other parameters not given by authors). A possible explanation for this observation may be the different absorption coefficients of water at those wavelengths: 12000 cm⁻¹ at $\lambda = 2.94 \mu\text{m}$, and 860 cm⁻¹ at $\lambda = 10.6 \mu\text{m}$. Keeping in mind the absorption coefficient of enamel and the inhomogeneous composition of this material (most of the water is thought to exist in pores), it is possible to estimate the absorption coefficients of HA at these wavelengths (which have not been found in the literature): $\simeq 300 \text{ cm}^{-1}$ at

$\lambda = 2.94 \mu\text{m}$, and $\simeq 800 \text{ cm}^{-1}$ at $\lambda = 10.6 \mu\text{m}$. This difference in the absorption coefficients implies that radiation at $\lambda = 10.6 \mu\text{m}$ is much more absorbed by HA than radiation at $\lambda = 2.94 \mu\text{m}$ and provides an explanation for the different surface temperatures observed for those lasers, as will be demonstrated further on in this Thesis. Nevertheless, both these wavelengths inflict thermal damage (like melting) to enamel to some extent, particularly if external water cooling is not used, as was discussed in Chapter 3.

Most authors agree that the main mechanism of ablation of enamel by Er:YAG lasers is the explosive vaporization of water. Fried et al. [63] observed that the irradiated surfaces present clean fractures at the rod boundaries, which is consistent with this ablation mechanism and also implies that the enamel microstructure (particularly the water pores, located mainly at the rod boundaries) play an important role in ablation. The ablation mechanism of enamel when the $\lambda = 10.6 \mu\text{m}$ is used, however, may vary according to the laser operating parameters, given that somewhat contradictory information has been found in the literature. For the CO_2 laser at $\lambda = 10.6 \mu\text{m}$ and microsecond pulse duration, Forrer et al. suggests that the dominant ablation mechanism (for bone) should be the explosive vaporization of water, despite the fact that water and mineral absorb radiation equally well at this wavelength. As one moves to the more highly absorbed CO_2 wavelengths, such as the $\lambda = 9.6 \mu\text{m}$, evidence suggests that the ablation mechanism is predominantly melting and vaporization of the mineral [63], at least if water cooling is not used. When water is used during $\lambda = 10.6 \mu\text{m}$ ablation, little or no melting, charring or carbonization is observed, which is consistent with the explosive vaporization mechanism of water. On the other hand, if water cooling is not used, extensive melting is observed, and it is possible that ablation takes place partly by explosive water vaporization and partly by melting of the mineral (which melts between 800 and 1200 °C [69]), in particular for the less absorbed CO_2 wavelengths such as the one being considered in this discussion. These observations strongly indicate that, in order to fine-tune the laser operating parameters to obtain the best results in enamel ablation by both Er:YAG and CO_2 lasers, one can build very similar models, given that the ablation mechanisms for both can be investigated in the same manner. Furthermore, the physical phenomena that lead to ablation of material occur at a micrometer scale and are highly dependent on enamel's inhomogeneous chemical composition and structure. Consequently, if the final objective is to fine-tune the laser operating parameters in order to obtain the best results in ablation, models must necessarily include this material's

microstructure at the relevant scale, something which has not been done to date.

Another parameter that influences the outcome of ablation is the pulse duration. According to the conclusions arrived in Chapters 2 and 3, the pulse durations most likely to produce the best results with respect to the outcome of ablation should be between 0.5 and 10 μs . These pulse durations are significantly shorter than the thermal relaxation time for enamel ($\simeq 50 \mu\text{s}$), which should keep the thermal damage to a minimum, but much longer than the acoustic relaxation time ($\simeq 1.5 \text{ ns}$), which should keep the stress transients at a minimum also. However, some experimental evidence suggests, unexpectedly, that even a 0.5 μs laser pulse may induce cracking in the material, which indicates that the matter of stress transients within this pulse duration range must be investigated further, in order to determine the optimal pulse duration. The study of the stress transients is further complicated by the fact that the means of delivering the laser pulse (via an optical fibre in contact with the material rather than a non-contact beam delivery) influence the frequency distribution generated, as was verified by Althshuler et al.. Althshuler et al. [117] have measured the acoustic signal emitted by enamel when ablated using a free-running Er:YAG laser (pulse duration = 200 μs , repetition rate = 10 Hz, fluence = 500 J/cm²), and have found that it is composed of frequencies lying in two different ranges: the low frequency range around 10 kHz, and a high frequency range around 100 kHz. This team verified that the low frequency range was significantly more intense when the optical fibre delivering the laser beam was in direct contact with the material, as opposed to a non-contact beam delivery setup, as can be seen in Fig. 4.1. Therefore, it is necessary that models give insight into this aspect of ablation, even at these pulse durations where one would not expect stress transients to play a large role. The models presented in this Thesis are able to simulate both the dynamic and static behavior of a material to laser irradiation (but are not able to simulate the effect of different beam delivery systems on the stress transients generated).

4.2 The role of water

The role of water, both that naturally existing in the tissues and that added during ablation, has been discussed extensively, especially in the context of mid-IR lasers. The water that exists in enamel (and dentine) is thought to play a vital role during ablation. Given that the amount of water in dental hard tissue is known to vary

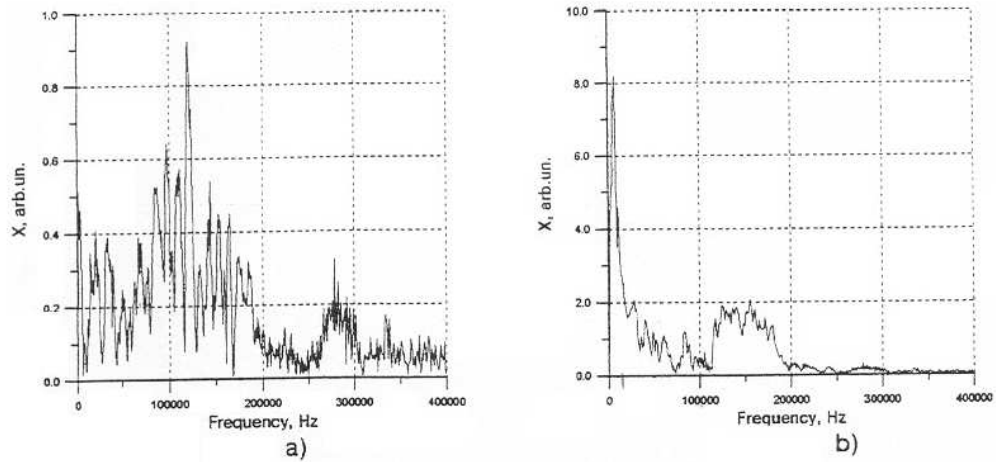


Figure 4.1: Fourier image of laser-induced acoustic signal obtained during human dental enamel processing by Er:YAG laser (pulse duration = $200 \mu\text{s}$, repetition rate = 10 Hz, fluence = 500 J/cm^2) with no water irrigation. (a) Non-contact laser irradiation, (b) Contact laser irradiation using a quartz fiber. Source: ref. [117].

significantly with the age of the tooth, between different teeth and even between different areas of the same tooth [11], this implies that a careful assessment of the results obtained with similar laser parameters and different samples must be done. Work by Apel et al. [118] supports these conclusions: Apel et al. have used Er:YAG and Er:YSGG lasers (pulse duration = $150 \mu\text{s}$ (FWHM), repetition rate = 5 Hz, no water cooling) to ablate dental enamel, and have found that the ablation threshold is lower in the cervical region, as a consequence of its higher water content.

Externally applied water, on the other hand, serves multiple purposes during ablation. The first purpose, and easiest to understand, is that of a coolant: applied water is indispensable to cool the ablation site for IR lasers, as was discussed in Chapter 3. Secondly, water plays a role during ablation, and influences the ablation rates: the ablation rates of enamel by Er:YAG lasers are higher when a water layer is previously applied to the ablation site, as was mentioned in Section 3. On the other hand, ablation rates by the CO_2 laser at $9.6 \mu\text{m}$ when water is used are lower than when water is not applied, and it is likely that the same behavior is observed for $\lambda = 10.6 \mu\text{m}$. Some authors (see refs. [82, 119]) have proposed that the increased ablation rates of enamel by Er:YAG lasers occur because the applied water gets inside the surface cracks and cavities and, when heated rapidly, expands and causes fracture and material removal to occur. While the same phenomenon

should take place during ablation by CO₂ lasers, it may be counteracted by the fact that, since this wavelength is highly absorbed by the mineral, the added water in effect decreases the efficiency of the energy coupling to the material thus making ablation less efficient.

Other authors, however, proposed that a hydrokinetic effect would be the cause for the increased ablation rates of enamel when water is used. The hydrokinetic effect hypothesis postulates that water droplets being sprayed onto the surface absorb part of the incident radiation. The vaporizing water then causes the droplets to accelerate towards the surface and hit it with high kinetic energy, thus enhancing material removal. Fried et al. [96] disproved this hypothesis since they found the ablation rates of enamel by Er:YAG lasers using a water layer at the surface of the ablated site (i. e., without water droplets to be accelerated) were still much higher than the ablation rates without water. Freiberg et al. [119] made a careful evaluation of the hydrokinetic effect hypothesis: they irradiated human dental enamel using an Er:YAG laser (pulse duration = 180 μ s, fluence \simeq 35 J/cm²) while hydrating it using water spray and an applied surface water layer. If the hydrokinetic effect is felt intensely during ablation of enamel, then there should be marked differences between the ablation efficiency in both those situations. Freiberg et al. found that there was no significant difference between the results obtained in both procedures: the ablation efficiency and the morphological characteristics of the surface were the same. They further tested the hydrokinetic effect hypothesis by irradiating various materials that do not absorb radiation at 2.94 μ m while using a water spray, and they found no evidence of ablation. These results strongly indicate that the hydrokinetic effect hypothesis does not hold. Consequently, the increase in enamel ablation efficiency observed using Er:YAG lasers with water cooling [82] is most likely caused by the rapid expansion and vaporization of water in surface cavities and cracks and by preventing or decreasing the extent of tissue desiccation, known to occur to a large extent when temperatures up to 300 °C are reached in enamel [65]. Despite this, Biolase still makes references to the hydrokinetic effect when marketing their Waterlase™...

A third and more subtle role of externally applied water is its influence on the chemical nature and morphology of the surface of the ablated site and, consequently, on the degree to which that surface will adhere to filling materials and on its tendency to dissolve under acid attack. Hydroxyapatite decomposes into other calcium phosphates, namely tricalcium phosphate (TCP) and tetracalcium phosphate, at higher temperatures. These calcium phosphates have poorer mechanical

properties than HA, and therefore it is not desirable that they are formed at the ablated site. Yamashita et al. have shown that heating of stoichiometric hydroxyapatite, nonstoichiometric oxyhydroxyapatite and Ca-deficient oxyhydroxyapatite films at temperatures up to 1200 °C favors their transformation into tricalcium phosphate, as can be seen in Fig. 4.2. However, the conversion of apatite into

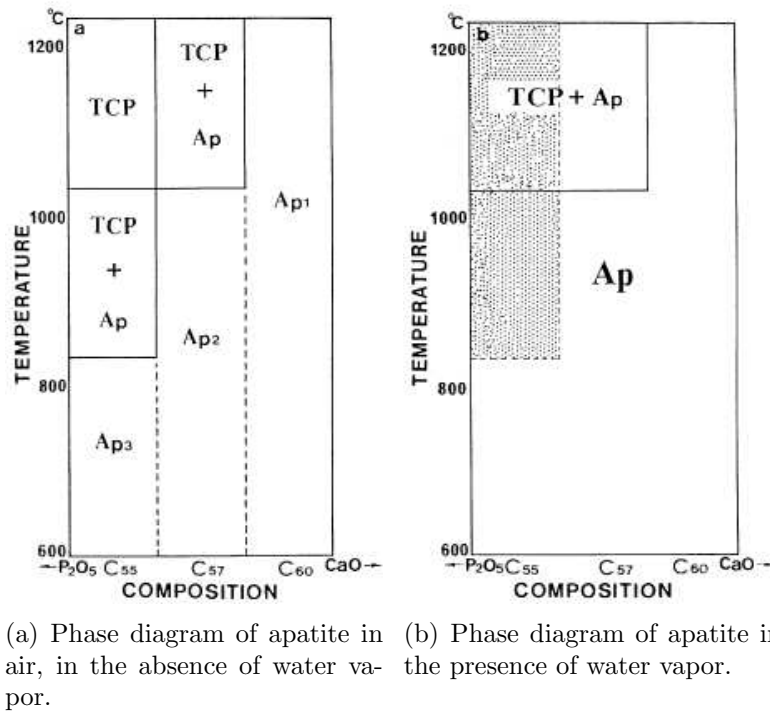


Figure 4.2: Simplified apatite phase relations for stoichiometric hydroxyapatite (Ap1), nonstoichiometric oxyhydroxyapatite or $Ca_{10}(PO_4)_6(HO)_{2-2x}O_x \diamond_x$ (Ap2) and Ca-deficient oxyhydroxyapatite films or $Ca_{10-y} \diamond_y (PO_4)_6(HO)_{2-2x-2y} O_{x+2y} \diamond_x$ (Ap3). The hatched area shows the region where the effect of the water vapor was observed. In the graphs, C55, C57 and C60 correspond to 55/45, 57/43 and 60/40 CaO/P₂O₅ molar ratios. Source: ref. [120].

TCP is pushed onto much higher temperatures if the heating takes place in the presence of water vapor. Consequently, wetting the ablation sites with water may prevent or decrease the extent to which undesirable calcium phosphates are created. This hypothesis is supported by work done by Fried, Ashouri et al. [84, 96]. These authors verified that when ablating enamel using Er:YAG and CO₂ (9.6 μm) lasers in the absence of water, non-apatitic phases such as mono, tri and tetra-calcium phosphate are formed at the ablated site, which does not happen when water is applied during ablation. Furthermore, the surface of the ablated site

present a uniform roughness when water is used, but a glassy appearance when water is not used. Ashouri et al. [84] propose that the recoil momentum associated to water vaporization that follows irradiation may help removing poorly attached surface debris, contributing to a less rough surface. While these observations provide good insight into the role of water during ablation, in order to understand the exact mechanism by which water influences the chemical and morphological characteristics of the ablated sites, it would be important to obtain the phase relations for biological apatite as a function of temperature and to introduce the phenomenon of phase change in the models, which was not work in this work.

While it is generally accepted that ablation of enamel by Er:YAG and CO₂ lasers takes place because of water heating and explosive vaporization, building models with predictive capabilities is not an easy task. The part played by water is more difficult to model than one can think at first sight. For one thing, water in pores is likely to be mixed with organic material, and it is not known how the organic component (which exists in a smaller proportion than water but is, nevertheless, significant) influences the optical, mechanical and thermal properties of the mix. For another, because the properties of pure water, in particular the absorption coefficient at 2.94 μm , change during ablation. The dynamic optical properties of water are particularly important for ablation by Er:YAG, because water absorbs radiation much more intensely than the mineral component. Vodop'yanov [121, 122] investigated the dynamic optical behavior of water at 2.94 and 2.79 μm . He found that at 2.94 μm , water is strongly bleached by high intensity (fluence per pulse = 0.1 – 100 J/cm²) laser radiation, when the pulse duration varies between 10⁻⁷ and 10⁻¹⁰ s. For example, when the fluence of the radiation is 100 J/cm², the average transmission rises to 90%, from an initial transmission of 0.15%. Vodop'yanov proposes that this phenomenon is a consequence of the increase in the temperature of the liquid: when the temperature increases, the hydrogen bonds between water molecules deform and weaken. This causes the absorption band of the OH groups to shift in the direction of higher frequencies and, consequently, the intensity of the band at 2.94 μm decreases. Because of this shift, the absorption band at 2.79 μm initially increases, but for higher fluences decreases again; the phenomenon corresponds to an even more pronounced shift of the absorption band to higher frequencies. These results are corroborated by experimental and theoretical work done by Shori et al. [123], as can be seen in Fig. 4.3.

Cummings et al. [124] built theoretical models of absorption of radiation as a

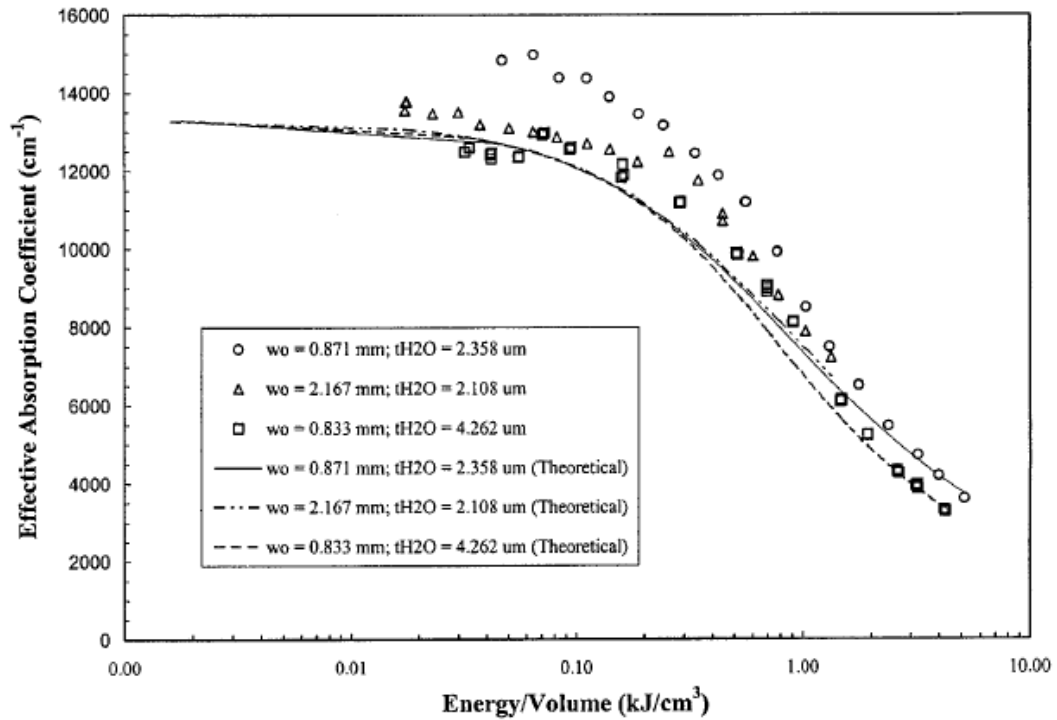
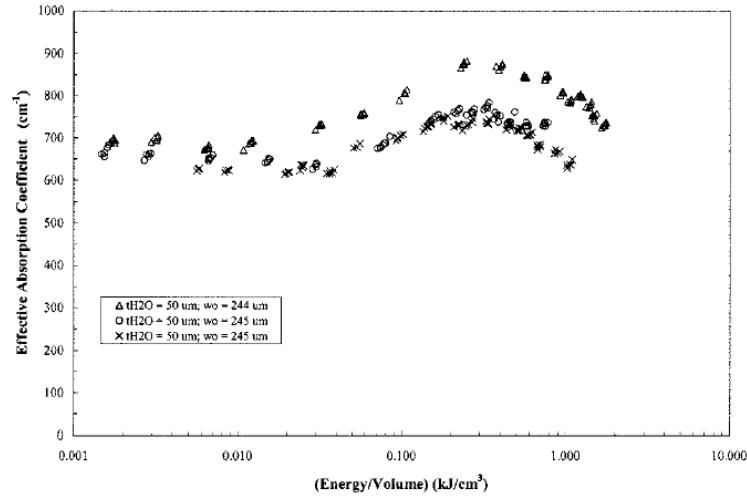


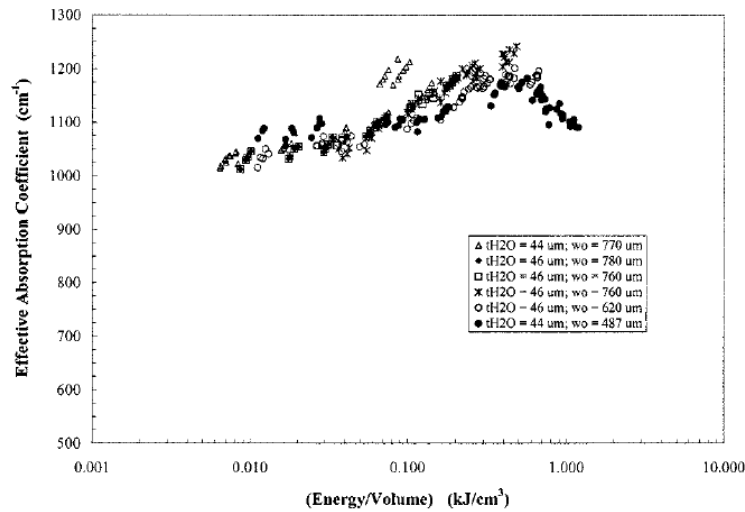
Figure 4.3: Experimental and theoretical changes in the effective absorption coefficient of water at $2.94 \mu\text{m}$ as a function of energy deposited per volume. Note that three different beam diameters w_0 and water layer thicknesses t_{H_2O} were used. Source: ref. [123].

function of depth in the absorbing material, based on Vodop'yanov's data, and concluded that the dynamic optical absorption coefficient of water will have a significant impact on the depth of penetration of radiation into the tissue: the optical penetration depth will be significantly larger than what could be expected based on the absorption coefficient at low laser intensities. Similar conclusions were reached by Shori et al. [123].

Shori et al. went beyond Vodop'yanov's work, and measured the changes in the absorption coefficient of water at 9.5 and $10.6 \mu\text{m}$ as a function of the energy density in water. At both these wavelengths, as can be seen in Fig. 4.4 the effective absorption coefficient of water does not change, provided that water bubbles are not formed at the irradiation site.



(a)



(b)

Figure 4.4: Change in the effective absorption coefficient of water as a function of energy deposited per unit volume ($(E/V)_{deposited}$) at (a) $\lambda = 9.6 \mu\text{m}$ and (b) $\lambda = 10.6 \mu\text{m}$. Bubble formation was observed for values of $(E/V)_{deposited}$ greater than $\simeq 0.25 \text{ kJ/cm}^3$. Note that different beam diameters w_0 and water layer thicknesses t_{H_2O} were used. Source: ref. [123].

These results are of significant importance for the modelling work which is the subject of this Thesis, because they provide the background for the modelling choices that were made regarding the absorption coefficient of water. More specifically, the changes in the optical absorption coefficient of water at $2.94 \mu\text{m}$ and $10.6 \mu\text{m}$ were not included because the energy per unit volume reached in our simulation conditions are still low enough to ensure that this effect plays a minor role in ablation. The author also did not include the phase transformation of HA into other phases as a function of temperature and presence or absence of water, although it is clear that this is something of interest, which should be included in future work to be done on this topic.

4.3 Influence of the laser spatial intensity profile

The influence of the laser beam spatial profile is felt strongly during ablation; various authors have suggested that an inhomogeneous laser spot, i. e., one without a "top-hat" profile, causes more extensive thermal damage to occur: in certain areas under the laser spot the fluence will not be high enough to provoke ablation, and thermal damage will occur instead. This hypothesis was verified experimentally by Meister et al. [125], who used an Er:YSGG laser with a Gaussian beam profile - also called TEM_{00} (transverse electromagnetic mode) - with the characteristic bell-shape in which the intensity of the laser beam is much higher in the center than at the sides of the laser beam. Meister et al. found that at a fluence per pulse of 13 J/cm^2 , the diameter of the crater is only about one third of the beam diameter at $1/e^2$ of the incident intensity. When the fluence per pulse is 19.5 J/cm^2 , the crater diameter becomes approximately two thirds of the beam diameter at $1/e^2$. Farrar et al. [126] also investigated the influence of the spatial profile of the free-running Er:YAG laser beam (pulse duration = $200 \mu\text{s}$, repetition rate = 8 Hz) on the morphology of the ablated crater in dentine and confirmed the results described above. They found that a "top-hat" profile yielded craters with more defined boundaries than a Gaussian-like intensity profile, which strongly suggests that a "top-hat" spatial intensity profile should be used in the tunnel preparation.

These results confirm the importance of calculating the actual threshold ablation fluence rather than taking the values normally indicated as the ablation threshold fluence for combinations of particular materials and lasers, which are actually averaged over the size of the laser spot and are somewhat different from

the local values of incident fluence at each point of the laser spot. For the purpose of comparing experimental results with theoretical ones, it is then important to quantify the relationship between local fluence, F_l , and average fluence (or simply, fluence, F), which can be done by simple calculations.

The spatial profile of a Gaussian laser pulse can be described in terms of incident local fluence by the following equation, which assumes that the radius of the laser beam at $1/e^2$ of the incident intensity is given by twice the variance, or 2ϕ [2]:

$$F_l(r) = F_{max} \exp\left(-\frac{r^2}{2\phi^2}\right) \quad (4.1)$$

Therefore, the energy contained in a ring located at distance r from the center of the laser spot and with thickness dr is:

$$dE(r) = F_l(r)2\pi r dr \quad (4.2)$$

The total energy of the laser pulse can then be calculated by the following integral:

$$E_t = \int_0^R F_l(r)2\pi r dr \quad (4.3)$$

that is,

$$E_t = -2\pi\phi^2 F_{max} \left[\exp\left(-\frac{R^2}{2\phi^2}\right) - 1 \right] \quad (4.4)$$

The average fluence is then given by

$$F = \frac{E_t}{\pi(2\phi)^2} = -\frac{F_{max}}{2} (\exp(-2) - 1) \quad (4.5)$$

which means that the maximum fluence is expressed in terms of the average fluence by

$$F_{max} \simeq 2.31F \quad (4.6)$$

Once the maximum fluence is known, it is possible to determine the local fluence at the edges of the ablated crater, which corresponds to the threshold ablation fluence that can be compared to theoretical results. As a quantitative example, one again uses the work of Meister et al.: they used an Er:YSGG laser with a Gaussian beam of diameter $800 \mu\text{m}$ at $1/e^2$ intensity level ($\phi = 200 \mu\text{m}$) to ablate

enamel, and found that the average ablation threshold fluence is $\simeq 13 \text{ J/cm}^2$. Therefore, the maximum fluence at the center of the laser spot is $\simeq 30 \text{ J/cm}^2$ and, since the ablation crater only has a width of $270 \text{ }\mu\text{m}$, the local fluence at the crater rim is $\simeq 24 \text{ J/cm}^2$. The value is significantly higher than the average threshold ablation fluence, and again confirms that the area of enamel lying within the laser spot but under lower fluences will suffer thermal damage to some extent. In the work presented in this Thesis, the fluence used is significantly lower than the average (and, consequently, the local) threshold ablation fluence.

4.4 Absorption and scattering by the ablation plume

Once ablation begins, the ablated enamel forms a small cloud close to the ablation site: the ablation plume. There is evidence to suggest that shielding by the ablation plume takes place under certain irradiation conditions, which may lead to loss of ablation efficiency since a part of the radiation does not reach the intended site and is instead absorbed by the plume. In order to determine how to minimize this effect it is necessary to understand by which mechanisms may shielding occur. This implies that some knowledge of the composition of the plume and the speed at which the various components move must be available.

Izatt et al. [127] investigated the composition and velocity of the plume produced by ablating bone using a $\lambda = 2.7 - 3 \text{ }\mu\text{m}$ (pulse duration = 350 ns, repetition rate = 0.5 Hz, fluence per pulse = 20 – 40 J/cm^2 , varying number of pulses per spot) and found that the plume was largely composed of particulates. The diameter of the particulates ranged from 100 nm to $5 \text{ }\mu\text{m}$, with an average diameter of 500 nm. They also found that the average velocity of the particulates was $\simeq 200 \text{ m/s}$, ranging between less than 100 m/s up to 500 m/s. Interestingly, their results are in agreement with those obtained by Serra et al. [128, 129], who ablated pure HA targets using a $\lambda = 248 \text{ nm}$ laser (pulse duration = 30 ns, fluence per pulse = 2.6 J/cm^2 , 1 pulse per spot). Serra et al. also found that one of the components of the laser plume were micrometer-size particulates travelling at a speed on the order of 10^2 m/s . This similarity of results obtained by both teams, despite the differences in material, pulse duration, wavelength and fluence, suggests that analogous findings should also be obtained in the case of ablation of

enamel by the wavelengths being considered here. Furthermore, it also indicates that results obtained by Serra et al. regarding the speed of the atomic and molecular cluster components of the ablation plume (which Izatt et al. did not look into) may also apply to the ablation of enamel. Serra et al. found that the ablation plume included an atomic/molecular component (mostly calcium atoms or single ions) that expanded at much higher speed than the particulate component: typically, on the order of 10^3 to 10^4 m/s. While it is unlikely that ablation by mid-IR lasers generates atomic or ionic calcium, it will certainly generate hot water steam. Since the water molecules have a mass on the same order of magnitude as the calcium ions, it is reasonable to think that the expansion of the water vapor will occur at speeds on the order of 10^3 to 10^4 m/s also. Assuming a pulse duration between 1 and 10 μ s, the average particulate will travel a distance of 0.2 – 2 mm during the laser pulse, and the average water molecule will travel a distance of 1 – 10 mm. If an average diameter of 0.5 mm is assumed for the spot, the obvious conclusion is that a significant fraction of the water vapor will escape the region under the laser beam before the end of the laser pulse. This conclusion indicates that the majority of the plume shielding effect will most likely be a consequence of shielding by the particulates, rather than shielding by the water vapor. Furthermore, the order of magnitude of the speed of the plume components indicates that shielding by the plume can be minimized if the repetition rate is kept below $\simeq 1000$ Hz, which should allow enough time for the plume to clear the ablation site between pulses. Shielding by the plume will decrease as the spot diameter is decreased also [130].

Shielding by the plume may occur because of two phenomena: absorption and scattering. At first sight, it seems unlikely that absorption may occur because of plasma formation in the plume since that would require extremely high values of the local electric field at the plume to form that plasma. For pulse durations on the order of 1 to 10 μ s, this translates into fluences on the order of 10^8 to 10^9 J/cm² [2], clearly much higher than the fluences being considered here. However, Fried et al. [131] verified experimentally that shielding by a plasma plume (detected by the sharp decrease in ablation efficiency and by the appearance of a luminous plume) occurs when ablating enamel using a microsecond laser pulse with a very high intensity spike in the first 100 – 200 ns (using a $\lambda = 9.6 \mu$ m at an average pulse fluence as low as 3 J/cm²). Further work by Fried et al. [132] indicates that, for $\lambda = 9.6 \mu$ m, if a laser pulse without a high intensity spike is used, average pulse fluences as high as 15 J/cm² may be used before the ablation efficiency decreases abruptly because of shielding by the plasma plume. Before the onset of

plasma, the ablation rate and ablation efficiency increase with increasing fluence, although not linearly, which indicates that the plume has some shielding effect due to (normal) absorption and/or scattering. Similar observations were made by Forrer et al. [113] using a $\lambda = 10.6 \mu\text{m}$ laser (pulse duration = $12.5 \mu\text{s}$, repetition rate = 0.5 Hz) on bone (for which the plasma threshold is 25 J/cm^2). Analogous conclusions were obtained by Izatt et al. [127] for the ablation of bone using a $\lambda = 2.7 - 3.0 \mu\text{m}$ laser with $350 - 1000 \text{ ns}$ pulse duration: at lower fluences per pulse (below 30 J/cm^2), ablation is associated with an audible crack but no visible spark. Above that threshold, they observed a visible plume and found that the efficiency and reproducibility of ablation was greatly reduced. Similarly to what happens with the CO_2 laser, below the plasma threshold, Izatt et al. found that the plume still produced some attenuation of the incident laser beam.

While the threshold for plasma shielding may differ from the values just mentioned because of differences in the wavelength and the material, the qualitative behavior of enamel under $\lambda = 10.6 \mu\text{m}$ and $\lambda = 2.9 \mu\text{m}$ should be similar to the one just described. Therefore, plasma shielding can most likely be successfully avoided if the pulse intensity profile and the maximum fluence of the laser pulse are carefully controlled to avoid high intensity spikes.

Assuming that plasma is avoided, only absorption and scattering (most likely by the ejected mineral particles, as was discussed previously) may play a role in the shielding by the plume. The effect of absorption by the plume will most likely be of lower intensity for the Er:YAG laser than for the $\lambda = 10.6 \mu\text{m}$ laser. This is a consequence of the fact that neither the mineral nor the water vapor are expected to absorb radiation very significantly at $\lambda = 2.94 \mu\text{m}$, since the absorption coefficient of the mineral at this wavelength is very low and water vapor practically does not absorb at $\lambda = 2.94 \mu\text{m}$ [121, 122, 133], as was discussed in Chapter 2. On the other hand, the mineral particulates are expected to continue to absorb at $\lambda = 10.6 \mu\text{m}$, which suggests that shielding by the plume may be somewhat significant. Discussing the influence of scattering on plume shielding is much more complex to do than discussing absorption, in particular because the wavelengths in question here are comparable to the dimensions of the majority of the components in the plume (the particulates), thus indicating that the dominant scattering mechanism will be Mie scattering rather than Rayleigh scattering. Thus, no attempt will be made here to discuss the possible role of scattering in the shielding by the plume, which limits the extent to which the plume shielding effect can be explained and predicted from a theoretical level. Some experimen-

tal observations do exist, fortunately, and those indicate that, in general, plume shielding at the wavelengths being considered here is not very significant (below the plasma threshold), as will be discussed next.

Forrer et al. [113] investigated the behavior of bone under $\lambda = 9.6$ and $10.6 \mu\text{m}$ (pulse duration = $12.5 \mu\text{s}$, repetition rate = 0.5 Hz , 4 pulses per spot), and found "a logarithmic dependence between the drilling depth, l , and the fluence, F ", which can be described through the equation:

$$l = \delta \ln \left[\frac{D}{\delta} \left(\frac{F}{F_0} - 1 \right) + 1 \right] \quad (4.7)$$

where δ is the attenuation depth in the debris, D is the attenuation depth in the bulk material and F_0 is the ablation threshold fluence. The exact same type of dependence was found for the ablation of bone by a $\lambda = 2.9 \mu\text{m}$ laser by Izatt et al. [127] below the plasma threshold (pulse duration = 350 ns , repetition rate = 0.5 Hz , 5, 10 or 20 pulses per spot) and by Majaron et al. [134] for a much longer pulse from a free-running Er:YAG laser and dentine (pulse duration = $100 \mu\text{s}$, repetition rate not given, fluence between 10 and 80 J/cm^2 , 10 pulses per spot). The fact that the same dependence was found for long and for short pulses, both for dentine and for bone, suggests that it may be possible to do the same thing for enamel, for which results using short pulses could not be found. The results obtained by Majaron et al. [134] using the Er:YAG laser on enamel indicate that the dependence of the crater depth with the incident fluence is better described by a linear instead of a logarithmical relationship, which indicates that screening by debris is much less important in ablation of enamel than in ablation of dentine at $\lambda = 2.9 \mu\text{m}$. This information could not be found in the literature for ablation of enamel by $\lambda = 10.6 \mu\text{m}$, but was determined by Fried et al. [132] for $\lambda = 9.6 \mu\text{m}$ (parameters given before), who found a slightly logarithmic dependence between the ablation rate and the incident fluence, for fluences between the ablation threshold and 10 J/cm^2 . Given that the ablation debris produced by dentine and enamel ablation should be entirely similar, the observed differences with respect to shielding by the plume are most likely a consequence of the *amount* of debris produced per pulse: the ablation rate of dentine is at least twice as high as for enamel, which implies that the cloud of debris is more dense, thus causing more intense shielding of the radiation.

In summary, shielding by the plume should not impair the ablation rates, provided that the fluence per pulse is kept low enough so that plasma is not

formed and that pulse repetition rates are kept below $\simeq 1000$ Hz, so that the plume generated by a laser pulse can clear before another pulse hits the target. Therefore, it was not found necessary to include the effect of the plume on the models presented in this Thesis.

4.5 Conclusion

The discussion in the present Chapter culminates in the conclusion that any models on the ablation of enamel by mid-IR lasers that aim to give further insight into the ablation mechanisms and allow determining the optimal values for the laser ablation mechanisms must necessarily include the mesoscale structure of this material at a micrometer scale, in particular the water pores. Furthermore, the models must be able to simulate the response of the material in the nanosecond to microsecond range. This implies that simple continuum models are not appropriate, since they will not be able to include the microstructure of the material. On the other hand, electronic, atomic or molecular scale models will not be able to accommodate the large spatial and temporal scales that is indispensable in this problem. The most appropriate tool to tackle the present problem thus seems to be the Finite Element Method, which is able to fill all the necessary requirements and which will be discussed further in Chapter 5.

Chapter 5

The modelling tools to use: the finite element method

In this Chapter, a brief description of the finite element (FE) method will be made where the general character of the method will be emphasized and the most important concepts associated with it will be described. After summarizing the general steps associated with building models and performing simulations, the issues surrounding the choice of the mesh of the models, the elements to use and the appropriate algorithms will be explained and the options made for the simulations reported here will be justified.

5.1 General description of the FE method

The Finite Element Method (FEM) is a generic mathematical method used to obtain numerical solutions to equations that are impossible to solve analytically. Such equations appear routinely in many areas of engineering and science, and obtaining a solution for them is sometimes of considerable practical importance. Although there is no limitation as to the type of equation that may be approximated using the FEM, to date this method has been most widely used in mechanical and civil engineering to solve problems in solid mechanics, heat conduction, fluid mechanics, acoustics and electromagnetism. The FEM is a powerful tool, capable of handling mathematical problems with a diverse range of features [135]:

- With the FEM it is possible to obtain approximate solutions to differential,

integral, integrodifferential or variational equations.

- Boundary-value problems (very frequently known as equilibrium or steady-state problems); eigenvalue problems (resonance and stability phenomena); initial-value problems (diffusion, vibration and wave propagation) can all be solved using the FEM.
- The region of space occupied by the system under study (the *domain* of the problem), may have any geometric shape.
- The physical properties of the systems may vary from point to point in the domain.
- The external perturbations imposed on the system (a force, pressure, boundary temperature or heat source applied to a system in equilibrium), called *loads*, may be of any kind.

The problem being addressed in this Thesis possesses all the characteristics itemized above. The relevant mechanisms of enamel ablation by mid-IR lasers are thought to occur at a micrometer scale and are related to the temperature (and, consequently, stress) induced at the irradiated site. Therefore, in order to understand the response of the material it is necessary to solve the equations that describe the evolution of temperature and stress in it. Given the complicated geometry of enamel at the micrometer scale, and the fact that the material properties will vary in space and, possibly, time, it is not possible to solve these equations analytically. The FEM thus seems the most adequate method to use for the computational study being proposed here.

The FEM has been used and perfected for years to solve problems in solid mechanics and heat transfer, analogous in their essence to the ones being addressed in this work. Several commercial FE codes exist today, capable of solving large and complex problems in one, two or three dimensions. Consequently, it did not seem appropriate to develop a FE code for the particular application in question here. Instead, the option was made to work with two commercially available codes: ALGOR and ABAQUS. ALGOR is a relatively simple, but powerful, code, used mostly during the initial work that led to this Thesis. ABAQUS is a more flexible and complex package than ALGOR, necessary to carry out analyzes inaccessible using ALGOR. All the simulations described in Chapter 6 were performed using ABAQUS. These codes are very similar in their essence, and a general description that applies to both is now given.

When initiating a simulation, it is necessary to define the *system* to study (the enamel) and the *domain* that will be simulated (the region of space and the interval of time that will be investigated). The domain must then be partitioned into smaller subdomains, or *elements*, of regular shape: typically, hexahedra ("bricks"), tetrahedra ("wedges") or pentahedra ("pyramids") for three-dimensional domains, thus forming what is commonly called a *mesh*. The elements are connected at points called the *nodes*, which normally correspond to the corners of the elements¹. These steps are done by drawing a structure and meshing it using pre-processors that are normally associated with the FE packages. Secondly, it is necessary to define the equations for each element. These are algebraic equations that approximate the original differential or integral equations expressing the conservation or minimization of a given property (such as the conservation of energy or the minimization of the potential energy of a system); in terms of the FE packages available, this step translates into selecting the *type* of element of a given geometrical shape to use. It is also necessary to define the *constitutive equations* describing the behavior of the material in each element. Thirdly, the element equations are numerically evaluated for each element, and the results are assembled into the *system equations* which need to be solved. Before solving them, however, it is necessary to impose the boundary conditions (normally with the help of the pre-processor), which means that some terms in the system equations will be modified. Subsequently, the system equations are solved, normally using the *displacement* (or *stiffness*) *method*, which is an *implicit* method that assumes the unknowns of the problem to be the displacements of the nodes. The equations could also be solved using the *force* (or *flexibility*) *method*, which assumes that the forces are the unknowns to the problem, but it has been shown that the stiffness method is computationally more efficient [136]. A solution to the problem may also be obtained using an *explicit* method, for which it is *not* necessary to solve a system of equations because the solution is advanced kinematically from one time increment to the next. Finally, the solution is evaluated by the user, normally with the help of a post-processor associated to the FE package.

¹There are elements that possess additional nodes at the middle of the edges.

5.2 Obtaining the temperature and stress maps

5.2.1 The equations to solve

In this subsection the actual element equations implemented in ABAQUS will not be presented, since a thorough description can be found in the literature accompanying that commercial package. Instead, a more simple version of the global equations for which a solution is needed is presented, with the aim of illustrating the type of problem being addressed in this work. A more detailed description of the thermal and stress equations can be found in refs. [135, 136].

One may think at first that the heat conduction and thermal stress equations which describe the effects of a mid-IR laser in any material should be solved simultaneously. However, this is often computationally very expensive, so whenever possible the thermal and stress problems should be decoupled. In the present case, the solution to the thermal problem is necessary to obtain the solution for the stress problem. However, the stress solution does not influence the thermal solution, at least before material removal takes place (under sub-ablation conditions as is the case in the models presented here). This independence of the thermal solution on the stress solution is a consequence of the fact that enamel is a brittle material. For this reason, mechanical energy-dissipation processes in this material are normally not associated with plastic straining, and the stress field does not generate heat. Therefore, in all the simulations described in this Thesis the thermal and mechanical solutions were obtained separately: the thermal solution was obtained first, and the solution for the thermal stress problem was obtained subsequently, taking the thermal solution as input.

The general form of the governing equations for the thermal problem can be understood using a simple, one-dimensional example such as the one in Fig. 5.1. Applying the energy conservation principle to the volume depicted in Fig. 5.1, the following equations are obtained

$$\begin{aligned} E_{in} + E_{generated} &= \Delta U + E_{out} \\ q_x A dt + Q A dx dt &= \Delta U + q_{x+dx} A dt \end{aligned} \quad (5.1)$$

where E_{in} is the energy entering the control volume, $E_{generated}$ is the energy generated (or disappearing, in case of a heat sink) in the material, ΔU is the change in internal energy in the volume and E_{out} is the energy coming out of the control

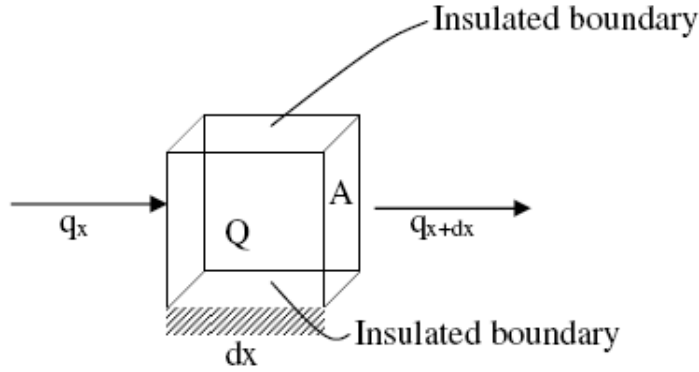


Figure 5.1: Control volume for one-dimensional heat conduction. Source: ref. [136].

volume. A is the cross-sectional area of the non-insulated faces of the control volume, q_x and q_{x+dx} are the heat fluxes (energy per unit time and per unit area) coming into and out of the volume, and Q is the internal heat source (energy per unit time and per unit volume). Now, q_x may be calculated using Fourier's law of heat conduction, that states that the heat flux in a given direction is proportional to the temperature gradient in that direction, according to the expression:

$$q_x = -\kappa_{xx} \frac{dT}{dx} \quad (5.2)$$

where κ_{xx} is the thermal conductivity of the material in direction xx . At point $x + dx$, Fourier's law takes the form:

$$q_{x+dx} = -\kappa_{xx} \frac{dT}{dx} \Big|_{x+dx} \quad (5.3)$$

The change in the energy stored can be expressed as

$$\Delta U = c \rho A dx dT \quad (5.4)$$

where c and ρ are the specific heat and the density of the material, respectively.

It is by substituting eqs. 5.2, 5.3 and 5.4 into eq. 5.1, that the one dimensional heat conduction equation is obtained:

$$\frac{\partial}{\partial x} \left(\kappa_{xx} \frac{\partial T}{\partial x} \right) + Q = \rho c \frac{\partial T}{\partial t} \quad (5.5)$$

The equation for the three-dimensional heat conduction problem will naturally be more complicated, but the basic energy balance shown in eq. 5.1 is also obeyed.

Solving the heat transfer equations will yield a temperature distribution throughout the domain for various instants in time. This temperature distribution is passed into the mechanical analyzes and will induce thermal stresses because of the constrained expansion of the structure. For a one dimensional problem, the equation describing the thermal stress is

$$\varepsilon_x = \frac{\sigma_x}{E} + \varepsilon_T \quad (5.6)$$

where ε_x is the strain of the material experiencing stress σ_x and ε_T is the thermal strain (the strain induced solely by the unconstrained thermal expansion of the material). This equation means that, whenever the temperature is different from the reference value at which the thermal strain is zero, thermal stress will be induced if the structure cannot move freely. The stress will be proportional to the difference between the actual configuration of the structure and the configuration that the structure would naturally have if allowed to expand at will.

5.2.2 The algorithms to use

There are both fundamental and practical differences between the implicit and the explicit algorithms that were used in the work presented in this Thesis. At a fundamental level, when obtaining a solution for a given instant in time using an implicit algorithm, one needs the values for nodal quantities (eg. the displacements) at the previous time increment but also the values of the loads experienced by the system at the current time increment. This method requires a system of equations to be solved at each time increment and, consequently, can become computationally very demanding, particularly for non-linear problems. When using the explicit method there is no system of equations to solve, and it is only necessary to use quantities obtained at the previous time increment. The differences between the two methods are illustrated in the following examples.

The examples are concerned with obtaining the stress and displacement suffered by the system in Fig. 5.2, in which a force P is applied to the free node (node 1) of a system of three rods of length l , area A and linear elastic behavior described by a Young's modulus E . The numbers in circles correspond to the element numbers (in this case, beam elements), the other numbers are the node numbers.

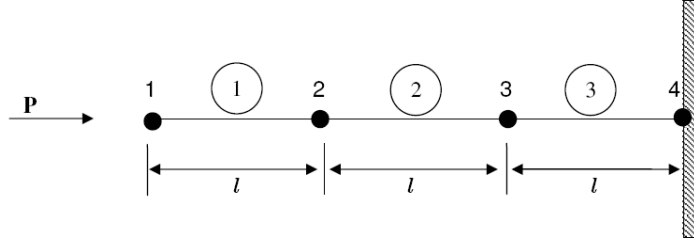


Figure 5.2: Initial configuration of a rod with a concentrated load, P , at the free end. Source: Abaqus 6.5 "Getting started" manual.

When using the *explicit method*, the solution is advanced kinematically from one time increment to the next. In the first time increment, force P confers to node 1 an acceleration, \ddot{u}_1 , which is calculated using Newton's Law

$$\ddot{u}_1 = \frac{P}{m_1}. \quad (5.7)$$

Therefore, node 1 will move with velocity \dot{u}_1 and, consequently, element 1 will experience strain rate $\dot{\varepsilon}_{el1}$:

$$\dot{u}_1 = \int \ddot{u}_1 dt \implies \dot{\varepsilon}_{el1} = -\frac{\dot{u}_1}{l} \quad (5.8)$$

It is thus possible to calculate the total strain experienced by element 1 at the first time increment by adding the initial strain of the increment, ε_0 with the strain caused by force P .

$$d\varepsilon_{el1} = \int \dot{\varepsilon}_{el1} dt \implies \varepsilon_{el1} = \varepsilon_0 + d\varepsilon_{el1} \quad (5.9)$$

Finally, the stress experienced by element 1 at the end of the first increment can be calculated according to

$$\sigma_{el1} = E \varepsilon_{el1} \quad (5.10)$$

In the second increment the stresses in element 1 apply internal forces to element 2 (see Fig. 5.3), which are then used to calculate the dynamic equilibrium accelerations at nodes 1 and 2:

$$\ddot{u}_1 = \frac{P - I_{el1}}{M_1} \implies \dot{u}_1 = \dot{u}_1^{old} + \int \ddot{u}_1 dt \quad (5.11)$$

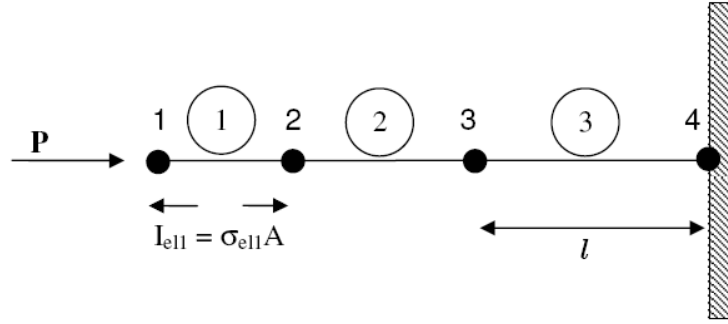


Figure 5.3: Configuration of a rod with a concentrated load, P , at the free end, at the beginning of the second increment. Source: Abaqus 6.5 "Getting started" manual.

$$\ddot{u}_2 = \frac{I_{el1}}{M_2} \implies \dot{u}_2 = \int \ddot{u}_2 dt \quad (5.12)$$

Similarly to what was described for the first increment, the velocities at the nodes can then be used to calculate the strain rate and, finally, the stress experienced by both elements.

$$\dot{\varepsilon}_{el1} = \frac{\dot{u}_2 - \dot{u}_1}{l} \implies d\varepsilon_{el1} = \int \dot{\varepsilon}_{el1} dt \quad (5.13)$$

$$\implies \varepsilon_{el1} = \varepsilon_1 + d\varepsilon_{el1} \quad (5.14)$$

$$\implies \sigma_{el1} = E \varepsilon_{el1} \quad (5.15)$$

This process is continued until the total time of the analysis is reached, or until equilibrium is attained.

The equilibrium configuration of the same system can be determined using an *implicit method*. Based on the free-body diagram presented in Fig. 5.4 (in which the displacements, d , are not presented because they have similar orientations as the forces), it is possible to write the element equations. The equation for element 1 is:

$$\begin{pmatrix} f_{1x}(1) \\ f_{2x}(1) \end{pmatrix} = \frac{EA}{l} \begin{pmatrix} E & -E \\ -E & E \end{pmatrix} \begin{pmatrix} d_{1x} \\ d_{2x} \end{pmatrix} \quad (5.16)$$

where the numbers in subscript refer to the nodes and the numbers in parenthesis refer to the element. The equations for elements 2 and 3 will not be presented since they are very similar to the equation for element 1 (it is assumed that the length, cross-sectional area and Young's modulus for the three elements in the system are the same).

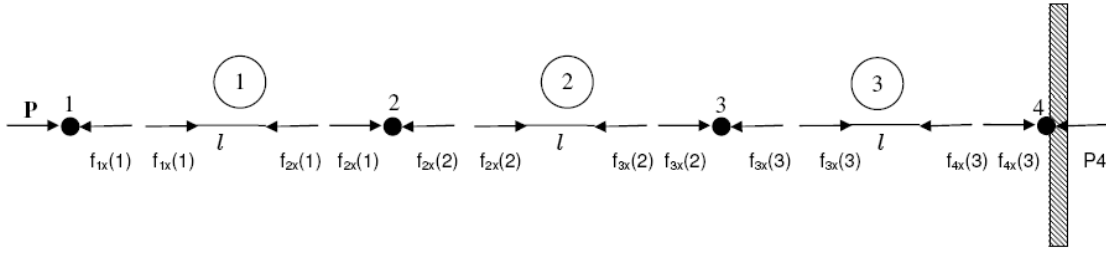


Figure 5.4: Free-body diagram of a rod with a concentrated load, P , at the free end. In the label for each force, the numbers in parenthesis refer to the elements and the numbers in subscript refer to the node number.

The nodal equilibrium equations can also be written, and have the form:

$$P = f_{1x}(1) \quad (5.17)$$

$$F_2 = f_{2x}(1) + f_{2x}(2) \quad (5.18)$$

$$F_3 = f_{3x}(2) + f_{3x}(3) \quad (5.19)$$

$$P_4 = f_{4x}(3) \quad (5.20)$$

Combining the nodal equilibrium equations with the constitutive equations for each element, one arrives at a system of equations that will yield the equilibrium solution for the system:

$$\begin{pmatrix} P \\ F_2 \\ F_3 \\ P_4 \end{pmatrix} = \frac{EA}{l} \begin{pmatrix} 1 & -1 & 0 & 0 \\ -1 & 2 & -1 & 0 \\ 0 & -1 & 2 & -1 \\ 0 & 0 & -1 & 1 \end{pmatrix} \begin{pmatrix} d_{1x} \\ d_{2x} \\ d_{3x} \\ d_{4x} \end{pmatrix} \quad (5.21)$$

In abbreviated notation, eq. 5.21 can be written as $F = Kd$, where F is the *global force vector*, K is the *global stiffness matrix* and d is the *global displacement vector*.

In this example it was attempted to determine the equilibrium stress and strain of a structure in which the material behavior is linear. Therefore, the system of equations would only have to be solved once. However, if the material had non-linear behavior or if a dynamic solution was desired, a system of equations would have to be solved at each temporal increment which makes this method very demanding, as was already mentioned previously. In this case, the equilibrium equations would include a term corresponding to the inertia forces, $M\ddot{u}$. The

dynamic example was not presented here because it is not the point of this Section to give a comprehensive explanation of the FEM but rather to illustrate important concepts of this method, which was achieved in this case by obtaining the more simple, static solution to the example given.

The fact that, in the explicit method, the solution is advanced kinematically from one time increment to the next implies that this method is appropriate to simulate fast events occurring in short timescales, giving insight into the dynamic evolution of the material. An implicit method can also be used to gain insight into the dynamic behavior of an event, but either at a higher computational cost or with some loss of information regarding the high-frequency dynamic behavior of the material, if longer time-increments are chosen. On the other hand, the implicit algorithm is unconditionally stable², which does not happen with the explicit algorithm. When using the implicit algorithm, the definition of the time increment is solely a function of the type of problem and the desired precision in the solution. For the explicit algorithm, the maximum value of the time increment is limited by the time a dilatational wave takes to traverse the smallest dimension found in any one element of the mesh; hence, this method becomes inadequate to study phenomena that occur in long timescales.

In the work presented here, both these algorithms were used: the implicit algorithm was always used to solve the dynamic heat transfer problem and to obtain information on the quasi-static stress state of a material at a given point in time; it was used occasionally to obtain some insight into the dynamic stress behavior of the modelled structures when the explicit algorithm was considered inappropriate or simply less practical. In general, the explicit algorithm was the preferred one to investigate the dynamical stress and strain response of enamel to laser radiation. In both the implicit and explicit procedures the automatic time incrementation schemes available in ABAQUS were used since, in general, they are known to perform better than user-defined incrementation procedures.

²At least for certain values of the algorithmic parameters.

5.3 Obtaining the natural frequencies of a structure: the natural frequency extraction algorithm

When developing appropriate boundary conditions for the models presented in this Thesis it was necessary to ascertain whether the frequencies of vibration induced by a single laser pulse, detected using the explicit algorithm, were representative of the modelled structure. In order to do this, natural frequency extraction analyses were performed. The principles behind the natural frequency extraction procedure will now be explained by making use of the simplest example possible: an oscillating spring with a mass attached to one end, as can be seen in Fig. 5.5.

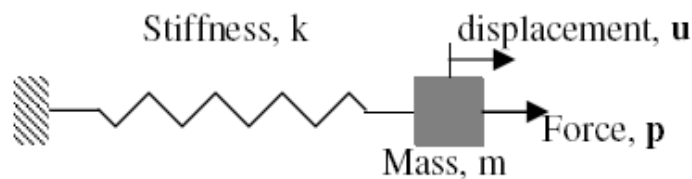


Figure 5.5: Mass-spring system.

The dynamic equation of motion of a mass-spring system is given by

$$p - ku = m\ddot{u} \quad (5.22)$$

If the mass is pulled and then released, the system will oscillate at a given frequency, called its *natural frequency*, and the equation of motion will be reduced to

$$ku + m\ddot{u} = 0, \quad (5.23)$$

when no damping exists. Solutions to this equation have the form

$$u = \phi \exp(i\omega t), \quad (5.24)$$

(ω is the angular frequency and t is the time) which, when substituted back into

eq. 5.23, yield the *eigenvalue* problem

$$k\phi = \omega^2 m\phi. \quad (5.25)$$

This system has n eigenvalues, where n is the number of degrees of freedom (DOF's) in the finite element model (in the case of the spring given as example above, only one natural frequency exists, with value $\omega = (k/m)^{1/2}$). For each eigenvalue, ω_i^2 , its square root is the *natural frequency* of the j th mode of the structure, and ϕ_j is the corresponding *eigenvector* or mode shape (the deformed shape of the structure when it vibrates in the j th mode).

The actual implementation of such a procedure to solve cases with large numbers of eigenvalues is of course much more complex than the description just given. A more thorough explanation of the numerical implementation of this procedure can be found in the manuals accompanying ABAQUS, and therefore will not be given here.

5.4 The mesh

The FEM provides an approximate solution to the mathematical formulation of a physical problem. The accuracy of that solution is in part a function of the algorithm used to solve it, but also of the degree to which the elements used and the density of elements throughout the domain of the problem are adequate. These choices cannot be automated and are left to the judgement of the researcher. The main issues concerning the elements and the mesh to use in models will now be described. The geometries of the domains simulated will not be discussed in this Chapter, since they vary from model to model. Only those aspects of the mesh which are common to all the models presented in Chapter 6 will be described in this subsection.

Elements are characterized by the following aspects: the family to which they belong (closely related to their geometric shape), the degrees of freedom (DOF) and the number of nodes they possess (the order of interpolation), their formulation and integration [137].

For the purpose of the system being investigated here, it was judged insufficient to approximate the system by a two-dimensional model because of the complex microstructure that enamel possesses. Also, it is known that elements with regular

shapes (such as hexahedra, or "bricks") provide more accurate solutions than less regular-shaped elements, such as tetrahedra. Therefore, families of three-dimensional elements were used to build the domains of the simulations, and brick elements were used whenever possible. Since the problem addressed by this work is concerned with the evolution of the temperature and stress fields in a material, only families of elements with temperature and displacement degrees of freedom were used.

The choice of the element formulation, integration and order of interpolation determines how well elements will behave under the particular loads applied. Because of the influence of these parameters on the quality of the results, they will be discussed in some detail and the choices made for the simulations presented in this Thesis will be justified. The temperature and displacement DOF's are only calculated at the nodes; values for other points in the element must be interpolated from the values obtained at the nodes. For elements with nodes only at the corners, a linear function is used to perform this interpolation; hence, these elements are called first order elements or linear elements. Elements with mid-side nodes will use quadratic interpolation, and consequently are called quadratic elements or second order elements. An example of linear and quadratic elements can be found in Fig. 5.6.

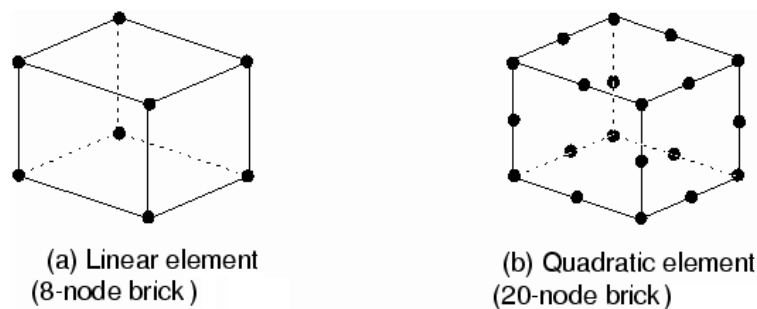


Figure 5.6: Example of linear and quadratic elements. Source: Abaqus manual.

The element formulation is related to the theory that defines the behavior of the model. All the elements used in this Thesis use the *Lagrangian*, or *material* formulation, in which the material inside an element remains inside that element throughout the entire analysis. The alternative formulation is called *Eulerian*, or *spatial*, in which the material flows through the elements and the elements are associated to spatial coordinates instead. Finally, the integration of an element refers to the number of integration points (Gauss points) that the element possesses, which are used in the FEM to numerically evaluate quantities over the volume of each element. Quantities such as the stress or heat flux per unit vol-

ume, associated to a volume rather than a point, are not evaluated at the nodes but at the integration points of an element. Elements may have *full integration* (element quantities are evaluated at all the Gauss points) or *reduced integration* (a reduced number of Gauss points are used to evaluate element quantities), as exemplified in Fig. 5.7.

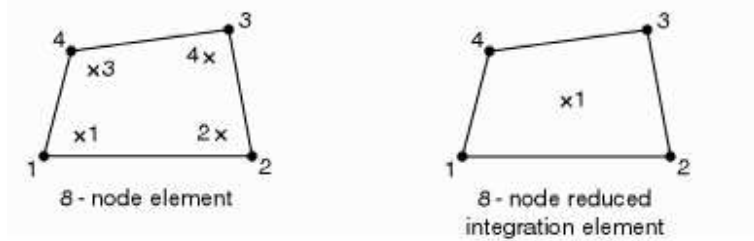


Figure 5.7: Example of full and reduced integration elements. Only half of the nodes that make up the element are shown. The fully integrated element on the left has a total of eight integration points; the reduced integration element on the right only has one integration point. Source: Abaqus manual.

While it may seem at first sight that fully integrated, quadratic elements may be the ones which yield the most accurate results, that is in fact not the case necessarily. Particular types of elements may perform better or worse depending on the type of loading (bending, direct or shear loads, for stress analyzes) they are expected to carry. Fully integrated linear elements are known to perform poorly under bending loads, even though they perform very well under shear or direct loads. They suffer from a numerical problem known as *shear locking*, which means that these elements are too stiff in bending. Shear locking is not a problem for fully integrated quadratic elements, but these elements also lock under complex stress states, so they should be used with caution and the results should be checked carefully. One option to avoid shear locking is to use incompatible mode elements. These use additional DOFs, internal to the element, to enhance the element's deformation gradient. They can produce excellent results at a low computational cost, provided that they are not heavily deformed. Linear and reduced integration elements behave oppositely to linear and fully integrated elements: they are too flexible in bending, because they suffer from a numerical problem called *hourglassing*. However, in ABAQUS these elements have been given a small amount of artificial "hourglass stiffness" to limit propagation of unphysical results in the mesh, which works well if a fine mesh is used and if the element is not heavily distorted during the analysis. If properly used, these elements perform very well at a low computational cost. Finally, quadratic and reduced integration elements are

also available. These elements do not experience locking and, provided a sufficient number of elements is used, hourglassing is also not a problem. Therefore, they tend to be very good choices for most types of simulations.

In the analyzes presented in this Thesis several types of elements were used. When using the implicit algorithm to solve thermal problems, three-dimensional linear elements with full integration were applied. For stress analyzes using the implicit algorithm, three-dimensional linear elements with full integration and incompatible modes were chosen, because of their low computational cost and good performance if the distortion is small, as is the case. When the explicit algorithm is used, three dimensional linear elements with reduced integration were chosen, since they also perform well at a low computational cost³.

With respect to the mesh of the models, automatic meshers were not used since they may produce irregular meshes and it is known that regular ones produce more accurate results. Instead, the mesh for each model was created "by hand", to ensure that the best elements and least deformed element-shapes were present in the models.

³Fully integrated elements are not available for the explicit algorithm.

Chapter 6

Description of models, results and discussion

6.1 Boundary conditions

The work presented in this Thesis intends to explicitly consider the structure of the material at mesoscopic scales, known to play an important role during ablation [138, 139]. However, attempting to simulate an entire tooth with micrometer-scale definition becomes computationally prohibitive, even if it is conceptually desirable. Therefore, one needs to use smaller models to attempt, at some level of approximation, to investigate the response of the entire system: the models presented in this Thesis represent micrometer-size pieces of the macroscopic tooth under laser radiation.

This approximation led to the important problem of determining which boundary conditions (BCs) should be applied to the FE models so that one could effectively simulate a piece of material which is a part of a larger object. Appropriate BCs are determinant to obtain meaningful results; however, this problem has not been specifically addressed in the literature. Authors such as Majaron or Zhigilei, who do computational and theoretical research on ablation, either choose periodic BCs for their models, or assume an infinite or semi-infinite material, [140, 141]. The work developed by these authors provided an important starting point for the elucidation of ablation mechanisms, but further work on the subject still needs to be done to fully understand the physics underlying laser ablation at mesoscopic scales. Developing easy-to-apply BCs for static and dynamic FE models and adequately accounting for the finite size and constraints of the region of material being simulated – at the micrometer scale – is necessary if the results obtained

are to be meaningful. This is the objective of the work presented in the coming Section.

The boundary conditions developed have been applied to all the FE models described in this Chapter: both to the FE models designed to investigate the role of the static stress in the ablation mechanisms and to the more complex models intended to capture the temperature and stress evolution taking place during and after a sub-ablative laser pulse.

6.1.1 Model description

Before giving a detailed account of the boundary conditions (BC's) that have been developed, the common features to all models used to develop and test these BC's will be described. All the models have a parallelepiped shape, although different models will have different sizes and all attempt to reproduce the behavior of a single piece of enamel. Despite the fact that dental enamel has a microstructure, this microstructure was not included in any of the models considered in this Section, since it would introduce unnecessary complexity at this point. Since the BC's are to be subsequently applied to models of enamel being heated by a mid-IR laser, laser heating was also used here.

The CO₂ laser was chosen because of the similar absorption coefficients of enamel and HA at this wavelength. The temperature rise experienced by the material is therefore a function of the absorbed radiation, which in turn depends on the incident intensity of the laser, the absorption and scattering coefficients of the material and also its reflectivity. Scattering in enamel can be neglected at 10.6 μm because of the high absorption coefficient at this wavelength, as was discussed previously in this Thesis. The reflectance has a value of 13% at $\lambda = 10.6 \mu\text{m}$ [66]. Therefore, the energy deposition is determined by this tissue's absorption coefficient and in first approximation all the incident radiation can be considered to be absorbed and transformed into internal kinetic energy of the material. Taking into account that the laser beam was considered perpendicular to the top and bottom surfaces of all the models, using a Gaussian spatial intensity profile and a constant temporal profile, the intensity of the beam inside the tissue, $I(r, z)$, is thus given by

$$I(r, z) = I_0 \exp(-\mu \cdot z) \exp\left(-\frac{2r^2}{w^2}\right) \quad (6.1)$$

where z is the depth inside the tissue, I_0 is the intensity of radiation at the surface

of the target, μ is the absorption coefficient of the tissue, w is the beam radius and r is the radial distance from the center of the laser spot [2]. The heat deposited per unit area and time, $S(r, z)$, over a slice of material of thickness dz is given by

$$S(r, z) = -\frac{\partial I(r, z)}{\partial z} = \mu I(r, z) \quad (6.2)$$

A single, short ($0.35 \mu\text{s}$) laser pulse with sub-ablative intensity was considered, which is compatible with the micropulse duration of free-running lasers and with the pulse duration of Q-switched lasers. The models were oriented so that the surface on which the laser shines is in the XY plane, and the optical axis of the laser beam corresponds to OZ. The laser parameters used in the simulations described in this Section are given in Table 6.1.

The analyzes investigated the evolution of the thermal and stress maps as a function of time for a total of $250 \mu\text{s}$, using the Implicit algorithm to obtain the thermal solution and the Explicit algorithm for the mechanical problem in the manner described in Chapter 5. It was assumed that the thermal stress in the model was zero at the temperature of $37 \text{ }^\circ\text{C}$.

Type of laser	CO ₂ ($10.6 \mu\text{m}$)
Pulse duration (μs)	0.35
Maximum absorbed intensity, I_0 ($\text{J}/\text{m}^2/\text{s}$)	1.2×10^{10}
Number of pulses	1
Laser beam radius (mm)	0.2
Duration of simulations (μs)	250

Table 6.1: Laser and simulation parameters used in models *Large*, *TestBC1* and *TestBC2*. Note that the intensity translates into a fluence per pulse of $0.42 \text{ J}/\text{cm}^2$, far below the ablation threshold of enamel for the CO₂ laser ($2 - 3 \text{ J}/\text{cm}^2$ for a $2 \mu\text{s}$ laser pulse, according to Fried et al. [132]).

Enamel is a brittle material with a pre-fracture behavior which can be described in first approximation by linear elastic relationships. Therefore, the mechanical properties necessary to obtain the solution to the stress problem are the Young's modulus and Poisson's ratio, provided one can ensure that cracking is avoided. In these simulations, a laser intensity several times below the ablation threshold was chosen, so that cracking can be avoided and the linear elastic material constitutive equations can be used. The thermal, mechanical and optical properties of enamel used in all the models are given in Table 6.2.

Now that the common features to all models in this Section have been related, the Boundary Conditions developed will be described.

6.1.1.1 Boundary conditions for stress analyzes

Despite the fact that the thermal analyzes are performed before the mechanical analyzes, it is more convenient for the purpose of this description to first consider the problem of determining the most appropriate BCs for the stress analyzes. Lateral periodic BCs may not be appropriate to laser ablation modelling because in this case the material can only expand upwards. Making the nodes at the lateral and bottom surfaces of the model entirely fix is also not appropriate for the same reason. However, it was conceived that a modified version of this second method would lead to more appropriate BCs. The modification consists of surrounding the core of the enamel model with a layer of another material (named *Restrain-layer*, or RL), which makes the transition between the lateral and bottom fixed nodes and the center of the model. The Restrain-layer must have properties that allow the center of the model to expand while accounting for the constraining effect and expansion of the bulk of the tooth. *In effect, the Restrain-layer as a whole imposes the BC's to the central part of the models:* by adjusting the material properties of the Restrain-layer, the center of the models can effectively reproduce the dynamic temperature, displacement and stress fields in the tooth.

	Enamel	Restrain-layer <i>TestBC1</i>
Absorption coefficient (cm^{-1})	825 [69]	825
Density (kg/m^3)	3.1×10^3 [142]	3.1×10^3
Thermal conductivity ($\text{J}/(\text{s.m.C})$)	1.3 [143]	1.3
Specific heat ($\text{J}/(\text{kg.C})$)	880 [143]	880
Youngs modulus (N/m^2)	1.1×10^{11} [144]	1.0×10^{10}
Poissons ratio	0.28 [145]	0.28
Expansion coefficient ($^{\circ}\text{C}^{-1}$)	1.6×10^{-5} [146]	$\alpha_{xx} = 1.8 \times 10^{-4}$ $\alpha_{yy} = 1.8 \times 10^{-4}$ $\alpha_{zz} = 1.6 \times 10^{-5}$

Table 6.2: Mechanical properties of enamel and Restrain-layer used in models *Large* and *TestBC1*.

In order to determine whether the proposed method to impose BC's actually functioned, it was necessary to have a reference against which results from models that use these boundary conditions could be compared. Given the impossibility

of comparing results with experimental data (the necessary information could not be found in the literature), the only possible way to assess the adequacy of the proposed BCs was resorting to modelling. Therefore, it was decided to create a large enamel model (named model *Large*) which is the reference against which the results obtained using smaller (test) models were compared. The test models intend to replicate the mechanical and thermal behavior of the central part of model *Large* and therefore need appropriate BC's, which are imposed by using Restrain-layers with appropriate material properties. Note that, at this point, none of the models intend to replicate the behavior of enamel *in a tooth*; they are ideal models that use the material properties of enamel but which are not related to real physical systems, and are only used to develop and test the BC's.

Model *Large* (dimensions $65 \times 65 \times 20 \mu\text{m}^3$), our reference, represents a single piece of human dental enamel. All the elements making up the model were assigned the material properties of hydroxyapatite (the main component of dental enamel), with the exception of the absorption coefficient, which is relative to human dental enamel (see Table 6.2). The first test model, called *TestBC1*, (dimensions $19 \times 19 \times 20 \mu\text{m}^3$) has a central region (the core of the model) made of enamel, and a lateral outer-layer made of a different material, the already mentioned Restrain-layer. Since *TestBC1* has a smaller cross-section but the same height as model *Large*, only the reduction in cross-sectional area needs to be addressed by its BC's. Therefore, only a Lateral Restrain-layer is considered for model *TestBC1* (see Fig. 6.1). The lateral and bottom nodes of model *TestBC1* are also fix, and the nodes at the top surface (on which the laser is shining) are free to move.

Up to now the general purpose of the Restrain-layer was described, but how this layer actually imposes adequate boundary conditions was not explained; this is the subject of the next lines. The mechanical properties of the Restrain-layer must have values such that nodes in surface B experience the same stress and displacement as nodes in surface A (see Fig. 6.1). In order to estimate these values, it was assumed that enamel obeys a linear-elastic stress-strain relationship until it fractures, as it was mentioned previously. For a bar, this relationship is

$$\sigma = E \frac{\Delta\ell}{\ell} \quad (6.3)$$

where σ is the stress, E is the Young's modulus of the material, $\Delta\ell$ the elongation suffered by the bar and ℓ is the initial length of the bar. The stress experienced by the Restrain-layer is not uniaxial as given in eq. 6.3, but three dimensional, so

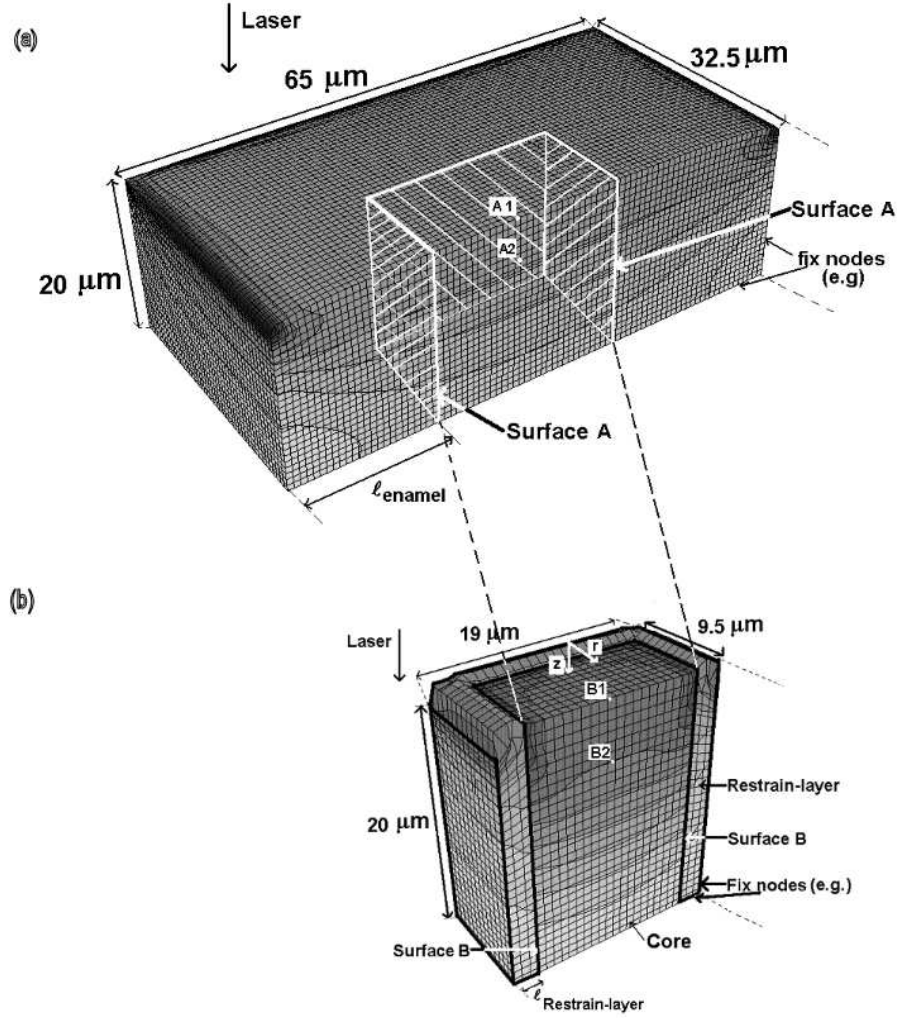


Figure 6.1: Geometry of models (a) *Large* and (b) *TestBC1*. Only half of both models is shown.

this relationship represents only a first-order approximation to the actual mechanical behavior. However, it was considered that using the full three-dimensional description would increase the complexity of the problem without a proportional increase in the quality of the BC's sought. By applying eq. 6.3 to models *Large* and *TestBC1*, and considering that the displacement experienced by the nodes making up surface A ($\Delta \ell_{en(surfaceA)}$) is equal to the displacement experienced by nodes in surface B ($\Delta \ell_{RL(surfaceB)}$), and the stress experienced by enamel in surface A ($\sigma_{en(surfaceA)}$) is equal to that experienced in surface B ($\sigma_{RL(surfaceB)}$) (see Fig. 6.1 to understand what is meant by surface A and B):

$$\Delta \ell_{en(surfaceA)} = \Delta \ell_{RL(surfaceB)}$$

$$\sigma_{en(surfaceA)} = \sigma_{RL(surfaceB)}$$

the following expression is obtained,

$$E_{RL} = E_{en} \frac{\ell_{RL}}{\ell_{en}} \quad (6.4)$$

where E_{RL} is the estimated Young's modulus for the Restrain-layer, ℓ_{RL} is the thickness of the Restrain-layer and ℓ_{en} is the thickness of enamel which is being replaced by the Restrain-layer.

The Restrain-layer must also account for the thermal expansion which the region it replaces experiences and its effect on the central part of the model. The thermal expansion coefficient, α , of a bar is given by

$$\alpha = \frac{\Delta\ell}{\ell} \frac{1}{\Delta T} \quad (6.5)$$

where $\Delta\ell$ and ℓ have the same meaning as described before and ΔT is the change in temperature. By applying Eq. 6.5 to models *Large* and *TestBC1*, and considering that the temperature and displacement at surface A and B must be equal in both models

$$\begin{aligned} \Delta\ell_{en(surfaceA)} &= \ell_{RL(surfaceB)} \\ T_{en} &= T_{RL} \end{aligned}$$

an expression to estimate the expansion coefficient of the Restrain-Layer, α_{RL} , as a function of the expansion coefficient of enamel, α_{en} , is obtained:

$$\alpha_{RL} = \alpha_{en} \frac{\ell_{en}}{\ell_{RL}} \quad (6.6)$$

Only the thermal expansion coefficients along the X and Y directions ($\alpha_{RL,xx}$ and $\alpha_{RL,yy}$) are scaled according to Eq. 6.6 because the Lateral Restrain-layer only deals with the reduction in the cross-section of the model.

Note that, since model *TestBC1* has the same height as model *Large*, only a lateral Restrain-layer is used. Because a model that attempts to simulate enamel from a tooth will not only be less wide but also *shorter* than the real thing, the question that arises is: what other BC's would be necessary for a model which is smaller than the original in all three dimensions? To answer it, a second test

model (*TestBC2*, with dimensions $3.1 \times 3.1 \times 1.3 \mu\text{m}^3$) was developed. Model *TestBC2* also serves the purpose of determining whether the BC's perform their function adequately when the model is one order of magnitude smaller than the original.

Clearly, a model that is both shorter and less wide than the original it intends to simulate will need both a Lateral Restrain-layer (LRL) and a Bottom Restrain-layer (BRL) so that adequate boundary conditions can be imposed. To obtain the material properties for the Bottom Restrain-layer, eqs. 6.4 and 6.6 should be used; the only difference is that only the expansion coefficient along the Z direction is scaled in this case. The linear dimensions of the Restrain-layers for models *TestBC1* and *TestBC2* and the linear dimensions of the material in model *Large* that they attempt to replace can be found in Table 6.3.

6.1.1.2 Boundary conditions for thermal analyzes

Model *Large* represents a piece of material which is thermally insulated from its surroundings by the lateral and bottom surfaces, at the center of a laser spot which is much wider than the cross-section of the model. At the same time, the laser spot (radius = 0.2 mm) is much larger than the optical penetration depth at $\lambda = 10.6 \mu\text{m}$ in enamel ($12 \mu\text{m}$). Therefore, the temperature gradient and, consequently, the heat transfer along XY (the direction parallel to the surface on which the laser shines) in all three models will be negligible. The top surface is in contact with the atmosphere, but heat losses by radiation and convection during $250 \mu\text{s}$ can be expected to be significantly smaller than the heat diffused into the material. For these reasons, all models have adiabatic BCs at the external surfaces during the thermal analysis.

If the model is shorter than the reference, as is the case in *TestBC2*, then adiabatic boundary conditions are not sufficient: it is necessary to adequately simulate the heat transfer occurring along OZ. This implies that the Bottom Restrain-layer must act as a heat sink (i.e., it must have approximately the same mass as the material it attempts to replace). At the same time, heat must diffuse along the thickness of the Bottom Restrain-layer in the same time period it would diffuse along the thickness of material it replaces, which means that the thermal conductivity of the Bottom Restrain-layer must be scaled using the equations that will now be derived.

According to the general diffusion equation [2], the heat flux per unit area ($dQ/(A dt)$) is proportional to the thermal conductivity, κ , of the material and the

Model	<i>Large</i>	<i>TestBC1</i>	<i>TestBC2</i>
Total dimensions of model (μm^3)	$65 \times 65 \times 20$	$19 \times 19 \times 20$	$3.1 \times 3.1 \times 1.3$
Number of nodes	204364	21762	49392
Number of elements	192296	19500	45387
L_{LRL} (μm)	Not applicable	2.3	0.8
ℓ_{en} (μm)	Not applicable	25.3	31.75
Δz_{BRL} (μm)	Not applicable	Not applicable	0.12
Δz_{en} (μm)	Not applicable	Not applicable	18.83

Table 6.3: Geometrical parameters for models *Large*, *TestBC1* and *TestBC2*. ℓ_{en} and Δz_{en} correspond to the thickness of enamel in model *Large* that the Lateral Restrain-layer (LRL) and the Bottom Restrain-layer (BLR), respectively, are replacing. ℓ_{LRL} and ℓ_{en} are identified in Fig. 6.1.

spatial gradient of the temperature. As explained before, the spatial gradient of the temperature can be considered in this case to be dT/dz .

$$\frac{dQ}{A dt} = -\kappa \frac{dT}{dz} \quad (6.7)$$

If the Bottom Restrain-layer is to be equivalent to a certain thickness of enamel, Δz_{en} , then the heat flux per unit area through the Bottom Restrain-layer of length Δz_{BRL} must be equivalent to the heat flux per unit area through Δz_{en} .

$$-\kappa_{BRL} \frac{\Delta T_{BRL}}{\Delta z_{BRL}} = -\kappa_{en} \frac{\Delta T_{en}}{\Delta z_{en}} \quad (6.8)$$

where κ_{en} is the thermal conductivity of enamel and κ_{BRL} is the thermal conductivity of the Bottom Restrain-layer. Simultaneously, the temperature difference along Δz_{en} in model *Large* must be the same as along Δz_{BRL} in model *TestBC2*. Therefore, it is possible to estimate the conductivity of the Bottom Restrain-layer according to:

$$\kappa_{BRL} = \kappa_{en} \frac{\Delta z_{BRL}}{\Delta z_{en}} \quad (6.9)$$

6.1.2 Results and discussion

The heat transfer simulations

For the purposes of assessing the performance of the BC's developed here, sev-

eral thermal and mechanical simulations were performed. Simulations for models *TestBC1* and *TestBC2* were performed either with or without the BC's as described above. Note that the outer nodes at the lateral and bottom surfaces in all mechanical simulations were fixed. The purpose of performing simulations using models *TestBC1* and *TestBC2* without using the appropriate BC's was to assess in what way the BC's in fact modify the results obtained using the *TestBC* models. A summary of the relevant differences between the simulations performed can be found in Table 6.4.

Name	Model	BC's
Large_ref	<i>Large</i>	Not applicable
TestBC1_withRL	<i>TestBC1</i>	yes
TestBC1_noRL	<i>TestBC1</i>	no
TestBC2_withRL	<i>TestBC2</i>	yes
TestBC2_noRL	<i>TestBC2</i>	no

Table 6.4: Distinguishing simulation parameters to assess the effect of using appropriate boundary conditions on the temperature and stress generated in a material.

The temperature distribution at all instants during the simulated 250 μ s is somewhat similar in all simulations, although quantitative differences occur. In all the models, the only noticeable temperature gradients occur in direction OZ, as expected, and the maximum temperature reached is around 160 °C. A temperature map for model *Large* at the end of the laser pulse in which this behavior is patent is shown in Fig. 6.2; this map is representative, from a qualitative point of view only, of the temperature maps obtained for all the models.

The temperature maps obtained for model *TestBC1* are identical to those obtained for model *Large*, which was expected given that both models have the same height. However, some important differences arise when model *TestBC2* is used with and without BC's.

Fig. 6.3 shows the temperature evolution at various nodes close to, or at, the irradiated surface and at the bottom nodes for simulations Large_ref, TestBC2_withRL and TestBC2_noRL. Because it is known that there are no appreciable gradients of temperature along the XY plane, analyzing the temperature evolution of a single node is representative of all nodes with the same z coordinate. Therefore, Fig. 6.3 illustrates the differences between the temperature maps for those models as a function of time.

It is apparent that, when the thermal BC's are not used in model *TestBC2*, the

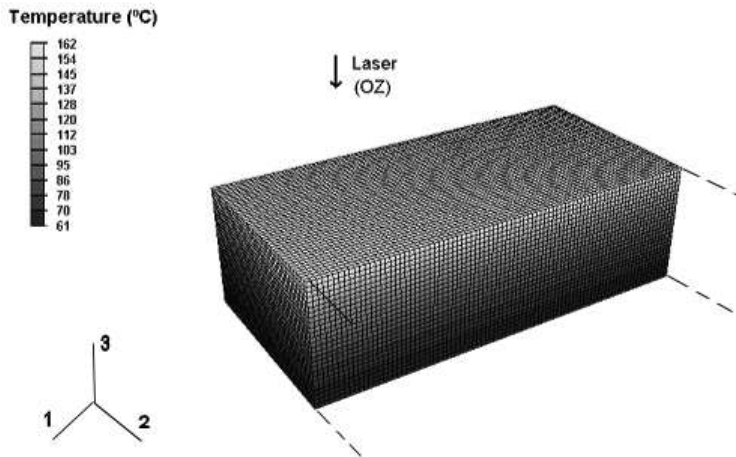


Figure 6.2: Temperature distribution for model *Large*, at the end of the laser pulse ($t = 0.35 \mu\text{s}$). Only half model is shown. Numbers 1, 2 and 3 next to the axes represent directions X, Y and Z, respectively. CO₂ laser, $I_0 = 1.2 \times 10^{10} \text{ J/m}^2/\text{s}$.

temperature evolution throughout this model differs markedly from that obtained using the reference model, model *Large*: the thermal equilibrium is reached at a temperature of 160 °C instead of close to 100 °C, and the temperature gradient between the top and the bottom of the model is not replicated. Imposing the thermal BC's on model *TestBC2* yields results much closer to those obtained using the reference model: the thermal equilibrium is reached earlier than in model *Large*, but at the temperature of 100 °C as expected, and the temperature gradient between the top and the bottom of the structure is closely mimicked. The usefulness of the thermal BC's is thus illustrated. Naturally, the mechanical simulations corresponding to model *TestBC2* which were subsequently performed used the temperatures obtained from simulation *TestBC2_withRL*.

The thermal stress simulations

In order to make sense of the results obtained from the mechanical simulations, two quantities were analyzed: the displacement and stress experienced at nodes and elements located at the center of the irradiated surface. However, instead of analyzing the components of the stress tensor individually, the equivalent Von Mises stress (VMS) was used (see ref. [62], pp. 45). The VMS is a useful quantity to which resort when analyzing results, because it combines the nine components of the stress tensor at each element into a single scalar, thus making the analysis of the stress at the structures much easier. Strictly speaking, it should not be used to analyze stress in brittle materials because normally they are more resistant in compression than in tension. Thus, the concept of "equivalent stress" does not apply to brittle materials. However, given that the models presented in this

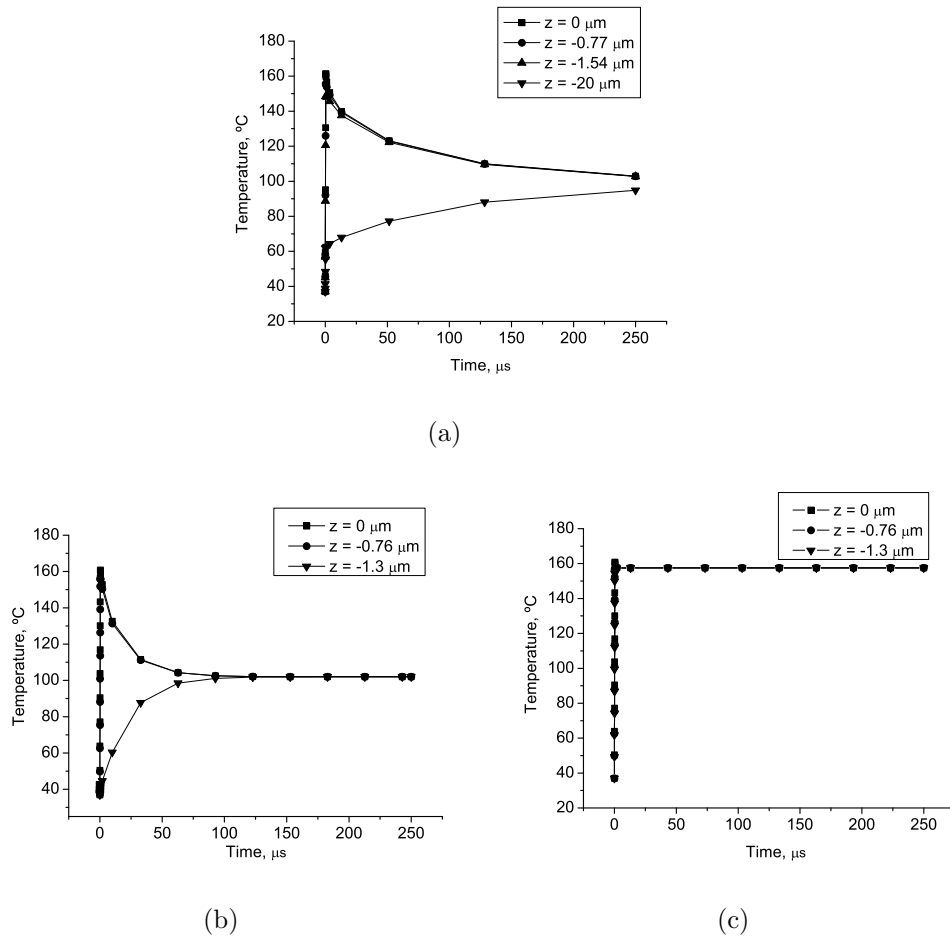


Figure 6.3: Temperature variation as a function of time for nodes located at different depths from the irradiated surface ($z = 0 \mu\text{m}$) in (a) model *Large*; (b) model *TestBC2* using the BC's described in Section 6.1.1.2, and (c) model *TestBC2* without BC's. The node with the smallest z is the bottom node for each model. CO_2 laser, $I_0 = 1.2 \times 10^{10} \text{ J/m}^2/\text{s}$.

Section describe the response of enamel in a regime where failure is not expected, and that the actual values of stress are relatively unimportant in this analysis, it was considered adequate to use it.

The VMS fields obtained at the end of $10 \mu\text{s}$ in model *Large* and model *TestBC1* (using the mechanical BC's described in subsection 6.1.1.1) are given in Fig. 6.4. It is obvious that the highest stress levels in *TestBC1* are experienced in the regions closer to the Restrain-layer. These high values have no physical significance, as can be confirmed by comparing with model *Large*. The central part of model *TestBC1*, on the other hand, shows a similar VMS field to model *Large*, at least

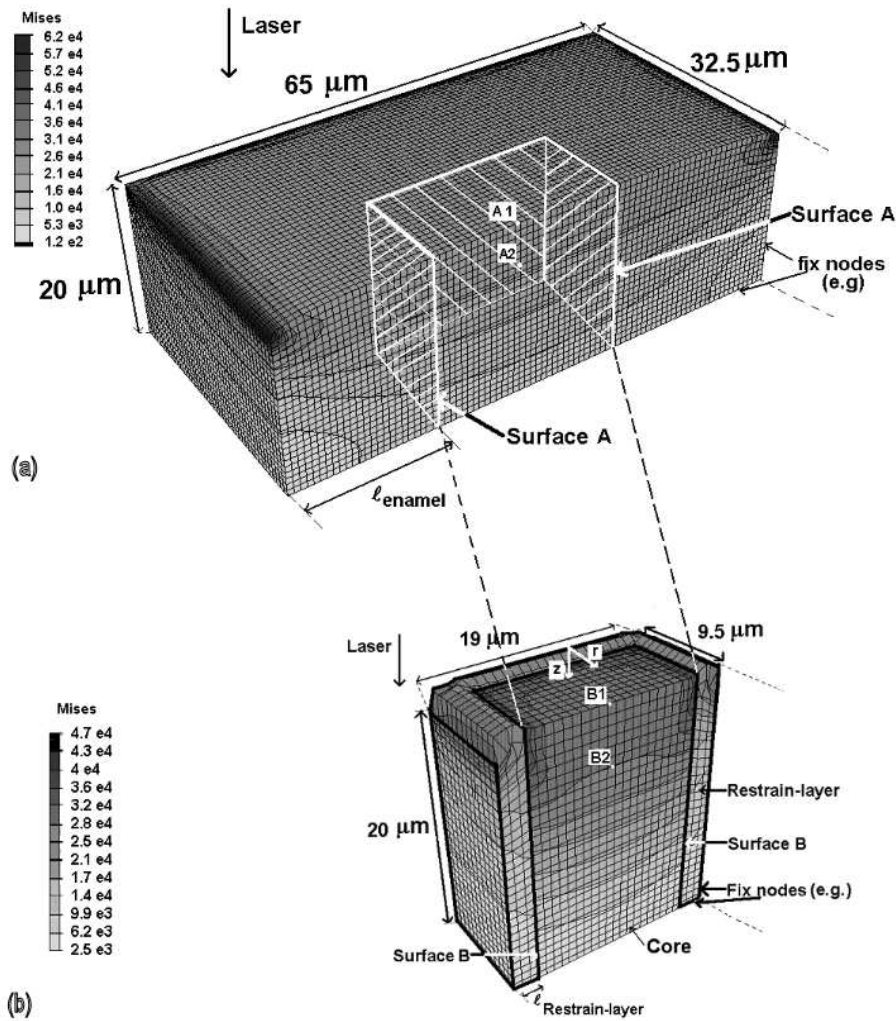
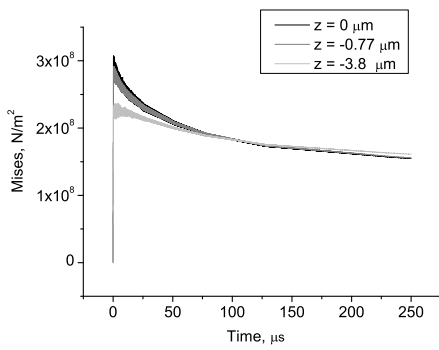
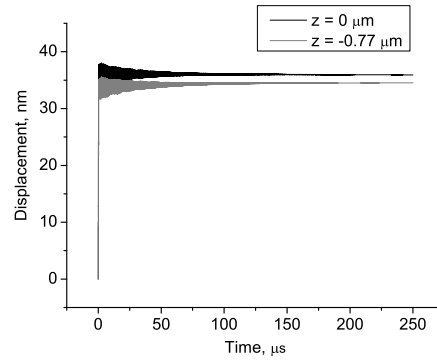


Figure 6.4: Von Mises stress (N/cm^2) for (a) model *Large* and (b) model *TestBC1*, for $t = 10 \mu\text{s}$. Regions A1, A2, B1 and B2 identify the location of the elements and nodes mentioned in Fig. 6.5. Only half model is shown in each image. CO_2 laser, $I_0 = 1.2 \times 10^{10} \text{ J}/\text{m}^2/\text{s}$.

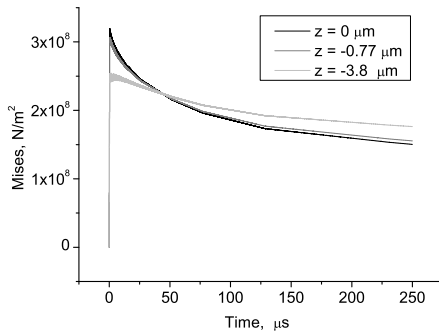
qualitatively: higher stress values are obtained at the surface of the model than deep inside it. This indicates that only the central part of the models should be analyzed in more detail. This more detailed analysis is accomplished resorting to Fig. 6.5, where the nodal displacements and the VMS stress as a function of time and depth for models *Large* and *TestBC1* are given.



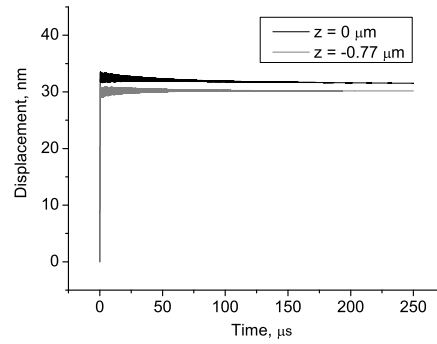
(a) VMS as a function of time for three elements in regions A1 and A2 of model *Large*.



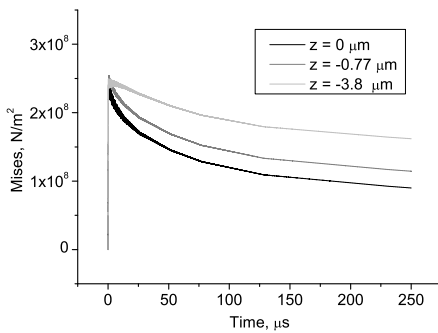
(b) Nodal displacement as a function of time for two nodes in regions A1 of model *Large*.



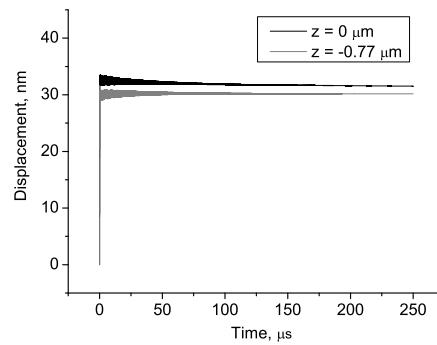
(c) VMS as a function of time for three elements in regions B1 and B2 of model *TestBC1*, using appropriate BC's.



(d) Nodal displacement as a function of time for two nodes in region B1 of model *TestBC1*, using appropriate BC's.



(e) VMS as a function of time for three elements in regions B1 and B2 of model *TestBC1*, *not* using appropriate BC's.



(f) Nodal displacement as a function of time for two nodes in region B1 *not* using appropriate BC's.

Figure 6.5: Comparing the nodal displacement and VMS values for models *Large*, *TestBC1* using appropriate BC's described in Section 6.1.1.1 and *TestBC1 not* using the appropriate BC's. The location of regions A1, A2, B1 and B2 is given in Fig. 6.4.

It is apparent that the nodal displacements obtained with model *TestBC1* behave in a qualitatively similar manner to those obtained with Model *Large*, regardless of the use or not of the appropriate BC's. The magnitude of the nodal displacement for model *TestBC1* is slightly smaller ($\simeq -10\%$) than, although of the same order of magnitude of, model *Large*, again not being dependent on the use of the appropriate BC's. The influence of the BC's used in model *TestBC1* is significantly more visible on the stress results: the dynamic evolution of the stress values at the center of model *TestBC1* is qualitatively identical and quantitatively very similar to model *Large*, when the appropriate BC's are used. When the appropriate BC's are not used, *TestBC1* is unable to reproduce even the qualitative behavior of the VMS in model *Large*: elements deeper in the structure consistently experience larger values of VMS, unlike what occurs in the reference simulation, in which the top elements experience the highest values of stress in the first 100 μs . When the appropriate BC's are used, both the maximum values of VMS and the VMS obtained at the end of 250 μs for *TestBC1* are much closer (they differ less than 20%) to those observed in model *Large* than when the appropriate BC's are not used, where differences can be higher than 40 %. These quantitative results are illustrated in Table 6.5. The difference in the VMS between *TestBC1* us-

Model	Depth in the model (μm)	Max. VMS ($\times 10^8 \text{ N/m}^2$)	Av. VMS between 200 and 250 μs ($\times 10^8 \text{ N/m}^2$)
<i>Large</i>		3.1	1.6
<i>TestBC1</i> (BC)	0	3.2	1.5
<i>TestBC1</i>		2.4	0.9
<i>Large</i>		2.9	1.6
<i>TestBC1</i> (BC)	-0.77	3.1	1.6
<i>TestBC1</i>		2.5	1.2
<i>Large</i>		2.2	1.6
<i>TestBC1</i> (BC)	-3.8	2.5	1.8
<i>TestBC1</i>		2.4	1.7

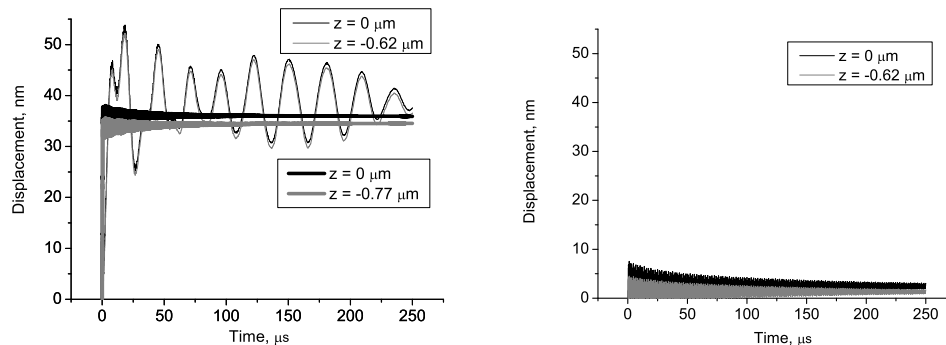
Table 6.5: Maximum and average Von Mises stress at the end of 250 μs for several elements in models *Large* and *TestBC1*.

ing appropriate BC's and the reference model does tend to increase with depth, which indicates that care must be used when interpreting results from regions deep inside the model, particularly from a quantitative perspective. The BC's were further tested by extracting the natural frequencies of vibration of models *Large* and *TestBC1* with and without the appropriate BC's. It was observed that the domi-

nant natural frequencies of vibration for model *Large* are around 1-15 MHz ($\sim 70\%$ of all natural frequencies extracted). When model *TestBC1* is used without adequate BC's, its natural frequencies lie between 15 and 25 MHz ($\sim 70\%$ of all natural frequencies extracted). When the same model is used with appropriate BC's, 80% of its natural frequencies lie between 8.5 and 10 MHz, which indicates that the BC's do succeed, at least partially, in reproducing the dynamic response of model *Large*; only its low frequency response is not reproduced.

The results obtained with model *TestBC1* indicate that the BC's applied to this model by modifying the material parameters for the Restrain-layers allow it to replicate the results obtained at the center of model *Large*. The BC's are simple in conception and easy to apply to any model of the nature of those presented here, in which material can be described by linear relationships such as those in eq. 6.3. However, it is important to investigate how the BC's perform when used in a model (model *TestBC2*) one order of magnitude smaller than the reference model. The analysis of the results obtained with model *TestBC2* is the subject of the next few lines.

The nodal displacements as a function of time experienced by two nodes located at the center of the irradiated face of model *TestBC2* at different depths are given in Fig. 6.6. To facilitate comparisons, the nodal displacements for model *Large*



(a) Nodal displacement as a function of time for two nodes at the center of the irradiated surface and different depths for model *TestBC2*, using appropriate BC's (narrow lines) and model *Large* (thick lines).
 (b) Nodal displacement as a function of time for two nodes at the center of the irradiated surface and different depths for model *TestBC2*, *not* using appropriate BC's.

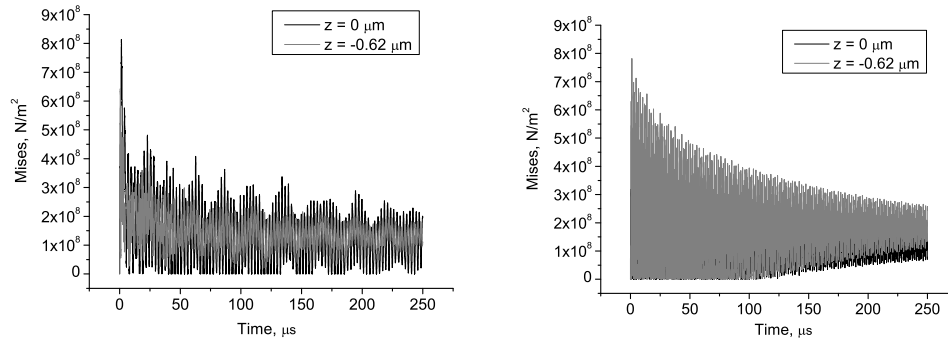
Figure 6.6: Comparing the nodal displacements as a function of time for models *Large* and *TestBC2*.

are again presented. Clearly, applying adequate boundary conditions allows model

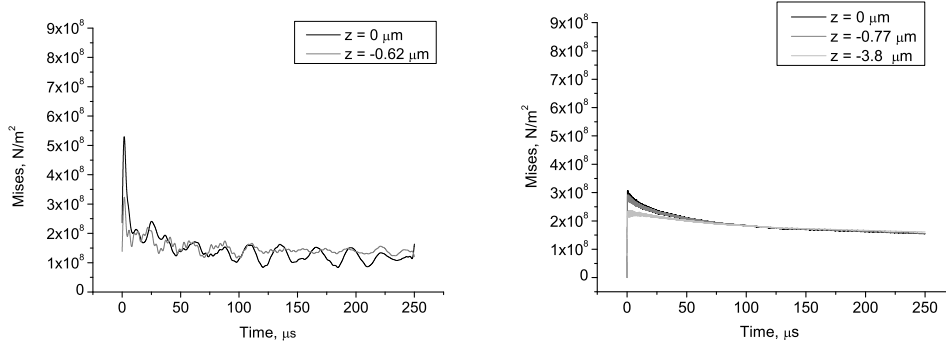
TestBC2 to more closely replicate the nodal displacements experienced by model *Large*, although it also increases the amplitude of those vibrations and introduces lower vibrational frequencies.

As for the VMS levels experienced at the center of model *TestBC2*, some representative values are given in Fig. 6.7 as a function of time. When appropriate BC's are not used, the VMS at the center of model *TestBC2* oscillates with very high amplitude and frequency; the results clearly do not replicate those obtained using model *Large*. When appropriate BC's are used, the VMS at the center of model *Large* still oscillates with high amplitude and frequency, being closer to (although still several times higher than) that experienced at the center of model *Large*. Natural frequency extraction analyzes confirm that model *TestBC2* does not have similar natural frequencies as model *Large*. This could induce readers to think that the BC's are not doing much good here, and that they could be discarded without significant loss. However, on a closer look one finds that it is not so, that the BC's allow model *TestBC2* to behave more closely to model *Large*, from a quantitative and, more important, from a qualitative point of view. For example, some of the qualitative features of the evolution of VMS in model *Large* are reproduced in Model *TestBC2* only when appropriate BC's are used: the top element experiences a higher VMS than the element below for several tens of microseconds after the laser pulse, and then its VMS becomes lower than that of the element below. Furthermore, the *average* VMS (Fig. 6.7 c) is in fact close to that obtained in model *Large* except at the end of the laser pulse, where it reaches values significantly higher than in model *Large*. The average VMS for model *TestBC2* is also higher for the top elements than for elements below during the first 50 μs , a feature that model *TestBC2* is unable to reproduce when appropriate BC's are not used.

The results presented in this Section have thus established that the BC's described in Sections 6.1.1.1 and 6.1.1.2 allow the use of small models to investigate the dynamical thermal and mechanical response of brittle materials to microsecond-long laser pulses by infrared lasers, and suggest that simply fixing the external nodes will produce less accurate results. Also, while periodic BC's were not tested and, therefore, could not be compared to the present BC's, it is suggested that periodic BC's will perform worse than the proposed BC's because they also do not allow for lateral expansion. Quantitative and qualitative features of the response of the reference model, such as the average VMS stress and the gradient of stress along OZ at the center of the model, were reproduced even when



(a) VMS as a function of time for two elements located at different depths in model *TestBC2* using appropriate BC's. (b) VMS as a function of time for two elements located at different depths in model *TestBC2* not using appropriate BC's.



(c) VMS (smoothed using FFT) as a function of time for two elements of model *TestBC2* using appropriate BC's, located at different depths. (d) VMS as a function of time for three elements of model *Large*, located at different depths (repeated here to facilitate comparison).

Figure 6.7: Comparing the Von Mises Stress values at the center of the irradiated face for models *Large*, *TestBC2* using appropriate BC's and *TestBC2* not using the appropriate BC's.

using a model (*TestBC2*) which is one order of magnitude smaller than the reference model, provided that the appropriate BC's are used. The results also indicate that models much smaller than the original may show high amplitude stress vibrations which have no physical meaning. Therefore, particular care must be used when interpreting this type of information.

Using these BC's is not limited to investigating the response of dental enamel to the CO₂ or Er:YAG lasers, however. They can be used to investigate the response of any material (in particular brittle materials) to heating, thus avoiding the use of computationally very intensive simulations, which makes them an interesting procedure for the scientific community in general.

6.2 Influence of the enamel structure on its response to laser irradiation: the water layer models

Once the appropriate BC's had been developed and their limits of validity had been established, one could begin developing models to investigate the response of enamel to mid-infrared radiation. From the beginning of this work, one of the objectives was to assess the influence of the enamel microstructure on the temperature and stress induced in this material by a laser. Thus, the first task was to build a model that included enamel's microstructure.

Since rods (prisms) are the building blocks of enamel at the micrometer scale, the work began by developing a model of a single enamel rod. The initial rod model that was developed had a square cross-section and a length of 100 μm . The inner core of the rods had the physical properties of HA at room temperature and was surrounded by a thin layer, representing the water/organic matrix, to which the physical properties of water at room temperature were attributed.

Several heat transfer analyzes were performed using this model, in order to investigate the effects of model parameters in the temperature distribution maps, such as the cross-section geometry, the number and dimensions of finite elements, and the number and duration of time steps. The results suggested that the temperature profiles are strongly influenced by cross-section geometry and that a square cross-section was an inappropriate representation of a rod. Therefore, several other rod models with different cross-section geometries and meshes were built and tested. The model that performed better was the one that resembled the shape of enamel rods more closely and can be seen in Fig. 6.8: it has a mineral core which is surrounded by a thin layer of water. Once the optimal basic three-dimensional structure was designed, it was repeated so that a model that represents an ensemble of enamel rods could be obtained. This larger model will be described in detail in the next Subsection.

6.2.1 Model description

The three-dimensional model which includes the enamel rod-structure was named model *RodsWL* (WL stands for water layer) and can be seen in Fig. 6.9. Note that, based on the geometry of the model and on the mass density of the materials, the

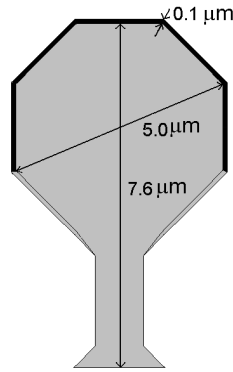


Figure 6.8: Cross-sectional view of enamel rod model. The dark area corresponds to the water/organic matrix at the rod sheath and the light area to the HA core. The thinner area is termed the tail or waist while the wider area is commonly described as the head of the rod.

percentage of water/organic material in the model is 4% by volume, or 1.3% by weight, which is consistent with available information about dental enamel.

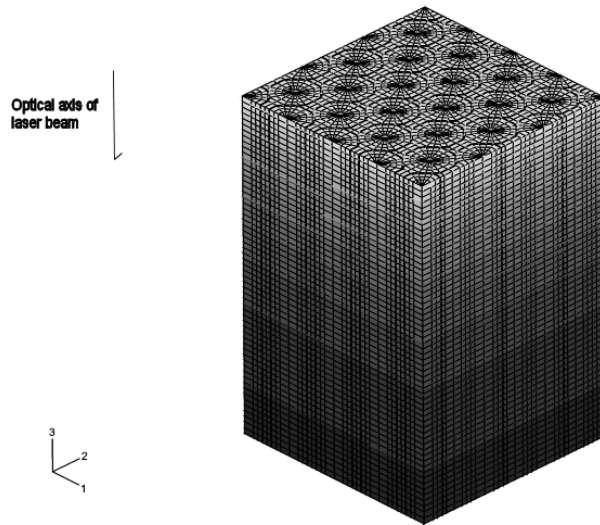


Figure 6.9: The structure of model *RodsWL*. Note that it is composed of several rods such as those shown in Fig. 6.8. Numbers 1, 2 and 3 next to the cartesian axes correspond to directions X, Y and Z, respectively. Dimensions of the model are $23 \times 23 \times 35$

Once the geometry of the model was ready, it was possible to conduct a first study to assess the influence of the microstructure on the temperature and stress in enamel when irradiated by both CO₂ and Er:YAG lasers, to compare differences induced by the different wavelengths and to evaluate the sensitivity of the results to the material parameters and to the mesh of the domain. The standard procedure was used: first, heat transfer simulations were performed in order to obtain the temperature maps as a function of time during and after a single laser pulse, for a

total time of 10 μs ; afterwards, the mechanical simulations were performed using the temperature maps obtained in the heat transfer analyzes. In order to avoid undue complexity at this early stage, the mechanical simulations performed were *not* dynamical; they were static stress simulations, and they used as input the temperature maps immediately after the end of the laser pulse. Using this type of simulation one can calculate the quasi-static stress induced by the temperature distribution obtained at the end of the laser pulse. This value represents an upper boundary for the quasi-static stress induced by the laser, which is thought to play a non-insignificant role in ablation [56]. However, in the particular case of ablation of enamel, the scientific community in general has minimized the role of the quasi-static stress relatively to that of the explosive vaporization of water. The simulations presented in this Section are thus a first attempt at getting more insight into this issue.

The laser parameters used in the set of simulations presented in this Section are given in Table 6.6. A pulse duration of 0.35 μs was considered appropriate because

Type of laser	CO ₂ (10.6 μm)	Er:YAG (2.9 μm)
Pulse duration (μs)	0.35	0.35
Maximum absorbed intensity, I_0 ($\text{J}/\text{m}^2/\text{s}$)	1.2×10^{10}	1.2×10^{10} 6.2×10^9
Number of pulses	1	1
Laser beam radius (mm)	0.2	0.2

Table 6.6: Laser parameters used in simulations that assess the effect of wavelength, intensity, mesh and the existence of water at the rod sheath on the temperature and static stress maps.

it is consistent, as mentioned before, with the duration of the micropulses in a free-running laser, for which the most abundant experimental information is available. It was decided to restrict this investigation to a single laser pulse. There would be no point in attempting to simulate the effect of several laser pulses since the material model used is not capable of simulating damage such as cracking, or indeed any kind of behavior other than linear-elastic. In order to ensure that subablative conditions were used, the laser fluence per pulse was given a value (0.42 J/cm^2 or 0.22 J/cm^2) significantly lower than the ablation threshold of enamel at these wavelengths (2 – 3 J/cm^2 for a CO₂ laser with a 2 μs laser pulse [132], 9 – 11 J/cm^2 for a free-running Er:YAG laser without water cooling [118]). This ensures that the maximum temperatures reached at the center of the laser spot are in the 150 – 170 $^\circ\text{C}$ range and, consequently, that only small deformations occur in the material

and that the material parameters should not vary significantly from their room temperature values. The laser spot radius (at $1/e^2$ of the incident intensity) was chosen to be 0.2 mm, since the tunnelling technique described in Chapter 1 requires tunnels of approximately 0.5 mm in diameter. All the incident radiation at $\lambda = 10.6 \mu\text{m}$ and $\lambda = 2.94 \mu\text{m}$ can be thought to be absorbed and transformed into internal kinetic energy of the enamel. The reflectivity of enamel at these wavelengths is very low and, since the absorption coefficient is high, scattering should not significantly alter the shape of the heated volume of material. Therefore, eqs. 6.1 and 6.2 can be considered valid and were used for both wavelengths. The optical axis of the laser beam is OZ, and the irradiated surface of the model lies in the XY plane (see Fig. 6.9).

The material parameters used in all the models in this Section are given in Table 6.7. While deciding which parameters to choose in order to model the

	Water and organic	Mineral	Bottom RL	Lateral RL_1	Lateral RL_2
Abs. coeff. at $2.94 \mu\text{m}$ ($\times 10^4 \text{ m}^{-1}$)	122.5[123]	3	3	NA	NA
Abs. coeff. at $10.6 \mu\text{m}$ ($\times 10^4 \text{ m}^{-1}$)	8.25	8.25 [69]	8.25	NA	NA
κ (J/(s.m. $^\circ\text{C}$))	0.6 [147]	1.3 [143]	1.3×10^{-4}	NA	NA
Spec. heat ($\times 10^2 \text{ J/kg/}^\circ\text{C}$)	42 (313 K) 53 (553 K)	8.8 [143]	8.8	NA	NA
E ($\times 10^6 \text{ N/m}^2$)	0.1 [148]	110000 [144]	1.5	55	73
ν	0.28	0.28 [145]	0.28	0.28	0.28
α ($\times 10^{-5} \text{ K}^{-1}$)	50 [147]	1.6 [146]	1.6 (x) 1.6 (y) 32 (z)	110 (x) 110 (y) 1.6 (z)	83 (x) 83 (y) 1.6 (z)
ρ ($\times 10^3 \text{ kg/m}^3$)	0.99 [147]	3.1 [142]	3100*	3.1	3.1

Table 6.7: Material properties employed in the models used to investigate the effect of wavelength, intensity, mesh and the existence of water at the rod sheath, on the temperature and static stress maps. Note that the parameters used only in the heat transfer simulations are not given for the Restrain-layers, since these are only used for the mechanical simulations. Also, the thermal expansion coefficient of the Restrain-layers is given in terms of the three directions in space, and the specific heat of water is given as a function of temperature. * Only used in the heat transfer simulation, to act as a heat sink; in the mechanical simulation, the density of HA was used.

mineral component was relatively straightforward, the same could not be said for choosing how to model the water/organic part. Does the material at the pores

behave similarly to a fluid (in which case an equation of state should be used), or does it behave like a soft, solid, material like gelatin? Both approaches make sense and, in fact, both were used in different stages of the work described in this Thesis. In the simulations presented in this Section the second approach was used, since it is more simple than the first. The material properties of water in Table 6.7 are a consequence of this option.

The absorption coefficient at $\lambda = 2.94 \mu\text{m}$, the thermal conductivity, the specific heat, the mass density and the thermal expansion coefficient of the water/organic part were considered those of pure water. This was judged a valid approximation since experimental evidence indicates that the water is four times more abundant than the organic material in enamel. The absorption coefficient of water at this wavelength was taken as constant, which is a reasonable approximation given that the temperature will not reach very high values (see work by Shori et al. [123], already discussed in Section 4.2). The thermal conductivity of water is known to vary significantly between room temperature and $175 \text{ }^\circ\text{C}$ [147]. However, this will have no influence on the results, since the parameter governing the maximum heat diffusion from the pore is the thermal conductivity of the mineral and not of water. Therefore, the room temperature value of the thermal conductivity of water was used. The specific heat of water was given as a function of temperature, since it varies quite significantly in the range of temperatures simulated. The Young's modulus was considered that of gelatin and the Poisson's ratio was given the value of 0.28 since this quantity only varies between 0 and 0.5 for standard materials, and in fact lies normally in the 0.25 – 0.35 range¹. The absorption coefficient of water at $10.6 \mu\text{m}$ is very close to that of human dental enamel and does not vary to any significant extent with temperature [123], so the value for enamel was used for both the organic and the mineral parts of the model.

The absorption coefficient of HA, μ_{HA} , at $\lambda = 2.94 \mu\text{m}$ was not available in the literature, to the best of the author's knowledge, so it was estimated based on the volume percentage of organic material (4%) and the absorption coefficient of enamel ($\mu_{enamel} = 800 \text{ cm}^{-1}$ [63]) and water ($\mu_{water} = 12250 \text{ cm}^{-1}$ [123]) at this wavelength, according to the expression:

$$0.04 \times \mu_{water} + 0.96 \times \mu_{HA} = \mu_{enamel} \quad (6.10)$$

¹Simulations were also performed in which the Poisson's ratio of the water/organic material was 0.499, to simulate a virtually incompressible material, and the results were very similar to those obtained when $\nu = 0.28$.

All the physical properties of the mineral were assigned values found in the literature for pure HA. No information was found with regards to the temperature dependence of these properties, so they were considered constant as a first-order approximation.

The properties of the Restrain-layers were calculated using the equations presented in Sections 6.1.1.1 and 6.1.1.2 and the geometric parameters given in Table 6.8. Parameters for two lateral Restrain-layers are given for model *Rods* because the geometry of the rods dictated that the Restrain-layer did not have the same thickness throughout the model (see Fig. 6.11). Note that the higher density of the Bottom Restrain-layer was only used during the heat transfer simulation, so that the Bottom Restrain-layer could act as a heat sink.

Model	<i>Rods</i>	<i>Cubes</i>
Total dimensions of model (μm^3)	$23 \times 23 \times 35$	$23 \times 23 \times 35$
Number of nodes	117242	198146
Number of elements	126720	187765
L_{LRL1} (μm)	2.91	2.8
L_{LRL2} (μm)	3.85	NA
ℓ_{en} (mm)	6	6
$\ell_{en,expanding}$ (mm)	0.2	0.2
κ_{en}	1.3	1.3
E_{en} (N/m^2)	1.1×10^{11}	1.1×10^{11}
Δz_{BRL} (μm)	0.6	0.56
Δz_{en+den} (mm)	6	6
$\Delta z_{en+den,expanding}$ (μm)	12	12
κ_{en+den}	1.3	1.3
E_{en+den} (N/m^2)	1.5×10^{10}	1.5×10^{10}

Table 6.8: Geometric parameters for models *Rods* and *Cubes*. See Fig. 6.11 to identify Lateral Restrain-layer 1 (LRL1) and Lateral Restrain-layer 2 (LRL2). $\ell_{en,expanding}$ corresponds to the thickness of enamel surrounding the model and which will suffer expansion, and it was given the value of the laser beam radius. $\Delta z_{en+den,expanding}$ corresponds to the thickness of enamel and dentine which will suffer expansion, and it was given the value of the optical penetration depth. The remaining quantities have been defined previously in this Thesis.

As in all the previous models, all the external nodes were fixed except those at the irradiated surface, which were free to move. The external surfaces were given adiabatic boundary conditions during the heat transfer simulations. All the nodes had an initial temperature of 37 °C, the normal body temperature, which was also

the stress-free reference temperature.

In order to evaluate the effect of the microstructure and wavelength on the response of enamel to laser radiation and to assess the sensitivity of the models to the mesh, several simulations were performed. The relevant parameters for the most representative ones are given in Table 6.9. Three of them use model *Rods* exactly as described until now in this Section, but two others have some important differences. One of the simulations that differs from what was described previously is called *RodsHom_CO2_1.2e10*. It uses the rod model and CO₂ laser parameters with an incident intensity of 1.2×10^{10} , but the model contains no water: the elements composing the thin layer surrounding the enamel rod were given the properties of HA also, and not those of water as was described previously (“Hom“ stands for “homogenous“). This model was created because, if the influence of the microstructure and the water at the rod sheath is to be assessed, it is necessary to compare the results with a reference in which these features are not present. The second simulation that differs from those described previously in this Section is called *CubesHom_CO2_1.2e10*. This simulation uses a different geometrical model, named model *Cubes*. This model has the same total dimensions of the *Rods* model but is composed only of a large number of cubic elements. It thus has a high-density and very regular mesh. Model *Cubes* was created to assess whether the high aspect-ratio elements present in the *Rods* model introduced high levels of uncertainty in the results. This assessment can be made by comparing its results with those obtained with the *RodsHom_CO2_1.2e10* simulation.

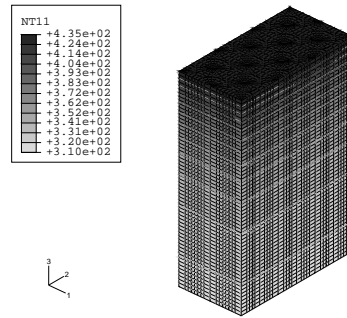
Name	Wavelength	Water	Laser intensity
<i>CubesHom_CO2_1.2e10</i>	CO ₂	no	1.2×10^{10}
<i>RodsHom_CO2_1.2e10</i>	CO ₂	no	1.2×10^{10}
<i>RodsWL_CO2_1.2e10</i>	CO ₂	yes	1.2×10^{10}
<i>RodsWL_Er_1.2e10</i>	Er:YAG	yes	1.2×10^{10}
<i>RodsWL_Er_6.2e9</i>	Er:YAG	yes	6.2×10^9

Table 6.9: Relevant simulation parameters to assess the effect of wavelength, intensity, mesh and the existence of water at the rod sheath on the temperature and static stress maps.

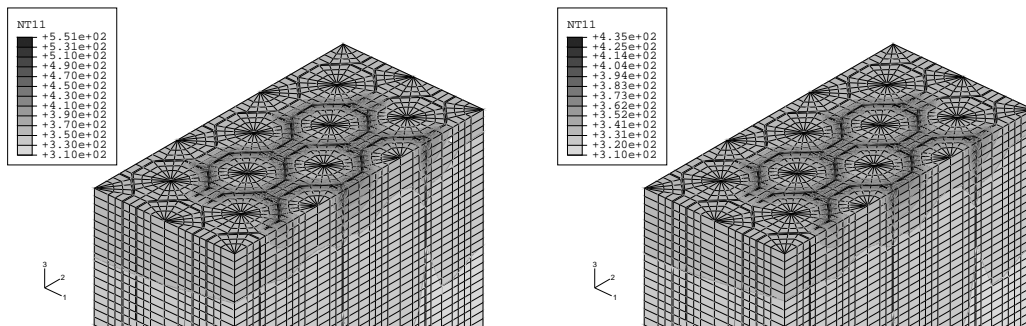
6.2.2 Results and discussion

6.2.2.1 The influence of the microstructure and the laser wavelength

The temperature distribution at the end of the laser pulse for four of the five simulations performed is given in Fig. 6.10. The existence or not of water seems



(a) Nodal temperature for simulations RodsHom_CO2_1.2e10 and RodsWL_CO2_1.2e10 at the end of the $0.35 \mu\text{s}$ laser pulse.



(b) Nodal temperature for simulation RodsWL_Er_1.2e10 at the end of the $0.35 \mu\text{s}$ laser pulse.

(c) Nodal temperature for simulation RodsWL_Er_6.2e9 at the end of the $0.35 \mu\text{s}$ laser pulse.

Figure 6.10: Temperature (in kelvin) maps at the end of the laser pulse for models with a water layer and a model composed only of mineral. The numbers 1, 2 and 3 next to the cartesian axes correspond to directions X, Y and Z, respectively.

to have no effect on the temperature maps when the CO_2 laser is used, which is not surprising since the water/organic and the mineral were assigned the same absorption coefficient at this wavelength. Therefore, the temperature distribution for simulations RodsHom_CO2_1.2e10 and RodsWL_CO2_1.2e10 is given in the same image, Fig. 6.10 a. For the CO_2 laser, the temperature is a function of depth only, and the maximum temperature reached (at the end of the laser pulse) is $\simeq 160 \text{ }^\circ\text{C}$, at the top surface. When the same laser intensity is used for the

Er:YAG laser, a much higher temperature (278 °C) is induced, as can be seen in Fig. 6.10 b. This is not unexpected, given that the water has an extremely high absorption coefficient at $\lambda = 2.9 \mu\text{m}$. Using only half the laser intensity, the Er:YAG laser induces a similar maximum temperature (for the water regions only) as that experienced for the CO₂ laser (see Fig. 6.10). The Er:YAG laser induces a lower temperature in HA than in water, which means that the temperature distribution obtained is highly inhomogeneous along the XY plane. In fact, at the end of the Er:YAG laser pulse there is a temperature difference of $\simeq 70 \text{ }^\circ\text{C}$ between the center of the enamel rods and the water/organic sheath, which means that the temperature gradient along the XY plane can be as high as $\simeq 30 \text{ }^\circ\text{C}/\mu\text{m}$. This high temperature gradient should have consequences in terms of the stress generated in the enamel.

The displacement maps obtained for the CO₂ and the Er:YAG laser (for simulations in which a water layer was included) can be seen in Fig. 6.11. They

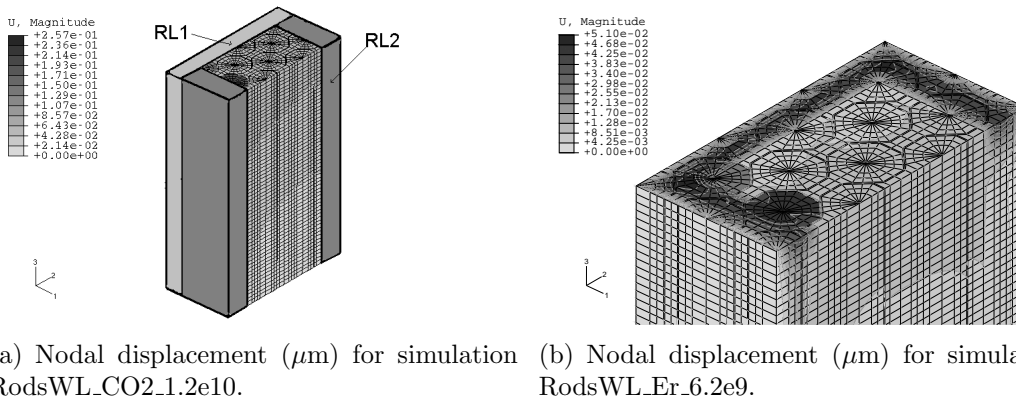


Figure 6.11: Nodal displacement at the end of $0.35 \mu\text{s}$ for models with a water layer. Numbers 1, 2 and 3 near the cartesian axes correspond to directions X, Y and Z, respectively. Only half of the model is visible in each image, so that the displacements at the center of the structure can be analyzed.

are qualitatively very similar. At the center of the model structure, larger displacements are obtained using the CO₂ laser than using the Er:YAG. This is not surprising, even though the maximum temperatures reached (at the water layers) are the same, because the temperature rise suffered by HA is much higher when using the CO₂ laser than when using the Er:YAG. This causes the HA to dilate more in the CO₂ case than in the Er:YAG case.

In order to analyze the stress maps, and because one is now interested in determining the areas most prone to cracking, the minimum and maximum principal

stresses were used instead of the Von Mises stress. Brittle materials typically fail in tension before they fail in compression, and therefore it is more appropriate to separately determine the areas in the models where the tensile and compressive stresses are maximum, rather than just determining the areas where the equivalent stress is higher ². The maps of the minimum and maximum principal stresses throughout the structure (when a water layer was used) are given in Fig. 6.12. The most striking feature in these maps is the fact that the elements located close

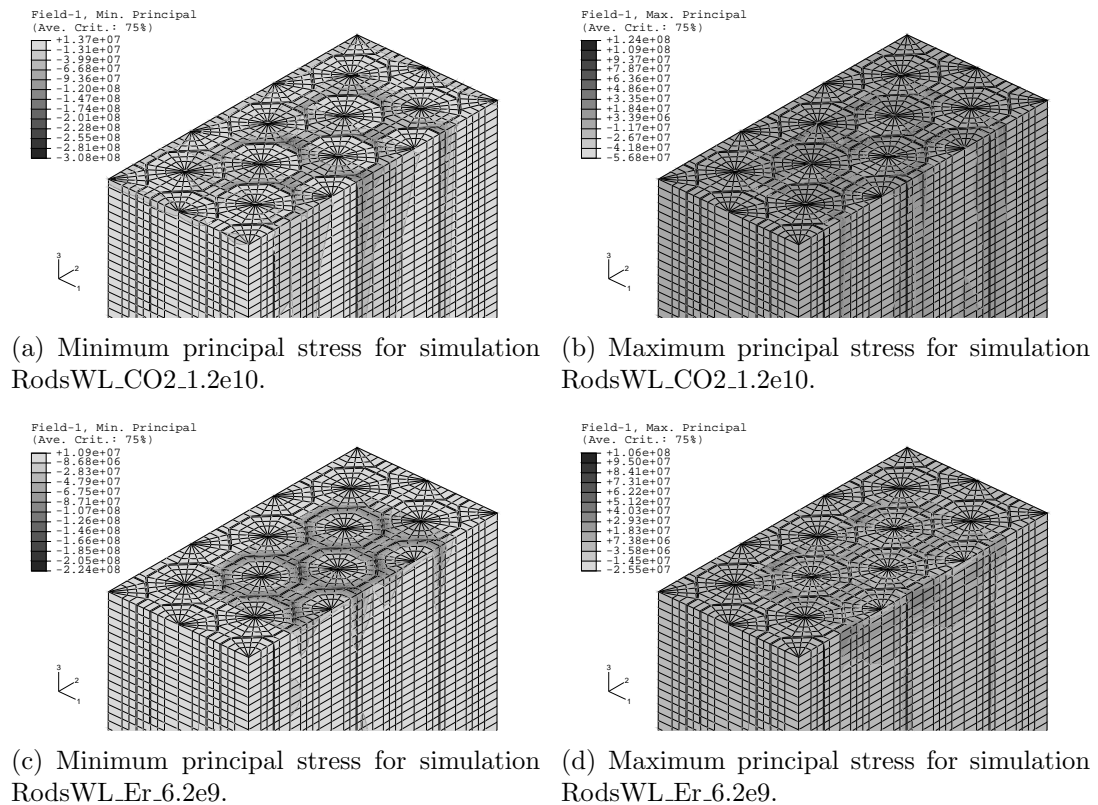


Figure 6.12: Minimum and maximum principal quasi-static stress (N/m^2) at the end of the $0.35 \mu\text{s}$ laser pulse for models with a water layer surrounding each rod head. A positive value represents tensile stress and a negative one represents compressive stress. Numbers 1, 2 and 3 near the cartesian axes correspond to directions X, Y and Z, respectively. Only half of the model is visible in each image, so that the stress at the center of the structure can be analyzed.

to the rod sheath and, in particular, those composing the tail of the rods experience the highest stress values (see Fig. 6.12), unlike what happens when a water

²In fact, the author compared the maximum and minimum principal stress maps to the VMS maps, and found that the VMS is a reasonably good indicator of the regions with the higher stresses. Therefore, some results in subsequent Sections are analyzed resorting to the VMS, for the sake of simplicity.

layer does not surround each rod head (see Fig. 6.13 a, b). The stress levels at

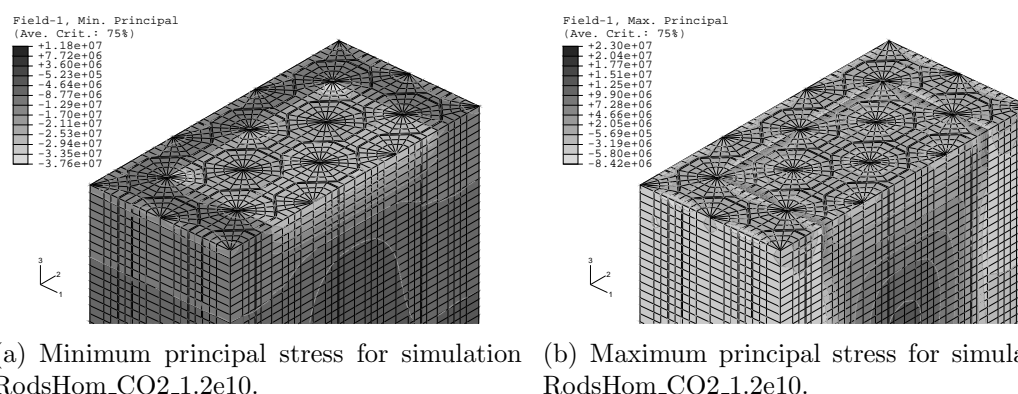


Figure 6.13: Minimum and maximum principal quasi-static stress (N/m^2) at the end of the $0.35 \mu\text{s}$ laser pulse for models without a water layer surrounding each rod head. A positive value represents tensile stress and a negative one represents compressive stress. Numbers 1, 2 and 3 near the cartesian axes correspond to directions X, Y and Z, respectively. Only half of the model is visible in each image, so that the stress at the center of the structure can be analyzed.

the rod tail are also higher (by one order of magnitude!) when the rod heads are surrounded by a water layer than when the water is not present. Furthermore, the stress values at the rod head seem to be higher for the Er:YAG laser than for the CO_2 laser (at the rod head), despite the fact that they attain the same maximum temperature at the rod sheath. This result is consistent with experimental evidence indicating that Er:YAG laser pulses can easily induce severe cracking in enamel even at sub-ablative fluences [94], unlike for the CO_2 laser. This may be a consequence of the high thermal gradients between the center and the sheath of the rod generated when the Er:YAG laser is used, which do not exist when the CO_2 laser is used. This qualitative analysis is supported by the data in Table 6.10, which consists of the minimum and maximum principal stress in elements located close to the XY center of each model and at various depths. Some of the elements are located at the head and others at the tail of the rods. This data indicates something that is not easy to detect by simply having a look at the stress maps: that the stress at the rod tail is always higher than the stress at the rod head when the water layer is present, which suggests that the tail of the enamel rods is mechanically more prone to cracking than the head.

Curiously, the models indicate that very high stresses can be generated in enamel solely due to the expansion of liquid water, without any vaporization taking place: as mentioned before, the top values of stress are raised by one order of

Depth (μm)		RodsWL_CO2_1.2e10		RodsWL_Er_6.2e90		RodsHom_CO2_1.2e10	
		Max. Pr. (N/m^2)	Min. Pr. (N/m^2)	Max. Pr. (N/m^2)	Min. Pr. (N/m^2)	Max. Pr. (N/m^2)	Min. Pr. (N/m^2)
0	H	1.2E6	-2.3E7	5.2E6	-9.7E6	3.0E6	-2.6E7
	T	1.9E7	-8.4E7	1.8E7	-2.7E7	9.5E4	-2.8E7
-0.58	H	3.1E6	-2.2E7	1.4E7	1.7E6	5.0E6	-2.2E7
	T	1.9E7	-7.8E7	2.4E7	-1.1E7	4.4E5	-2.4E7
-4.1	H	2.5E6	-1.1E7	7.4E6	-9.2E5	9.0E6	-5.4E6
	T	1.2E7	-5.1E7	5.3E6	-1.6E6	6.3E6	-5.4E6
-6.4	H	3.6E6	-8.2E6	2.8E6	-2.2E6	1.1E7	-3.5E6
	T	9.7E6	-4.0E7	3.7E6	-4.3E6	1.0E7	-2.9E6

Table 6.10: Minimum and maximum principal quasi-static stress at the end of the $0.35 \mu\text{s}$ laser pulse for *Rods* models with a water layer. The letters *H* and *T* correspond to elements located at the head and at the tail of the rod, respectively.

magnitude when the rod sheath includes water. Now, one could think that at the temperatures reached in these models water vaporization would take place, which would make the present models inadequate and the conclusions untrustworthy. In fact, strong experimental evidence suggests that assuming the water will not vaporize at a temperature of $160 - 280 \text{ }^\circ\text{C}$ is very reasonable, given that heating takes place rapidly. Liquid water has been shown to be heated up to $300 \text{ }^\circ\text{C}$ at normal pressure without vaporizing, provided that the heating takes place rapidly as is the case here [149, 150].

While the actual values of stress listed in Table 6.10 should not be taken at face value because of the uncertainty associated with the approximations made when developing the model, it is nevertheless interesting that the stresses generated are comparable to, or even greater than, the ultimate tensile and compressive strength of HA, given in Table. 6.11. Although it is possible that the stress is overestimated in the results presented here, these nevertheless suggest that the quasi-static stress at the end of the laser pulse will reach high values and should play a role in ablation even before water vaporization takes place.

	Ultimate tensile strength (MPa)	Ultimate compressive strength (MPa)
Enamel	10.3 [151]	384 [152]
HA	115 [146]	917 [146]

Table 6.11: Ultimate tensile and compressive strength for enamel and hydroxyapatite.

These results indicate that, even under soft radiation conditions, the Er:YAG and CO₂ lasers should lead to qualitatively different temperature distributions within enamel which seem to induce different stress distributions in this material. The enamel microstructure has been shown to have an important effect on the thermally induced stresses: the locations close to the water experience much higher stress. As a consequence, the rod tails seem to have a higher tendency to fail mechanically than the rod heads.

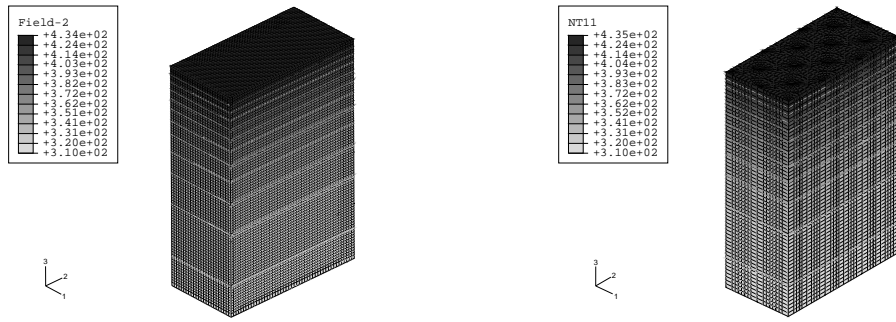
6.2.2.2 The influence of the mesh and material parameters

Once the first results were obtained and analyzed, another important question arose: how sensitive are these results to the mesh used and to the particular material parameters chosen? To answer it, several simulations were performed and compared with the reference values presented in the previous Subsection. The sensitivity of the models was tested to changes in the following parameters: shape, dimensions and number of finite elements, number of time steps, mass density, thermal conductivity, specific heat, Young's modulus and thermal expansion coefficient of the organic/water, the HA and the Restrain-layers.

To test the sensitivity of the results on the mesh, model *Cubes* was created as described previously. The temperature and stress maps obtained using model *Cubes* are given in Figs. 6.14 and 6.15. To facilitate comparison, the results obtained using identical laser and material parameters but model *Rods* (already discussed in the previous Section) are also presented.

The more irregular mesh and the high aspect-ratio elements used in the model *Rods* do not have any effect on the temperature obtained at the end of the laser pulse: the temperature maps using the *Rods* model and the *Cubes* model are identical. Simulations using meshes that were significantly coarser and finer than the one described in the previous Section were also performed, and the results are very similar to the reference values. This indicates that the mesh used in model *Rods* is acceptable as far as the thermal simulations are concerned. The stress maps obtained under the same conditions are qualitatively identical: the higher and lower stress zones are located in the same regions. From a quantitative point of view, the stress maps are not identical but are certainly very similar for both meshes. In order to illustrate this point, the minimum and maximum principal stresses at elements located at the XY center of the irradiated surface and at various depths are given in Table 6.12.

These results indicate that the mesh used for model *Rods* is adequate, and that,



(a) Nodal temperature for simulation Rod-CubesHom_CO2_1.2e10 at the end of the $0.35 \mu\text{s}$ laser pulse. (b) Nodal temperature for simulations sHom_CO2_1.2e10 and RodsWL_CO2_1.2e10 at the end of the $0.35 \mu\text{s}$ laser pulse.

Figure 6.14: Temperature (in kelvin) at the end of the $0.35 \mu\text{s}$ CO₂ laser pulse for models *RodsHom* and *CubesHom*. Numbers 1, 2 and 3 near the cartesian axes correspond to directions X, Y and Z, respectively. Only half of each model is shown so that the temperature distribution on the inside can be seen.

CubesHom_CO2_1.2e10			RodsCO2_hom_1.2e10		
Depth (μm)	Max. Pr. (N/m^2)	Min. Pr. (N/m^2)	Max. Pr. (N/m^2)	Min. Pr. (N/m^2)	Depth (μm)
-0.54	2.29E+05	-2.46E+07	4.37E+05	-2.38E+07	-0.58
-4.53	7.26E+06	-3.14E+06	6.31E+06	-5.42E+06	-4.1
-6.17	1.03E+07	-9.07E+05	1.03E+07	-2.93E+06	-6.4

Table 6.12: Minimum and maximum quasi-static principal stress values at the end of the $0.35 \mu\text{s}$ CO₂ laser pulse for models without water and using different meshes.

while the high aspect-ratio elements seem to introduce some numerical uncertainty in the results obtained with this model, results are quite acceptable.

Although all the simulations reported above were performed using ABAQUS's automatic time incrementation schemes, several other simulations were performed to assess the influence of the time-step duration on the quality of the results. It was found that increasing this duration did not modify the results to any significant extent, so the automatic time incrementation schemes were used in all the simulations presented in this Thesis.

The mass density of HA was varied between $2900 \text{ kg}/\text{m}^3$ and $3150 \text{ kg}/\text{m}^3$, an interval which reflects the uncertainty associated with the density of this material. The temperature distribution maps obtained using these values remained qualitatively identical, and the maximum temperatures reached varied by 3% compared to the reference values. The mass density of the organic/water part was varied

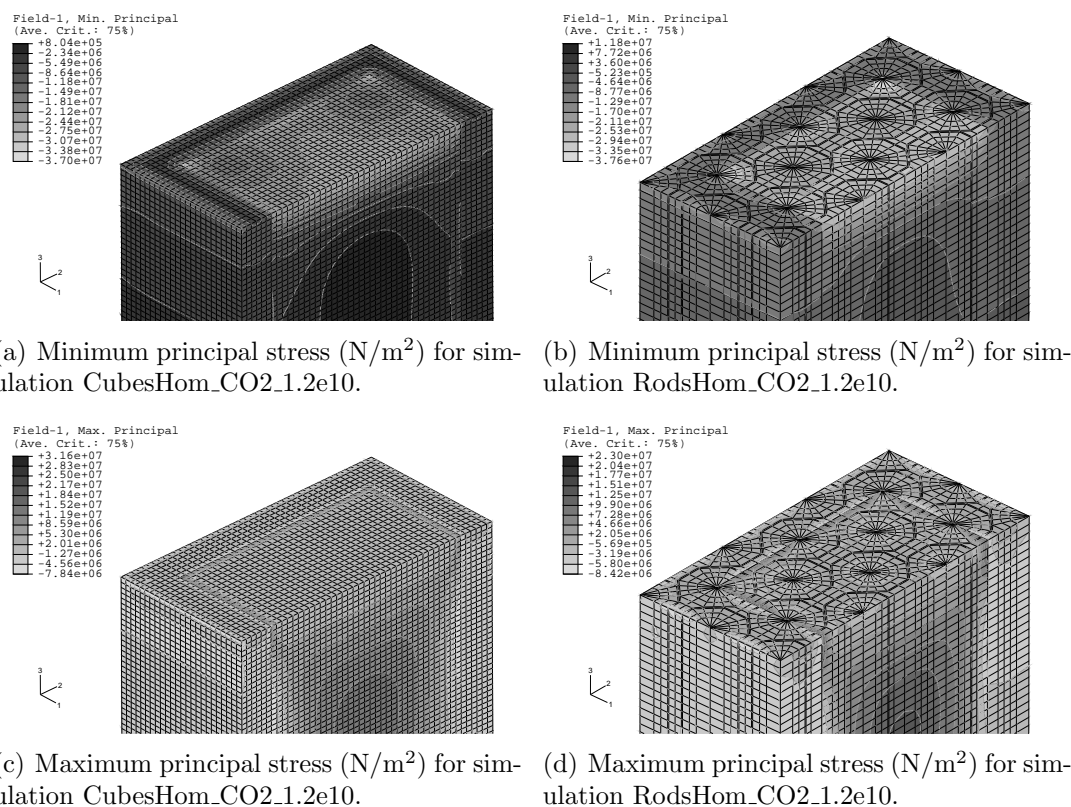


Figure 6.15: Quasi-static stress maps at the end of the $0.35 \mu\text{s}$ CO_2 laser pulse for models composed only of mineral and using different meshes. Numbers 1, 2 and 3 near the cartesian axes correspond to directions X, Y and Z, respectively. Only half of each model is shown so that the stress distribution on the inside can be seen.

between 995 kg/m^3 and 1005 kg/m^3 , also a reasonable estimate for the possible variation of this quantity for a mix of water with protein. No differences were observed on the temperature maps. Therefore, the models are not sensitive to small changes in the values of the density.

Varying the values of the thermal conductivity of water/organic and HA and the specific heat of water by $\pm 15\%$ did not induce any changes on the temperature maps, which indicates that the model is not sensitive to these parameters. Varying the specific heat of HA by $\pm 15\%$, however, led to some changes on the temperature maps; for example, the maximum temperature reached varied by $\pm 10\%$. Qualitatively, however, the temperature maps remained unchanged. The models are thus somewhat sensitive to the particular values of the specific heat of HA used but the uncertainty associated with this in no way precludes the results from being considered valid, especially from a qualitative point of view.

The values of the modulus of elasticity of the restrain layers used in the stress

analyses were varied by $\pm 20\%$ in relation to the values displayed in Table 6.7, and the stress maps obtained were qualitatively and quantitatively very similar. The Young's modulus of the mineral was varied between 95 GPa and 130 GPa. The displacement maps were not modified by the use of these values, but the stress maps did show a quantitative modification: the maximum stress observed was, in the worst case, 15% higher than the reference value. This indicates that results are sensitive to the values used for Young's modulus for the mineral, so it is important to get good estimates of this quantity. The Young's modulus of the water/organic, E_{water} , was varied by \pm one order of magnitude. Increasing E_{water} caused the stress values to decrease by 1/3 to 1/2, but decreasing this quantity had no visible effect on the stress maps. While in all situations the stress maps remained qualitatively the same, these results indicate that the quantitative results are somewhat dependent on the value of E_{water} .

The thermal expansion coefficients of water/organic and HA, α_{water} and α_{HA} , were separately varied by plus or minus one order of magnitude in relation to the values in Table 6.7. Varying α_{water} had little or no effect on the stress maps, but varying α_{HA} led to changes up to one order of magnitude in the stress values. However, the qualitative description of the stress maps remained the same. These results indicate that the model is sensitive to the thermal expansion coefficient HA from a quantitative point of view.

The results indicate that the *Rods* model is not sensitive, from a qualitative point of view, to the value of any of the material parameters that were tested. However, from a quantitative point of view, the model seems to be sensitive to the values of the thermal expansion coefficient and modulus of elasticity used for HA, which indicates that good estimates of these quantities should be obtained. Furthermore, results also indicate that the response of enamel to laser radiation may vary from sample to sample or even from location to location within the same sample, because of local variations in the mechanical properties of enamel.

6.3 Influence of water pores on the response of enamel: the macropores model

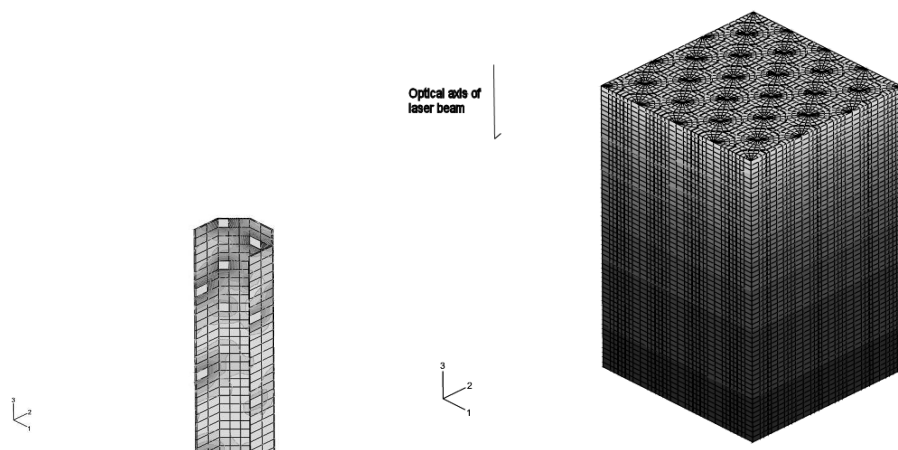
While it is known that more water exists at the boundary of the rods than on their inside, the exact fraction of water in enamel, the pore size distribution and connectivity are not known [3, 153]. The results discussed in the previous Section

represent a first attempt to ascertain the role of water in ablation, by modelling the water-rich rod sheath like a thin water-layer surrounding the rods. Even accounting for the fact that this is a somewhat crude approximation to reality, there is no getting away from the fact that the results strongly suggest the water existing in enamel should play an important role in ablation. Therefore, it was decided to continue to investigate this line of thought.

The next question to arise was: would the effect of water on the stress maps still be this evident if the water content at the rod sheath was lower? To answer this question, a new model, similar in geometry to those described in the previous Section, was developed.

6.3.1 Model description

This new model is based on the geometry of model *Rods*, but now only a few selected areas at the rod sheath – which can be considered wide and flat macropores – have the properties of water. Therefore, it differs from the previously described *Rods* models only in its total water content and distribution: the model has 0.27% v/v water, instead of 4% as model *Rods* with a water-layer. This model was called *RodsPores* (see Fig. 6.16 for the pore distribution). Each pore has



(a) The location of pores in model *RodsPores*. (b) The structure of model *RodsPores*.

Figure 6.16: The geometry of model *RodsPores*. The pores correspond to the squares that stand out in white in image (a). In (a) only the rod sheath is shown in order to make the pores visible. Numbers 1, 2 and 3 near the cartesian axes correspond to directions X, Y and Z, respectively.

length and width on the order of $1 \mu\text{m}$, and thickness of $0.1 \mu\text{m}$. The material properties assigned to the mineral and water/organic part of the models are those

in Table. 6.7, and will not be presented again. The laser parameters used are given in Table 6.13. Again, a single laser pulse of sub-ablative intensity was modelled.

Type of laser	CO ₂ (10.6 μm)	Er:YAG (2.9 μm)
Pulse duration (μs)	0.35	0.35
Maximum absorbed intensity, I_0 ($\text{J}/\text{m}^2/\text{s}$)	1.2×10^{10}	1.2×10^{10}
Number of pulses	1	1
Laser beam radius (mm)	0.2	0.2

Table 6.13: Laser parameters used in simulations that assess the effect of water macropores at the rod sheath, used in model *RodsPores*.

In order to make it easier for the reader to understand what simulations were performed and the main differences between them, a list of the names and distinguishing laser parameters for the simulations performed are presented in Table 6.14. Note that results from the first two simulations have already been analyzed in Section 6.2, and are repeated here because they will be compared with the results obtained with model *RodsPores*. This time, the same laser intensity is

Name	Wavelength	Water	Laser intensity
RodsHom_CO2_1.2e10	CO ₂	no	1.2×10^{10}
RodsWL_CO2_1.2e10	CO ₂	yes	1.2×10^{10}
RodsPores_CO2_1.2e10	CO ₂	yes	1.2×10^{10}
RodsPores_Er_1.2e10	Er:YAG	yes	1.2×10^{10}

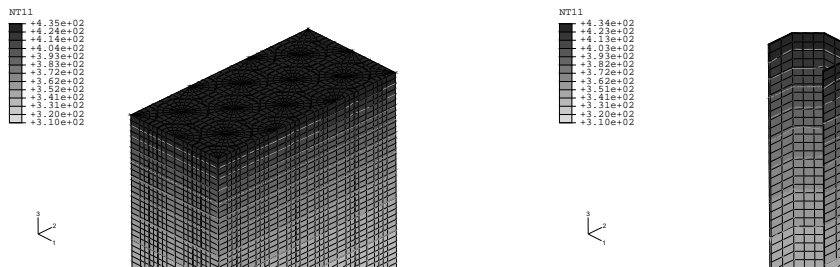
Table 6.14: Distinguishing simulation parameters used for models *RodsHom*, *RodsWL* and *RodsPores*, in order to assess the effect of wavelength and water distribution on the temperature and static stress maps. The first two simulations, corresponding to having a model without water and one in which the rod is surrounded by a water layer, have already been analyzed in Section 6.2, and are repeated here because their results will be compared with the results obtained with model *RodsPores*.

used for the CO₂ and Er:YAG laser because, as it will be seen when the results are analyzed, the same maximum temperature will be reached at the end of the laser pulse.

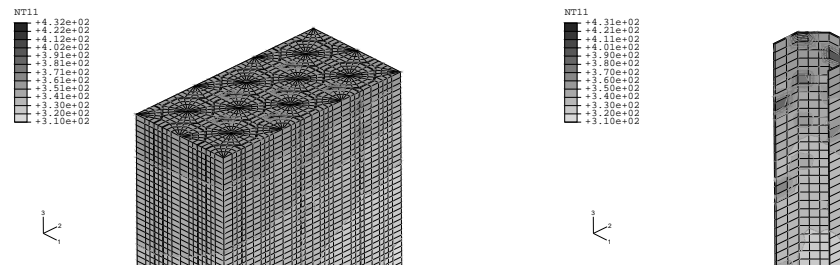
The simulations were performed in the same manner described for *RodsWL* (model *Rods* with a water layer): first the heat transfer simulations were performed, for a total duration of 10 μs . Subsequently, the linear static stress simulations were performed taking as input the temperature map generated at the end of the laser pulse.

6.3.2 Results and discussion

The temperature distribution at the end of the laser pulse for all the simulations is given in Fig. 6.17. There are no differences in the temperature maps between models *RodsWL* and *RodsPores* when the CO₂ laser is used. Similarly to what was observed for model *RodsWL*, the temperature distributions for model *RodsPores* are qualitatively different for the CO₂ and for the Er:YAG laser: the CO₂ laser induces appreciable temperature gradients only along OZ, that is, parallel to the optical axis of the laser beam, while the Er:YAG laser induces significantly higher temperatures at the regions with higher water content.



(a) Nodal temperature for model *RodsPores* and for the CO₂ laser. Only half the model is shown. (b) Nodal temperature at the rod sheath for model *RodsPores* and for the CO₂ laser.



(c) Nodal temperature for model *RodsPores* and for the Er:YAG laser. Only half the model is shown. (d) Nodal temperature at the rod sheath for model *RodsPores* and for the Er:YAG laser.

Figure 6.17: Temperature (in kelvin) at the end of a single 0.35 μ s laser pulse for model *RodsPores*. Numbers 1, 2 and 3 near the cartesian axes correspond to directions X, Y and Z, respectively.

The maximum temperature reached in all *RodsPores* models was approximately 160 °C, which was rather unexpected. If the reader remembers the results obtained using model *RodsWL* (presented in Section 6.2), the Er:YAG laser induced a maximum temperature of 278 °C when the same laser intensity of 1.2×10^{10} J/m²/s was used in this model. This suggests that the maximum temperature induced at the pores by the Er:YAG laser may be a function of the pore size, something which

may have significant implications for understanding and controlling the ablation of enamel using this laser.

The minimum and maximum quasi-static stress maps at the end of the laser pulse for the *RodsPores* models are given in Figs. 6.18 and 6.19. To facilitate comparisons, the stress maps for models in which the rod sheath is composed entirely of mineral and entirely of water are presented again (they were already analyzed earlier in Section 6.2). In Fig. 6.19, only the rod sheath is shown.

Clearly, the water distribution and the wavelength used make a significant difference on the stress maps. When using the CO₂ laser, the stress distribution for model *RodsPores* is almost identical to model *RodsHom*, the only differences being that the stress in and around the water pores tends to be compressive rather than tensile and an increase in the minimum principal stress (which traduces an increase in the highest compressive stress). The concentration of stress around the rod tail seen in model *RodsWL* (with a higher content of water around the rod) is no longer present. When the Er:YAG laser is used, however, there is a clear increase in both the minimum and maximum principal stresses throughout the model, which means that the model experiences higher tensile and compressive stresses than model *RodsHom*. Nevertheless, the stress levels are significantly lower than those observed in model *RodsWL*. Similarly to what is observed for the CO₂ laser, the stresses around the pores tend to be compressive.

These results indicate that the local temperature gradient generated around the pores when the Er:YAG laser is used induce higher stress concentrations than when the CO₂ laser is used, despite the fact that the same incident fluence was applied for both lasers and the same maximum temperature is reached at the pores. They also indicate that the amount and distribution of water in enamel should have a significant influence on the temperature and stress generated in this material. This suggests that the results of ablating enamel using both lasers may be dependent on conditions that alter the water content of the tooth (age, location of irradiated site, type of tooth, level of hydration for *in vitro* teeth). Therefore, it seems that experimentalists may want to plan their experiments and analyze their results taking those factors in consideration, in particular when using the Er:YAG laser for which this effects seems to be more intense.

The differences observed between the models that have a water-layer surrounding the rod sheath and those that have large, flat pores at the same location suggested that the response of the material may be a function of pore-size. In order to investigate this issue, a new set of simulations were performed and are now

presented in the next Section.

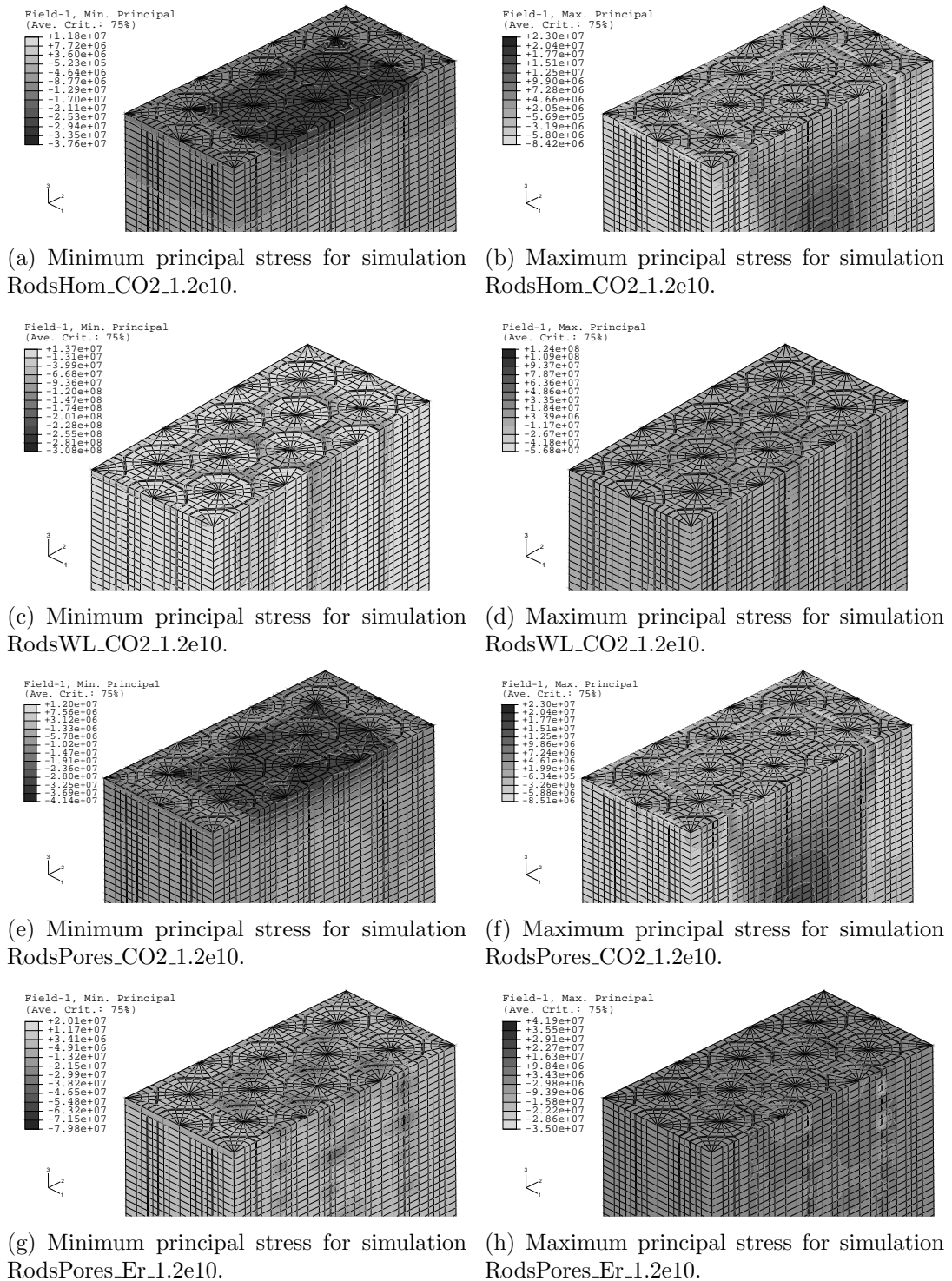
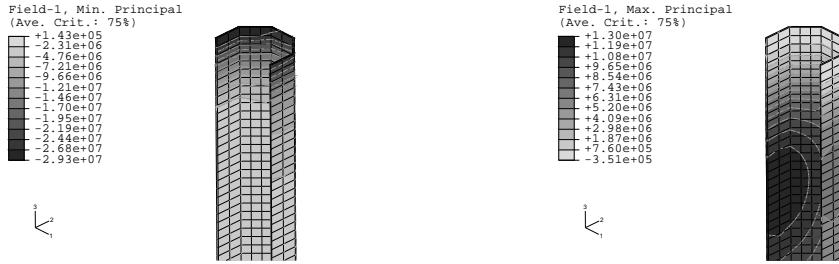
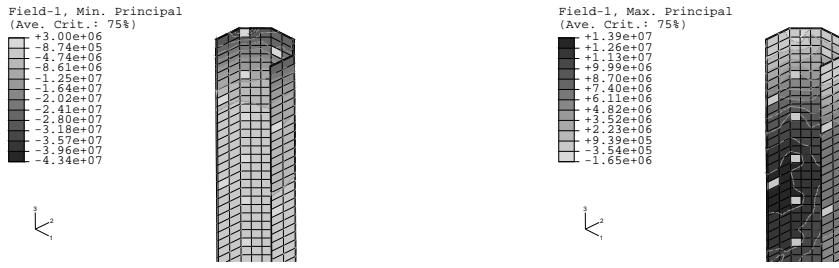


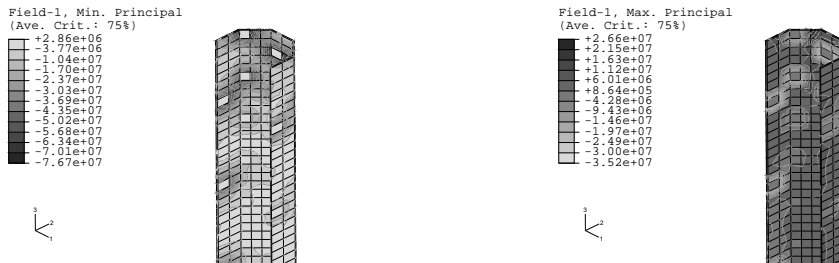
Figure 6.18: Minimum and maximum principal quasi-static stress (N/m^2) at the end of the $0.35 \mu\text{s}$ laser pulse for models: **(a,b)** without water; **(c,d)** with a water-layer at the rod sheath and **(e-h)** with water-pores at the rod sheath. A positive value represents tensile stress and a negative one represents compressive stress. Numbers 1, 2 and 3 near the cartesian axes correspond to directions X, Y and Z, respectively. Only half of the model is visible in each image, so that the stress at the center of the structure can be analyzed.



(a) Minimum principal stress for simulation RodsHom_CO2_1.2e10. (b) Maximum principal stress for simulation RodsHom_CO2_1.2e10.



(c) Minimum principal stress for simulation RodsPores_CO2_1.2e10. (d) Maximum principal stress for simulation RodsPores_CO2_1.2e10.



(e) Minimum principal stress for simulation RodsPores_Er_1.2e10. (f) Maximum principal stress for simulation RodsPores_Er_1.2e10.

Figure 6.19: Minimum and maximum principal quasi-static stress (N/m^2) at the end of $0.35 \mu\text{s}$ for models: (a,b) *RodsHom*; (c,d) *RodsWL* and (e,f) *RodsPores*. A positive value represents tensile stress and a negative one represents compressive stress. Numbers 1, 2 and 3 near the cartesian axes correspond to directions X, Y and Z, respectively. Only the sheath of a single rod is shown for each model.

6.4 Influence of pore size on the temperature and stress distribution: the nanoscale pore models

In the previous Section, the effect of having wide, flat pores instead of a water layer at the rod sheath was investigated. However, there is some evidence to suggest that the majority of pores in enamel will be significantly smaller than this. Pores as small as a few tens of nanometers and as large as a few hundreds of nanometers are thought to exist, mostly at the rod sheath [7]. The question that naturally arose, then, was whether water in pores as small as this would still induce similar stress-concentrations to those observed for the *RodsPores* models. In order to investigate the effect of the pore size on the response of enamel to the CO₂ and Er:YAG lasers, a new model was developed. This model does *not* attempt to include the rod microstructure characteristic of enamel. Including this microstructure while at the same time modelling pores with characteristic nanometer-scale sizes would produce huge models which would be too computationally demanding. Instead, the new models represent a single pore surrounded by mineral.

Results presented earlier in this Thesis indicate that the models are somewhat sensitive, from a quantitative point of view at least, to variations in the Young's modulus of the water/organic material, E_{water} , contained in the pores, in particular to increases in this value. Furthermore, the combination of Young's modulus ($1 \times 10^5 \text{ N/m}^2$) and Poisson's ratio (0.28) used for the content of the pores implies that the water/organic is modelled as a material that is five orders of magnitude more compressible than water, which may introduce uncertainty also from a qualitative point of view ³. In order to reduce the level of uncertainty associated with the results, it was decided to follow an entirely different approach now: the material in the pores is assumed to be pure water, and is modelled using an Equation of State for this substance. Therefore, the compressibility of the material is now modelled more adequately, since it is a function of both pressure and temperature.

Finally, the stress results presented until now refer only to the quasi-static stress induced in the material at the end of the laser pulse. However, it is important to understand the dynamical evolution of stress during and after the laser pulse. For

³The bulk modulus for the water/organic material model is $K = E/3/(1 - 2\nu) = 7.6 \times 10^4 \text{ N/m}^2$, and for liquid water at 50 °C and pressure between 1 and 20 MPa is $K = \rho dP/d\rho \simeq 1 \times 10^9 \text{ N/m}^2$. Data for liquid water from ref. [147].

this reason, both thermal and mechanical simulations presented in this Section have a dynamical nature.

6.4.1 Description of the finite element model

In order to investigate the effect of pore size on the stress distributions induced by mid-infrared laser pulses, three Finite Element models – representing a piece of HA surrounding a single cubic pore containing only water – were developed (see Fig. 6.20 for a representation of the model). The total dimensions of the models are $3.1 \times 3.1 \times 1.3 \mu\text{m}^3$, which makes them much smaller than any of the models presented thus far. The three models differ only on the size of the pore: the length of the pore edges considered are 30, 70 and 130 nm and, for this reason, the models are called *SmallPore30*, *SmallPore70* and *SmallPore130*.

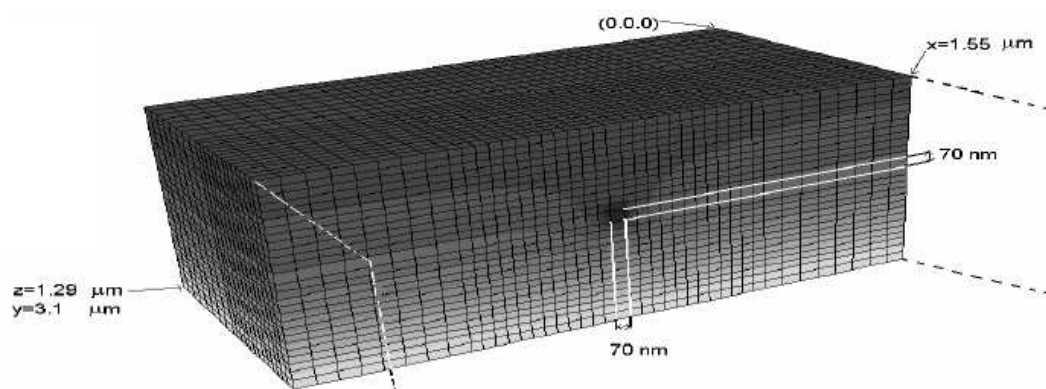


Figure 6.20: Geometry of model *SmallPore70*; only half of the model is shown, so that the pore can be seen. The geometry of models *SmallPore30* and *SmallPore130* is similar, only differing in the dimensions of the pore.

As mentioned in the introduction to this Section, the results obtained by prior models indicate that they are sensitive, from a quantitative point of view, to the value of the Young's modulus of the material contained at the pores. Also, it is likely that the water/organic material was assigned an excessively high compressibility, which may influence the stress maps in a significant manner. Therefore, at this point it was judged more appropriate to model this material as a fluid, using an Equation of State instead of using a solid-material model. Since the water is more abundant in the pores than the organic material, an Equation of State (EOS) for pure water was implemented through subroutine UMAT, used during the stress simulations. Note that, since the temperature maps were not particularly sensitive to variations in the material parameters of water, the content of the pores during

the heat transfer simulations is still modelled using the density, specific heat and thermal conductivity of water. The EOS is only used for the stress analyzes.

In order to decide which EOS would be used (a number of them exist to model the behavior of water under different experimental conditions) it was necessary to determine whether the water in the pores would behave like liquid bulk water. The factors that most influence the behavior of water are the pore dimensions and the hydrophilic character of the pore surface: as either of them increases, the water in a pore will behave more like liquid bulk water. Work done by Giaya, Liu, Borggreven and co-workers [8, 9, 10] strongly suggests that water contained in pores of width larger than 30 nm and pore walls made of HA will behave like liquid bulk water, because HA is an ionic substance and, consequently, can be expected to have a strong hydrophilic character. Therefore, the remaining task was to select an EOS that described the behavior of water accurately in the range of temperatures and pressures expected to develop during and after a single laser pulse.

After reviewing the literature, it was decided to use the EOS described by Lyons [154], which relates the water pressure, P , in the pore at a given temperature, T , and volume per unit mass, V_m , according to:

$$P = B_T \exp \left[\left(-\frac{V_m - V_{0T}}{V_{0T} \times A_T} \right) - 1 \right] \quad (6.11)$$

where V_{0T} , A_T and B_T are those defined in eqs. 6.12, 6.13 and 6.14. This particular EOS was chosen because of its accuracy and simplicity.

$$V_{0T} = V_{P_0T_0} \left(1 + \xi_1 T + \xi_2 T^2 + \xi_3 T^3 + \xi_4 T^4 + \xi_5 T^5 \right) \quad (6.12)$$

$$A_T = A_0 \left(1 + \eta_1 T + \eta_2 T^2 + \eta_3 T^3 \right) \quad (6.13)$$

$$B_T = B_0 \left(1 + \varsigma_1 T + \varsigma_2 T^2 + \varsigma_3 T^3 \right) \quad (6.14)$$

The values of constants $V_{P_0T_0}$, A_0 , B_0 , ξ_i , η_i and ς_i used in eqs. 6.12, 6.13 and 6.14 can be found in Table 6.15. Lyons obtained these values by fitting equation 6.11 to experimental measurements of temperature, pressure and mass-volume for liquid water. He established the validity of eq. 6.11 for temperatures in the 0 to 100 °C range and pressures between 0.1 and 100 MPa, which is insufficient for the models described here. However, the author of this Thesis compared the results of eq. 6.11 with experimental data in references [147, 155], and found that it

B_0 (N/m ²)	2.71000000000E+08
A_0	1.38000000000E-01
V_{p0t0} (m ³ /kg)	1.00021195720E-03
ξ_1 (°C ⁻¹)	-6.10804506610E-05
ξ_2 (°C ⁻²)	8.26422147620E-06
ξ_3 (°C ⁻³)	-6.25191522510E-08
ξ_4 (°C ⁻⁴)	3.96577772140E-10
ξ_5 (°C ⁻⁵)	-1.03766115850E-12
η_1 (°C ⁻¹)	1.83447912390E-03
η_2 (°C ⁻²)	-3.94832209280E-05
η_3 (°C ⁻³)	1.32756265960E-07
ς_1 (°C ⁻¹)	9.43239862720E-03
ς_2 (°C ⁻²)	-1.43696702930E-04
ς_3 (°C ⁻³)	4.56081249050E-07

Table 6.15: Parameters used for the Equation of State for water.

holds well for temperatures up to 200 °C and pressures up to 500 MPa, sufficient for the purposes of the work described here.

The material parameters used to model the content of the pores (for the thermal simulation) and the mineral are given in Table 6.16. The reasons for choosing these values have already been given in Section 6.2, so they will not be repeated here. The values for the Restrain-layers were calculated according to the equations presented in Section 6.1.1.2 and 6.1.1.1, and using the geometrical parameters given in Table 6.17.

Similarly to all the previous simulations, all the external nodes were fixed in the stress analyzes with the exception of the nodes at the irradiated surface, which were left unconstrained. All the nodes were given an initial temperature of 37 °C, which was also the stress-free reference temperature.

As usual, first the transient heat transfer simulations were performed, which yielded the temperature maps during and after the laser pulse, for a total simulation time of 10 μ s. The laser parameters, similar to those used in the previously reported work, are given in Table 6.18. Subsequently, the temperature distribution was used as input to the dynamic stress simulations, from which the stress and displacement experienced throughout the model were obtained. The EOS of water (necessary for the mechanical simulations) was implemented using subroutine UMAT. In UMAT, the volume of the pore at each increment was made a state variable; this quantity is calculated in each increment by taking the volume of

	Water	Hydroxyapatite	BRL	LRL
Abs. coeff. at $2.94 \mu\text{m}$ ($\times 10^4 \text{ m}^{-1}$)	122.5 [123]	3	3	NA
Abs. coeff. at $10.6 \mu\text{m}$ ($\times 10^4 \text{ m}^{-1}$)	8.25	8.25 [69]	8.25	NA
κ (J/(s.m. $^\circ\text{C}$))	0.6 [147]	1.3 [143]	2.5×10^{-5}	1.3
Spec. heat ($\times 10^2 \text{ J/kg/}^\circ\text{C}$)	42 (313 K) [147] 44 (453 K) 47 (503 K) 53 (553 K)	880 [143]	8.8	8.8
E ($\times 10^6 \text{ N/m}^2$)	Not applicable	110000 [144]	0.289	15
ν	Not applicable	0.28 [145]	0.28	0.28
α ($\times 10^{-5} \text{ K}^{-1}$)	Not applicable	1.6 [146]	160	400 (x) 400 (y) 1.6 (z)
ρ ($\times 10^3 \text{ kg/m}^3$)	0.99 [147]	3.1 [142]	15.5* 3.1 [#]	3.1

Table 6.16: Properties of enamel used in models *SmallPore*. Note that the parameters used only in the heat transfer simulations are not given for the Lateral Restrain-layer (LRL), since this layer is only used for the mechanical simulations. Also, the thermal expansion coefficient of the Lateral Restrain-layer is given in terms of the three directions in space, and the specific heat of water is given as a function of temperature. * Used in the heat transfer simulation, to act as a heat sink. [#] Used in the mechanical simulation.

the pore in the previous increment and the current strain tensor passed into the subroutine. Having determined the volume of the pore, the stress tensor can easily be calculated by taking the temperature at the pore and using eqs. 6.11, 6.12, 6.13 and 6.14: the direct stress components are equal to the pressure calculated using eq. 6.11, and the shear stress components are zero at every instant. An example of the UMAT subroutine can be found in Annex 2. All analyzes were performed using ABAQUS implicit algorithm, using the automatic incrementation scheme available except those for models without water, which used the Explicit algorithm ⁴

A number of simulations were performed, to assess the effect of the pore size and the different wavelengths on the results. A few simulations were performed

⁴The Explicit algorithm is better than the Implicit one to obtain insight into the dynamic behavior of the model, and in fact should have been used for all analyzes reported in this Section. This was not done because of difficulties in implementing the EOS of water, indispensable to model the water at the pores, in a manner that it could be used in the Explicit algorithm. For this reason, the *SmallPore* models are not analyzed in detail with respect to their dynamic stress response to the laser pulse.

Model	<i>SmallPore30</i>	<i>SmallPore70</i>	<i>SmallPore130</i>
Total dimensions of model (μm^3)	$3.1 \times 3.1 \times 1.3$		
Number of nodes	49392	49392	38400
Number of elements	45374	45374	31936
L_{LRL} (μm)	0.96		
ℓ_{en} (mm)	6		
$\ell_{en,expanding}$ (mm)	0.2		
E_{en} (N/m^2)	1.1×10^{11}		
Δz_{BRL} (μm)	0.116		
Δz_{en+den} (mm)	6		
κ_{en}	1.3		
E_{en+den} (N/m^2)	1.5×10^{10}		

Table 6.17: Geometrical parameters for models *SmallPore*. ℓ_{en} and (Δz_{en+den}) correspond to the thickness of enamel (or enamel + dentine) considered to surround the modelled structure and that is being replaced by the Lateral Restrain-layer and the Bottom Restrain-layer, respectively.

Type of laser	CO ₂ (10.6 μm)	Er:YAG (2.9 μm)
Pulse duration (μs)	0.35	0.35
Maximum absorbed intensity, I_0 ($\text{J}/\text{m}^2/\text{s}$)	1.2×10^{10}	2×10^{10}
Number of pulses	1	1
Laser beam radius (mm)	0.2	0.2

Table 6.18: Laser parameters used in models *SmallPore*.

with the aim of comparing the results obtained using model *SmallPores* with the larger *Cubes* model, thus establishing to what extent the model size influences the results. The names of the most relevant simulations performed and a highlight of the relevant parameters for each is given in Table 6.19 for the convenience of the reader.

Before proceeding to the discussion of results, it is necessary to make a few comments on the choices made for the analysis that will be presented. The results of the stress simulations will be analyzed based on the Von Mises stress maps obtained for the mineral. While it is known that the concept of equivalent stress does not apply to brittle materials, the results obtained with previous models indicate that the VMS reproduces fairly well the minimum and maximum principal stress distributions in the regions close to the water pores, at least from a qualitative

Name	Wavelength	Water	Laser intensity
Cubes_CO2_1.2e10	CO ₂	no	1.2×10^{10}
SmallPore70CO2_hom_1.2e10	CO ₂	no	1.2×10^{10}
SmallPore70CO2_water_1.2e10	CO ₂	yes	1.2×10^{10}
SmallPore30CO2_water_1.2e10	CO ₂	yes	1.2×10^{10}
SmallPore130CO2_water_1.2e10	CO ₂	yes	1.2×10^{10}
SmallPore70Er_water_2e10	Er:YAG	yes	2×10^{10}
SmallPore30Er_water_2e10	Er:YAG	yes	2×10^{10}
SmallPore130Er_water_2e10	Er:YAG	yes	2×10^{10}

Table 6.19: Simulation parameters for models *SmallPore* and for model *Cubes*, to assess the influence of model size, pore size and wavelength on the temperature and stress in enamel.

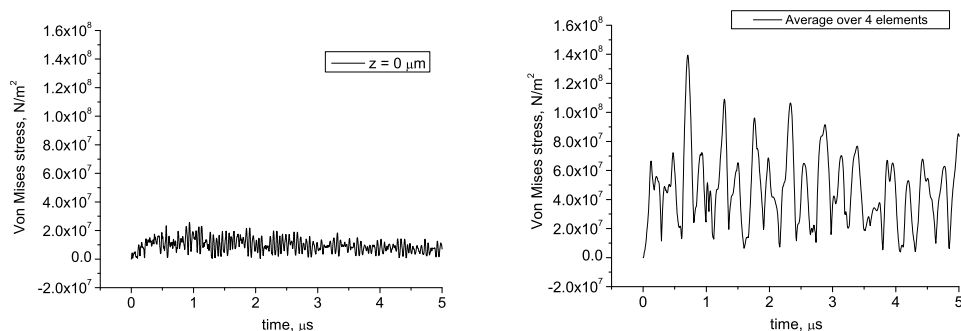
point of view. Provided that the readers keep in mind the limitations of using the VMS stress and do not dwell too closely on the actual values obtained, it is thus reasonable to analyze results using this approach. Keep in mind, however, that the stress results *at the pore* are analyzed in terms of *pore pressure* and not VMS, and for this reason are not subject to the same words of caution. Furthermore, while the mechanical simulations performed have a dynamical nature and, consequently, the stress results are obtained as a function of time, graphs of stress as a function of time will not be analyzed or presented at this stage. The justification for this choice lies in the fact that the time-step used in the mechanical simulations (determined by the automatic incrementation scheme available in the program) is too long to capture the high-frequency stress oscillations generated. Therefore, plots of stress as a function of time do not yield much useful information. The author attempted to run the simulations using the implicit algorithm and very short, user-controlled, time-steps, but it proved computationally too demanding. The author also attempted to perform the same simulations using the explicit algorithm, for which a very short time-step is naturally available, but difficulties in implementing the EOS of water made it impossible. Since the temporal definition of the stress results is not sufficient to yield useful information, only the stress (or pressure) at the end of the laser pulse is reported, since it represents an upper boundary for the stress values.

6.4.1.1 Results and discussion

Before performing the main set of simulations, it was necessary to assess in what way the small size of model *SmallPore* could induce changes in stress and temper-

ature maps when compared to the larger models presented previously. In order to this, two preliminary simulations using models *SmallPores70* and *Cubes* were performed. Neither of the models at this stage includes water, and both use CO₂ laser parameters (see parameters for simulations *Cubes_CO2_1.2e10* and *SmallPore70CO2_hom_1.2e10* in Table 6.19).

The thermal analysis indicates that the maximum temperature (160 °C) for simulation *SmallPore70CO2_hom_1.2e10* is reached at the irradiated surface, at the end of the laser pulse, and slowly decreases until the end of the simulation, a similar result to the one obtained with model *Cubes*. With respect to the results from the mechanical simulations, the Von Mises stress levels reached at the end of the laser pulse in the current model are one order of magnitude higher than the ones obtained when dynamical stress simulations are performed using model *Cubes_CO2_1.2e10*, as is illustrated in Fig. 6.21. Also, the results using model



(a) VMS for a single element of height 0.4 μm for simulation *Cubes_CO2_1.2e10*. (b) VMS averaged over 4 elements located at depths between 0 and 0.6 μm for simulation *SmallPore70CO2_hom_1.2e10*.

Figure 6.21: Von Mises stress between 0 and 5 μs for elements located at the XY center of the irradiated surface of models: (a) *Cubes* and (b) *SmallPore70*. In (b) the VMS is averaged over 4 elements that are roughly at the same location as the single element mentioned in (a), because model *SmallPore70* has a much finer mesh than model *Cubes*.

SmallPore70 show a high-amplitude oscillation of the stress values like in model *Cubes* but the amplitude of that oscillation is also one order of magnitude higher than what it should be. The *time-averaged* VMS values obtained with the *SmallPore70* model give much more promising results: they are within the same order of magnitude of those obtained using the *Cubes* models, although still higher than in model *Cubes*, as can be seen in Table 6.20. Note that the maximum VMS values reached concentrate at the end of the laser pulse, for both model sizes. These results suggest that qualitative inferences on the stress behavior may be made from

Simulation	Cubes_CO2_1.2e10	SmallPore70CO2_hom_1.2e10
VMS at the end of the laser pulse (N/m ²)	1.3×10^7	4.6×10^7
VMS between 4 and 5 μ s (N/m ²)	7.3×10^6	3.9×10^7

Table 6.20: Time-averaged Von Mises Stress values for simulations Cubes_CO2_1.2e10 and SmallPore70CO2_hom_1.2e10 for the elements mentioned in Fig. 6.21. The VMS at the end of the laser pulse was averaged between 0.35 and 0.36 μ s.

the current results using models *SmallPore* and that the time-averaged VMS values give an idea of the correct order of magnitude of the stress reached in enamel, but the actual instantaneous values of stress should not be taken at face value. This is not unexpected, since in Section 6.1.1.1 a similar behavior was observed for the smaller model used to test the boundary conditions applied to the mechanical simulations.

Having established the confidence with which the results may be interpreted, simulations were then performed using model *SmallPore70* and CO₂ laser parameters, but this time considering the water pore to be totally filled with liquid water. The results of this simulation, named SmallPore70CO2_water_1.2e10, will be compared with the results from simulation SmallPore70CO2_hom_1.2e10, thus assessing the influence of the water pore on the stress generated in enamel. The stress levels at the water pore became one order of magnitude higher than when that region is made of mineral only. As a consequence, the stress levels at the mineral directly surrounding the pore were also elevated. This suggests that the water pores can have a significant impact in the stress distributions in enamel and can play an important role in ablation, even for relatively low temperature elevations such as the one predicted using the laser parameters in Table 6.18. It should be noted that the temperatures reached in the material do not allow for water vaporization, because they are always lower than the vaporization temperature at the pressures felt inside the pore. The high pressures in the water pore are solely due to the thermal expansion of the water, its low compressibility and the high rigidity of HA, which means that even very small volume variations translate into high mechanical pressures. These results suggest that cracking of enamel may take place even before water-vaporization begins, and that it is possible that vaporization may actually begin only after the pore walls have cracked. This is in qualitative agreement with results obtained by Apel et al. [94], who found that the

Er:YAG laser could cause extensive cracking in enamel even when fluences lower than the ablation threshold were used.

The mechanical properties of HA seem to have some influence on the stress maps (see Section 6.2), but this influence was not investigated in the context of this new, smaller, model. This fact, together with the knowledge that a biological material like enamel may experience significant changes in its properties depending on its location, made it necessary to re-assess the influence of the mechanical properties of HA, E_{HA} and ν_{HA} , on the stress levels reached. Both those parameters were independently varied by $\pm 10\%$ and $\pm 25\%$, using model *SmallPore70* and CO₂ laser parameters. It was found that varying E_{HA} or ν_{HA} within the tested range has little effect on the water pressure reached at the pore: the maximum variation experienced was approximately 3%. Some significant differences were observed, however, on the stress values at the mineral that directly surrounds the pore when E_{HA} was varied: the VMS becomes 15% higher when E_{HA} is raised by 25% and 5% lower when E_{HA} is lowered by 25%. While the actual figures obtained should not be taken at face value because of the uncertainty associated with the results, this does suggest that different values of E_{HA} will cause some non-intuitive variations on the stress levels experienced throughout enamel. Regardless of the changes in the VMS when E_{HA} or ν_{HA} are modified, the general behavior of the stress remains the same: the higher levels of stress are felt in the pore and in the mineral that surrounds the pore.

The influence of the pore size on the stress levels reached in enamel when using the CO₂ laser was assessed by performing simulations using models *SmallPore30* and *SmallPore130* (simulations *SmallPore30CO2_water_1.2e10* and *SmallPore130CO2_water_1.2e10*). It was found that the temperature behavior was identical to that observed in model *SmallPore70*, which was expected because the absorption coefficients of HA and water were considered identical. The pressure at the water pores remained unchanged in all three models, consistent with the identical thermal results in all those models. The VMS of the material that directly surrounds the water pore, however, increased significantly (over 50%) from model *SmallPore30* to *SmallPore130*, which was not expected given that the water pressure remained approximately the same in all three models. This result suggests that the size of the water pores by itself may influence the stress levels reached by the material, independently of the temperature reached at the pore. However, given the uncertainty associated with the actual values of the results, further work is necessary to determine whether this assumption will hold.

Finally, simulations using the three geometric models with water pores, but using Er:YAG laser parameters were performed, to assess the influence of pore size and wavelength of laser on the temperature and stress induced in enamel (simulation *SmallPore30Er_water_2e10*, *SmallPore70Er_water_2e10* and *SmallPore130Er_water_2e10*). The temperature map at $t = 0.35 \mu\text{s}$ for model *SmallPore70* and the Er:YAG laser can be seen in Fig 6.22. The qualitative features in this image are common to all the simulations in which the Er:YAG laser was used; the only differences are the actual temperature values.

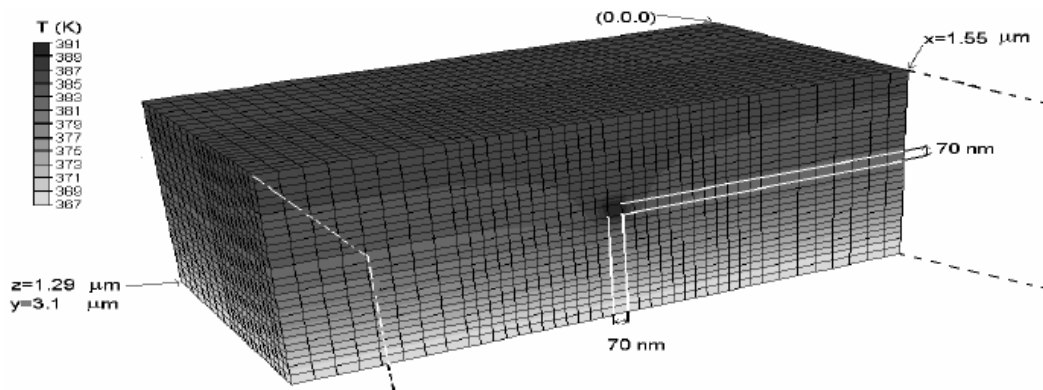


Figure 6.22: Temperature distribution for model *SmallPore70* at the end of a single $0.35 \mu\text{s}$ laser pulse by the Er:YAG laser with intensity $2 \times 10^{10} \text{ N/m}^2$. Only half of the model is shown, so that the water pore can be seen.

As expected, the water pore is the site with the highest temperature in each model, because of the difference in the absorption coefficients of water and HA. The maximum temperature reached at the water pore (at the end of the laser pulse) seems to be a strong function of the pore size for Er:YAG, as can be seen in Table 6.21. This can easily be explained if one remembers that smaller pores have

Pore dimensions (nm^3)	Er:YAG		CO_2	
	Maximum temperature ($^\circ\text{C}$)	Maximum pressure (N/m^2)	Maximum temperature ($^\circ\text{C}$)	Maximum pressure (N/m^2)
$30 \times 30 \times 30$	113	8.3×10^7	153	1.5×10^8
$70 \times 70 \times 70$	116	8.3×10^7	153	1.5×10^8
$130 \times 130 \times 130$	138	8.9×10^7	153	1.5×10^8

Table 6.21: Maximum temperature and pressure reached at the pores at the end of the laser pulse, for the various pore-sizes in models *SmallPore*.

higher area-to-volume ratios and, therefore, lose heat to their surroundings more rapidly than larger pores. One microsecond after the laser pulse, the pore reaches

thermal equilibrium with its surroundings and the temperature in all three models is close to 100 °C. The actual temperature values should not be considered entirely accurate because of the uncertainty associated with the material parameters used, in particular the absorption coefficient of water at $\lambda = 2.9 \mu\text{m}$. However, since the minimum value that the absorption coefficient of water can reach is $\simeq 10000 \text{ cm}^{-1}$ (according to work by Shori et al. [123]), which is still significantly higher than the absorption coefficient for HA (300 cm^{-1}), one can confidently suggest that CO_2 and Er:YAG lasers will induce different responses in dental enamel.

Consistent with the temperature maps obtained for Er:YAG laser parameters, the stress maps (see Fig. 6.23 for an example) indicate that the water pores reach

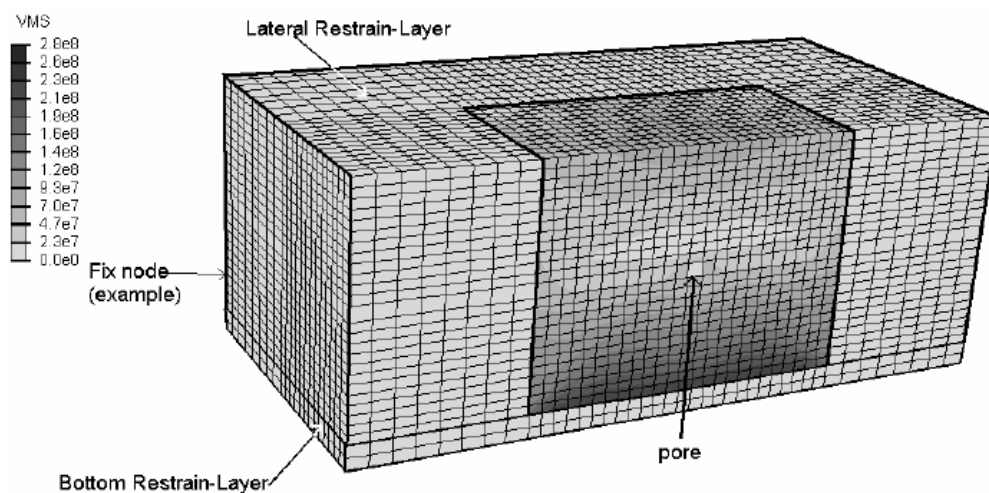


Figure 6.23: Von Mises stress (N/m^2) at $t = 0.44 \mu\text{s}$ for the 70 nm pore model with Er:YAG laser. Only half of the model is shown, so that the pore can be seen.

a maximum pressure at the end of the laser pulse. This maximum pressure varies with pore size as can be seen in Table 6.21: there is a 7% increase in peak-pressure from the SmallPore30Er_water_2e10 to the SmallPore130Er_water_2e10 simulations. This is a consequence of the increase in the pore peak-temperature.

Similarly to what was observed for the *Rods* models, even the relatively low temperatures induced by the lasers (up to 160 °C) seem to induce high stress concentrations around the pore which are solely caused by the thermal expansion of liquid water. The VMS of the material that surrounds the pore is comparable to, or even higher than, the ultimate strength of enamel. Again, while the actual numerical results reported here should not be given too much importance, they do suggest strongly that cracking of enamel may commence before water vaporization can take place and before ablation starts.

The results have thus established that there should be a direct relationship between the temperature reached at the pores and the pore pressure, and that the pore temperature at the end of the laser pulse should be dependent of pore size for the Er:YAG laser and virtually independent of pore size for the CO₂ laser. Therefore, it is possible to qualitatively assess the effects in terms of stress of having pores of different sizes by simply determining its temperature. Comparing the results from equally-sized *SmallPore* models and different lasers, one finds that in all situations the maximum VMS in the mineral, and the corresponding maximum pressure at the water pore, are always higher for the CO₂ laser. This is consistent with the fact that, despite the higher laser intensity used for the Er:YAG laser, a lower temperature is reached at the end of the laser pulse in this case because heat is lost very rapidly through the pore walls. This is an opposite behavior to that observed with the *RodsWL* models (that have a thin water layer surrounding each rod), in which the Er:YAG laser induced the same temperature change using half the laser intensity that was used for the CO₂ laser. The difference between both cases lies in the dimensions of the pore: in the *Rods* models, the water layer is 0.1 μm thick and covers a large area at the rod sheath, whereas pores are significantly smaller than that in models *SmallPores*.

Clearly, model *Rods* and model *SmallPores* represent two extreme cases. The actual morphology of enamel should be somewhere in between these two extremes, where a large number of small pores, relatively close to each other, can be found at the rod sheath. What the present results suggest is that the main ablation mechanism for the CO₂ laser should also be the explosive vaporization of water (at least at lower fluences), and that the CO₂ laser should be less sensitive to the pore size than Er:YAG ablation. This may have significant practical implications, because it is known that enamel may present abnormally large regions with high water/organic content (enamel tufts, lamellae and spindles). An Er:YAG laser irradiating these areas will thus generate much higher temperatures (and, consequently, pressures) than the CO₂ laser using the same laser intensity. This means that the likelihood of the Er:YAG laser inducing large local stress concentrations and thus creating large local cracks in enamel is higher. Therefore, it seems that unwanted mechanical damage such as cracking should be easier to control when using the CO₂ laser. It also suggests that the enamel ablation threshold using the CO₂ laser should be more reproducible than using the Er:YAG laser. The results suggest that both the CO₂ and the Er:YAG laser should induce very high pressures at the pores, capable of inducing cracking, even when using sub-ablative fluences.

This is in agreement with experiment as far as the Er:YAG laser is concerned [94], but not for the CO₂ laser. In fact, cracking is normally not observed when using the CO₂ laser at sub-ablative fluences to increase enamel's resistance to acid attacks. This may be explained by the fact that the mineral will reach higher temperatures when the CO₂ laser is used, which may induce a brittle-to-ductile transition which delays the onset of cracking. Unfortunately, it is not possible at the moment to satisfactorily verify these claims because the available experimental literature on ablation of enamel by both lasers reports a myriad of operating conditions which renders the direct comparison of results by one laser or the other impossible.

6.4.2 Description of the analytical stress model

The results obtained with previous models provided very useful insight, mainly from a qualitative point of view, into the laser-induced stress fields generated in enamel by the CO₂ and the Er:YAG lasers. However, since the purpose of this Thesis is to determine the laser operating parameters that produce the best results, it would be advantageous if one could have more confidence on the results from a quantitative point of view. This is particularly the case for models *SmallPores*, for which the uncertainty associated with the results is thought to be higher than for the *Rods* models because models *SmallPores* are much smaller than model *Rods*. Since there is no experimental information available that could be used to validate the models, the only possible way to do this is resorting to modelling. If models based on different techniques produce similar results, one may have a higher degree of confidence on the results. This is not the same as validating the model but, since that is not possible, it is nevertheless useful.

In order to estimate the pore pressure at the end of a laser pulse, and to further test whether water vaporization is likely to initiate or not before the onset of cracking, an analytical model of a single water pore in human dental enamel was built. This model only intends to simulate the mechanical response of enamel and uses temperature values as input only. Temperatures in the range of those that have been obtained with the *SmallPore* models presented in the previous Section will be used in this analytical model. The model consists of a spherical pore completely filled with water and surrounded by an infinite thickness of HA. The relationship between the specific volume (volume per unit mass), V , of the

pore and the pressure, P , experienced at the pore is [140]

$$V = V_0 \left[1 + \frac{1 + \nu_{HA}}{2E_{HA}}(P - P_0) \right]^3 \quad (6.15)$$

where V_0 is the initial specific volume of water when the pressure at the pore is P_0 , ν_{HA} is Poisson's ratio and E_{HA} is the Young's modulus for HA. The values used to obtain the results presented here are given in Table 6.22. For the particular

P_0 (Pa)	(1×10^5)
V_0 (m ³ /kg)	0.00100888
E (N/m ²)	1.1×10^6 [144]
ν	0.28 [145]

Table 6.22: Parameters used in the stress-strain relationship for a spherical pore surrounded by an infinite medium.

system being studied, P_0 is the atmospheric pressure and V_0 is the specific volume of water at pressure P_0 and temperature 37 °C.

On the other hand, the specific volume of water in the pore is a function of water temperature and pressure; this relationship can be expressed by the EOS already used for the finite element model *SmallPore* described earlier, which is now presented under a slightly different form:

$$V = V_{0T} \left[1 - A_T \ln \left(1 + \frac{P}{B_T} \right) \right] \quad (6.16)$$

where V_{0T} , A_T and B_T are defined in equations 6.12, 6.13 and 6.14, repeated below for the convenience of the reader.

$$\begin{aligned} V_{0T} &= V_{P_0T_0} \left(1 + \xi_1 T + \xi_2 T^2 + \xi_3 T^3 + \xi_4 T^4 + \xi_5 T^5 \right) \\ A_T &= A_0 \left(1 + \eta_1 T + \eta_2 T^2 + \eta_3 T^3 \right) \\ B_T &= B_0 \left(1 + \varsigma_1 T + \varsigma_2 T^2 + \varsigma_3 T^3 \right) \end{aligned}$$

The values for the constants used in the EOS can be found in Table 6.15. Using eqs. 6.15 and 6.16, the expression that relates the pressure at the pore with the

pore temperature was obtained:

$$V_0 T \left[1 - A_T \ln \left(1 + \frac{P}{B_T} \right) \right] = V_0 \left(1 + \frac{1 + \nu_{HA}}{2E_{HA}} (P - P_0) \right)^3 \quad (6.17)$$

It should be emphasized that, according to this model, the pressure at the pore is not a function of pore size, but of the temperature at the pore and the mechanical properties of the elastic medium surrounding the pore only, which suggests that the increase of pore pressure with pore size described in the previous Subsection for models *SmallPore* should be the result of numerical uncertainty and may not translate a physical effect.

Analytically solving this new equation with respect to the pressure so that a general solution can be obtained is not practical. Instead, Maple 8.0 was used to solve it numerically using the material parameters for HA and temperatures between 118 and 176 °C, which are given in Table 6.23.

Similarly to what was done with models *SmallPores*, the influence of the particular values of E_{HA} and ν_{HA} on the results was assessed by independently varying both those parameters by $\pm 20\%$. To further test the influence of E_{HA} on the results, this quantity was varied by ± 1 and ± 2 orders of magnitude. The consequences of varying Poisson's ratio more than $\pm 20\%$ were not investigated since for most materials it can only take values between 0 and 0.5 and it is not likely that ν_{HA} will be close to those extreme values.

6.4.2.1 Results and discussion

Equation 6.17 has non-trivial solutions in the temperature range under discussion (between 100 and 200 °C); the results obtained are shown in Table 6.23. These results are in excellent agreement, both qualitative and quantitative, with those obtained using the FE models *SmallPores*. Results obtained using both types of models indicate that there is a clear dependence between the pore pressure and pore temperature. For a pore temperature of 118 °C both the FE and the analytical models predict a pore pressure between $1.0 - 1.1 \times 10^8$ Pa; for a pore temperature of 134 – 135 °C, both models predict a pore pressure of $1.3 - 1.4 \times 10^8$ Pa. This agreement between the values of the pore pressure obtained using these two models suggests that quantitative inferences may be made from them, rather than just qualitative ones. As mentioned previously, the results indicate that very high pressures may be reached in the absence of water vaporization, caused solely by

Pore temperature (°C)	Pore pressure (N/m ²)
113	1.1×10^8
125	1.2×10^8
135	1.4×10^8
138	1.5×10^8
145	1.6×10^8
153	1.8×10^8
165	2.0×10^8
175	2.2×10^8

Table 6.23: Maximum pressure reached at the pores as a function of temperature. Results obtained using the analytical model.

the thermal expansion of liquid water. Indeed, the pressures reached in either the FE *SmallPore* models or the analytical model, for pore temperatures superior to 120 °C, are higher than the ultimate tensile stress (UTS) for polished, fully dense HA (1.15×10^8 Pa, [146]). If one assumes that cracking will take place whenever any component of the stress tensor in HA exceeds this material's UTS, then cracking should occur before the onset of ablation. This is in qualitative agreement with experimental results obtained by Apel et al. for the Er:YAG laser [94], as was mentioned before. However, the fluences at which the mineral is expected to crack in these models are lower by at least one order of magnitude from those used by Apel et al.

In order to determine a possible source of uncertainty in the model that could reduce the gap between the results presented here and the experimental evidence (that indicates that the pore pressures are overestimated by the models), it was decided to evaluate the influence of the chosen values of E_{HA} and ν_{HA} on these results, now using the analytical model. To achieve this, equation 6.17 was solved for the temperatures indicated in Table 6.23 but varying E_{HA} and ν_{HA} independently by $\pm 20\%$. The values of pressure varied by 2% or less, which indicates that the results are not particularly sensitive to small variations in E_{HA} and ν_{HA} . Subsequently, E_{HA} was varied by ± 1 order of magnitude, and it was found that while using $E_{HA} = 1 \times 10^{12}$ Pa (one order of magnitude higher) only caused a 5% increase in pore pressure, using $E_{HA} = 1 \times 10^{10}$ Pa (one order of magnitude lower) caused a very significant 33% decrease in pore pressure. Using $E_{HA} = 1 \times 10^{13}$ Pa (two orders of magnitude higher) caused a mere 6% increase in pore pressure, but

using $E_{HA} = 1 \times 10^9$ Pa (2 orders of magnitude lower) caused a 81% decrease in pore pressure. Now, the default value of E_{HA} used for all the simulations in this Thesis (1.1×10^{11} Pa) lies on the upper range of experimental values of E available for enamel or HA. This means that the models may be improved slightly by using a lower value of E, which would produce results closer to the experimentally observed ones. However, it is also possible that the simple material model being used does not suffice, and that a more accurate model of enamel, accounting for the properties of the the protein that is thought to surround the enamel crystallites should be used in the future [156].

Even considering that the local mechanical properties of hydroxyapatite may vary significantly from the average values (of both E and UTS) that are available in the literature and that the value of E_{HA} may have been overestimated in this work, the results obtained using both the analytical and the FE *SmallPore* models strongly suggest that the thermal expansion of liquid pore water may play a significant role in cracking and ablation of human dental enamel. Because the pressure experienced at the water pores is high enough to prevent water vaporization from taking place, water vaporization may begin only after cracking of the pore walls has occurred, a hypothesis that so far has not been considered by other authors.

The results indicate that the CO₂ laser may ablate enamel in a more reproducible manner than the Er:YAG, which makes it a better choice for the tunnelling technique being developed by Pearson to treat dental caries. The Er:YAG laser may induce higher local stress concentration than the CO₂ laser if regions like lamellae or tufts (which have dimensions on the order of tens of microns) are irradiated, and this may generate large cracks. Therefore, the CO₂ laser seems to be a better choice than the Er:YAG laser to ablate enamel.

6.5 Investigating the influence of the pulse duration on the stress levels: the pulse duration models

One of the most important factors governing the outcome of laser irradiation of a material is the pulse duration, which was discussed in Chapter 2. The effect of pulse duration on ablation by IR lasers has been extensively studied. In general, it

is accepted by the scientific community that to minimize thermal damage around the ablated site, the pulse duration, τ_p , should be inferior to the characteristic thermal relaxation time, τ_{ther} . If $\tau_p \ll \tau_{ther}$, the temperature at the irradiated site is maximized because only small amounts of energy diffuse out of it during the laser pulse, and the laser is operating under thermal confinement. If τ_p is significantly shorter than the acoustic relaxation time, τ_{ac} , then it is said that ablation occurs under conditions of stress or inertial confinement. Under stress confinement conditions, the stress transients are normally much higher than the quasi-static thermal stress generated in the material and, consequently, mechanical damage such as cracks is much more likely to occur. For most materials, $\tau_{ac} \ll \tau_{ther}$ [56]. While these general guidelines are known and are used to determine the order of magnitude of τ_p to use for particular procedures, they do not easily allow the optimization of this quantity beyond this, as discussed already in Chapter 2. In particular, the behavior of materials under laser pulses with $\tau_{ac} < \tau_p < \tau_{ther}$ is particularly difficult to predict based on these generic rules. For example, Er:YAG and CO₂ laser pulses with a duration of 0.15 μs have been reported to induce significant mechanical damage on enamel and dentine despite the fact that these pulses are significantly longer than τ_{ac} for these materials [157]. There is consequently a need for models with sufficient predictive capability to allow the fine-tuning of laser operating parameters, in particular the pulse duration, easily adaptable to different materials and lasers. In this Section a finite element model of human dental enamel under radiation by the CO₂ laser is used to investigate the thermal and mechanical dynamical response of this material to pulses of varying duration, in the regime $\tau_p \geq \tau_{ac}$.

6.5.1 Model description

Model *Cubes*, already described in Section 6.2, is used in all the simulations performed here. If the reader remembers, it has dimensions $23 \times 23 \times 35 \mu\text{m}^3$ but does not account for enamel's microstructure or inhomogeneous chemical composition at this scale. As usual, the thermal simulations were performed, using the implicit algorithm available in ABAQUS Standard. Subsequently, the temperature as a function of time at each node was passed into the mechanical analyzes, performed using the Explicit algorithm available in ABAQUS because this algorithm is more suitable to study rapid events like laser pulses. The total duration of the simulations varied between 100 and 250 μs ; the duration of the laser pulses

varied between 0.1 and 150 μs , ranges for which the thermal interaction with the material dominates.

In order to distinguish between effects caused by the lower temperatures reached in the material when longer pulses are used (because of heat diffusion) and effects caused by the actual pulse duration, a second set of simulations were performed. All the mechanical simulations in this second set share the same temperature distribution, the one obtained in the first set of simulations for a 0.35 μs laser pulse. This temperature distribution was divided into two parts, part A containing the temperature as a function of time during the laser pulse for all nodes in the model, and part B containing the temperature as a function of time after the laser pulse. In this set of simulations the timescale of part A was compressed or extended so that those temperature values were applied in different time intervals in the mechanical analyzes, corresponding to different pulse durations: 0.1, 1, 10 and 100 μs . To continue the mechanical simulation for longer times than the laser pulse, part B of the temperature distribution in question was applied to the model without any change. In this manner one could ascertain whether the observed behavior of the model in terms of stress derived from the lower temperatures reached when longer pulses are used and the same incident fluence is kept, or if they are in fact a consequence of the duration of the laser pulse.

6.5.2 Results and discussion

The temperature distributions obtained for all simulations share the same qualitative features: the maximum temperature is reached at the surface of the model and at the end of the laser pulse, and the only appreciable temperature gradients are along OZ (the optical axis of the laser beam), similarly to what was reported previously. The temperature maps are not shown here since they are similar to those already given in Fig. 6.14. The maximum temperatures obtained for the first set of simulations, in which the same amount of energy is deposited by the laser in all simulations, are given in Table 6.24. It is apparent that pulse durations between 0.1 and 2 μs cause little change in the maximum temperature reached (less than 10 $^{\circ}\text{C}$), but longer laser pulses are associated with significantly lower maximum temperatures (up to 45 $^{\circ}\text{C}$ lower). Both the mean and the maximum VMS reached at the center of the irradiated face of the modelled structure, also given in Table 6.24, are higher for shorter pulse durations if τ_p is shorter than 10 μs . However, the increase of the maximum VMS with shorter pulses is very large while

Max. abs. intensity, I_0 (J/(m ² s ¹))	τ_p (μ s)	Max. temp. reached ($^{\circ}$ C)	Max. stress reached (N/m ²)	Mean stress at the end of the laser pulse (N/m ²)
4.20×10^{10}	0.1	162	4.5×10^7	1.6×10^7
2.10×10^{10}	0.2	162	2.9×10^7	1.3×10^7
1.20×10^{10}	0.35	160	2.7×10^7	1.2×10^7
7.00×10^9	0.6	159	1.9×10^7	1.2×10^7
4.20×10^9	1	158	1.7×10^7	1.2×10^7
2.10×10^9	2	155	1.3×10^7	1.1×10^7
4.20×10^8	10	147	5.5×10^6	4.8×10^6
8.40×10^7	50	132	8.0×10^6	7.7×10^6
4.20×10^7	100	123	1.2×10^7	1.2×10^7
2.80×10^7	150	117	1.3×10^7	1.2×10^7

Table 6.24: Mean and maximum Von Mises stress stress and maximum temperature reached at the center of the irradiated face of model *Cubes* at the end of the CO₂ laser pulse, as a function of the maximum absorbed intensity, I_0 , and pulse duration, τ_p . For each simulation, the mean VMS was averaged over 1 μ s after the end of the laser pulse. Note that the incident fluence was maintained constant at 0.42 J/cm².

the increase of the mean VMS after the laser pulse is only moderate. In fact, the maximum VMS for $\tau_p = 0.1 \mu$ s is 55% higher than the equivalent value for $\tau_t = 0.2 \mu$ s, even though the maximum temperature reached by the model is the same in both cases. The magnitude of the difference between the stress values at longer and shorter pulse durations is more evident in Fig. 6.24, which shows the VMS values at the center of the irradiated face of the model for 0.1 and 10 μ s laser pulses, representative of results obtained for analyzes with τ_p up to 1 μ s and τ_p between 2 and 100 μ s, respectively. In this figure it is readily apparent that, while the mean VMS for both analyzes is relatively similar, the VMS for the short pulse simulation oscillates significantly around its mean value but the VMS for the longer pulse analysis does not. The stress at the free surface of the laser reaches a minimum value between 10 and 20 μ s, a non-intuitive result present for all pulse durations that explains the fact that the lowest VMS is reached when $t = 10 \mu$ s and not towards the end of the simulated time period. These results suggest that short laser pulses can generate large stress oscillations in the irradiated objects even when the pulse is far too long to be under stress confinement conditions (τ_p should be shorter than 20 ns in this case). Furthermore, these results suggest that τ_p influences the amplitude of the stress vibrations experienced by the irradiated object, independently of the maximum temperature reached.

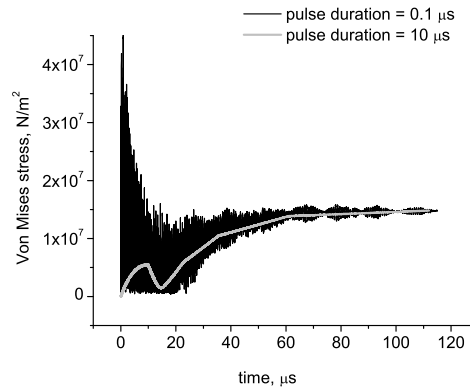


Figure 6.24: Von Mises stress as a function of time for the central top element of model *Cubes* for two different pulse durations: 0.1 and 10 μs .

To further test these hypotheses, a second set of simulations was performed according to what was previously described. The results obtained in this set are given in Table 6.25.

Pulse duration (μs)	Max. temperature reached ($^{\circ}\text{C}$)	Max. stress reached (N/m^2)	Mean stress at the end of the laser pulse (N/m^2)
0.1	160	4.5×10^7	1.6×10^7
0.35	160	2.6×10^7	1.6×10^7
1	160	1.8×10^7	1.2×10^7
10	160	1.3×10^7	1.2×10^7
100	160	1.3×10^7	1.2×10^7

Table 6.25: Mean and maximum VMS stress and maximum temperature reached at the center of the irradiated face of the modelled structure as a function of the pulse duration. For each simulation, the mean VMS was averaged over 1 μs after the end of the laser pulse. Note that the same temperature distribution was used as input to the mechanical analyzes reported.

It is apparent that, while the temperature distribution used as input to the mechanical simulations is the same, the maximum VMS reached at the center of the irradiated face of the modelled structure is significantly higher for the shorter τ_p 's. At the same time, the mean VMS stress at the same location is only slightly higher for the shorter τ_p 's. An analysis of plots of VMS as a function of time (not presented, since they are similar to those given in Fig. 6.24) again indicates that a τ_p shorter than 1 - 2 μs will generate a high frequency and high amplitude oscillation in the VMS stress values reached, the amplitude being higher for $\tau_p = 0.1 \mu\text{s}$.

This is in agreement with results obtained by Fried et al. [157], which suggest that laser pulses with a duration of $0.15 \mu\text{s}$ induce large stress transients and significant cracking in enamel [157], contrary to laser pulses of duration close to $10 \mu\text{s}$. However, the results cannot yet be fully compared against experimental data since existing studies have not directly compared, under controlled conditions, the results of ablating dental enamel when $0.1 < t_p < 10 \mu\text{s}$. Therefore, one cannot be certain whether the magnitude of the effect of the pulse duration described in this work in the ablation procedure will be this high in reality, although the fact that a similar behavior was observed in simulations performed using pulses with various durations between 0.35 and $10 \mu\text{s}$ and a much smaller enamel model (similar to that presented in section 6.4, and not described in more detail in the present section) suggests that this results may in fact be quite solid.

Keeping these limits of validity in mind, the results described in this Section may facilitate the search of the optimal laser parameters to ablate dental hard tissue and to modify the surface of enamel to make it less susceptible to caries. The higher stress transients experienced by the material when shorter (less than $2 \mu\text{s}$) laser pulses are used suggest that these pulses may be more efficient than longer pulses at ablating tissue but, at the same time, they are more likely to inflict unwanted damage in the material. For the same reasons, these results also suggest that $\tau_p < 2 \mu\text{s}$ are less adequate to irradiate the surface of enamel to increase its resistance to acid attack. These results indicate that free-running lasers, which normally have a long macropulse ($100 - 300 \mu\text{s}$) composed of several micropulses, each with a duration of approximately $1 \mu\text{s}$, may not be the most appropriate to use for enamel surface modification. However, further work investigating the response of the material to multiple pulses must be done to support this conclusion. These results can be extrapolated to other wavelengths commonly used to ablate dental hard tissue, such as the Er:YAG laser at $\lambda = 2.9 \mu\text{m}$, and thus provide an explanation as to why the free-running Er:YAG produces worse results in enamel surface modification [94] than longer pulsed CO_2 lasers [132].

Chapter 7

Conclusions and future work

The main accomplishments of the work presented in this Thesis are: 1) having developed a new set of boundary conditions for Finite Element models that allow to effectively simulate the static and dynamic behavior of a piece of material which is a part of a larger object, thus avoiding computationally prohibitive larger models; 2) having elucidated the role of the mesostructure on the stress distribution induced in enamel by two wavelengths very frequently used in dentistry, the CO₂ and Er:YAG lasers; 3) providing a possible explanation for the observed differences in ablation of enamel by these lasers, despite the fact that this material has the same absorption coefficient for both of them, and 4) presenting evidence which supports the choice of a particular laser (the CO₂ laser at $\lambda = 10.6 \mu\text{m}$) and pulse duration (around $10 \mu\text{s}$) as the laser operating parameters that will produce the best results in ablation of enamel at the lowest cost and with fewer side effects. This is the most significant accomplishment of this Thesis, since it represents a direct contribution to the optimization of the laser operating parameters for the ablation of enamel.

The results obtained when the set of BC's developed during the work that led to this Thesis were applied were shown to compare much more favorably to reference values than the results of models in which these BC's were not applied. The BC's described in this Thesis represent a simple but effective way of investigating phenomena taking place in a material at a small scale without having to create large models that include the entire structure being modelled. The method developed to apply BC's has a very general nature, so it can be applied not only to investigate laser ablation of dental materials but to study the mesoscale response of various materials to thermal or mechanical loads, such as ablation of ceramics

or mechanical response of thin films to heating. It is thus a tool that may be of use to the scientific community.

The results presented in this Thesis have contributed to clarifying the role of the enamel mesostructure on the temperature and stress distributions when this material is irradiated with CO₂ or Er:YAG lasers: results indicate that, despite the fact that the average absorption coefficient for enamel is the same for both lasers, the temperature distribution generated in enamel is very different for both lasers.

When using the CO₂ laser, for which the water and the mineral have similar absorption coefficients, water and mineral reach the same temperature both during and after the laser pulse. Despite reaching the same temperature as the mineral, the water pores seem to act as stress concentration points, generating pressures which are much higher than those induced at the mineral. The magnitude of this effect should vary with the magnitude of the thermal expansion coefficient and the bulk modulus of the material at the pores and the Young's modulus of the mineral. This indicates that, at least at lower fluences for which the melting point of hydroxyapatite is not reached, the dominant ablation mechanism of enamel by the CO₂ laser should be the explosive vaporization of water.

When using the Er:YAG laser, the water at the pores reaches different temperatures from the mineral, at least before thermal equilibrium is reached between them, which occurs after the end of the laser pulse for the pulse durations and laser intensity investigated here. Also, for the same laser intensity, the temperature reached in the water pore at the end of the laser pulse is a function of the pore size: for small pores, which have a higher area-to-volume ratio, the pore loses heat very rapidly, and thus tends to reach lower temperatures; for large pores, the heat loss is much slower and the pores reach much higher temperatures. This indicates that the effect of the Er:YAG laser in enamel will vary more strongly according to the enamel microstructure than when the CO₂ laser is used, which may have significant practical implications. For one thing, it suggests that optimal Er:YAG laser operating parameters may differ between deciduous or permanent teeth, since enamel in deciduous teeth has a higher content in water. For another, it implies that very high stresses may be induced in enamel when large regions richer in water and organic material (such as enamel spindles, tufts and lamellae) are irradiated by the Er:YAG laser, thus generating large cracks in the material. The fact that the effect of the CO₂ laser seems to be much less dependent on the microstructure than the effect of the Er:YAG laser indicates that the CO₂ laser

should yield more reproducible results and, consequently, that it is most likely a better choice to ablate enamel. For the same reasons, the CO₂ laser is also a better choice to irradiate enamel using sub-ablative fluences, a procedure under study to provide enamel with a more acid-resistant surface.

Having collected evidence that supported the choice of the CO₂ laser in detriment of the Er:YAG laser, the next step was to understand how to tune the parameters of this laser to obtain better results. A review of the literature indicated that the spatial profile most likely to generate the least thermal damage at the rim of the irradiated site is a top-hat profile. With respect to the optimal temporal intensity profile, evidence in the literature strongly indicated that a constant profile is the most adequate, and that intensity spikes should be avoided because they may trigger the existence of a plasma which will then stall the ablation rates. For the same reason, the optimal fluence range would be just below the plasma threshold, but a reliable numerical estimate of this threshold could not be obtained. To minimize shielding by the plume below the plasma threshold, the repetition rate should be kept below 1000 Hz. Finally, the effect of the laser pulse was investigated and it was found that a pulse duration of less than 2 μs induced much more intense stress transients than a pulse duration of 10 μs or longer, despite the fact that both pulse durations are above the acoustic relaxation time and lower than the thermal relaxation time of the material. On the other hand, when pulse durations higher than 10 μs are used, a significant amount of energy is capable of diffusing out of the heated volume before the end of the pulse, and thus thermal damage increases. Therefore, it was concluded that a laser pulse with a duration of $\simeq 10 \mu\text{s}$ seems to be the most adequate to produce the best results when ablating enamel.

These results represent a contribution to the task of finding the optimal laser operating parameters to ablate enamel, but much more is left to do. One aspect that still needs to be addressed is the ablation fluence. While general guidelines have been provided by the work presented in this Thesis as to the best fluence to conduct ablation, the optimal range of values for this parameter is still to be found. Another issue that needs further investigation is the matter of externally applied water to serve as coolant. Since experimental evidence suggests that cooling of the irradiated sites is necessary in order to keep melting and recrystallization to a minimum, it is important to determine how the externally applied cooling water will influence ablation. There are two aspects to this question: it is necessary to determine how a thin layer of externally applied water alters the ablation rates

and also whether accumulation of water at the crater will prevent ablation from taking place.

In order to provide answers to these questions it is important to improve the existing models. The current models give good qualitative insight into ablation but do not go further than that (for example, the threshold cracking fluence of enamel is largely underestimated). One of the key issues to be addressed is the question of the theory used to model the mineral. In the work presented here, the mineral was modelled in a simplistic manner as a linear elastic solid. However, the mineral in enamel is in fact a nanocomposite, and several material-models exist that will describe its behavior with more accuracy. The work by Ji et al. [156] is a good starting point to improve this aspect of the model. It is also necessary to understand if a simple cracking criterium such as assuming that the material cracks when stress becomes higher than the material's ultimate tensile strength, or if a more complex model, including material fatigue for example, is necessary to make accurate predictions. Future models should also investigate the effect of cooling water on the temperature and stress maps.

Finally, another issue that should be addressed in the future is that of model validity. The author is aware that only limited validation of the models was possible by comparison with experimental results, because of difficulty in finding the information in the literature. While the number of papers on the topic of enamel laser ablation is high, a large fraction of them do not report the full set of experimental parameters used by their authors. Only a few works report the data carefully and with detail, but most of them not in the range of values suggested in this Thesis. Therefore, it would be important to add an experimental component to future investigation in this topic, to test the inferences made from the results.

Bibliography

- [1] Richard Ten Cate, editor. *Oral Histology - Development, Structure and Function*. Mosby, London, 5th edition, 1998.
- [2] H. Markolf Niemz. *Laser-Tissue Interactions - Fundamentals and applications*. Springer-Verlag, Berlin, 1st edition, 1996.
- [3] G. H. Dibdin. The water in human dental enamel and its diffusional exchange measured by clearance of tritiated-water from enamel slabs of varying thickness. *Caries Research*, 27(2):81–86, 1993.
- [4] F. S. L. Wong, P. Anderson, H. Fan, and G. R. Davis. X-ray microtomographic study of mineral concentration distribution in deciduous enamel. *Archives of Oral Biology*, 49:937–944, 2004.
- [5] T. Kodaka, K. Debari, and M. Kuroiwa. Mineral-content of the innermost enamel in erupted human teeth. *Journal of Electron Microscopy*, 40(1):19–23, 1991.
- [6] S. N. Bhaskar. *Histologia e embriologia oral de orban*. Livraria Editora Artes Médicas, 8th edition, 1978.
- [7] G. H. Dibdin and D. F. G. Poole. Surface-area and pore-size analysis for human-enamel and dentine by water-vapor sorption. *Archives of Oral Biology*, 27(3):235–241, 1982.
- [8] J. M. P. M. Borggreven, F. C. M. Driessens, and J. W. E. Vandijk. Diffusion through bovine tooth enamel as related to the water- structure in its pores. *Archives of Oral Biology*, 25(5):345–348, 1980.
- [9] Ying-Chun Liu, Qi Wang, and Ling-Hong Lu. Water confined in nanopores: its molecular distribution and diffusion at lower density. *Chemical Physics Letters*, 381:210–215, 2003.
- [10] A. Giaya and R. W. Thompson. Water confined in cylindrical micropores. *Journal of Chemical Physics*, 117(7):3464–3475, 2002.
- [11] J. L. Cuy, A. B. Mann, K. J. Livi, M. F. Teaford, and T. P. Weihs. Nanoin-dentation mapping of the mechanical properties of human molar tooth enamel. *Arch.Oral.Biol.*, 47(4):281–291, 2002.

- [12] S. Habelitz, S. J. Marshall, G. W. Marshall Jr, and M. Balooch. Mechanical properties of human dental enamel on the nanometre scale. *Arch.Oral.Biol.*, 46:173–183, 2001.
- [13] I. R. Spears, R. Vannoort, R. H. Crompton, G. E. Cardew, and I. C. Howard. The effects of enamel anisotropy on the distribution of stress in a tooth. *Journal of Dental Research*, 72(11):1526–1531, 1993.
- [14] Mathilde C. Peters and Mary Ellen McLean. Minimally invasive operative care I. minimal intervention and concepts for minimally invasive cavity preparations. *The Journal of Adhesive Dentistry*, 3(1):7–16, 2001.
- [15] Mathilde C. Peters and Mary Ellen McLean. Minimally invasive operative care II. contemporary techniques and materials: an overview. *The Journal of Adhesive Dentistry*, 3(1):17–31, 2001.
- [16] NHS Centre for Reviews and Dissemination. Effective health care: Dental restoration: what type of filling? Technical report, University of York, April 1999.
- [17] J. M. White and W. S. Eakle. Rationale and treatment approach in minimally invasive dentistry. *Journal of the American Dental Association*, 131:13S–19S, 2000.
- [18] A. Sheiham. Minimal intervention in dental care. *Medical Principles and Practice*, 11:2–6, 2002.
- [19] M. J. Tyas, K. J. Anusavice, J. E. Frencken, and G. J. Mount. Minimal intervention dentistry - a review - FDI commission project 1-97. *International Dental Journal*, 50(1):1–12, 2000.
- [20] A. Ribeiro, C. Rousseau, J. Girkin, A. Hall, R. Strang, C. J. Whitters, S. Creanor, and A. S. L. Gomes. A preliminary technique for investigation of a spectroscopic the diagnosis of natural caries lesions. *Journal of Dentistry*, 33(1):73–78, 2005.
- [21] D. Ericson, Edwina Kidd, Dorothy McComb, Ivar Mjor, and Michael J. Noack. Minimally invasive dentistry - concepts and techniques in cariology. In *European Festival of oral Science*, volume 1 of *Oral and preventive dentistry*, pages 59–72, Cardiff, UK, 2002.
- [22] K. Yamagishi, K. Onuma, T. Suzuki, F. Okada, J. Tagami, M. Otsuki, and P. Senawangse. A synthetic enamel for rapid tooth repair. *Nature*, 433(7028):819–819, 2005.
- [23] D. Crawley, C. Longbottom, V. P. Wallace, B. Cole, D. Arnone, and M. Pepper. Three-dimensional terahertz pulse imaging of dental tissue. In Glenn S. Edwards, Joseph Neev, Andreas Osterdorf, and John Sutherland, editors,

Commercial and Biomedical Applications of Ultrafast and Free-Electron Lasers, volume 4633 of *Proceedings of SPIE*, pages 84–89. SPIE, 2002.

- [24] C. Longbottom, D. Crawley, B. Cole, D. Arnone, V. Wallace, and M. Pepper. Potential uses of terahertz pulse imaging in dentistry: caries and erosion detection. In P. Rechmann, D. Fried, and T. Hennig, editors, *Lasers in Dentistry VIII*, volume 4610 of *Proceedings of SPIE*, pages 109–112. SPIE, 2002.
- [25] Hans Jorg Staehle. Minimally invasive restorative treatment. *The journal of adhesive dentistry*, 1(3):267–284, 1999.
- [26] E. G. Borisova, T. T. Uzunov, and L. A. Avramov. Early differentiation between caries and tooth demineralization using laser-induced autofluorescence spectroscopy. *Lasers in Surgery and Medicine*, 34(3):249–253, 2004.
- [27] R. F. Z. Lizarelli, J. C. Bregagnolo, R. Z. Lizarelli, J. M. C. Palhares, and G. E. P. Villa. A comparative in vitro study to diagnose decayed dental tissue using different methods. *Photomedicine and Laser Surgery*, 22(3):205–210, 2004.
- [28] R. J. Jeon, A. Mandelis, and S. H. Abrams. Depth profilometric case studies in caries diagnostics of human teeth using modulated laser radiometry and luminescence. *Review of Scientific Instruments*, 74(1):380–383, 2003.
- [29] L. Zach and G. Cohen. Pulp responde to externally applied heat. *Oral Surgery Oral Medicine Oral Pathology Oral Radiology and Endodontics*, 19(4):515–530, 1965.
- [30] Randall Saaf, Brian J. F. Wong, Thomas E. Milner, George Peavey, and Bahman Anvari. Acoustic measurements during Erbium : YAG laser ablation of porcine calcified tissues. In R. Rox Anderson et al., editor, *Lasers in Surgery: Advanced Characterization, Therapeutics, and Systems VIII*, volume 3245 of *Progress in Biomedical Optics*, pages 250–257. SPIE, 1998.
- [31] G. B. Altshuler, A. V. Belikov, V. N. Baline, A. S. Gook, S. P. Kropotov, V. L. Selivanov, A. V. Skrypnik, and C. V. Prikhodko. Results of clinical application of YAG : Er laser in dentistry. In *Medical Applications of Lasers in Dermatology, Cardiology, Ophthalmology, and Dentistry II*, volume 3564 of *Proceedings of SPIE*, pages 194–196. SPIE, 1998.
- [32] Aldo Brugnera Jr, F. Zanin, Marcelo Moura, Fábio Seixas, Cyntia R. A. Estrela, Carlos Estrela, and Jesus D. Pcora. Microbial contamination of the environment after the irradiation of Er : YAG laser in infected root canals. In Peter Rechmann, Daniel Fried, and Thomas Hennig, editors, *Lasers in Dentistry IX*, volume 4950, pages 195–202. SPIE, 2003.

- [33] A. V. Belikov, G. B. Altshuler, B. T. Moroz, and I. V. Pavlovskaya. Investigation of IR absorption spectra of oral cavity bacteria. In *Laser Applications in Medicine and Dentistry*, volume 2922 of *Proceedings of SPIE*, pages 113–118. SPIE, 1996.
- [34] R. Hibst, K. Stock, R. Gall, and U. Keller. Controlled tooth surface heating and sterilisation by Er : YAG laser radiation. In *Laser Applications in Medicine and Dentistry*, volume 2922 of *Proceedings of SPIE*, pages 119–126. SPIE, 1996.
- [35] David M. Harris and Michael Yessik. Therapeutic ratio quantifies laser antiseptis: Ablation of porphyromonas gingivalis with dental lasers. *Lasers in Surgery and Medicine*, 35:206–213, 2004.
- [36] J. A. Williams, G. J. Pearson, M. J. Colles, and M. Wilson. The photo-activated antibacterial action of toluidine blue O in a collagen matrix and in carious dentine. *Caries Research*, 38(6):530–536, 2004.
- [37] Drian O A Murgu, Blanche Cerruti, Marcela L Redgolo, and Maria C Chavantes. Effects of a superpulsed CO₂ laser on human teeth. In Reginald Birngruber and Hubert van den Bergh, editors, *Laser-tissue interactions*, volume 4433 of *Proceedings of SPIE*, pages 103–106, San Jose, California, 2001. SPIE.
- [38] J.M. Ferreira, J. Palamara, P.P. Phakey, W.A. Rachinger, and H.J. Orams. Effects of continuous-wave CO₂-laser on the ultrastructure of human dental enamel. *Archives of Oral Biology*, 34(7):551–562, 1989.
- [39] J. Palamara, P. P. Phakey, H. J. Orams, and W. A. Rachinger. The effect on the ultrastructure of dental enamel of excimer-dye, argon-ion and CO₂ lasers. *Scanning Microscopy*, 6(4):1061–1071, 1992.
- [40] M. A. Pogrel, D. F. Muff, and G. W. Marshall. Structural-changes in dental enamel induced by high-energy continuous wave carbon-dioxide laser. *Lasers in Surgery and Medicine*, 13(1):89–96, 1993.
- [41] J. Neev, L .B. da Silva, M. D. Feit, M. D. Perry, A. M. Rubenchik, and B. C. Stuart. Ultrashort pulse lasers for hard tissue ablation. *IEEE Journal of Selected Topics in Quantum Electronics*, 2(4):790–800, 1996.
- [42] A. A. Oraevsky, L. B. da Silva, A. M. Rubenchik, M. D. Feit, M. E. Glinsky, M. D. Perry, B. M. Mammini, W. Small, and B. C. Stuart. Plasma mediated ablation of biological tissues with nanosecond-to-femtosecond laser pulses: relative role of linear and nonlinear absorption. *IEEE Journal of Selected Topics in Quantum Electronics*, 2(4):801–809, 1996.
- [43] A. Vogel, J. Noack, G. Mittmann, and G. Paltauf. Femtosecond-laser-produced low-density plasmas in transparent biological media: A tool for

- the creation of chemical, thermal and thermomechanical effects below the optical breakdown threshold. In Glenn S Edwards, Joseph Neev, A. Ostendorf, and John Sutherland, editors, *Commercial and Biomedical Applications of Ultrafast and Free- Electron Lasers*, volume 4633 of *Proceedings of SPIE*, pages 23–37. SPIE, 2002.
- [44] M. D. Feit, A. M. Rubenchik, B. M. Kim, L. B. da Silva, and M. D. Perry. Physical characterization of ultrashort laser pulse drilling of biological tissue. *Applied Surface Science*, 129:869–874, 1998.
- [45] B. A. Auld. *Acoustic fields and waves in solids*, volume 1. Krieger Publishing Company, Malabar, Florida, 2nd edition, 1990.
- [46] D. Perez and L. J. Lewis. Molecular-dynamics study of ablation of solids under femtosecond laser pulses. *Physical Review B*, 67(18):184102, 2003.
- [47] H. Y. Zheng, W. Zhou, H. X. Qian, T. T. Tan, and G. C. Lim. Polarisation-independence of femtosecond laser machining of fused silica. *Applied Surface Science*, 236(1-4):114–119, 2004.
- [48] N. Barsch, K. Korber, A. Ostendorf, and K. H. Tonshoff. Ablation and cutting of planar silicon devices using femtosecond laser pulses. *Applied Physics A-Materials Science & Processing*, 77(2):237–242, 2003.
- [49] J. Kruger, W. Kautek, and H. Newesely. Femtosecond-pulse laser ablation of dental hydroxyapatite and single-crystalline fluoroapatite. *Applied Physics A-Materials Science & Processing*, 69:S403–S407, 1999.
- [50] A. V. Rode, E. G. Gamaly, B. Luther-Davies, B. T. Taylor, J. Dawes, A. Chan, R. M. Lowe, and P. Hannaford. Subpicosecond laser ablation of dental enamel. *Journal of Applied Physics*, 92(4):2153–2158, 2002.
- [51] A. A. Serafetinides, M. I. Makropoulou, A. K. Kar, and M. Khabbaz. Picosecond and femtosecond laser ablation of hard tissues. In G. B. Altshuler et al., editor, *Conference on Laser Applications in Medicine and Dentistry*, volume 2922, pages 200–208. SPIE, 1996.
- [52] W. B. Armstrong, J. A. Neev, L. B. da Silva, A. M. Rubenchik, and B. C. Stuart. Ultrashort pulse laser ossicular ablation and stapedotomy in cadaveric bone. *Lasers in Surgery and Medicine*, 30(3):216–220, 2002.
- [53] M. H. Niemz. Ultrashort laser pulses in dentistry: advantages and limitations. In Joseph Neev, editor, *Applications of Ultrashort-Pulse Lasers in Medicine and Biology*, volume 3255 of *Proceedings of SPIE*, pages 84–91. SPIE, 1998.
- [54] E. J. Swift, G. S. Edwards, J. Perdigão, J. Y. Thompson, M. F. Nunes, D. E. Ruddell, and A. Negishi. Free-electron laser etching of dental enamel. *Journal of Dentistry*, 29(5):347–353, 2001.

- [55] L. V. Zhigilei, E. Leveugle, B. J. Garrison, Y. G. Yingling, and M. I. Zeifman. Computer simulations of laser ablation of molecular substrates. *Chemical Reviews*, 103(2):321–347, 2003.
- [56] G. Paltauf and P. E. Dyer. Photomechanical processes and effects in ablation. *Chemical Reviews*, 103(2):487–518, 2003.
- [57] R.F.Z. Lizarelli, C. Kurachi, L. Misoguti, and V.S. Bagnato. A comparative study of nanosecond and picosecond laser ablation in enamel: Morphological aspects. *Journal of Clinical Laser Medicine & Surgery*, 18(3):151–157, 2000.
- [58] M. N. Ediger, G. H. Pettit, and L. S. Matchette. In vitro measurements of cytotoxic effects of 193 nm and 213 nm laser pulses at subablative fluences. *Lasers in Surgery and Medicine*, 21(1):88–93, 1997.
- [59] T. Hennig and P. Rechmann. Basics of the application of pulsed lasers in dentistry. In *Laser Applications in Medicine and Dentistry*, volume 2922 of *Proceedings of SPIE*, pages 64–73. SPIE, 1996.
- [60] V. N. Bagratashvili, A. I. Omel’chenko, A. P. Sviridov, E. N. Sobol, E. V. Lunina, Y. N. Zhitnev, G. L. Markaryan, and V. V. Lunin. An EPR and optical spectroscopy study of the effect of laser radiation on biological tissues. *High Energy Chemistry*, 35(6):423–429, 2001.
- [61] M. C. D. N. Huysmans and J. M. Thijssen. Ultrasonic measurement of enamel thickness: a tool for monitoring dental erosion? *Journal of dentistry*, 28(3):187–191, 2000.
- [62] Carlos A. G. Moura Branco. *Mecânica dos Materiais*. Fundação Calouste Gulbenkian, Porto, 3rd edition, 1998.
- [63] D. Fried, M. J. Zuerlein, J. Featherstone, W. Seka, Clifford Duhn, and Sandra M. McCormack. IR laser ablation of dental enamel: mechanistic dependence on the primary absorber. *Applied Surface Science*, 127-129:852–856, 1998.
- [64] J. B. Zhu, Y. G. Li, N. Q. Liu, G. Q. Zhang, M. K. Wang, G. Wu, X. P. Yan, Y. Y. Huang, W. He, Y. M. Dong, and X. J. Gao. Primary experimental studies on mid-infrared FEL irradiation on dental substances at BFEL. *Nuclear Instruments & Methods in Physics Research Section A - Accelerators Spectrometers Detectors and Associated Equipment*, 475(1-3):630–634, 2001.
- [65] D. W. Holcomb and R. A. Young. Thermal-decomposition of human tooth enamel. *Calcified Tissue International*, 31(3):189–201, 1980.
- [66] D. Fried, R. E. Glena, J. D. B. Featherstone, and W. Seka. Permanent and transient changes in the reflectance of CO₂ laser-irradiated dental hard tissues at $\lambda=9.3, 9.6, 10.3,$ and $10.6 \mu\text{m}$ and at fluences of 1-20 J/cm². *Lasers in Surgery and Medicine*, 20(1):22–31, 1997.

- [67] Jaap R. Zijp. *Optical properties of dental hard tissues*. PhD thesis, University of Groningen, 2001.
- [68] D. Fried, S. R. Visuri, J. D. B. Featherstone, J. T. Walsh, W. Seka, E. R. Glana, S. M. McCormack, and H. A. Wigdor. Infrared radiometry of dental enamel during Er : YAG and Er : YSGG laser irradiation. *J Biomedical Optics*, 1:455–465, 1996.
- [69] M. J. Zuerlein, D. Fried, J. D. B. Featherstone, and W. Seka. Optical properties of dental enamel in the mid-IR determined by pulsed photothermal radiometry. *IEEE Journal of Selected Topics in Quantum Electronics*, 5(4):1083–1089, 1999.
- [70] S. E. Strawn, J. M. White, G. W. Marshall, L. Gee, H. E. Goodis, and S. J. Marshall. Spectroscopic changes in human dentine exposed to various storage solutions - short term. *Journal of Dentistry*, 24(6):417–423, 1996.
- [71] Harumitsu Nishikawa. Thermal behavior of hydroxyapatite in structural and spectrophotometric characteristics. *Materials Letters*, 50:364–370, 2001.
- [72] Sushmita Franklin, P. Chauhan, A. Mitra, and R. K. Thareja. Laser ablation of human tooth. *Journal of Applied Physics*, 97(094919), 2005.
- [73] M. J. Zuerlein. *Interactions of IR lasers with dental hard tissues at clinically relevant wavelengths*. PhD thesis, University of California at San Francisco and at Berkeley, 1999.
- [74] D. Fried, M. J. Zuerlein, C. Q. Le, and J. D. B. Featherstone. Thermal and chemical modification of dentin by 9-11 μm CO₂ laser pulses of 5-100 μs duration. *Lasers in Surgery and Medicine*, 31(4):275–282, 2002.
- [75] P. Serra, J. M. Fernandez-Pradas, J. Navarro, and J. L. Morenza. Study of the plume generated by Nd : YAG laser ablation of a hydroxyapatite target. *Applied Physics A - Materials Science & Processing*, 69:S183–S186, 1999.
- [76] J. L. Arias, M. B. Mayor, J. Pou, B. Leon, and M. Perez-Amor. Stoichiometric transfer in pulsed laser deposition of hydroxylapatite. *Applied Surface Science*, 154:434–438, 2000.
- [77] J. L. Arias, M. B. Mayor, J. Pou, B. Leon, and M. Perez-Amor. Transport of ablated material through a water vapor atmosphere in pulsed laser deposition of hydroxylapatite. *Applied Surface Science*, 186(1-4):448–452, 2002.
- [78] J. L. Arias, M. B. Mayor, J. Pou, B. Leon, and M. Perez-Amor. Laser ablation rate of hydroxylapatite in different atmospheres. *Applied Surface Science*, 208:57–60, 2003.

- [79] T. Wesendahl, P. Janknecht, B. Ott, and M. Frenz. Erbium : YAG laser ablation of retinal tissue under perfluorodecaline: Determination of laser-tissue interaction in pig eyes. *Investigative Ophthalmology & Visual Science*, 41(2):505–512, 2000.
- [80] Alfredo Dela Rosa, Anupama V. Sarma, Charles Q. Le, Robert S. Jones, and Daniel Fried. Peripheral thermal and mechanical damage to dentin with microsecond and sub-microsecond 9.6 μm , 2.79 μm , and 0.355 μm laser pulses. *Lasers in Surgery and Medicine*, 35:214–228, 2004.
- [81] Egberto Munin, Marcela L. Redgolo, Raquel de Almeida Ribeiro, Guilherme P. Scarpel de Mello, Thas Cachut Paradella, and Marcos Tadeu T. Pacheco. Effects of acid and laser treatments on the dentin nanocrystals. In Peter Rechmann, Daniel Fried, and Thomas Hennig, editors, *Lasers in Dentistry VII*, volume 4249 of *Proceedings of SPIE*, pages 115–120. SPIE, 2001.
- [82] B. Majaron, D. Sustercic, and M. Lukac. Influence of water spray on Er : YAG ablation of hard dental tissues. In Gregory B. Altshuler et al., editor, *Medical Applications of Lasers in Dermatology, Ophthalmology, Dentistry, and Endoscopy*, volume 3192 of *Progress in Biomedical Optics*, pages 82–87. SPIE, 1997.
- [83] J. R. Matson, E. Matson, R. S. Navarro, J. S. Bocangel, R. G. Jaeger, and C. P. Eduardo. Er : YAG laser effects on enamel occlusal fissures: An in vitro study. *Journal of Clinical Laser Medicine & Surgery*, 20(1):27–35, 2002.
- [84] Nahal Ashouri, Ramesh Shori, Jason M. Cheung, and Daniel Fried. Infrared laser ablation of dental enamel: influence of an applied water layer on ablation rate and peripheral damage. volume 4249 of *Lasers in dentistry VII Proceedings of SPIE*, pages 72–148, 2001.
- [85] Toru Eguro, Toru Maeda, Midori Tanabe, Masahito Otsuki, and Hisayoshi Tanaka. Adhesion of composite resins to enamel irradiated by the Er : YAG laser: application of the ultrasonic scaler on irradiated surface. *Lasers in Surgery and Medicine*, 28:365–370, 2001.
- [86] Y. Ishizaka, T. Eguro, T. Maeda, and H. Tanaka. Effects of Er : YAG laser irradiation on human dentin: polarizing microscopic, light microscopic and microradiographic observations, and FT – IR analysis. *Lasers in Surgery and Medicine*, 31(3):171–176, 2002.
- [87] T. Eguro, T. Maeda, M. Otsuki, Y. Nishimura, I. Katsuumi, and H. Tanaka. Adhesion of Er : YAG laser-irradiated dentin and composite resins: application of various treatments on irradiated surface. *Lasers in Surgery and Medicine*, 30(4):267–272, 2002.
- [88] M. Stock, R. Hibst, and U. Keller. Comparison of Er : YAG and Er : YSGG laser ablation of dental hard tissues. In *Medical Applications of Lasers*

in Dermatology, Ophthalmology, Dentistry, and Endoscopy, volume 3192 of *Proceedings of SPIE*, pages 88–95. SPIE, 1997.

- [89] M. A. Mackanos, E. D. Jansen, B. L. Shaw, J. S. Sanghera, I. Aggarwal, and A. Katzir. Delivery of midinfrared (6 to 7 μm) laser radiation in a liquid environment using infrared-transmitting optical fibers. *Journal of Biomedical Optics*, 8(4):583–593, 2003.
- [90] B. Ivanov, A. M. Hakimian, G. M. Peavy, and R. F. Haglund. Mid-infrared laser ablation of a hard biocomposite material: mechanistic studies of pulse duration and interface effects. *Applied Surface Science*, 208:77–84, 2003.
- [91] M. Otsuki, T. Eguro, T. Maeda, and H. Tanaka. Comparison of the bond strength of composite resin to Er : YAG laser irradiated human enamel pre-treated with various methods in vitro. *Lasers in Surgery and Medicine*, 30(5):351–359, 2002.
- [92] R. P. Ramos, D. T. Chimello, M. A. Chinelatti, T. Nonaka, J. D. Pecora, and R. G. P. Dibb. Effect of Er : YAG laser on bond strength to dentin of a self-etching primer and two single-bottle adhesive systems. *Lasers in Surgery and Medicine*, 31(3):164–170, 2002.
- [93] C. Apel, J. Meister, N. Schmitt, H. G. Graber, and N. Gutknecht. Calcium solubility of dental enamel following sub-ablative Er : YAG and Er : YSGG laser irradiation in vitro. *Lasers in Surgery and Medicine*, 30:337–341, 2002.
- [94] C. Apel, J. Meister, H. Gotz, H. Duschner, and N. Gutknecht. Structural changes in human dental enamel after subablative erbium laser irradiation and its potential use for caries prevention. *Caries Research*, 39(1):65–70, 2005.
- [95] B. N. Cavalcanti, J. L. Lage-Marques, and S. M. Rode. Pulpal temperature increases with Er : YAG laser and high-speed handpieces. *Journal of Prosthetic Dentistry*, 90(5):447–451, 2003.
- [96] D. Fried, N. Ashouri, T. Breunig, and R. Shori. Mechanism of water augmentation during IR laser ablation of dental enamel. *Lasers in Surgery and Medicine*, 31(3):186–193, 2002.
- [97] Christian Lee, Jerome Ragadio, and D. Fried. Influence of wavelength and pulse duration on peripheral thermal and mechanical damage to dentin and alveolar bone during IR laser ablation. volume 3910 of *Proceedings of SPIE*, pages 193–203, 2000.
- [98] N.M. Fried and D. Fried. Comparison of Er : YAG and 9.6 μm TEA CO₂ lasers for ablation of skull tissue. *Lasers in Surgery and Medicine*, 28(4):335–343, 2001.

- [99] E. Papagiakoumou, D. N. Papadopoulos, M. G. Khabbaz, M. I. Makropoulou, and A. A. Serafetinides. The influence of the Q-switched and free-running Er : YAG laser beam characteristics on the ablation of root canal dentine. *Applied Surface Science*, 233(1-4):234–243, 2004.
- [100] Marcelo Sampaio Moura, Fátima A. Zanin, Aldo Brugnera Jr., Cyntia Rodrigues de Araújo Estrela, Carlos Estrela, and Jesus Djalma Pécora. Antimicrobial effect of Er : YAG laser irradiation in infected root canals: an in vitro study. In Peter Rechmann, Daniel Fried, and Thomas Hennig, editors, *Lasers in Dentistry IX*, volume 4950 of *Proceedings of SPIE*, pages 203–210, San Jose, California, 2003. SPIE.
- [101] Hisashi Watanabe, Kenzo Kataoka, Hideo Iwami, Takeshi Shinoki, Yoshihide Okagami, and Isao Ishikawa. Low-power irradiation of Er : YAG laser using broom-type probe for dentine hypersensitivity. In P. Rechmann, Daniel Fried, and T. Hennig, editors, *Lasers in Dentistry IX*, volume 4950 of *Proceedings of SPIE*, pages 110–114. SPIE, 2003.
- [102] P. WilderSmith, S. Lin, A. Nguyen, L. H. Liaw, A. M. A. Arrastia, J. P. Lee, and M. W. Berns. Morphological effects of ArF excimer laser irradiation on enamel and dentin. *Lasers in Surgery and Medicine*, 20(2):142–148, 1997.
- [103] F. Sánchez, A. J. E. Tost, and J. L. Morenza. ArF excimer laser irradiation of human dentin. *Lasers in Surgery and Medicine*, 21(5):474–479, 1997.
- [104] M. L. Walter, M. E. Domes, R. A. Diller, J. Sproedt, and U. H. Joosten. Photoablation of bone by excimer laser radiation. *Lasers in Surgery and Medicine*, 25(2):153–158, 1999.
- [105] G. J. Pearson. The application of excimer laser radiation to dental hard tissue. *Nanobiology*, 3:223–232, 1994.
- [106] J. P. Moss, B. C. M. Patel, G. J. Pearson, G. Arthur, and R. A. Lawes. Krypton fluoride excimer-laser ablation of tooth tissues - precision tissue machining. *Biomaterials*, 15(12):1013–1018, 1994.
- [107] Daniel Fried and T. S. Breunig. Infrared spectroscopy of laser irradiated dental hard tissues using the advanced light source. In Peter Rechmann, Daniel Fried, and Thomas Hennig, editors, *Lasers in Dentistry VII*, volume 4249 of *Proceedings of SPIE*, pages 99–103. SPIE, 2001.
- [108] B. C. M. Patel, J. Moss, and G. J. Pearson. Excimer-laser (248 nm) drilling of tooth tissue - preliminary investigation. *Lasers in medical Science*, 9(4):243–248, 1994.
- [109] C. R. Wheeler, D. Fried, J. D. B. Featherstone, L. G. Watanabe, and C. Q. Le. Irradiation of dental enamel with Q-switched $\lambda=355$ nm laser pulses: Surface morphology, fluoride adsorption, and adhesion to composite resin. *Lasers in Surgery and Medicine*, 32(4):310–317, 2003.

- [110] K. K. Sheth, M. Staninec, A. V. Sarma, and D. Fried. Selective targeting of protein, water, and mineral in dentin using UV and IR pulse lasers: The effect on the bond strength to composite restorative materials. *Lasers in Surgery and Medicine*, 35(4):245–253, 2004.
- [111] K. Matsumoto, M. Hossain, M. M. I. Hossain, H. Kawano, and Y. Kimura. Clinical assessment of Er, Cr : YSGG laser application for cavity preparation. *Journal of Clinical Laser Medicine & Surgery*, 20(1):17–21, 2002.
- [112] D. G. A. Nelson, J. S. Wefel, W. L. Jongebloed, and J. D. B. Featherstone. Morphology, histology and crystallography of human dental enamel treated with pulsed low-energy infrared-laser radiation. *Caries Research*, 21(5):411–426, 1987.
- [113] M. Forrer, M. Frenz, V. Romano, H. J. Altermatt, H. P. Weber, A. Silenok, M. Istomyn, and V. I. Konov. Bone-ablation mechanism using CO₂ lasers of different pulse duration and wavelength. *Applied Physics B-Photophysics and Laser Chemistry*, 56(2):104–112, 1993.
- [114] Y. Kimura, K. Takahashi-Sakai, P. Wilder-Smith, T.B. Krasieva, L.H.L. Liaw, and K. Matsumoto. Morphological study of the effects of CO₂ laser emitted at 9.3 μm on human dentin. *Journal of Clinical Laser Medicine & Surgery*, 18(4):197–202, 2000.
- [115] Michael J. Zuerlein, Daniel Fried, and John D. B. Featherstone. Modeling the modification depth of carbon dioxide laser treated-dental enamel. *Lasers in Surgery and Medicine*, 25(4):335–347, 1999.
- [116] T. Ertl and G. Muller. Hard-tissue ablation with pulsed CO₂-lasers. *Proceedings of Lasers in Orthopedic, Dental, and Veterinary Medicine II*, 1880:176–181, 1993.
- [117] G. B. Altshuler, A. V. Belikov, A. V. Erofeev, and A. V. Scrypnik. Research of hard tooth tissue acoustic response under contact YAG : Er laser radiation processing. In *Laser Applications in Medicine and Dentistry*, volume 2922 of *Proceedings of SPIE*, pages 228–232. SPIE, 1996.
- [118] C. Apel, J. Meister, R. S. Ioana, R. Franzen, P. Hering, and N. Gutknecht. The ablation threshold of Er : YAG and Er : YSGG laser radiation in dental enamel. *Lasers in Medical Science*, 17(4):246–252, 2002.
- [119] Robert J. Freiberg and Colette Cozean. Pulsed erbium laser ablation of hard dental tissue: the effects of atomized water spray *vs* water surface film. In Peter Rechmann, Daniel Fried, and Thomas Hennig, editors, *Lasers in Dentistry VIII*, volume 4610 of *Proceedings of SPIE*, pages 74–82. SPIE, 2002.

- [120] K. Yamashita, M. Matsuda, T. Arashi, and T. Umegaki. Crystallization, fluoridation and some properties of apatite thin films prepared through RF-sputtering from CaO – P₂O₅ glasses. *Biomaterials*, 19(14):1239–1244, 1998.
- [121] K. L. Vodopyanov. Bleaching of water by intense light at the maximum of the $\lambda \simeq 3 \mu\text{m}$ absorption band. *Soviet Physics JETP – USSR*, 70(1):114–121, 1990.
- [122] K. L. Vodopyanov. Saturation studies of H₂O and HDO near 3400 cm⁻¹ using intense picosecond later-pulses. *Journal of Chemical Physics*, 94(8):5389–5393, 1991.
- [123] R. K. Shori, A. A. Walston, O. M. Stafsudd, D. Fried, and J. T. Walsh. Quantification and modeling of the dynamic changes in the absorption coefficient of water at $\lambda = 2.94 \mu\text{m}$. *IEEE Journal of Selected Topics in Quantum Electronics*, 7(6):959–970, 2001.
- [124] J. P. Cummings and J. T. Walsh. Erbium laser ablation - the effect of dynamic optical-properties. *Applied Physics Letters*, 62(16):1988–1990, 1993.
- [125] J. Meister, R. Franzen, C. Apel, and N. Gutknecht. Influence of the spatial beam profile on hard tissue ablation, Part II: pulse energy and energy density distribution in simple beams. *Lasers in Medical Science*, 19(2):112–118, 2004.
- [126] S. R. Farrar, D. C. Attrill, M. R. Dickinson, T. A. King, A. S. Blinkhorn, and R. M. Davies. Dentine ablation dependency on incident Er : YAG (2.94 μm) laser irradiation conditions. In *Laser Applications in Medicine and Dentistry*, volume 2922 of *Proceedings of SPIE*, pages 209–219. SPIE, 1996.
- [127] J. A. Izatt, N. D. Sankey, F. Partovi, M. Fitzmaurice, R. P. Rava, I. Itzkan, and M. S. Feld. Ablation of calcified biological tissue using pulsed hydrogen-fluoride laser-radiation. *IEEE Journal of Quantum Electronics*, 26(12):2261–2270, 1990.
- [128] P. Serra and J. L. Morenza. Analysis of hydroxyapatite laser ablation plumes in a water atmosphere. *Applied Physics A-Materials Science & Processing*, 67(3):289–294, 1998.
- [129] P. Serra and J. L. Morenza. Imaging and spectral analysis of hydroxyapatite laser ablation plumes. *Applied Surface Science*, 129:662–667, 1998.
- [130] A. Vogel and V. Venugopalan. Mechanisms of pulsed laser ablation of biological tissues. *Chemical Reviews*, 103(2):577–644, 2003.
- [131] D. Fried, M. W. Murray, J. D. B. Featherstone, M. Akrivou, K. M. Dickenson, C. Duhn, and O. P. Ojeda. Dental hard tissue modification and removal using sealed TEA lasers operating at $\lambda = 9.6$ and $10.6 \mu\text{m}$. volume 3593 of *Proceedings of SPIE*, pages 196–203. SPIE, 1999.

- [132] Daniel Fried, Jerome Ragadio, Maria Akrivou, J. Featherstone, Michael W. Murray, and Kevin M. Dickenson. Dental hard tissue modification and removal using sealed transverse excited atmospheric-pressure lasers operating at 9.6 and 10.6 micrometers. *Journal of Biomedical Optics*, 6(2):231–238, 2001.
- [133] G. V. Yuhnevich. *Infrared spectroscopy of water*. Nauka, 1973, in K. L. Vodopyanov, Bleaching of water by intense light at the maximum of the wavelength $\lambda \simeq 3 \mu\text{m}$ absorption band, *Soviet Physics Jetp-Ussr*, 70(1): 114-121, 1990.
- [134] Boris Majaron and Matjaz Lukac. Thermo-mechanical laser ablation of hard dental tissues: an overview of effects, regimes, and models. In John D. B. Featherstone, P. Rechmann, and D. Fried, editors, *Lasers in dentistry V*, volume 3593 of *Proceedings of SPIE*, pages 184–195. SPIE, 1999.
- [135] David S. Burnett. *Finite element analysis: from concepts to applications*. Addison-Wesley Publishing Company, Reading, Massachusetts, 1988.
- [136] Daryl L. Logan. *A first course in the Finite Element Method using AlgorTM*. Brooks/Cole Thompson Learning, Pacific Grove, California, USA, 2001.
- [137] ABAQUS. *Getting started with ABAQUS 6.5*. ABAQUS, Inc., USA, 2005.
- [138] Marshall Stoneham, Marta M. D. Ramos, and Ricardo Mendes Ribeiro. The mesoscopic modelling of laser ablation. *Applied Physics A*, 69(supplement):S81–S86, 1999.
- [139] A. M. Stoneham and J. H. Harding. Not too big, not too small: The appropriate scale. *Nature Materials*, 2(2):77–83, 2003.
- [140] B. Majaron, P. Plestenjak, and M. Lukac. Thermo-mechanical laser ablation of soft biological tissue: modeling the micro-explosions. *Applied Physics B - Lasers and Optics*, 69(1):71–80, 1999.
- [141] Leonid V. Zhigilei, Prasad B. S. Kodali, and Barbara J. Garrison. Molecular dynamics model for laser ablation and desorption of organic solids. *Journal of Physical Chemistry B*, 101:2028–2037, 1997.
- [142] L. G. Berry and Brian Mason. *Mineralogy - concepts, descriptions, determinations*. A series of books in geology. W. H. Freeman and Company, USA - San Francisco, 1 edition, 1959.
- [143] H. H. Moroi, K. Okimoto, R. Moroi, and Y. Terada. Numeric approach to the biomechanical analysis of thermal effects in coated implants. *International Journal of Prosthodontics*, 6:564–572, 1993. (In "Dental Tables" at <http://www.lib.umich.edu/>).

- [144] M. Braden. Biophysics of the tooth. In Yojiro Kawamura, editor, *Physiology of Oral Tissues*, volume 2 of *Frontiers of Oral Physiology*, pages 1–37. S. Karger AG, Basel, 1976.
- [145] D. E. Grenoble, J. L. Katz, K. L. Dunn, R. S. Gilmore, and K. L. Murty. The elastic properties of hard tissues and apatites. *Journal of biomedical materials research*, 6(3):221–223, 1972. (In "Dental Tables" at <http://www.lib.umich.edu/>).
- [146] J. Czernuszka. Hydroxyapatite. In David Bloor, M. C. Flemings, R. Brook, S. Mahajan, and R. Cahn, editors, *The encyclopedia of advanced materials*, volume 4, page 1076. Elsevier Science Ltd, Cambridge, Great Britain, 1st edition, 1994.
- [147] Jeffery R. Cooper and Edwin J. Le Fevre. *Thermophysical properties of water substance - Student's tables in SI units*. Edward Arnold Ltd, London, 1975.
- [148] R. Q. Erkamp, S. Y. Emelianov, A. R. Skovoroda, X. Chen, and M. O'Donnell. Exploiting strain-hardening of tissue to increase contrast in elasticity imaging. In *2000 IEEE Ultrasonics Symposium Proceedings, Vols 1 and 2*, Ultrasonics Symposium, pages 1833–1836. IEEE, New York, 2000.
- [149] S. A. D. Wiesche, C. Rembe, and E. P. Hofer. Boiling of superheated liquids near the spinodal: I general theory. *Heat and Mass Transfer*, 35(1):25–31, 1999.
- [150] S. A. Wiesche, C. Rembe, and E. P. Hofer. Boiling of superheated liquids near the spinodal: II application. *Heat and Mass Transfer*, 35(2):143–147, 1999.
- [151] R. L. Bowen and M. S. Rodriguez. Tensile strength and modulus of elasticity of tooth structure and several restorative materials. *Journal of the American Dental Association*, 64(3):378–387, 1962. (In 'Dental Tables' at <http://www.lib.umich.edu/>).
- [152] R. G. Craig, D. W. Johnson, and F. A. Peyton. Compressive properties of enamel, dental cements, and gold. *Journal of Dental Research*, 40(5):936–945, 1961. (In 'Dental Tables' at <http://www.lib.umich.edu/>).
- [153] J. C. Elliott, F. S. L. Wong, P. Anderson, G. R. Davis, and S. E. P. Dowker. Determination of mineral concentration in dental enamel from X-ray attenuation measurements. *Connective Tissue Research*, 39(1-3):61–72, 1998.
- [154] C. G. Lyons. Simple equation of state for dense fluids. *Journal of Molecular Liquids*, 69:269–281, 1996.

- [155] S. Wiryana, L. J. Slutsky, and J. M. Brown. The equation of state of water to 200 °C and 3.5 GPa: model potentials and the experimental pressure scale. *Earth and Planetary Science Letters*, 163(1-4):123–130, 1998.
- [156] B. H. Ji and H. J. Gao. Mechanical properties of nanostructure of biological materials. *Journal of the Mechanics and Physics of Solids*, 52(9):1963–1990, 2004.
- [157] D. Fried, R. Shori, and C. Duhn. Backspallation due to ablative recoil generated during Q-switched Er:YAG ablation of dental hard tissue. volume 3248 of *Proceedings of SPIE*, pages 78–85. SPIE, 1998.

Annex 1: names of input files for the simulations reported

The purpose of this Annex is to allow anyone intending to continue this work to relate the models described in this Thesis with the input and results electronic files produced during this work.

Model	Simulation names
Large	s14, s15
Large, Natural frequencies	testBC_large_NatFreq, s137, s138, s159, s160, s161
TestBC1	s1, s2, s43
TestBC1, Natural frequencies	s135, s136, s180, s181
TestBC2	s10, s12, s16
CubesHom_CO2_1.2e10	cube_mesh7_Thermal, s57
RodHom_CO2_1.2e10	s44, s53
RodWL_CO2_1.2e10	s45, s54, s58, s59
RodWL_Er_1.2e10	s48
RodWL_Er_6.2e9	s49, s56
RodsPores_CO2_1.2e10	s47,s61
RodsPores_Er_1.2e10	s51, s63
SmallPore30	s75, s76, s79, s80
SmallPore70	s55, s64, s65, s70 to s74, s83 to s85
SmallPore130	s77, s78, s81, s82
Models to investigate the effect of the pulse duration	s17 to s40

Annex 2: example of a UMAT subroutine used to model the EOS of water

```

C Real variables start with the letters A through H and O through Z
C Integers start with I,J,K,L,M,N
C Vol = STATEV(1); current volume of the element
C V0 = STATEV(2); initial volume of the element (NEEDS TO BE STATEV BECAUSE NEEDS TO PASS TO
UEXPAN)
C R = is specific gas constant for water vapour, in J/kg/°K; CHECK THIS!,
cccccccccccccccccccccccccccccccccccccccccccccccccccccccccccccccccccccccccccccccccccc
cccccc
C
C SUBROUTINE UMAT(STRESS,STATEV,DDSDDE,SSE,SPD,SCD,
1 RPL,DDSDDT,DRPLDE,DRPLDT,STRAN,DSTRAN,
2 TIME,DTIME,TEMP,DTEMP,PREDEF,DPRED,MATERL,NDI,NSHR,NTENS,
3 NSTATV,PROPS,NPROPS,COORDS,DROT,PNEWDT,CELENT,
4 DFGRD0,DFGRD1,NOEL,NPT,KSLAY,KSPT,KSTEP,KINC)
C
C INCLUDE 'ABA_PARAM.INC'
C
C CHARACTER*80 MATERL
C DIMENSION STRESS(NTENS),STATEV(NSTATV),
1 DDSDDT(NTENS,NTENS),DDSDDT(NTENS),DRPLDE(NTENS),
2 STRAN(NTENS),DSTRAN(NTENS),TIME(2),PREDEF(1),DPRED(1),
3 PROPS(NPROPS),COORDS(3),DROT(3,3),
4 DFGRD0(3,3),DFGRD1(3,3)
C PARAMETER (Patm =99865.0)
C
C -----
C
C STATEV(1) = volume of element that represents the gas
C
C IF ((NOEL .EQ. 45163)) THEN
C IF (NPT .EQ. 1) THEN
C PRINT*," "
C END IF
C print*, "UMAT kstep and kinc is :", kstep, kinc
C print*,"element and integration point number are :",NOEL,NPT
C END IF
C
C ccccccccccccccccccccccccccccccccccccccccccccccccccccccccccccccccccccccccccccccccccccc
C IF ((kstep .EQ. 1) .AND. (kinc .EQ. 0)) THEN
C GO TO 100
C END IF
C
C ccccccccccccccccccccccccccccccccccccccccccccccccccccccccccccccccccccccccccccccccccccc
C if ((KSTEP .EQ. 1) .AND. (KINC .LE. 1)) THEN
C Initializing the shear components of stress, which don't have meaning in a gas.The init
ial stress is zero (it's the gauge pressure)
C DO 40 K1=1, NTENS
C stress(k1) = 0.
C 40 continue
C
C Initializing the user state variables (V is divided by the number of integration points
)
C V0 = props(1)/8.0
C STATEV(1) = props(1)/8.
C
C STATEV(2) = V0
C
C Initializing other variables.
C
C RPL = 0.
C DRPLDT=0.
C DO 60 K1=1, NTENS
C ddsddt(k1)=0.
C DRPLDE(k1)=0.
C DO 59 K2=1, NTENS
C DDSDDT(K1,K2) =0.
C 59 continue
C 60 continue
C END IF
C -----
C Calculate mass of water in 1/8 of the pore (at T = 37 °C and P = 1e5 Pa, v_m is 1.006726865
E-03 m3/kg)
C Vol = STATEV(1)
C V0 = STATEV(2)
C RmL = V0/(1.006726864759450E-03*1e18)

```

```

Tf = temp + dtemp

IF ((NOEL .EQ. 45163)) THEN
    print*,"current volume of 1/8 of the element ", Vol
    print*,"1/8 of volume of the cavity at the beginning of analysis
& is ", V0
C
C-----
C Calculate current increment in Volume
C
    print*,"strain increments are", dstran(1), dstran(2), dstran(3)
    print*,"temperature increment is ",dtemp
    End IF
C Calculate the increment in volume that the element undergoes in this iteration
    RDV = dstran(1)*Vol
    Vol = Vol + RDV
    RTDV = RDV
    IF ((NOEL .EQ. 45163)) THEN
        print*,"RDV IS ",RDV
        print*,"Vol IS ",Vol
        END If
    RDV = dstran(2)*Vol
    Vol = Vol + RDV
    RTDV = RTDV + RDV

    IF ((NOEL .EQ. 45163)) THEN
        print*,"RDV IS ",RDV
        print*,"Vol IS ",Vol
        END If
    RDV = dstran(3)*Vol
    Vol = Vol + RDV
    RTDV = RTDV + RDV
    IF ((NOEL .EQ. 45163)) THEN
        print*,"RTDV (change of volume of 1/8 of the element) is ",RTDV
        print*,"Current (updated) vol of 1/8 of the element is",statev(1)
        END If
c Update state variables to new values
    STATEV(1) = Vol
c
    Volm = Vol*1e-18
C Converting volume in microns3 to metres3
C
C Converting the temperature in kelvin to the temperature in Celsius
    Tc = Tf - 273.0

C Calculate Jacobian (the sign is inverted because compressive stress is
C negative in abaqus)
    DO 70 K1=1, NDI
        DO 69 K2=1, NDI
            CALL KDDSDDE(RmL,Volm,Tc,V0_T,A_T,B_T,DSDE)
            DDSDDDE(K1,K2) = - DSDE*1.0e-12
69 continue
70 continue
C Calculate ddsddt, using an approximation of the equation by Lyons (see
C file DerivingDDSDDTForEOSwater.mws
    DO 80 K1=1, NDI
        CALL KDDSDDT(Tc,DSDT)
        DDSDDT(K1) = - DSDT*1.0e-12
80 continue
C Calculate stress
    call KStressInLiquid(RmL,Volm, strs,Tc,NOEL,V0_T,A_T,B_T)
    Gstress = strs - Patm
    IF (Gstress .LT. 0.0) THEN
        print*,"gauge stress is less than zero",NOEL,Kinc
    END IF
C The above calculation is done in N/m2.
    DO 90 K1=1, NDI
        stress(k1) =-Gstress*1.0e-12
c The minus sign means stress is compressive; 1e-12 is converting stress to N/m2
90 continue
C
Cpossibly define Pnewdt.
100 IF ((NOEL .EQ. 45163)) THEN
    print*,"Final Vol of the element", STATEV(1)
    print*,"temperature at the end is ", Tf
    print*," updated stress is", stress(1), stress(2), stress(3)

```

```

        print*,"-----"
        IF ((NPT .EQ. 1) .AND. (kstep .EQ. 1)) THEN
            PRINT*," "
        END IF
    END IF
    RETURN
END
c

C
CCCCCCCCCCCCCCCCCCCCCCCCCCCCCCCCCCCCCCCCCCCCCCCCCCCCCCCCCCCCCCCCCCCCCCCCCCCCCCCCCCCCCCCCCCCCCCCCCCCCCCCCCCCC
C
    SUBROUTINE KStressInLiquid(RmL,Vol, strs,T,NOEL,V0_T,A_T,B_T)
    INCLUDE 'ABA_PARAM.INC'

C        Rm_Vol is the mass per unit volume in m3/kg. Not necessary for anything I think.Vol i
s the volume of
C        the element. The parameters to fit an EOS for water were
C        obtained from Lyons. Check file: initialPressureWaterForEOS100MPa.xls

    Vol_M = Vol/RmL

    strs = B_T*(EXP(1.0/A_T*(1.0 - Vol_M/V0_T)) - 1.0)
    IF ((strs .LT. 0.9e5) .OR. (strs .GT. 150e6)) THEN
        print*,strs,NOEL,"WARNING!!STRESS OUTSIDE BOUNDARIES!in N/m2:"
        print*,"temperature (°C) is",T
        print*,"volume (m3) of the cavity is",Vol
        print*,"mass (kg) of water in the cavity is",RmL
        print*,"V0_T is",V0_T
        print*,"A_T is",A_T
        print*,"B_T is",B_T
        print*,"stress is (in Pa) ",strs
        print*,"Volume per unit mass (m3/kg) of water ",Vol_M
        print*,"*****"
    END IF
    IF (T .GT. 200.0) THEN
        print*,"WARNING! TEMPERATURE OUTSIDE BOUNDARIES"
    END IF
    IF ((NOEL .EQ. 45163)) THEN
        print*,"temperature (°C) is",T
        print*,"volume (m3) of the cavity is",Vol
        print*,"mass (kg) of water in the cavity is",RmL
        print*,"V0_T is",V0_T
        print*,"A_T is",A_T
        print*,"B_T is",B_T
        print*,"stress is (in Pa) ",strs
        print*,"Volume per unit mass (m3/kg) of water ",Vol_M
    END IF
    END SUBROUTINE KStressInLiquid
CCCCCCCCCCCCCCCCCCCCCCCCCCCCCCCCCCCCCCCCCCCCCCCCCCCCCCCCCCCCCCCCCCCCCCCCCCCCCCCCCCCCCCCCCCCCCCCCCCCCCCCCCCCC

    SUBROUTINE KDDSDDE(RmL,Vol,T,V0_T,A_T,B_T,DSDE)
    INCLUDE 'ABA_PARAM.INC'
    PARAMETER (csi1=-6.108045066100000E-05,csi2=8.264221476200000E-06,
& csi3=-6.251915225100000E-08, csi4=3.965777721400000E-10,
& csi5=-1.037661158500000E-12, eta1=1.834479123900E-03,
& eta2=-3.948322092800E-05, eta3=1.327562659600E-07,
& zeta1=9.432398627200E-03, zeta2=-1.436967029300E-04,
& zeta3=4.560812490500E-07,V_p0t0=0.0010002119572,A0=0.13848005907,
& B0=270541232.2)

    V0_T = V_p0t0*(1.0 + csi1*T + csi2*T**2 + csi3*T**3 + csi4*T**4 +
& csi5*T**5)
    A_T = A0*(1.0 + eta1*T + eta2*T**2 + eta3*T**3)
    B_T = B0*(1.0 + zeta1*T + zeta2*T**2 + zeta3*T**3)

    DSDE = -Vol/V0_T/RmL/A_T*exp(-(Vol - V0_T*RmL)/V0_T/RmL/A_T)*B_T
    print*,"V0_T, A_T, B_T, Vol,RmL, dsde",V0_T,A_T, B_T, Vol,RmL,dsde

    END SUBROUTINE KDDSDDE

    SUBROUTINE KDDSDDT(T,DSDT)
    INCLUDE 'ABA_PARAM.INC'

```

```
IF (T .LT. 60.0) THEN
  DSDT=778526.
ELSE IF ((T .LT. 100.0) .AND. (T .GT. 60.0)) THEN
  DSDT = 0.12e7
ELSE IF ((T .LT. 200.0) .AND. (T .GT. 100.0)) THEN
  DSDT=0.16e7
END IF
print*,"dsdt is",dsdt
END SUBROUTINE KDDSDDT
```

Annex 3: summary table for Chapter 3

	Thermal damage	Mechanical damage	Surface morphology	Adhesion strength to resin	Chemical modification of the surface	Resistance to acids	Ablation rates	Pulpal Long tunnels temperature	Toxic effect
Er:YAG, free-running	enamel, water	some	micro cracks	rods exposed; scaly and uneven	bad, but can be improved by other treatments	some non-HA phases	ok	water may cause problems	ok
	enamel, no water	bad	bad				bad because of cracks, but can be fixed by applying fluoride		
	dentine, water	none	none	exposed dentinal tubules, scaly	bad, but can be improved by other treatments	minor	ok	water may cause problems	ok
	dentine, no water	bad	some; extensive				ok		
Er:YAG, Q-switched	enamel, water	small	none					maybe	
	enamel, no water	not good							medium-high
	dentine, water								medium-high
ArF, 193 nm	enamel, no water	none at low fluences	none at low fluences				low, but OK		high
	dentine, no water	none at low fluences	none at low fluences	sealed dentinal tubules at high F			low, but OK		high
KrF, 248 nm	enamel, no water	some	none	exposed rods at low F		none at low F	low, but OK	yes	lower
	dentine, no water	little	bad	exposed tubules at low F			low, but OK	yes	lower

	Thermal damage	Mechanical damage	Surface morphology	Adhesion strength to resin	Chemical modification of the surface	Resistance to acids	Ablation rates	Pulpal Long tunnels temperature	Toxic effect
Nd:YAG, 355 nm	enamel, water enamel, no water dentine, water dentine, no water	none; a lot at high F none even greater extensive	exposed rods highly uniform	ok, but needs improvement	none	lower, but can be fixed by applying			
Er:YSGG, free-running	enamel, water enamel, no water dentine, water dentine, no water	some extensive ? extensive	brushes off easily brushes off easily			bad because of cracks	ok ok		
Er:YSGG, Q-switched	enamel, water enamel, no water dentine, water dentine, no water	none; some ? ?	uniform	ok, but needs improvement			ok		
Er,Cr:YSGG, free-running	enamel, water enamel, no water dentine, water dentine, no water	none ? ?	smooth		none				

	Thermal damage	Mechanical damage	Surface morphology	Adhesion strength to resin	Chemical modification of the surface	Resistance to acids	Ablation rates	Pulpal temperature	Toxic effect
CO ₂ , 9.3 μm, long pulse	enamel, water enamel, no water dentine, water dentine, no water	some	some; extensive				increased		
CO ₂ , 9.3 μm, short pulse	enamel, water enamel, no water dentine, water dentine, no water	bad	bad		extensive non-HA phases at high F		increased		
CO ₂ , 9.6 μm, long pulse	enamel, water enamel, no water dentine, water dentine, no water	some some; extensive	none none		extensive non-HA phases at high F extensive non-HA phases at high F				
CO ₂ , 9.6 μm, short pulse	enamel, water enamel, no water dentine, water dentine, no water	variable bad little some	ok bad none none	ok, but needs improvement	little extensive non-HA phases at high F none		increased ok		

	Thermal damage	Mechanical damage	Surface morphology	strength to resin	modification of the surface	Resistance to acids	Ablation rates	Pulpal Long tunnels temperature	Toxic effect
CO ₂ , 10.3 μm, long pulse enamel, water enamel, no water dentine, water dentine, no water									
CO ₂ , 10.3 μm, short pulse enamel, water enamel, no water dentine, water dentine, no water	bad	bad			extensive non-HA phases at high F				
CO ₂ , 10.6 μm, long pulse enamel, water enamel, no water dentine, water dentine, no water							ok		
CO ₂ , 10.6 μm, short pulse enamel, water enamel, no water dentine, water dentine, no water	bad	bad			extensive non-HA phases at high F				
CO ₂ , 10.6 μm, short pulse dentine, plasma is formed no water	higher when plasma is formed						ok		

F - fluence

? - inconclusive based on the articles read